Technical Report Documentation Page

1. Report No. FHWA/TX-09/0-5825-1	2. Government Accession No.	3. Recipient's Catalog No.
4. Title and Subtitle Effect of Verification Cores on Tip Capacity of Drilled Shafts		5. Report Date October 2008; Revised February 2009
		6. Performing Organization Code
7. Author(s) Fulvio Tonon, Heejung Youn, Anay P. Raibagkar		8. Performing Organization Report No. FHWA/TX-08/0-5825
9. Performing Organization Name and Address Center for Transportation Research The University of Texas at Austin 3208 Red River, Suite 200 Austin, TX 78705-2650		10. Work Unit No. (TRAIS)
		11. Contract or Grant No. 0-5825
12. Sponsoring Agency Name and Address Texas Department of Transportation Research and Technology Implementation Office P.O. Box 5080 Austin, TX 78763-5080		13. Type of Report and Period Covered Technical Report September 2006-August 2008
		14. Sponsoring Agency Code
15. Supplementary Notes Project performed in cooperation with the Texas Department of Transportation and the Federal Highway Administration.		

16. Abstract

This research addressed two key issues:

1) Will verification cores holes fill during concrete backfilling? If so, what are the mechanical properties of the filling material? In dry conditions, verification core holes always completely fill with concrete whose compressive strength is of equal strength to the concrete in the drilled shaft column. In wet conditions, the bottom half of the verification core hole fills with non-cemented gravel-sand mixture ($\varphi = 52°$), while the upper half of the verification core hole filled with weakly cemented material ($V_p = 2000$ fps).

2) When drilling in materials, such as shales, susceptible to degradation: does this degradation specifically around shaft verification core holes affect point bearing capacity? The shear strength of Del Rio Clay and Eagle Ford Shale is not affected by drying-duration, but is related to water content; the shear strength of Taylor Marl and Navarro Shale decreases considerably as drying-duration increases. The elastic modulus of all four clay shales drops significantly when clay shales are dried and then wetted.

When shales are first dried and then rewetted and concrete is poured in the wet, the verification core hole reduces tip capacity by a maximum of 10% (14% for Taylor Marl). In all other cases, the verification core does not decrease the tip capacity.

17. Key Words Drilled shafts; clay shales; verification core; concrete flow.	18. Distribution Statement No restrictions. This document is available to the public through the National Technical Information Service, Springfield, Virginia 22161; www.ntis.gov.
19. Security Classif. (of report) Unclassified	20. Security Classif. (of this page) Unclassified	21. No. of pages 398	22. Price

Form DOT F 1700.7 (8-72) Reproduction of completed page authorized

Effect of Verification Cores on Tip Capacity of Drilled Shafts

Fulvio Tonon
Heejung Youn
Anay P. Raibagkar

Disclaimers

Author's Disclaimer: The contents of this report reflect the views of the authors, who are responsible for the facts and the accuracy of the data presented herein. The contents do not necessarily reflect the official view or policies of the Federal Highway Administration or the Texas Department of Transportation (TxDOT). This report does not constitute a standard, specification, or regulation.

Patent Disclaimer: There was no invention or discovery conceived or first actually reduced to practice in the course of or under this contract, including any art, method, process, machine manufacture, design or composition of matter, or any new useful improvement thereof, or any variety of plant, which is or may be patentable under the patent laws of the United States of America or any foreign country.

Notice: The United States Government and the State of Texas do not endorse products or manufacturers. If trade or manufacturers' names appear herein, it is solely because they are considered essential to the object of this report.

Engineering Disclaimer

NOT INTENDED FOR CONSTRUCTION, BIDDING, OR PERMIT PURPOSES.

Project Engineer: Fulvio Tonon
Professional Engineer License State and Number: Texas No. 101441
P. E. Designation: "Research Supervisor"

Acknowledgments

Table of Contents

List of Figures

xiv

List of Tables

PREFACE

Verification cores are important tools in ascertaining the condition and properties of the bedrock at the bottom of drilled shafts. Item 416.3 B of the TxDOT Standard Specifications for Construction and Maintenance of Highways, Streets and Bridges (2004) states: "Core Holes. If directed, take cores to determine the character of the supporting materials. Use a method that will result in recovery of an intact sample adequate for judging the character of the founding material. Such cores should be at least 5 ft. deeper than the proposed founding grade or a depth equal to the diameter of the shaft, whichever is greater. Take these cores when the excavation is approximately complete." For example, it is usual practice in the Dallas District to obtain one verification core at least at every bridge bent.

However, the influence of verification cores on the point bearing capacity of drilled shafts is still unknown. This research addressed two key issues:

1) Will the verification cores fill during concrete backfilling? If so, what are the mechanical properties of the filling material?
2) When drilling in materials, such as shales, susceptible to degradation: how are the mechanical properties of shales affected by a cycle of drying and re-wetting?

With this knowledge at hand we then investigated the overall effect of verification cores on the point bearing capacity. The work plan, completed in two years (between September 2006 and August 2008), comprised eight tasks as follows:

1) Review of the existing literature.
2) Lab tests and scale lab tests of borehole at bottom of shaft.
3) Large degradation tests on moisture sensitive materials.
4) Tests on concrete filling.
5) Numerical modeling of the detrimental effect of coring.
6) Remedial actions that could be taken to lessen the impact of verification holes.
7) Report writing.
8) Coordination meetings with PC, PD, and PAs.

Tasks 1 through 4 were meant to provide the data to proceed with numerical modeling of the detrimental effect of coring at the base of a drilled shaft. Task 6 was not carried out because we found that the impact of the verification core is minimal.

Chapter 1 reports on Tasks 1 through 3, Chapter 2 covers Task 4, and Chapter 3 deals with Task 5.

Chapter 1. DEGRADATION OF TEXAS SHALES AROUND VERIFICATION CORES

1.1 INTRODUCTION

1.1.1 Problem Statement

For many projects involving drilled shafts, cores are to be taken below the shaft base for visual identification of the underlying material. For example, the Texas Department of Transportation (TxDOT) requires a core length of at least 1.5 m (5 ft) or equal to the shaft diameter, whichever is greater, at the shaft base (Item 416, Texas Department of Transportation, 2004). The TxDOT geotechnical manual also recommends using the point bearing capacity obtained from the softer layer if the softer layer exists twice within the shaft diameter (Texas Department of Transportation, 2006). This signifies the importance of obtaining core at the base. State Departments of Transportation recommending these cores include Alabama, Colorado, Connecticut, Florida, Georgia, Hawaii, Kansas and Texas (Vipulanandan et al., 2007). Such cores are called "verification cores." Although the verification cores are to be excavated at the shaft tip, TxDOT does not have provisions to eliminate the effect of the verification core hole on the point bearing capacity. The point bearing capacity of drilled shafts may be reduced by 40% when the verification core hole whose diameter is 40% of shaft diameter (D) is not filled during concrete placement (Vipulanandan et al., 2007).

In Chapter 2, it is shown that the verification core hole is filled with concrete in dry pour and with a sand-gravel mixture in a wet or "underwater" pour. The sand-gravel mixture results from the cement passed being washed out of the concrete mixture as the fluid is displaced out of the core hole. This finding is crucial since the point bearing capacity of drilled shafts with an unfilled hole at the shaft tip should be significantly lower than that of drilled shafts without a verification hole. Furthermore, it may assure that the verification core does not negatively impact the point bearing capacity of drilled shafts. However, the exposure of the core holes to air drying may have an adverse effect on the point bearing capacity, especially when the founding material is susceptible to weathering. In addition, the engineering behavior of sand-gravel mixture may result in reduced point bearing capacity. In Chapter 1, the effect of the verification core hole on the point bearing capacity has been thoroughly investigated with emphasis on changes in the material properties of four clay shales (Del Rio Clay, Eagle Ford Shale, Taylor Marl, and Navarro Shale) in central Texas.

1.1.2 Objective of Chapter 1

Clay shales are sedimentary rocks that frequently cause difficulties in geotechnical practice because of their unpredictable behavior and poor durability. In north-central Texas, clay shales that contain large amounts of expansive minerals are commonly encountered at construction sites. These clay shales are notorious for their high swelling potential in the presence of water and shrinkage upon drying, which creates challenges for construction of slopes, highway embankments, dam abutments, and

3

foundations. The current research arises because the shafts drilled in Texas are frequently constructed on such unfavorable clay shales. The main objective of Chapter 1 is to evaluate the point bearing capacity of drilled shafts with the verification core hole at the shaft tip.

Figure 1.1.1 exhibits the probable process of degradation as a result of advancing the verification core hole during construction. The verification core holes are excavated at the bottom of drilled shafts, which allows unweathered clay shales to contact with air and to dry. The clay shales surrounding the verification hole tend to crack through the weakest bedding planes as a result of moisture loss. Clay shales adjacent to the verification core hole start drying first, consequently inner shales dry with continued exposure to air. The verification core hole stops drying when either water flows into the core hole or concrete is poured.

Reduction of point bearing capacity may occur when the dried clay shales at the perimeter of the verification core come in contact with water. Water typically flows into the core due to a high ground water table. The clay shales with high slaking potential degrade considerably, especially at the surface of the core. The degradation is magnified due to water migration through developed cracks, which results in slaking through them in addition to the slaking at the surface. The schematic degraded zone around the verification core hole is depicted in Figure 1.1.1 (d). The extent of degradation may vary widely depending on founding materials, drying-duration, geometry of the verification core hole, and many other factors.

In order to assess any change in point bearing capacity by the verification core, two questions should be answered. 1) How much is the degradation of engineering properties of clay shales induced by drying and wetting? Three kinds of laboratory tests were conducted on six formations, four clay shales and two relatively hard, durable sedimentary, rocks. Series of multi-stage triaxial tests were carried out to evaluate the decrease in strength of the formation as drying-duration changes. The slake durability test and jar slake test were carried out to evaluate the durability of the formation. 2) How far does the degraded zone extend at the perimeter of the verification core hole? In order to investigate the thickness of the degraded zone, a full scale condition degradation test was carried out in Eagle Ford Shales by drilling and drying 18 non-production, drilled, shaft holes. Engineering properties of Eagle Ford Shale obtained from the full scale condition test were measured in terms of the unconfined compressive strength test (UCS) and point load test (PLT). Results from the full scale condition test were later used to predict the thickness of the degraded zone.

After the engineering properties and the limits of the degraded zone were determined, a series of numerical analyses were performed to estimate the effect of the verification core hole on the point bearing capacity. Engineering properties including friction angle, cohesion, and elastic modulus were derived from results of laboratory testing, and the properties were assigned to the predetermined degraded zone determined from the full scale condition test. Furthermore, the engineering properties of the material that in fills the verification core hole were obtained from Chapter 2 and were assigned to the material in the core hole: either concrete or sand-gravel mixture. The Finite Element Method (FEM) software, PLAXIS, was used for parametric studies for evaluating the effect of the verification core on point bearing capacity. The analyses quantify the effect of the verification core hole on the point bearing capacity of drilled shafts.

Shaft Hole

Introduction of air
to core holes

Unweathered
Shale

Verification
Core hole

(a) Air drying the verification core hole

Air drying

Possible cracks
created by air drying
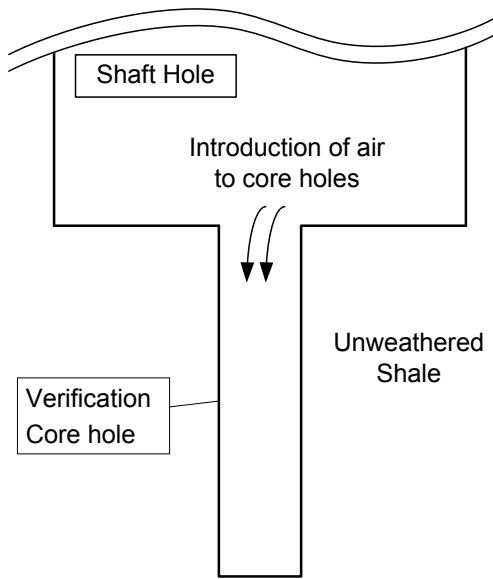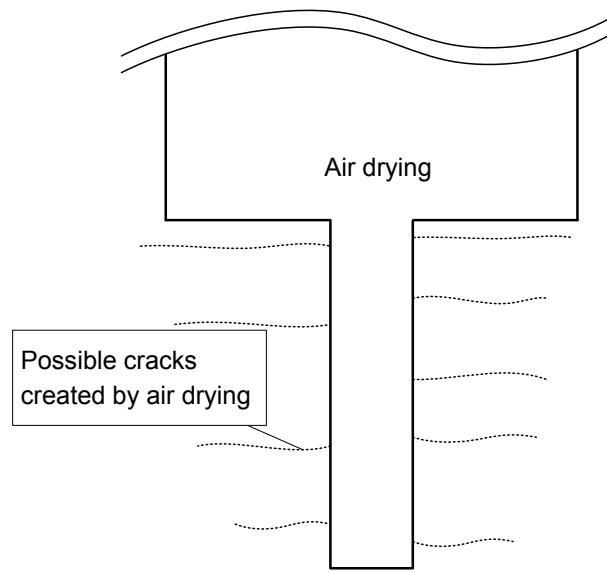
(b) Crack start developing at
the perimeter of the core

Water inflow

Slaking
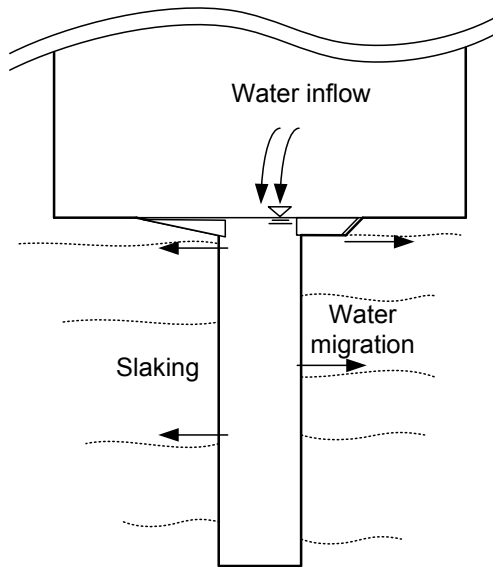
Water
migration

(c) Water flows into the core, and
slaking occurs at the surface and
through the cracks

Falling shale
chips
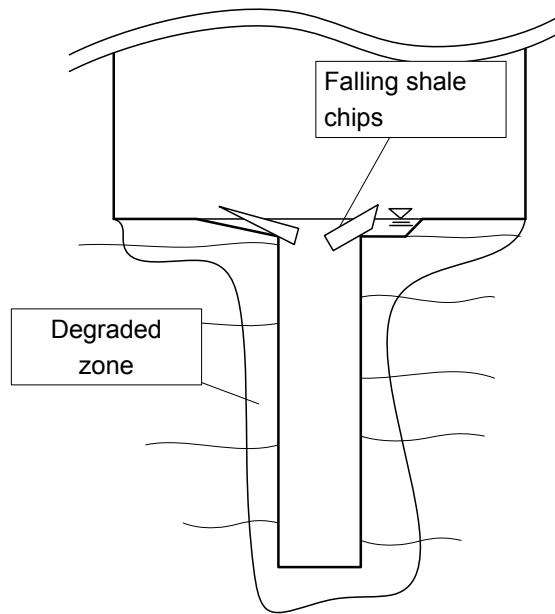
Degraded
zone

(d) Degraded zone at the perimeter
of verification core

Figure 1.1.1 Schematic procedure of drying and wetting induced by a verification core hole

1.1.3 Organization

Section 1.2 presents rock classification systems for weak rock and clay shales, weathering phenomenon of clay shales, and the literature review of drilled shafts in weak rock. In Section 1.3, geology of the Dallas and Austin area is reviewed, and available literature of engineering properties are collected for reference. Index tests to evaluate water reactivity of clay shales were carried out and the results are displayed. Section 1.4 presents laboratory testing devices and methodology adopted to perform the triaxial test, unconfined compressive strength test, point load test, slake durability test, and jar slake test. Section 1.5 provides the engineering properties of four clay shale formations and two hard rock formations after they were dried and wetted. All tests follow the procedures described in Section 1.4, and the results obtained are used to determine whether the tested clay shales are degradable or not. In Section 1.6, the thickness of the degraded zone around the verification core is determined from a full scale condition degradation test. The cores from the full scale condition test were tested in the laboratory, and the results used to define the degraded zone.

1.2 LITERATURE REVIEW

1.2.1 Introduction

Argillaceous rock, which comprises about half the sedimentary rock on earth, is made chiefly of fine-grained aluminosillicates, particularly clay minerals such as montmorillonite, kaolinite, illite, and chlorite. Other minerals include quartz and feldspar, mica, serpentine, iron minerals, calcite, dolomite, and organic matter (Goodman, 1993). The depositional environment of argillaceous rocks is under lakes, ocean seawater, or swamps where the finest particles settle very slowly. In spite of their frequent appearances on the earth, the geological classification for argillaceous rocks has not been standardized (Goodman, 1993). Moreover, in geotechnical practice, the classification system needs to be based on engineering properties rather than geological characteristics. Another important factor to the argillaceous rock is durability since the rock contains large amounts of clay minerals. The clay minerals contribute significantly to the durability of the rocks. Therefore, the incipient engineering properties may vary according to the various environmental influences during the design life of structures.

In this section, various rock classifications are introduced to define weak rock and contrast it to strong or durable rock. The mechanisms of disintegration of weak and/or non-durable rock, which are induced by a drying wetting cycle, then are reviewed. In addition, a database of tip resistance of drilled shafts is developed and reviewed.

1.2.2 Rock Classification

The clay shales are an intermediate geo-material. Soil engineers, who consider such formations soil, and geologists, who consider them rock, have compromised with the terms clay shale or clayey shale (Morgenstern, 1979). In spite of the compromise, intermediate geo-materials are still difficult to identify and classify.

From the engineering point of view, fresh rocks, as opposed to weathered rocks, are typically less problematic because most fresh rock units tend to display stiff and strong behavior to the applied structural load. Furthermore, strong rock tends to resist environmental attacks (durable). On the other hand, weak rocks attract many engineers' attention, as weak rocks tend to be softer and degrade easily upon weathering (non-durable). Therefore, various well-developed classification systems have been suggested to distinguish the problematic non-durable rocks from durable rocks, particularly when the structure is susceptible to water.

Typical attributes of intact rock that maybe used to characterize rock are tabulated in Table 1.2.1. The number of such attributes implies the wide variability of rocks. Existing classification systems for intact samples are typically based on five properties: 1) strength, 2) Young's modulus, 3) lithology, 4) anisotropy, and 5) durability.

Table 1.2.1 Typical attributes of intact rock sample classification systems (Deen, 1981)

Anisotropy	Moisture content
Lithology	Petrofabrics
Slake durability	Porosity
Tensile strength	Seismic velocity
Compressive strength	Shear
Density	Swelling
Drillability	Tangent modulus
Dry specific gravity	Texture
Failure characteristics	Toughness
Hardness	Unit weight
Hysteresis	Weatherability

Table 1.2.2 Typical attributes of classification system for in situ rock (Deen, 1981)

Rock quality
    bedding character
    joint frequency
    joint characteristics
    faulting characteristics
    weatherability or alteration
 	
Orientation of discontinuities
 	
Deformation characteristics
 	
Velocity ratio
 	
Engineering performance
    slope stability
    powder factor
	Intact sample tests
	    uniaxial compression
	    sonic
	    saturated sonic
	    static modulus
	    point loading
	    slake
	
	In situ tests
	    seismic
	    plate jacking
	    permeability
	
	Ground water condition
	
	Lithology

As compared to intact rock samples, the rock mass may behave differently. Accordingly, the rock mass classification is based on different characteristics from the five properties. Conventional rock mass classifications utilize the combined information of testing on intact rock samples and of the field conditions. The most commonly used classifications encompass Rock Mass Rating (RMR) (Bieniawski, 1993), Q classification

8

(Barton et al., 1974), and Geological Strength Index (GSI) system (Hoek, 1994). Several attributes used to classify rock mass are listed in Table 1.2.2. Typically, rock is hardly intact from a macroscopic point of view; and the behavior of structures on rock is a function of the behavior of rock mass as a whole.

Classification of Weak Rock

On the surface, it seems easy to differentiate "weak" from "strong," but the definition of weak rock in depth can be ambiguous. Conceptually, as a geotechnical engineer, strong rock indicates that the structure on top of it does not undergo any stability problem during its lifetime. Then, the term "strong" should satisfy long-term conditions as well as short-term conditions, otherwise the rock should be regarded "weak". Weak rocks may be identified by determining several engineering properties such as strength, durability, swelling, water content, clay particle contents, and the extent of weathering. One of the common classification systems is the one utilizing strength of rock as shown in Figure 1.2.1. However, discrepancies exist among the proposed systems per each authority or author in determining the category of rock. In North America, about 50 MPa of unconfined compressive strength (UCS) was selected as a boundary between weak or low strength rock and strong rock (Bieniawski, 1973; Coates, 1964; Deere and Miller, 1966). On the other hand, the British Geological Society defined about 10 MPa of UCS as a boundary between moderately strong and moderately weak. The ISRM (1981) divides the weak rock into weak, very weak, and extremely weak. Rock with UCS lower than 25 MPa is considered weak, between 1 and 5 MPa is very weak, and between 0.25 and 1 MPa is considered to be extremely weak. The division between stiff soil and weak rock may be located between 0.6 and 1.8 MPa with practical value of 1 MPa (Santi and Doyle, 1997).

Another classification of rock that was developed for easy use in the field is shown in Table 1.2.3. In the table, 25 MPa of UCS is considered the lower limit of strong rock. In addition to UCS, point load index (PLI, ASTM D5731) is displayed for reference because PLI is readily available in the field by breaking a piece of rock chunk, and the coefficient factor (typically 25 for strong rock) is multiplied by the PLI to estimate UCS. Basically, this classification system is based on both the strength of the rock obtained from UCS and PLI, and field estimate of strength using geological hammer, pocket knife, and thumbnail. The strength of very weak rock ranges from 1 – 5 MPa, and the rock can be recognized by peeling the rock by knife and by crumbling with geological hammer. Extremely weak rock whose strength is less than 1MPa will be scratched with a fingernail.

In addition to strength-based classification, the components of the rock unit and the reaction of rock in the presence of water may be used. Figure 1.2.2 presents several proposed classification criteria from various research groups; the proposed criteria are the amount of matrix, clay content, jar slake value, slake durability index, the magnitude of free swelling, and moisture content. Weak rock typically consists of strong clasts interacting with a soft and weak matrix embracing them. The engineering behavior of such formation is mainly controlled, not by strong cores, but by matrix. Therefore, the units containing matrix amounting to more than 50 – 75% of the entire unit are significantly affected by the property of matrix, and considered weak rock. Clay content is the sole factor used to distinguish shale from non-shale. Usually, the rock containing the half clay content is defined as shales or argillaceous rock from geological point of

view. However, for engineering purposes, 15% of clay particle content is sufficient to make the rock behave like shale (Mead, 1938; Santi and Doyle, 1997).
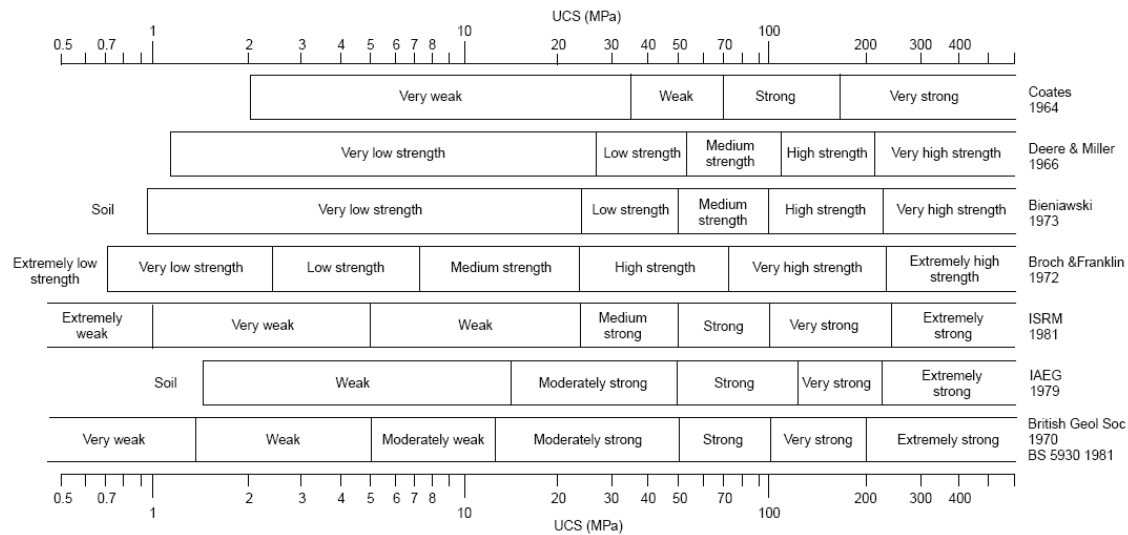
Figure 1.2.1 Comparison of some well-known rock strength terms

Rock that disintegrates severely into smaller fragments during design life should be classified as weak rock. In the cycles of rock life, various types of weathering processes are imposed physically and chemically. Physical weathering caused by drying and wetting is the process that has the most significant effect on weak rock such as clay shales. Hence, the reaction mode to water can be used to identify non-durable rock from durable rock. Both the Jar Slake test (Lutton, 1977) and the slake durability test (Franklin and Chandra, 1972), usually 2 cycles of the slake durability test, are representative tests to evaluate the durability of rocks both descriptively and quantitatively. Detailed procedure and durability assessment is discussed in Section 1.4. During the Jar Slake test, the slaking modes of test specimens are used to determine weak and strong rock after soaking the rock for 24 hours. After classifying the slaking modes into six Jar Slake values (1–6), the rock is defined as weak/soil-like/non-durable, or as strong/rock-like/durable rocks (Santi, 1995; Welsh et al., 1991; Wood and Deo, 1975). The rock is non-durable and/or soil-like when the jar slake value is less than 2, which means the intact rock under water changes into flakes or mud. The second-cycle slake durability test provides quantitative values associated with the durability of rocks. Higher value indicates the rock is more durable. A rock with the second cycle of slake durability index (Id_2) larger than 90% is durable, and rock-like, and Id_2 lower than 75% indicates the rock is non-durable and soil-like (Franklin, 1981; Wood and Deo, 1975). For igneous rocks, the division is made at much higher Id_2 (Lee and de Freitas, 1989)

Table 1.2.3 Field estimates of unconfined compressive strength
(Hoek and Brown, 1997)

Grade	Term	UCS (MPa)	PLI (MPa)	Field estimate of strength	Examples
R6	Extremely Strong	> 250	> 10	Specimen can only be chipped with a geological hammer	Fresh basalt, chert, diabase, gneiss, granite, quartzite
R5	Very Strong	100 – 250	4 – 10	Specimen requires many blows of a geological hammer to fracture it	Amphibolite, sandstone, basalt, gabbro, gneiss, granodiorite, limestone, marble, rhyolite, tuff
R4	Strong	50 – 100	2 – 4	Specimen requires more than one blow of a geological hammer to fracture it	Limestone, marble, phyllite, sandstone, schist, shale
R3	Medium Strong	25 – 50	1 – 2	Cannot be scraped or peeled with a pocket knife, specimen can be fractured with a single blow from a geological hammer	Claystone, coal, concrete, schist, shale, siltstone
R2	Weak	5 – 25	**	Can be peeled with a pocket knife with difficulty, shallow indentation made by firm blow with point of a geological hammer	Chalk, rocksalt, potash
R1	Very Weak	1 – 5	**	Crumbles under firm blows with point of a geological hammer, can be peeled by a pocket knife	Highly weathered or altered rock
R0	Extremely Weak	0.25 – 1	**	Indented by thumbnail	Stiff fault gouge

* Grade is based on Brown (1981)
** Point load tests on rocks with an unconfined compressive strength below 25 MPa are likely to yield highly ambiguous results

The free swelling test is designed to predict the swelling strain of swelling rock under unconfined conditions when it is immersed in water (ISRM, 1979). The free swelling test is an alternative to determine durable and non-durable rock. Fundamentally, the swelling property of weak rock is relevant to the expandable clay content, which is also relevant to the slaking behavior of weak rock. In other words, both swelling and slaking are predominantly determined by the percentage of expandable clay minerals

(e.g. montmollilonite). Thus, rocks swelling more than 3 – 4 % are non-durable or unfavorable (Underwood, 1967; Welsh et al., 1991). Similarly, natural water content of weak rock may be used for classification as shown in Figure 1.2.2. Water content is relatively convenient to measure, and is, therefore, a good and quick indicator of weak rock. At higher water content, the rock tends to be less durable or unfavorable (Hopkins and Deen, 1983; Lee and de Freitas, 1989; Underwood, 1967).

Morgenstern and Eigenbrod (1974) described the amount of slaking according to the liquid limit. The proposed classification is shown in Figure 1.2.3. The durability of clay shales relies highly on the liquid limit: the shales with high liquid limits tend to slake when immersed in water. The degree of slaking is high for material with liquid limit over 90. The rate of slaking is classified according to the change in liquidity index after 2 hours of immersion. The change in liquidity index is calculated from:

$$\Delta I_L = \frac{\Delta w}{w_L - w_p}$$
Equation 1.2-1

where Δw is the change in water content of the rock or soil before and after 2 hour soaking, w_L is the liquid limit, and w_P as the plastic limit. If the change in liquidity index is over 0.75, the material is believed to slake quickly.
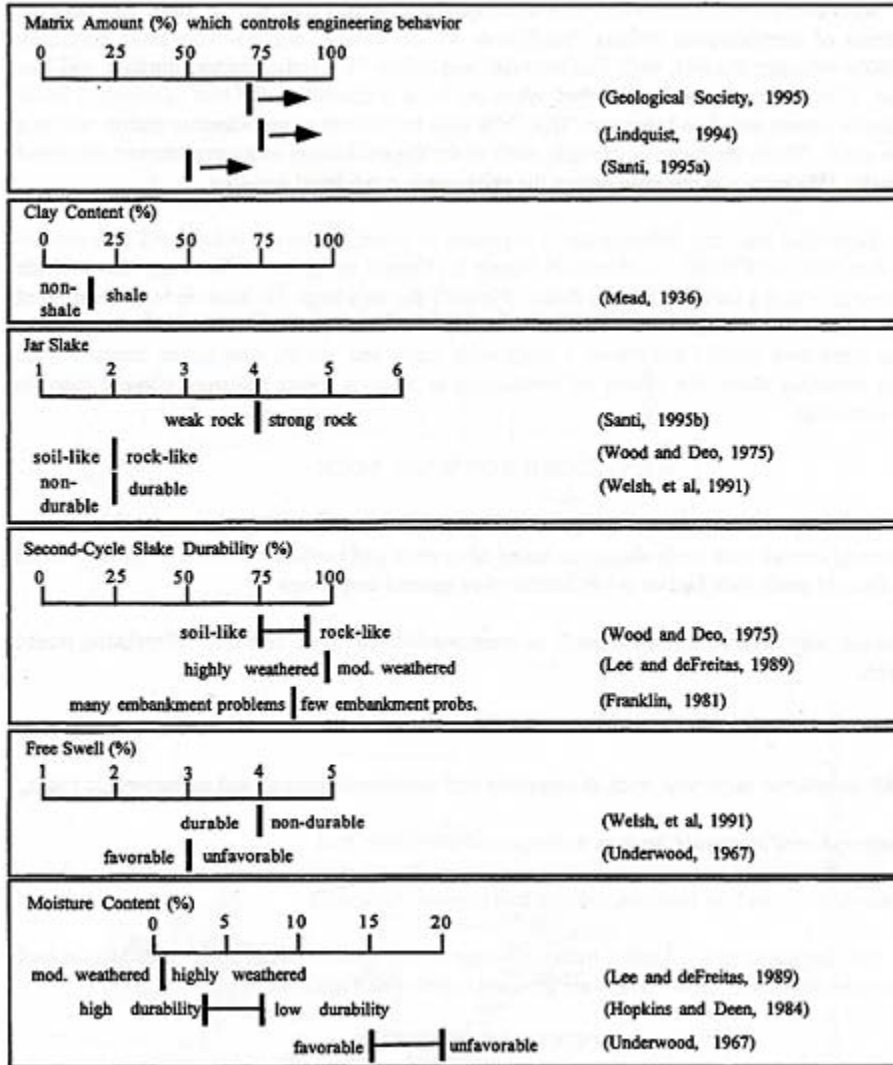
Figure 1.2.2 Identification of weak rock from component-based and water reaction-based tests (Santi and Doyle, 1997)

Liquid Limit (%)

```
0        20        40        60        80        100       120       140
┌──────────────────────────────────────────────────────────────────────┐
│          │             │                    │                │        │
└──────────────────────────────────────────────────────────────────────┘
 Very Low  │     Low     │      Medium        │      High      │ Very High
```
Amount of Slaking

Change in Liquidity Index after Soaking 2 hour

```
0                                           0.75                1.25
┌──────────────────────────────────────────────────────────────────────┐
│                                            │                   │      │
└──────────────────────────────────────────────────────────────────────┘
                 Slow                        │       Fast        │ Very Fast
```
Rate of Slaking
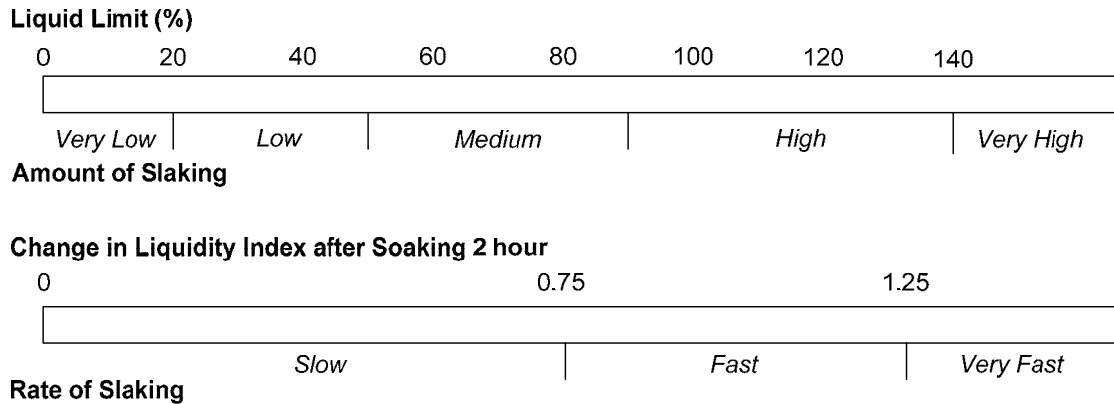
Figure 1.2.3 Estimation of the amount of slaking based on liquid limit modified from (Morgenstern and Eigenbrod, 1974)

In spite of discrepancies among the engineering properties used to define weak rock in various research studies, the following standards may be used as quick indicators to evaluate weak rock (Santi and Doyle, 1997):

- Unconfined compressive strength ranges between 1 and 20 MPa

- Softened strength (after immersion) is lower than 40 - 60% of dry shear strength

- Standard Penetration Test (SPT) is between 50 and 300 blows per ft

- Rock Quality Designation (Deere, 1968) is lower than 25 – 75

- Seismic Wave Velocity is less than 7000 ft/s

- Weaker weathered matrix exceeds 50 – 70% of whole rock mass

- Clay content of the rock is greater than 15%

- Jar Slake value is lower than 2 – 4

- Second-cycle Slake Durability Index is lower than 90%

- Free swell of the rock exceeds 3 – 4%

- Water content is greater than 5 – 15% for argillaceous rock

- Liquid Limit is over 90.

Classification of Clay Shale

The initial attempt was made to classify shale into "soil-like" and "rock-like" shale as displayed in Figure 1.2.4. In the chart, the "soil-like" shales are compaction shales without good cementation, which are divided into clay shale, silty shale, sandy shale, and black shale according to grain size and organic content (Mead, 1938; Underwood, 1967). The "soil-like" shale consisting of 50% or more clay size particles is classified into clay shale. The disadvantage of this chart is the ambiguity of the criterion to distinguish compaction shale and cemented shale. Moreover, dependency solely on the clay particle contents may lead to crude and inaccurate classification.

14
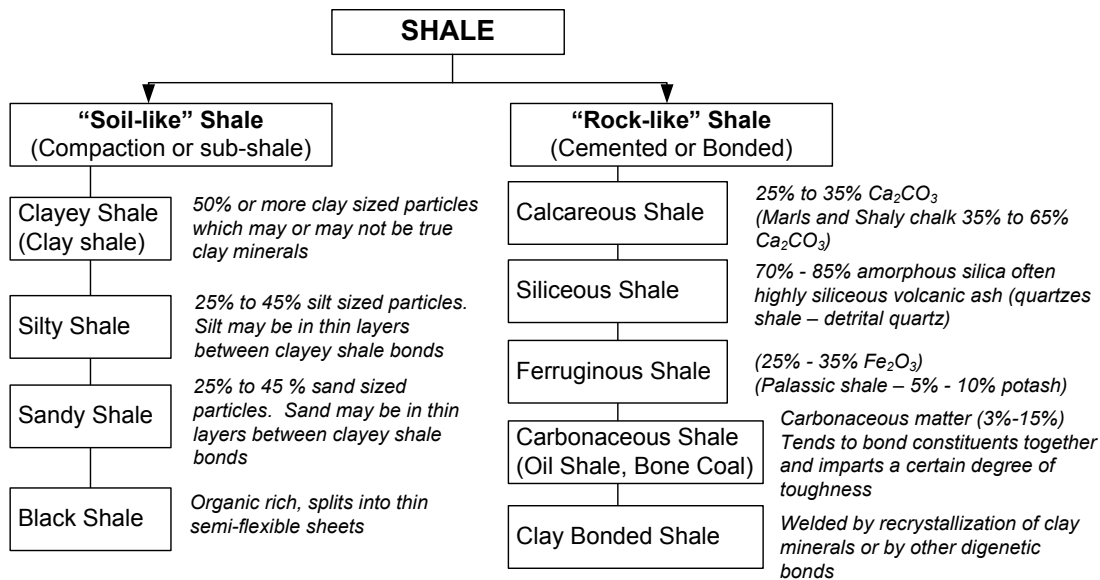
Figure 1.2.4 Geological classification of shale (Mead, 1938; Underwood, 1967).

Another simple classification of mudrocks is presented in Table 1.2.4 that makes use of two attributes: percent clay size particles and lamination. The terminology "mudrock" indicates fine-grained, siliciclastic sedimentary rocks. The distinct difference between "stone" and shale is defined by whether or not the rock is laminated. In addition, silts, mud, and clays is determined by the content of clay size particles. Clay shale, for instance, contains 50% or more clay content and is laminated.

Table 1.2.4 Geological classification of mudrocks (Blatt, 1982)

	Percent clay-sized particle		
	0 – 32%	33 – 49%	50 – 100%
Non-laminated	Siltstone	Mudstone	Claystone
Laminated	Silt Shale	Mud Shale	Clay Shale

Figure 1.2.5 presents a slightly complicated but precise classification diagram proposed by Morgenstern and Eigenbrod (1974) that considers four factors: 1) initial undrained shear strength before softening, 2) change in strength after softening, 3) change in water content after softening, and 4) elapsed time to soften the material resulting in 50% loss in strength. The argillaceous material is regarded as clay when: 1) the undrained shear strength is less than 1.7 MPa (250 psi), 2) the reduction in undrained shear strength is more than 60% of the initial value, and 3) the change in water content is more than 1% after softening. The mudstone is vice-versa. Then, the elapsed time to when the reduction in strength is more than half is used to classify the clay into hard, stiff and soft clay. The

15

hard clay, according to their chart, is clay shale whose strength reduces to half after 1 day.

Although foregoing classifications have been widely used and accepted for classifying soft rocks, they lack qualitative assessment of durability that is critical to define the behavior of soft rock. Gamble (1971) included quantitative assessment of durability on the transitional geo-material in addition to evaluation of geological characteristics. In his study, argillaceous materials are classified based on series of two cycles of slake durability tests. Beforehand, it is helpful to review several terminologies that are defined in his dissertation.

Indurated – Rock hardened by pressure, cementation, or heat; includes both compacted and cemented hardened materials.

Massive – Nonfissile or nonshaly material, breaks in apparently random directions in blocky or irregular shapes.

Fissile – splits or breaks into flakes, chips, or thin flat pieces approximately parallel to bedding.

Siltstone – massive indurated rock composed predominantly of silt. Often contains small amounts of fine sand, is grittier and usually harder than adjacent claystones or mudstones.

Claystone – Massive indurated rock composed predominantly of clay. Smooth to touch.

Mudstone – Massive indurated mixture of undetermined amounts of silt and clay, with possible minor amounts of sand.

Silty Shale – Fissile, shaly, or laminated indurated rock composed predominantly of silt.

Clayey Shale – Fissile, shaly, or laminated indurated rock composed predominantly of clay.

Shale – Fissile, shaly, or laminated indurated mixture of undetermined amounts of silt and clay with possible minor amounts of sand.

ARGILLACEOUS MATERIALS

$S_{uo} < 250$ psi
$\Delta s_u > 0.6\, S_{uo}$
$\Delta w > 1\%$

$S_{uo} > 250$ psi
$\Delta s_u < 0.4\, S_{uo}$
$\Delta w < 1\%$

CLAY

MUDSTONE

| Medium to Soft $t_{50} < 1$ hr | Medium to Soft $t_{50} < 1$ hr | Medium to Soft $t_{50} < 1$ hr | Claystone | Siltstone *Shale if fissile |

S_{uo} = undrained shear strength at natural water content
(Q test using 50 psi chamber pressure
Δs_u = strength loss after softening to equilibrium water content
Δw = change in water content after softening
t_{50} = time of softening for loss of 50% of S_{uo}
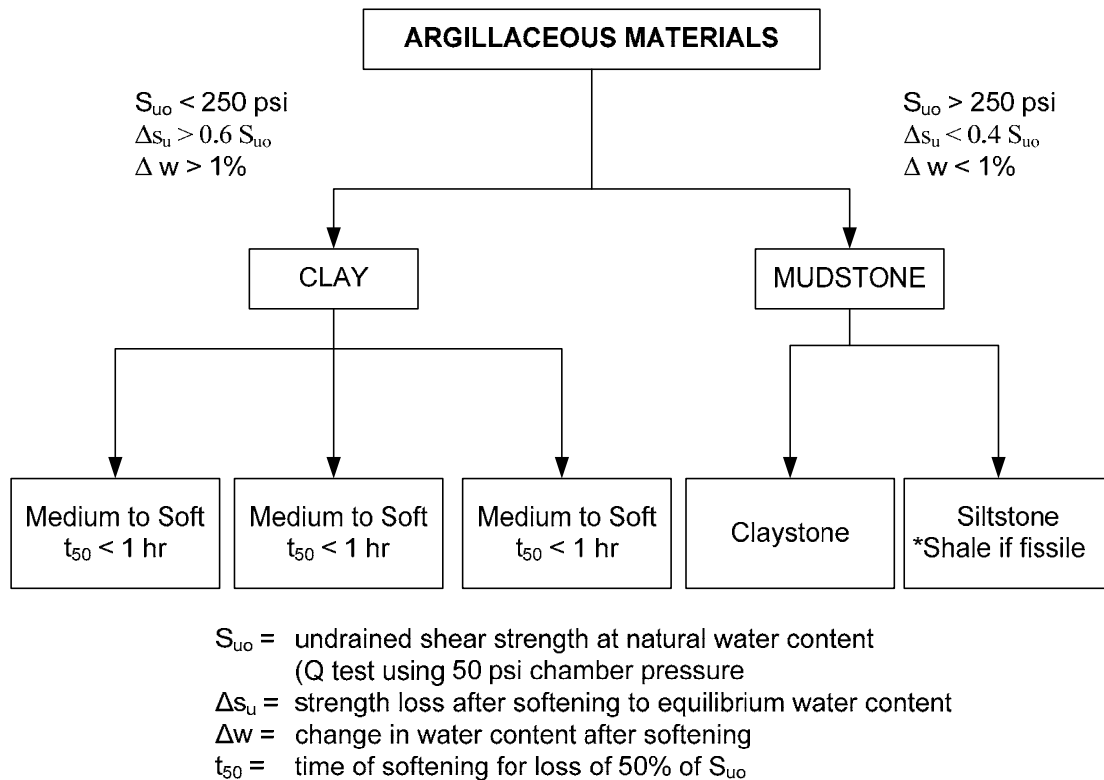
Figure 1.2.5 Engineering classification of Argillaceous materials
(Morgenstern and Eigenbrod, 1974)

In his definition, clay shale is indurate, fissile, or shaly consisting predominantly of clay. The suggested geological classification of argillaceous materials is shown in Table 1.2.5. In the table, the indurated group of mudrocks includes both compaction shale and cemented shale whereas the unindurated group of mudrocks comprises soils. The indurated group is divided, depending on the clay size particle content and existing fissures, into six sub categories. The definition of each term introduced above can be used for further engineering judgment. The geological information of mudrocks is correlated with other engineering properties such as slake durability index and plasticity index in Figure 1.2.6. According to the figure, the plasticity index tends to increase, but the slake durability index decreases as clay content increases and/or as the portion of montmorillonite increases. The slake durability index increases as the extent of cementation increases while the plasticity index being constant. The weathering and fracturing are also closely associated with slake durability index. In addition, it was found that the slake durability index is influenced by clay mineral content, calcite content, and the presence of microcracks (Russell, 1982).

Table 1.2.5 Suggested geological classification of argillaceous materials (Gamble, 1971)

Unindurated Group	Indurated Group Breaking characteristics of Mudrocks		After incipient Metamorphism	Metamorphic Equivalents
	Massive	Fissile or Shaly		
Silt	Siltstone	Silty shale	Argillite	Slate, phylite, or schist
Mud	Mudstone	Shale		
Clay	Claystone	Clayey shale		

A rigorous classification chart accounting for compressive strength, durability (slake durability index), composition of quartz, and anisotropy is suggested by Grainger (1984). According to Figure 1.2.7, mudrock can be classified into soil, non-durable rock, and durable rock based on the UCS of intact rock. The magnitude of UCS (3.6 MPa) coincides with the undrained shear strength (1.8 MPa) proposed in Figure 1.2.5, but UCS is bounded by the lower limit (0.6 MPa) for weak rock. Even though the mudrocks whose strength exceeding 3.6 MPa are separated from non-durable rocks, the durability of the rocks are estimated and the rocks whose durability is less than 90 are classified into non-durable rocks. Hence, the strong rock with low durability is regarded as non-durable rock.
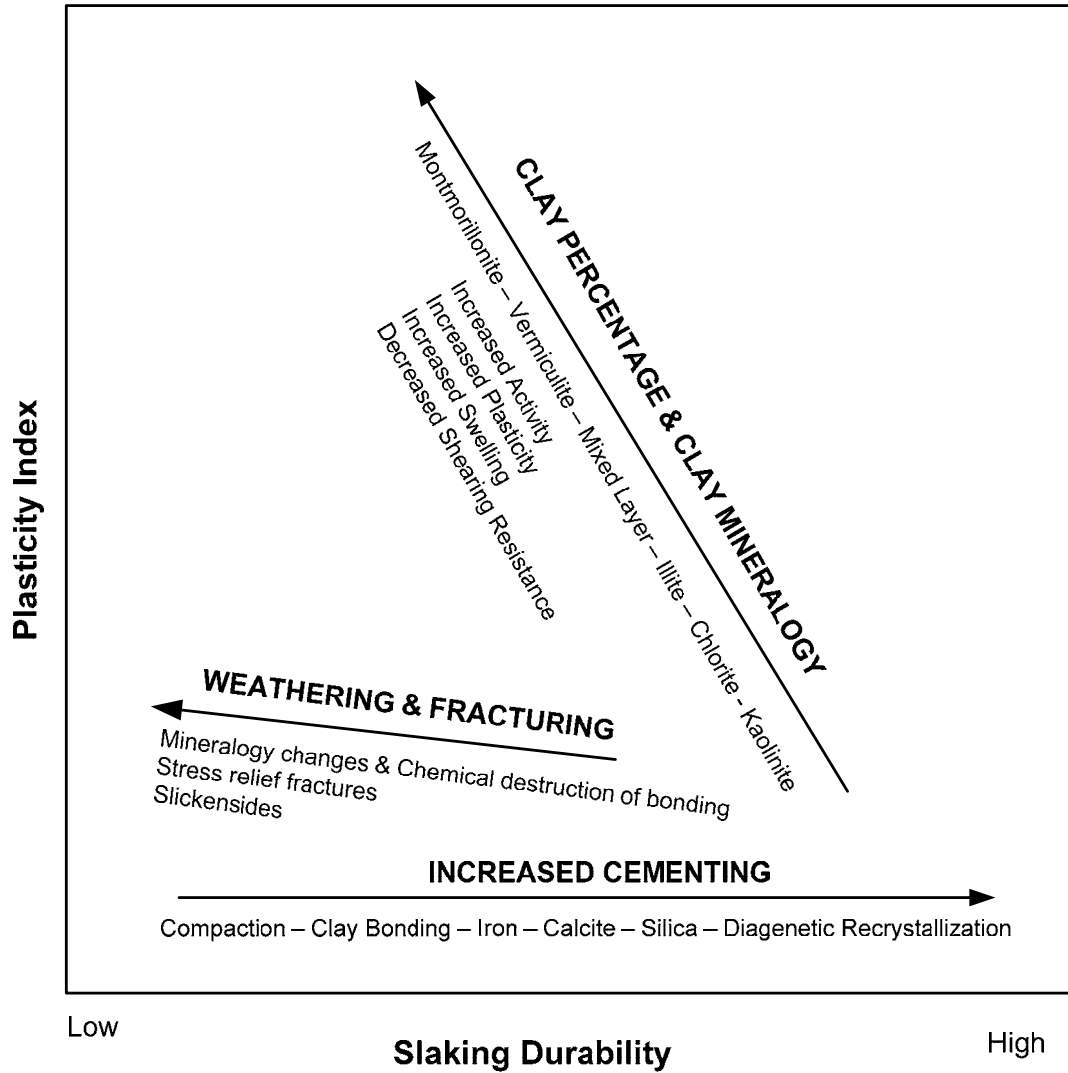
Figure 1.2.6 Relationships of factors affecting the engineering classification of transitional materials (modified from Deen, 1981)
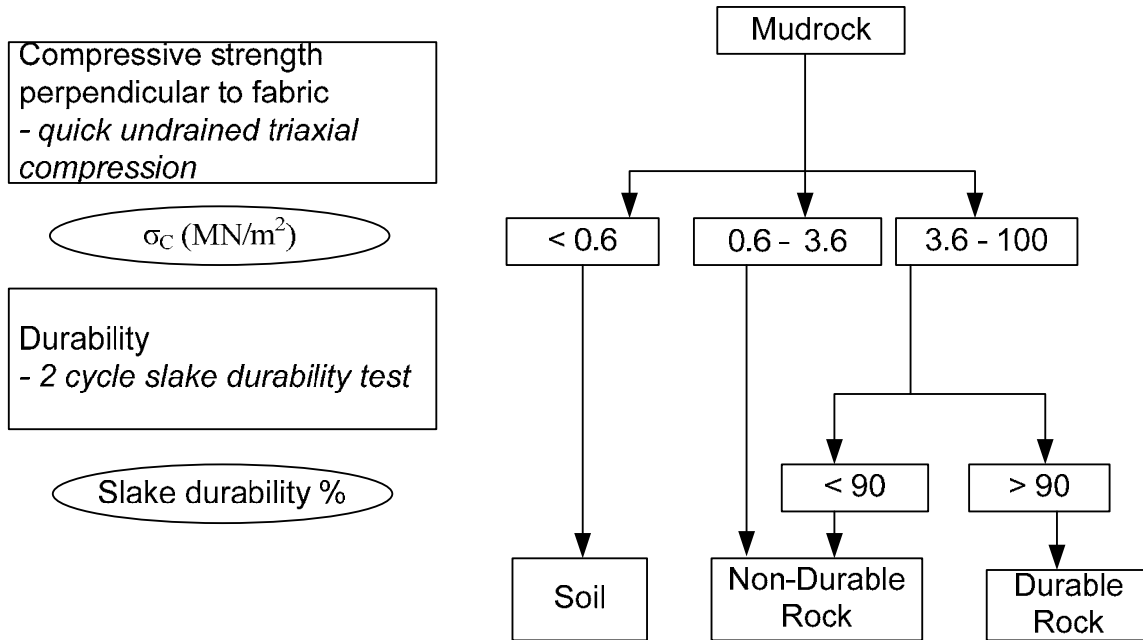
Figure 1.2.7 The classification of mudrock by strength and durability (Grainger, 1984)

The non-durable mudrock is divided into five members as shown in Figure 1.2.8. While other classification charts (for example Figure 1.2.4) uses clay content, the suggested classification charts utilize the percent weight of quartz. When quartz is less than 20% the total weight, the non-durable mudrock is classified into either non-durable claystone or clay shale. Then flakiness ratio is used to determine final categorization. The flakiness ratio is a ratio of shortest dimension divided by intermediate dimension of particles, and it represents the anisotropy of the formation. When the ratio is less than two thirds, the non-durable mudrock containing 20% or less quartz is regarded as clay shale. Other classifications are non-durable claystone, silty clay shale, non-durable mudstone, and non-durable siltstone. The complete classification chart is displayed in Figure 1.2.9, which can be used as an overview of entire procedure.
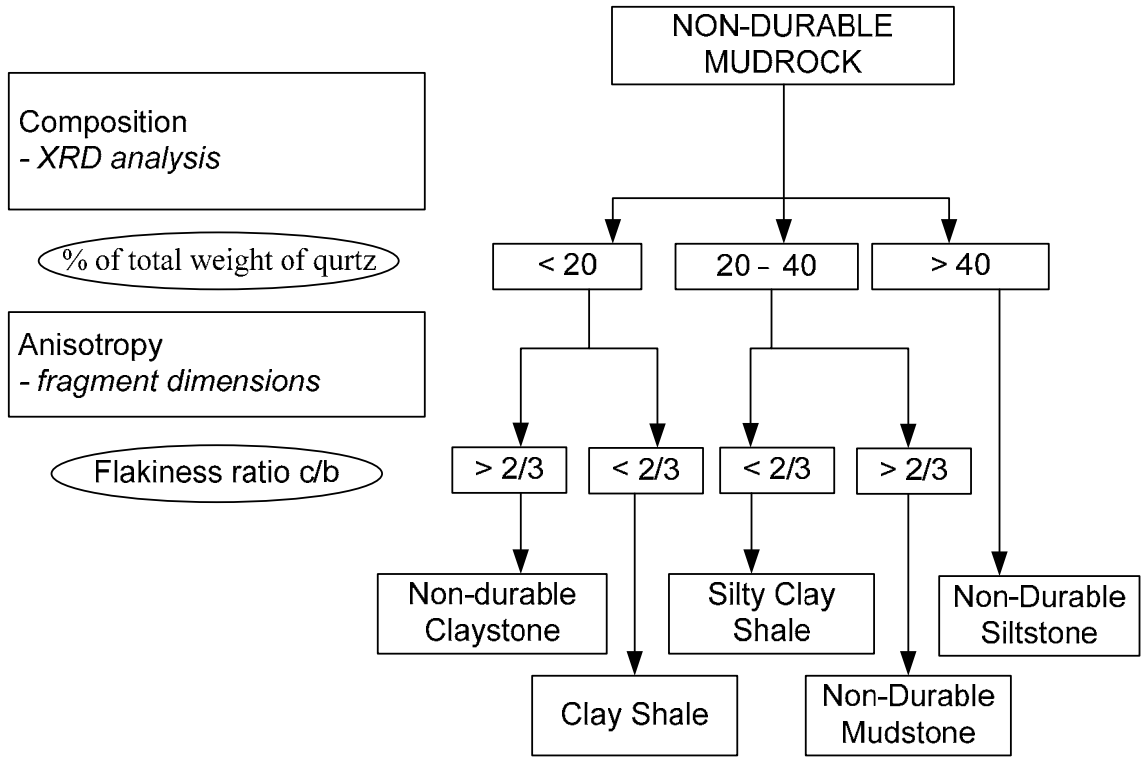
Figure 1.2.8 Classification of non-durable mudrock (Grainger, 1984)

1.2.3 Weathering

Clay shales are materials that are very sensitive to the changes in moisture due to their high clay content. In such materials, weathering is a significant factor that impacts the overall performance structures. As a result, weathering of these materials has been extensively studied (Gulla et al., 2006; Marques et al., 2005; Martin and Hencher, 1986; Taylor, 1988). The resistance of weak rocks to weathering is called durability and is usually measured by means of slaking tests.

This section presents characteristics of clay shales, general weathering process, and slaking mechanisms of clay shales. Literatures regarding weathering properties of weak rocks are also reviewed.

Increasing grain size

Silt (M-Soil) | Silty Clay | Shaly Silty Clay | *Flakiness* | Clay

A - line

$\sigma_C = 0.6 \ \text{MN/m}^2$ — ratio 2/3

undeformed

Non-durable Siltstone | Non-durable Mudstone | Silty Clay Shale | Clay Shale | Non-durable Claystone

40 % quartz

$\sigma_C = 3.6 \ \text{MN/m}^2 \ \& \ \text{SDI} = 90\%$

Durable Siltstone | Durable Mudstone | Silty Shale | Shale | Durable Claystone

20 % quartz

Anistoropy 2 | *Anistoropy 2*

Increasing strength

With slaty cleavage | Slaty Silty Shale | Slaty Shale

Figure 1.2.9 Summary of the complete classification (Grainger, 1984)

Clay Shale

Clay shales are one kind of mudrock that is fine-grained, argillaceous sedimentary rocks. For engineering purposes, clay shales are typically considered intermediate material between hard soils and soft rocks. This type of material induces many problems during construction of civil engineering projects because of its low durability upon weathering. The strength of such non-durable rock deteriorates significantly as a result of change in water content (Greene and Schaffer, 1997). Hence, predictability of the behavior of clay shales is hindered by a wide range of geological features including the degree of weathering, composition of the clay shale, and environmental effects. The risky behavior of clay shales can be characterized by swelling, slaking, shrinkage, and dispersion, which frequently leads to slope failures, foundation damage, mine failures, and shale embankment failure in many construction sites (Dick and Shakoor, 1992; Strohm, 1980).

Clay shales are composed of four basic constituents: 1) clay minerals, 2) non-clay minerals, 3) inter-particle bonds or cements (carbonate, silica, iron oxides, organic matter, etc.), and 4) a pore space filled with water or air (Seedsman, 1986). Among these components, the water reactivity of clay shales is chiefly governed by the portion of clay minerals, especially expandable clay minerals. The clay shales containing large amounts of expandable clay minerals (e.g. montmorillonite) are prone to swell, shrink, and slake

upon weathering, and exhibit plastic behavior (Botts, 1986). Many efforts have been made to differentiate problematic non-durable rocks from durable rocks. As the durability of such weak rock is dominated by water content, the reaction of weak rock to water is a widely accepted approach to estimate the durability. Popular durability tests include: descriptive tests such as the jar slake test, quantitative measurement such as the slake durability test (Franklin and Chandra, 1972), and the free swell test (Olivier, 1979).

As marl and shale are of particular interest in this research, it seems appropriate to review the definition of marl and shale. Marl comprises of various clay minerals bonded tight by, mainly, calcium carbonate ($CaCO_3$), and is typically deposited in an ocean environment. Marl is indurate, but can be weakened and softened when exposed to water and allowed to swell because the calcium carbonate may be dissolved in acidic environments. Shale, on the other hand, refers to a fine-grained sedimentary rock consisting predominantly of clay minerals or mud without cementation of calcium carbonate. Shale is represented by many fissures and high amounts of clay minerals; the fissures are frequently found parallel to the bedding plane. Another characteristic of shales and marls is the wide range of material properties even for the same rock unit. This reflects the fact that 1 cm thick clay shale is deposited over very long period of time such that the depositing environment is not uniform through the period.

Weathering Process

Weathering is defined as the physical and chemical alteration of rock nature including deterioration of strength, permeability, and deformability (Watters, 1997). The deterioration may be as large as three orders of magnitude (Martin and Hencher, 1986). Weathering processes can be classified according to two categories; physical and chemical weathering.

Physical weathering is the deterioration caused by stress changes in the rock structure by cycles of wetting and drying, freezing and thawing, and erosion. As a result of physical weathering, mother rock masses disintegrate into smaller fragments without change in chemical property (Watters, 1997). Physical weathering is a significant reason for weakening rock mass containing non-durable layer in which the weathered layers dominate the overall behavior of the rock mass. Introducing weathering agents such as water into such rock mass significantly deteriorate the engineering properties by weakening non-durable layers. Figure 1.2.10 illustrates the possible causes and effects of physical weathering in rock masses. The existing discontinuity that is closed under *in situ* confining pressure is open and weakened by stress relief and physical weathering. Eventually, the rock mass fails along the existing and/or propagating discontinuities as a result of physical weathering.

Chemical weathering is degradation caused by leaching of carbonate, oxidation of pyrite, and loss of cations. During chemical weathering, original minerals are replaced with new minerals, which results in alteration of structure, water content, and subsequent strength change in the rock mass over time (Watters, 1997). Figure 1.2.11 displays the chemical weathering process in rock mass with an example of chemical alteration. Chemical weathering is time dependent; often the process is very steady. For example, the calcium carbonate of limestone is dissolved over a long period of time by introducing water. The chemical alteration is expressed as:

$$CaCO_3 + H_2O + CO_2 \rightarrow Ca(HCO_3)_2$$
Therefore, the limestone is often found to contain many cavities.
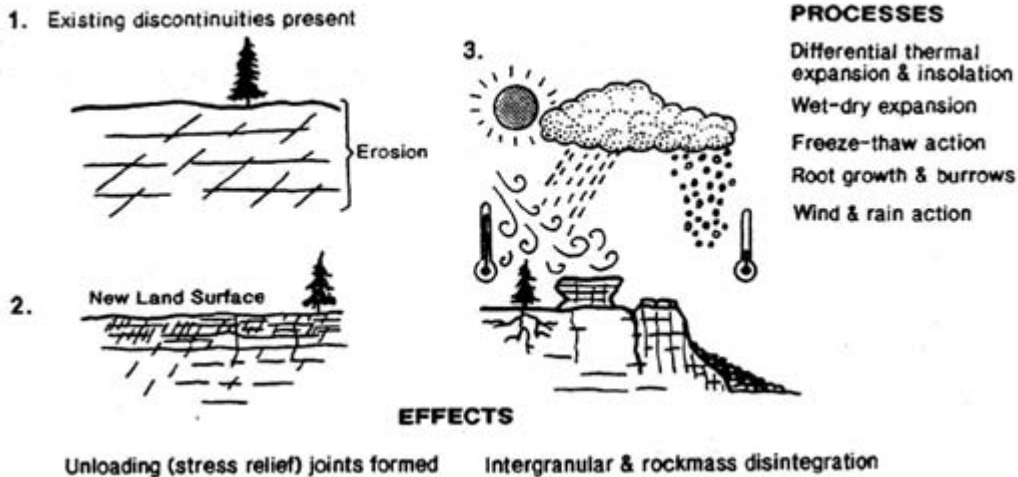
Figure 1.2.10 Physical weathering (Watters, 1997)
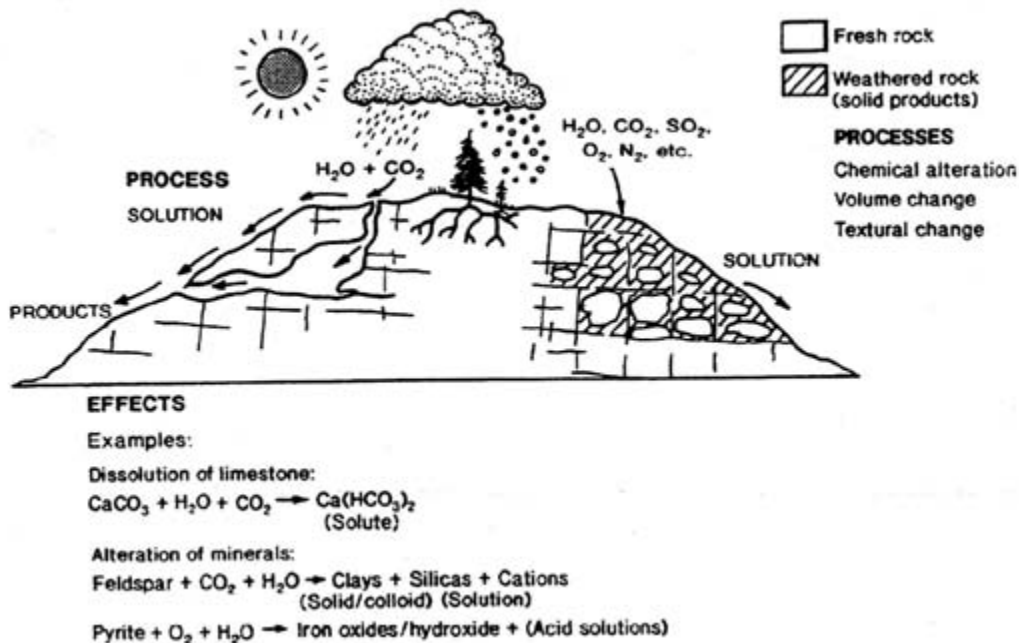
Figure 1.2.11 Chemical weathering process (Watters, 1997)

Drying and Wetting

Drying effect

  The shales which are subject to air drying deteriorate significantly when exposed to water, whereas the shales in natural water content do not react to water (Santos et al., 1996). It is clear that the air drying prior to soaking modifies important attributes of clay

shales, thus the behavior of dried clay shales is different from that of non-dried clay shales. In order to understand why and how drying affects the characteristics of clay shales, the capillary of clay shales is reviewed.

Capillary pressure develops when fluid exists between two different materials, and the magnitude increases as the distance between the two materials narrows. The capillary pressure results from surface tension. The height of a capillarity in a certain diameter of tube may be calculated by solving the force equilibrium equation between downward gravity force of the water and the upward dragging force by surface tension. The equilibrium equations are as following:

Downward force by gravity: $$\sum F\downarrow = h_c \left(\frac{\pi d^2}{4} \right) \rho_w\, g$$

Upward force by surface tension: $$\sum F\uparrow = T \cos\theta\, \pi d$$

where d is a tube diameter, g is gravity acceleration, ρ_w is a unit density of water, T is tension, and θ is the angle between tension and the surface of tube. T is about 73 mN/m for water at 20°C according to the Handbook of Chemistry and Physics (1977). Therefore, the capillary height can be rearranged as:

$$h_c = \frac{-4T}{\rho_w\, g\, d}$$

Equation 1.2-2

The magnitude of capillary pressure in the tube is then:

$$u_c = h_c\, \rho_w\, g = \frac{-4T}{d}$$

Equation 1.2-3

In the derived equation, capillary pressure is solely a function of surface tension T and the tube diameter d. In the end, only the tube diameter is associated with the pressure since the T is the known value for specific conditions. The capillary pressure rises when the diameter of the tube is very narrow. The capillary pressure in the theoretical tube is easy to estimate; in reality, however, the pores of geo-materials are not uniform such that precise estimation is challenging.

Capillary phenomenon is a good theory to explain how clay shales are altered by air drying, and how they will behave after drying. When clay shales start drying, the water evaporation inside pores induces negative pore pressure. As evaporation continues, the radii of meniscus get smaller and the negative capillary pressure of the pore fluids continues increasing. Negative pore pressure due to capillary development applies suction to the structure of clay particles, which results in the shrinkage of the structure until equilibrium is reached between the developed negative pore pressure and strength of structure. When the negative capillary pressure exceeds the bonding strength, cracks occur along the weakest region of samples, and the bonding breakage is irreversible when negative capillary pressure disappears. For clay, this irreversible action is called overconsolidation because the clay will behave differently from normally consolidated clay. However, in clay shales, the irreversible action is represented by crack development and eventual disintegration of the formations.

Current research indicates that water starts evaporating initially from the surface of a clay shale sample and later from the internal region. The weight of evaporated water

25

after 48 hours was measured as approximately 50 – 60% of the total weight of contained water for the tested clay shales. These results will be detailed in Section 1.5. This observation implies that the water evaporated not only from the surface but also inside the sample cores. Therefore, air drying test clay shales is believed to induce high capillary pressure and destroy significant amount of bonding of clay particles. When water is reintroduced into the sample, the established capillary force will disappear, and the geo-material structure will not return to the original shape.

In porous medium, the pore diameter *d* for capillary effect can be estimated from pore size distribution. The pore size distribution of Tournemire shale is shown in Figure 1.2.12 (Schmitt et al., 1994). Using 0.01μm of pore diameter and Equation 1.2-3, the capillary pressure was calculated to be 58.4 MPa (T was 72.3 mN/m). Note that the UCS of tested clay shales in this study normally does not exceed 5 MPa.
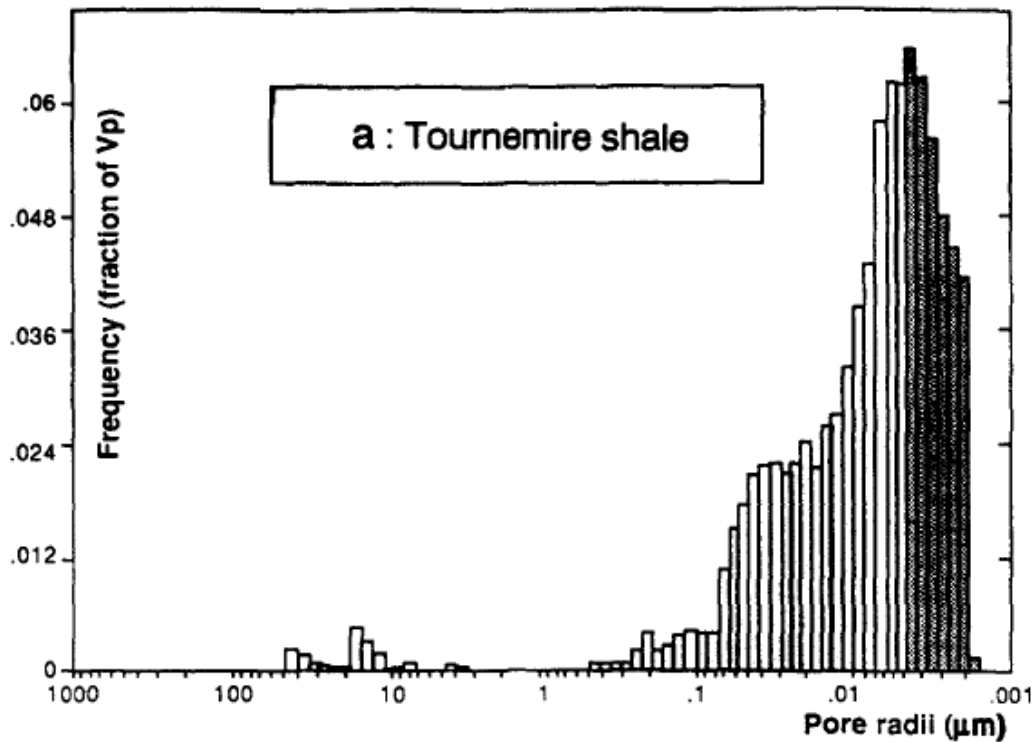
Figure 1.2.12 pore size distribution of Tournemire shale

Slaking mechanism

Slaking may be defined as the structural disintegration of an intact mass into smaller particles due to a change in water content (Akai, 1993). The disintegration of clay shales can be explained by increasing air pressure entrapped among clay particles or coarse grains (Schmitt et al., 1994; Taylor, 1988). When clay shales are dehydrating, water evaporates from larger pores by creating meniscus in the small pores. Since the pressure in the smaller pore is higher than that of larger pores, water in the larger pores starts evaporating prior to the water in the small pore. If not dried completely, most water is believed to reside in relatively small pores. Upon re-introducing water, the water first

fills the narrow pores then larger pores in sequence. However, air is believed to be entrapped in the pores during rehydration.

According to Schmitt et al. (1994), air bubbles can be trapped in the pores during hydration due to following reasons:

- Total immersion results in capillary imbibition occurring simultaneously at the surface of the rock, consequently air cannot escape and is compressed in the rock;

- The short circuit is narrower than the macropore such that air is entrapped while capillirary imbibitions occur (Figure 1.2.13 (a));

- Air may be trapped by the rough surface of macropore (Figure 1.2.13 (b)); and

- Capillary condensation first occurs in the smaller space, which encloses the air trapped in the macropore (Figure 1.2.13 (c)).

As the hydration continues, the air bubbles entrapped in the shale will be pressurized causing damage to samples. Also, tensile failure of weak inter-crystalline bonds occurs when the air drying-induced pore water pressure exceeds the bonding strength (Taylor and Smith, 1986). In some formations, slaking may develop from a number of cycles of wetting and drying rather than one cycle. Such cases occur when cementation is being removed by cycles of wetting and drying (Hudec, 1982). In addition, the dispersion of clay minerals in the presence of water is another cause of disintegration during slaking.

Besides the pressurized air bubble, pre-existing fissures are another significant cause for the reduction in strength of clay shales because of the softening behavior of the fissure in response to water (Botts, 1986). In his paper, Botts explains the three key roles of fissures on the behavior of clay shales: 1) the fissures act as weak planes through which shear failure can occur, 2) the opening fissures increase permeability, and 3) the open fissures increase the surface area to weathering agents. Slaking is expedited considerably by allowing weathering agents to migrate through fissures and by increasing the surface area. Botts proposed a schematic model representing progressive deterioration of clay shales as shown in Figure 1.2.14. At Stage 1 in Figure 1.2.14, the strength of clay shales is controlled by geometry and strength of inherent fissures. The shear plane of the shale is likely to pass through the fissures, which are often the weakness failure plane. The failure through existing fissures is more significant at low effective stress level because the interlocking between hard lumps loosens. At high confining stress, the fissure tends to close, and the effect of fissure on developing failure plane through fissures becomes less important. Such explanation is applicable only when fissures are not weakened by wetting and drying. When water is absorbed through fissures, the strength of the shales depends on the combined strength of fissures and surrounding softening region. The softening region results from increase in water content by water migration through fissures. Afterwards, in Stage 3, the clay shales comprise soft clay matrix around un-softened, relatively strong region. Clay shales are considered as fully softened at Stage 4, and the strength is totally altered from the original clay shales.
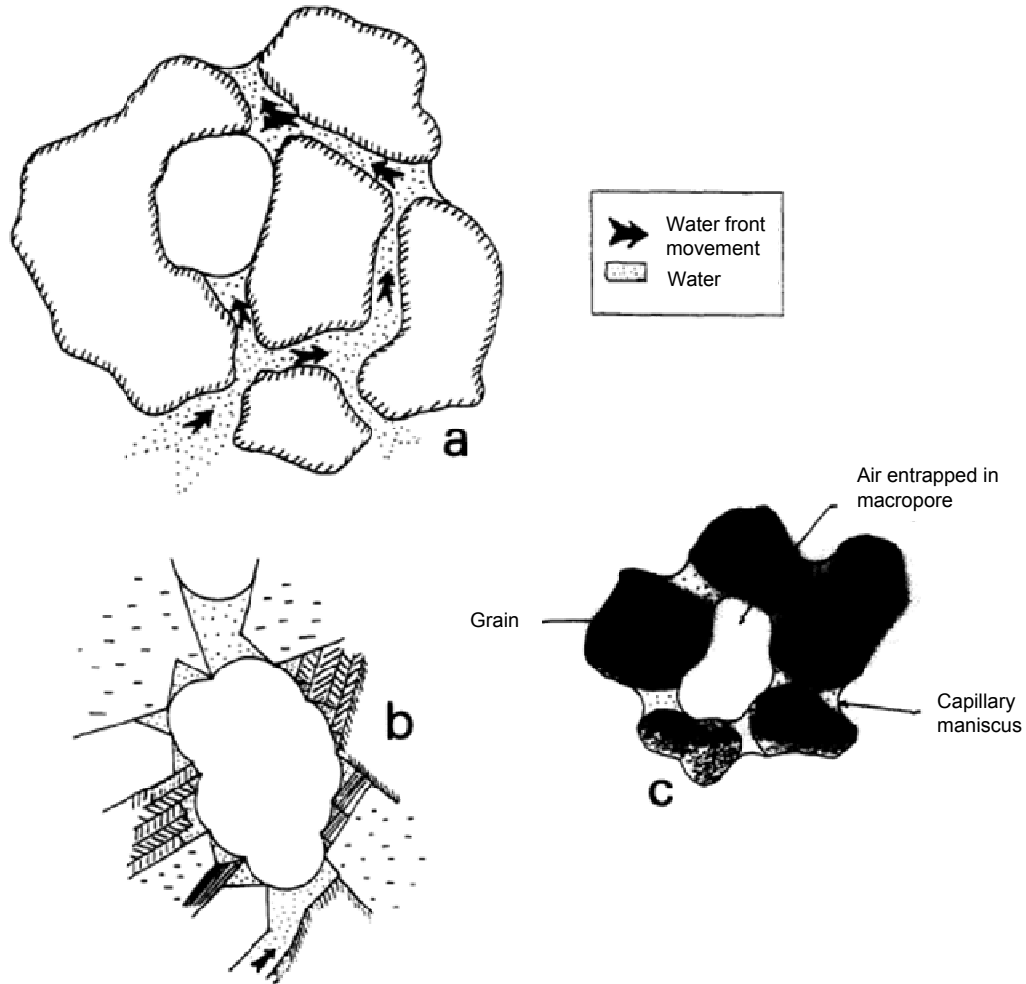
Figure 1.2.13 Air entrapment may occur by (a) short-circuit of macropore, (b) in a rough macropore, and (c) by condensation of water in pore accesses (Schmitt et al., 1994)

Stress relief induced from underground excavation is another reason for softening of rock masses. Stress redistribution takes place, which results in plastic deformation of underground structures such as tunnels (Yoshida et al., 1991). Such softening characteristics of degradable rock mass progresses with time, and, subsequently, long term stability analysis should be accounted for in projects related to such materials. Yoshida commented that dilatancy was not observed in the specimen which was allowed to swell freely under low confining pressure. Softening seems to be induced by destroying the dilatancy of the material as a result of absorbing water through fissures, and by softening indurate clay lump surrounding the fissures.

1.2.4 Drilled Shafts in Weak Rock

Drilled shaft foundations are very favorable for use in "intermediate" geomaterial not only because its' resistance is sufficient for most constructions but also because the augered hole is stable. In spite of frequent installation and long history of drilled shafts, many departments of transportation offer geotechnical manuals that directly relate the

Standard Penetration Test (SPT) or Texas Cone Penetration Test (TCPT) to allowable resistance at the point and side (Abu-Hejleh et al., 2003; Texas Department of Transportation, 2006). In this section, the full scale load tests on drilled shafts are reviewed, and the database of point bearing capacity of drilled shafts are collected.
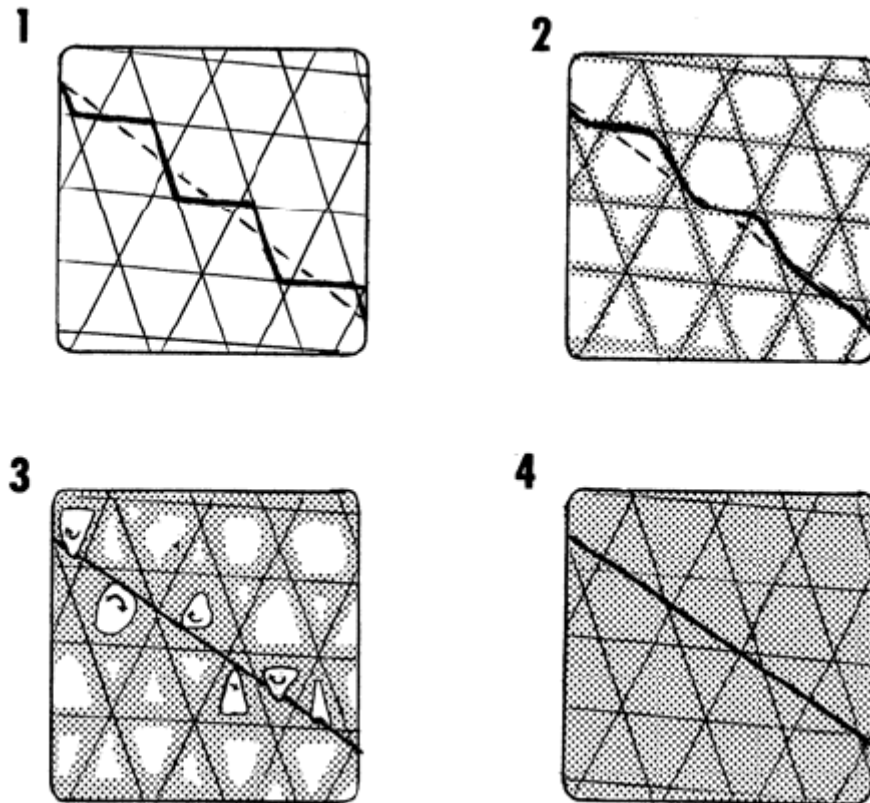
Figure 1.2.14 Schematic of a model for progressive deterioration of a fissured clay shale. Softened areas indicated by stipple pattern. Potential failure planes indicated by solid and dashed lines (Botts, 1998)

Full-Scale Load Test Database

Full scale load tests are typically conducted to assure the functionality of the drilled shafts, and are carried out on both tested and production shafts. As the production shafts will need to support the structure after construction, these shafts cannot be loaded to failure. Thus, the ultimate axial resistance is often unavailable in spite of a large number of load tests in the field. Compounding this matter is the fact that the engineering properties of underlying materials are rarely obtained at practice level. The behavior of drilled shafts have been investigated and evaluated in numerous studies, and attempts have been made to collect such scattered information (Nam, 2004; Vipulanandan et al., 2007; Zhang and Einstein, 1998). A database was established to propose reasonable quantification of total and point bearing capacity of drilled shafts in soft to hard rocks. The existing database is combined and reproduced in Table 1.2.6 showing ultimate point bearing capacity of drilled shafts. The rock formation, ultimate point bearing capacity,

geometry of test drilled shafts, and the ratio between UCS and point bearing capacity are displayed in the table.

Table 1.2.6 Database of load tests on drilled shafts

Number	Rock description	Diameter (mm)	Overburden thickness (m)	UCS (MPa)	Point bearing capacity (kPa)	Qmax/UCS	Reference
1	Hard Clay with Calcareous material	610	1.9	0.5	1642.4	3.3	(Reese and Hudson, 1968)
2	Clay Shale	760	5.8	0.6	3637.2	6.1	(Vijayvergiya et al., 1969)
3	Hard Clay	760	9.8	0.4	3328.6	8.3	(Engeling and Reese, 1974)
4	Clay Shale	790	5.9	1.4	5697.7	4.1	(Aurora and Reese, 1976)
5	Clay Shale	790	6.1	1.4	5123.2	3.7	(Aurora and Reese, 1976)
6	Clay Shale	760	5.8	1.4	6128.6	4.4	(Aurora and Reese, 1976)
7	Clay Shale	970	4.7	0.6	2441.9	4.1	(Aurora and Reese, 1976)
8	Clay Shale	770	3.8	0.8	1085.0	1.4	(Sheikh et al., 1985)
9	Claystone /Sandstone	1070	2.0	0.4	2633.4	6.6	(Abu-Hejleh et al., 2003)
10	Claystone	1220	0.6	0.5	2542.4	5.1	(Abu-Hejleh et al., 2003)
11	Claystone /Sandstone	1070	1.4	2.6	11299.7	4.3	(Abu-Hejleh et al., 2003)
12	Sandstone /Claystone	1370	3.2	11.4	15225.8	1.3	(Abu-Hejleh et al., 2003)
13	Limestone	1500	18.6	2.8	8809.9	3.1	(McVay et al., 2003)
14	Limestone	1800	21.1	2.8	3830.4	1.4	(McVay et al., 2003)

Table 1.2.6 Database of load tests on drilled shafts (Continued)

Number	Rock description	Diameter (mm)	Overburden thickness (m)	UCS (MPa)	Point bearing capacity (kPa)	Qmax/UCS	Reference
15	Limestone	1500	22.6	2.8	4213.4	1.5	(McVay et al., 2003)
16	Franconia Sandstone	1220	0	4.3	3700	0.9	(O'Neill, 1998)
17	Argilite Shale	n/a	n/a	22.1	23940	1.1	(Osterberg, 2001)
18	Shale with limestone and coal seams	n/a	n/a	2.3	6894.7	3.0	(Osterberg, 2001)
19	Shale	710	0.6	11.1	2652.1	0.2	(Horvath et al., 1983)
20	Mudstone	600	n/a	0.5	4510.0	9.0	(Williams, 1980)
21	Mudstone	1000	n/a	0.6	5530.0	9.2	(Williams, 1980)
22	Mudstone	300	n/a	0.7	6390.0	9.1	(Williams, 1980)
23	Mudstone	1000	n/a	2.5	5880	2.4	(Williams, 1980)
24	Mudstone	1000	n/a	2.3	6620	2.9	(Williams, 1980)
25	Mudstone	1000	n/a	2.3	7000	3.0	(Williams, 1980)
26	Mudstone	1000	n/a	2.3	6660	2.9	(Williams, 1980)
27	Marl (Cooper formation)	600	n/a	0.14	957.6	6.8	(Thompson, 1994)
28	Marl (Cooper formation)	600	n/a	0.14	2735	19.5	(Thompson, 1994)

Table 1.2.6 Database of load tests on drilled shafts (Continued)

Number	Rock description	Diameter (mm)	Overburden thickness (m)	UCS (MPa)	Point bearing capacity (kPa)	Qmax/UCS	Reference
29	Clay/Chalk	1700	n/a	0.6	2212	3.7	(Thompson, 1994)
30	Mudstone	670	6	4.2	6880	1.6	(Wilson, 1976)
31	Clay Shale	762	8.8	0.81	4690	5.8	(Goeke and Hustad, 1979)
32	Shale w/ sand layers	457	13.7	3.82	10800	2.8	(Hummert and Cooling, 1988)
33	Unweathered shale	305	2.4	1.08	3660	3.4	(Jubenville and Hepworth, 1981)
34	Gypsum	1064	4.2	2.1	6510	3.1	(Leung and Ko, 1993)
35	Gypsum	1064	4.2	4.2	10900	2.6	(Leung and Ko, 1993)
36	Gypsum	1064	4.2	5.4	15700	2.9	(Leung and Ko, 1993)
37	Gypsum	1064	4.2	6.7	16100	2.4	(Leung and Ko, 1993)
38	Gypsum	1064	4.2	8.5	23000	2.7	(Leung and Ko, 1993)
39	Gypsum	1064	4.2	11.3	27700	2.5	(Leung and Ko, 1993)
40	Till	762	n/a	0.7	4000	5.7	(Orpwood et al., 1989)
41	Till	762	n/a	0.81	4150	5.1	(Orpwood et al., 1989)
42	Till	762	n/a	1.0	5500	5.5	(Orpwood et al., 1989)

Table 1.2.6 Database of load tests on drilled shafts (Continued)

Number	Rock description	Diameter (mm)	Overburden thickness (m))	UCS (MPa)	Point bearing capacity (kPa)	Qmax/UCS	Reference
43	Highly weathered diabase	615	12.2	0.52	2650	5.1	(Webb, 1976)
44	Hardpan	1281	18.3	1.38	5840	4.2	(Baker Jr., 1985)
45	Till	1920	20.7	0.57	2290	4.0	(Baker Jr., 1985)
46	Hardpan	762	18.3	1.11	4790	4.3	(Baker Jr., 1985)
47	Sandstone	610	15.6	8.36	10100	1.2	(Glos and Briggs, 1983)
48	Sandstone	610	16.9	9.26	13100	1.4	(Glos and Briggs, 1983)
49	Shale	n/a	n/a	34	28000	0.8	(Thorne, 1980)
50	Sandstone	n/a	n/a	12.5	14000	1.1	(Thorne, 1980)
51	Sandstone	n/a	n/a	27.5	50000	1.8	(Thorne, 1980)
52	Shale	n/a	n/a	55	27800	0.5	(Thorne, 1980)
53	Siltstone	705	7.3	9	13100	1.5	(Radhakrishnan and Leung, 1989)
54	Marl	1200	18.5	0.9	5300	5.9	(Carrubba, 1997)
55	Diabase	1200	19	15.0	8900	0.6	(Carrubba, 1997)
56	Limestone	1200	13.5	2.5	8900	3.6	(Carrubba, 1997)

Point Bearing Capacity

The easiest, simplest, and most popular way to estimate the point bearing capacity is to correlate the unconfined compressive strength (UCS) of rock with the unit point bearing. Typically, a linear equation is preferred for its simplicity, as follows:

$$q_{tip} = N_c \, \sigma_c \qquad\qquad\qquad \text{Equation 1.2-4}$$

where N_c is an end bearing capacity factor, σ_c is unconfined compressive strength (UCS) at twice the shaft diameter below the shaft tip, and q_{tip} is an ultimate unit point bearing. It is important to note that UCS is twice the undrained shear strength: thus, N_c becomes twice the value when undrained shear strength is used. Theoretically, the end bearing capacity factor is calculated to be 4.5 for deep foundation when the failure surface from the shaft tip does not extend to the ground surface. The equation is theoretically applicable to intact rock, which is not the case when dealing with a rock mass. The N_c should be smaller than the theoretical value for drilled shafts imbedded into considerably fractured rock. The recommended bearing capacity factor can be as low as 2.5 when the length of the socket is larger than 1.5 times the socket diameter (D) (Abu-Hejleh et al., 2003). Indeed, the low end bearing capacity accounts for the possible weakening or softening of rock mass with time (O'Neill and Reese, 1999). It is certain that the value can be lower than 2.5 under severe circumstances.

Zhang and Einstein (1998) investigated the point bearing capacity of drilled shafts embedded in rock by back-analyzing a database of 39 drilled shaft load tests. The analyzed rocks are relatively soft with RQD between 70 and 100 and mostly closed horizontal joints. Figure 1.2.15 exhibits the developed database for point bearing capacity of drilled shafts and corresponding UCS. The equation correlating the UCS and unit point bearing is obtained by best-fitting data sets. The equation is nonlinear, unlike equation Equation 1.2-4, and the correlation coefficient of the regression, r^2, was 0.81. The equation is given below.

$$q_{tip} = 4.83 \, \sigma_c^{\,0.51} \qquad\qquad\qquad \text{Equation 1.2-5}$$

where the units of q_{tip} and σ_c are in MPa. The linear correlation between UCS and unit point bearing capacity appears to be unacceptable through the entire range of UCS. In fact, the bearing capacity factor tends to decrease as the UCS increases, implying the strong rock mass tends to be governed by other features instead of the strength of strong rock core. The other features may include the fractures and weak and thin layers of soft material (clay). On the other hand, possible fractures in soft rock may not be the main cause of overall failure of rock mass. Especially, the effect of fractures is trivial when the fractures are parallel to the loading direction that is expected under the shaft tip resting on sedimentary rocks.

The bearing capacity factors obtained from the back analyses are as high as 6.9 for 0.5 MPa (10 ksf), and decline to 2.24 and 1.56 for 5 MPa (100 ksf) and 10 MPa (200 ksf) of UCS. Based on the database, the lower bound and upper bound of unit point bearing is recommended when the embedment ratio of the drilled shaft is greater than 3.0 (Zhang and Einstein, 1998):

Lower bound: $q_{tip} = 3.0 \, (\sigma_c)^{0.5}$
Upper bound: $q_{tip} = 6.6 \, (\sigma_c)^{0.5}$
Mean: $q_{tip} = 4.8 \, (\sigma_c)^{0.5}$
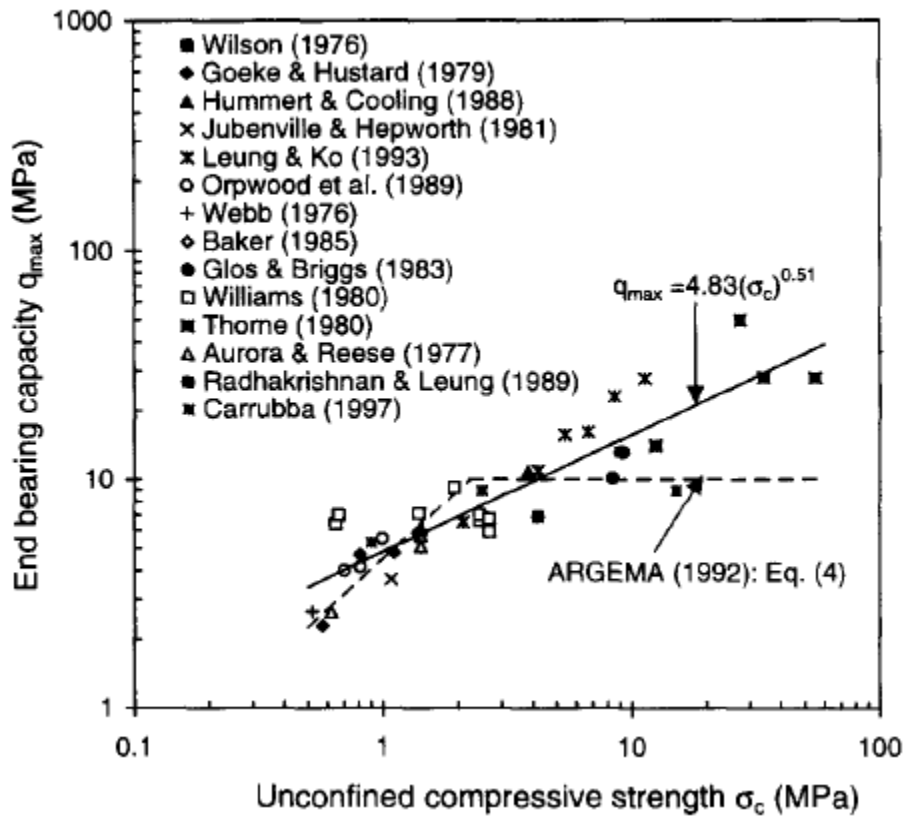
Figure 1.2.15 Relation between UCS and unit point bearing capacity (Zhang and Einstein, 1998)

It should be noted that the data sets are rare at relatively high strength rock (over 20 MPa), because the drilled shafts on such rock are unlikely to fail by normal capacity load testing system. Therefore, the equation may apply appropriately to the rock whose strength is less than 20 MPa. However, normal structures on such strong rock should perform safely and do not attract engineers' attention. Another full scale load test was performed in Colorado to assess the point bearing capacity of drilled shafts embedded in soil-like claystone using Osterberg cell load test (Abu-Hejleh et al., 2003). The soil-like claystone is medium hard to hard, brown interbedded with sandstone seams. The UCS of the layer was measured to be 0.6 MPa (13.1 ksf), and the bearing capacity factor was calculated to be 3.8 for such strength range.

Limited information was used to develop the relationship between the UCS of clay shales near the Dallas area and point bearing capacity. The bearing capacity factor relating point bearing capacity and UCS is calculated to be 4.04 (Vipulanandan and Moon, 2005). The correlation for soft rocks was updated by adding new data sets in their later study (Vipulanandan et al., 2007). Load test results are documented for soft rocks with strength less than 2.5 MPa and used to develop a nonlinear relationship between ultimate point bearing capacity and UCS. The utilized UCS of the soft rock ranges from 0.14 MPa to 2.5 MPa, and the ultimate unit point bearing ranges from 1.0 MPa to 9.2 MPa. The nonlinear relationships were obtained using least-square best fit of 21 data points, and are given by:

$$q_{tip} = 3.53\,\sigma_c^{\,0.56}$$
Equation 1.2-6

where the units are in MPa. The nonlinear relation created for soft rocks is toward the proposed lower bound by Zhang and Einstein (1998).

Datasets of Table 1.2.6 are used to build updated correlation between ultimate unit point bearing capacity and UCS. The regression with power law was employed, and the updated equation is shown below.

$$q_{tip} = 4.64 \, \sigma_c^{\,0.52}$$

Equation 1.2-7

As shown, the equation is very close to the proposed equation by Zhang and Einstein (1998) with slightly lower correlation coefficient (r^2) of 0.68. The new data sets are plotted in Figure 1.2.16 and present the expected pattern: the end bearing capacity factor decreases as UCS increases. The correlation between the bearing capacity factor and the available range of UCS is exhibited in Figure 1.2.17. It is shown that the bearing capacity factor becomes as low as 0.5 when UCS of rock is as high as 55 MPa. The rock type of that case was shale with thin mud seams, which seems to result in early failure of drilled shafts (Thorne, 1980).

The theoretical bearing capacity factor of 4.5 corresponds to the UCS of approximately 0.82 MPa in Figure 1.2.17. This UCS value is slightly above the lower limit (0.6 MPa) of UCS for non-durable rock or clay shale (Grainger, 1984; Morgenstern and Eigenbrod, 1974). This observation is intriguing because the key characteristic of rock (not soil) is the existence of fractures or fissures and their influences on the overall behavior of rock mass. The drilled shafts embedded into the rock stronger than 0.82 MPa appears to be ruled by other geological features.
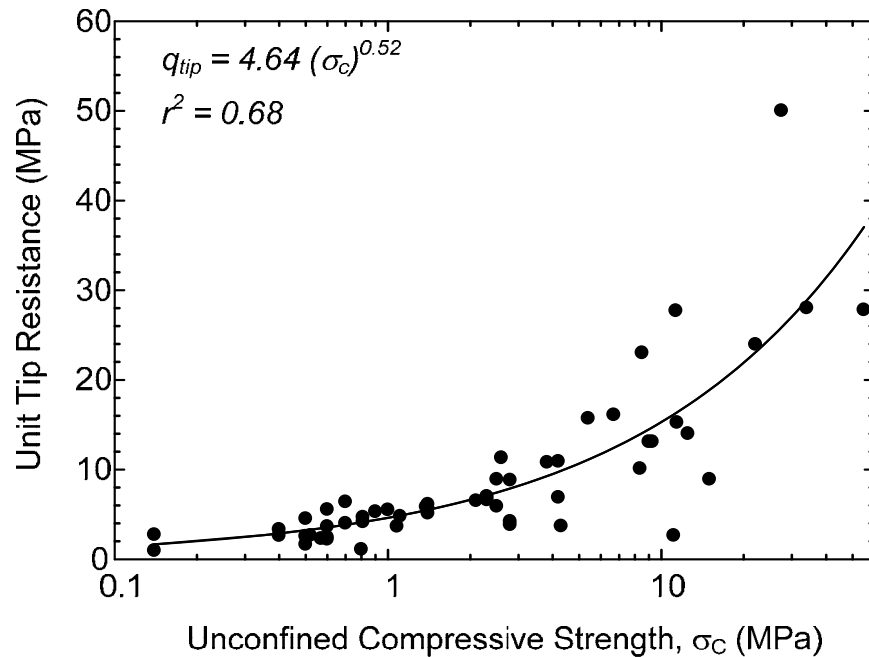
Figure 1.2.16 Unconfined compressive strength and unit tip resistance: all data in Table 1.2.6
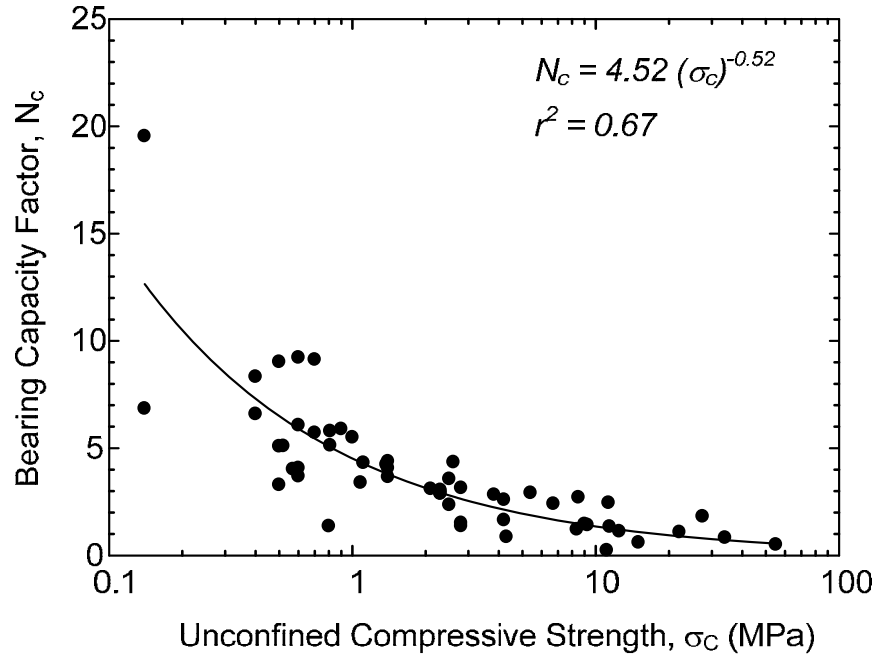
Figure 1.2.17 Relation between bearing capacity factor and UCS: all data in Table 1.2.6

As previously discussed, the bearing capacity factor of drilled shafts in strong rock is different from that in soft rock possibly because of the fractures. Therefore, a different database should be established for different strengths of rock. Grainger (1984) defines non-durable rock as the rock whose strength falls between 0.6 and 3.6 MPa; thus the database of drilled shafts tipping on the non-durable rock is established excluding unnecessary database. The new database includes other kinds of formations such as till, gypsum, and limestone in a range of strength. Figure 1.2.18 and Figure 1.2.19 present the variation of unit tip resistance and end bearing capacity factor with respect to UCS. The same fitting equation was adopted, and the obtained correlations for soft rock are shown below. No significant difference in the equations is observed.

$$q_{tip} = 4.69 \, \sigma_c^{\,0.43} \qquad\qquad \text{Equation 1.2-8}$$

$$N_c = 4.65 \, \sigma_c^{\,-0.53} \qquad\qquad \text{Equation 1.2-9}$$
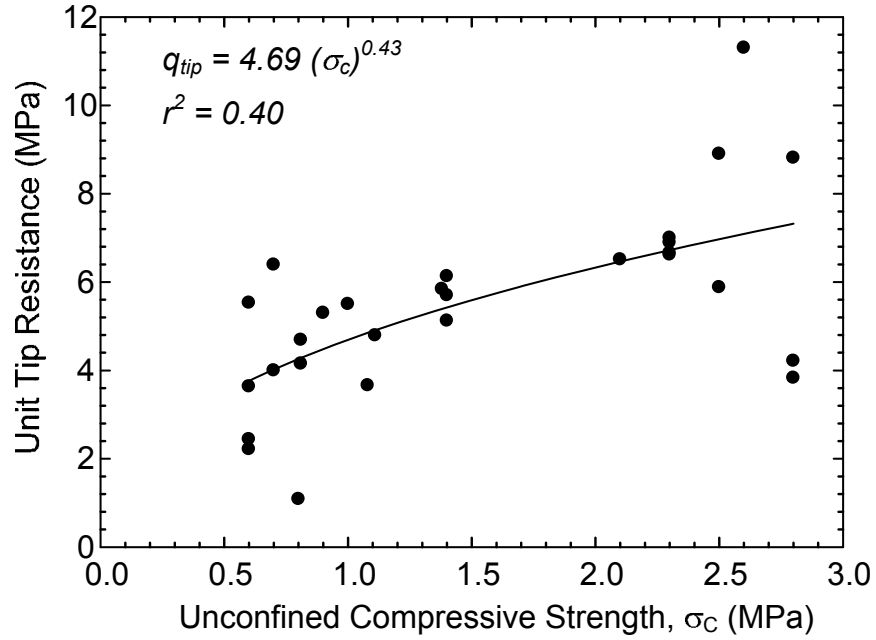
Figure 1.2.18 Unconfined compressive strength and unit tip resistance: Data for 0.6 MPa ≤ UCS ≤ 3.6 MPa in Table 1.2.6
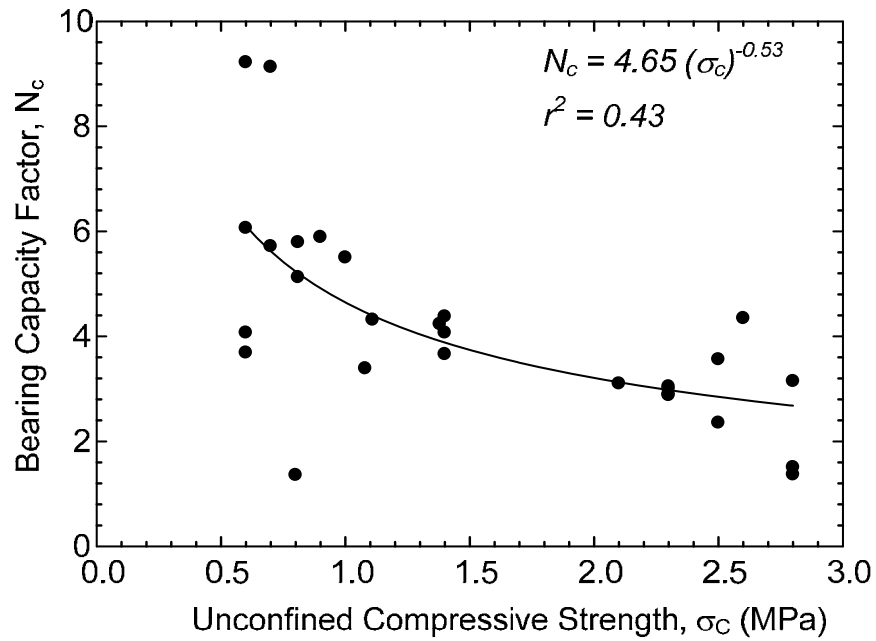
Figure 1.2.19 Relation between bearing capacity factor and UCS: Data for 0.6 MPa ≤ UCS ≤ 3.6 MPa in Table 1.2.6

1.3 PROPERTIES OF TEXAS ROCKS

1.3.1 Introduction

Geology and existing engineering properties of the six studied formations, Cation Exchange Capacity test, and adsorption isotherm test are presented in this Chapter. The boring location sampled and analyzed includes the following geologic formation and groups (from oldest to youngest): Edwards Limestone, Del Rio Group, Eagle Ford Group, Austin Chalk, Taylor Group, and Navarro Group. All are of Cretaceous age (144 m.y. to 66 m.y.).

The sampling locations of five of the six Texas formations studied are shown in Figure 1.3.1. Only the Edwards Limestone formation was not studied at this level because the boring logs are unavailable. The Del Rio Clay was cored near Round Rock, located north of Austin, and the other four formations were obtained at the outskirt of Dallas, Texas. The closed up location will be discussed in the geology section. On the map of Figure 1.3.1, specific locations of the formations are marked with a two letter abbreviation of the full name. For example, Del Rio Clay was named "DR," and Eagle Ford Shale was named "EF" in the figure. Figure 1.3.2 presents the generalized stratigraphy of North Central Texas. The Edwards Limestone, Del Rio Clay, Eagle Ford Shale, Austin Chalk, and Taylor Marl and Navarro Shale were deposited from oldest to youngest during the Cretaceous period (144 m.y. – 66 m.y.).

After reviewing geology of each formation, engineering properties of each are extensively collected and reviewed. Large amounts of information are available from the Superconducting Super Collider (SSC) project that was planned near the City of Dallas. Test results from site investigation for the Waco Dam and Austin Tunnels are also reviewed and added to the database. Moreover, additional tests are carried out to characterize clay shales: using cation exchange capacity, Atterberg limit, and the adsorption isotherm test. The test results are introduced at the end of this section.
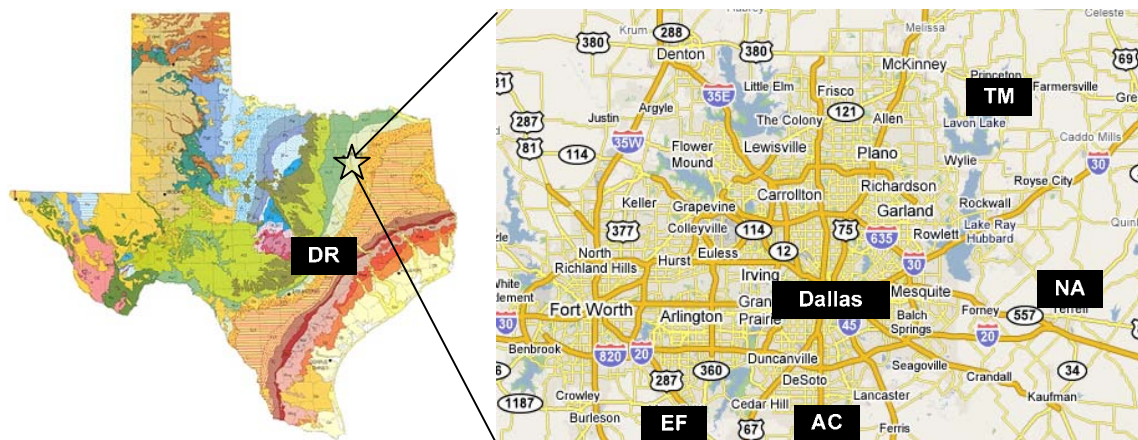
AC: Austin Chalk, Red Oak, Texas
EF: Eagle Ford, Mansfield, Texas
TM: Taylor Marl, Princeton, Texas

NA: Navarro, Terrell, Texas
DR: Del Rio, Round Rock, Texas

Figure 1.3.1 Sampling location of the five Texas formations

Era	Period	Age (m.y.)	Formation/Group
CENOZOIC	TERTIARY	PALEOCENCE (56 – 66)	WILCOX
			MIDWAY
MESOZOIC	CRETACEOUS	GULFIAN (66 – 100)	NAVARRO
			TAYLOR
			AUSTIN
			EAGLE FORD
			WOODBINE
		COMANCHEAN (100 – 127)	BUDA
			DEL RIO
			GEORGETOWN
			EDWARDS

Figure 1.3.2 Generalized stratigraphic chart showing the deposition order of North-Central Texas. (Hinds and Berg, 1990)

1.3.2 Geology

Dallas District

The City of Dallas is located in north central Texas and is geologically located on the border of Ku1 (Austin, Eagle Ford, Woodbine, and U. Washita Groups) and Ku2 (Navarro and Taylor Groups) geological groups. Because deposits are gently tilted and dip to the East in an otherwise flat geomorphology, Navarro Group and Taylor Groups outcrop on the west side of the City of Dallas, whereas Austin Chalk, Eagle Ford Shale, Woodbine Groups spread on the east side.

Eagle Ford Shale

The Eagle Ford shale was named after the City of Eagle Ford, located in Dallas County, by Hill in 1887 (Nichols et al., 1968). In Central Texas, the Eagle Ford Shale contains abundant clay minerals, generally consisting of smectite (Dawson, 2000). The Eagle Ford Shale is a surface deposit in the City of Dallas formed in the upper Cretaceous Gulfian Age under very high sea levels. The formation is known as highly fissile, typically parallel to bedding plane, and is black calcareous to noncalcareous interbedded with thin flaggy limestone (Allen and Flanigan, 1986). Clay minerals are dominant constituents in Eagle Ford Shale and consist chiefly of smectites. The Eagle Ford Shale is about 145 m (475 ft) thick in the Dallas area and is divided

into two members: Acadia Park and the Britton in descending order. Austin Chalk unconformably overlies Acadia Park. The Acadia Park member is differentiated from the Britton member by about 1 m (1 – 3 ft) thick limestone, which is called Kamp Ranch Limestone, and is approximately 30 m (100 – 120 ft) thick overlying the limestone. The Arcadia Park member is dark gray to grayish black, noncalcareous, and laminated. The general Eagle Ford Shale comprises 40 percent montmorillonite, 7 percent illite, 5 percent kaolinite, 2-8 percent calcite, 11 percent quartz, and 27 percent of other minerals. The Britton member is further divided into lower and upper Britton. The lower Britton is about 26 m (85 ft) thick, moderately hard, and very calcareous clay shale with interlayering bentonite seams. The upper Britton has approximately 38 m (125 ft) thickness in the Dallas area with frequent concretions bearing clay shales. The lower Britton is more calcareous and indurated than the upper Britton member (Allen and Flanigan, 1986). The engineering properties of Eagle Ford Shale in the Dallas area vary widely depending on the location and depth of boring. Hence, the allowable bearing capacity and settlement of foundation also range widely from 0.1 MPa (1 tsf) to 1.8 MPa (18 tsf) (Allen and Flanigan, 1986).

The Eagle Ford Shale used in this study was cored near Mansfield, Texas, located southwest of the City of Dallas. The member of the Eagle Ford Shale is Britton, but it is not clear whether it is the lower or upper member of Britton. The boring location was marked on the topographic map as shown in Figure 1.3.3, which is part of a 7.5 minute quadrangle map of Britton. The site was located besides State Highway 360, which is not recorded in the map. According to the map, the elevation of the boring was about 152 m (500 ft) above sea level.
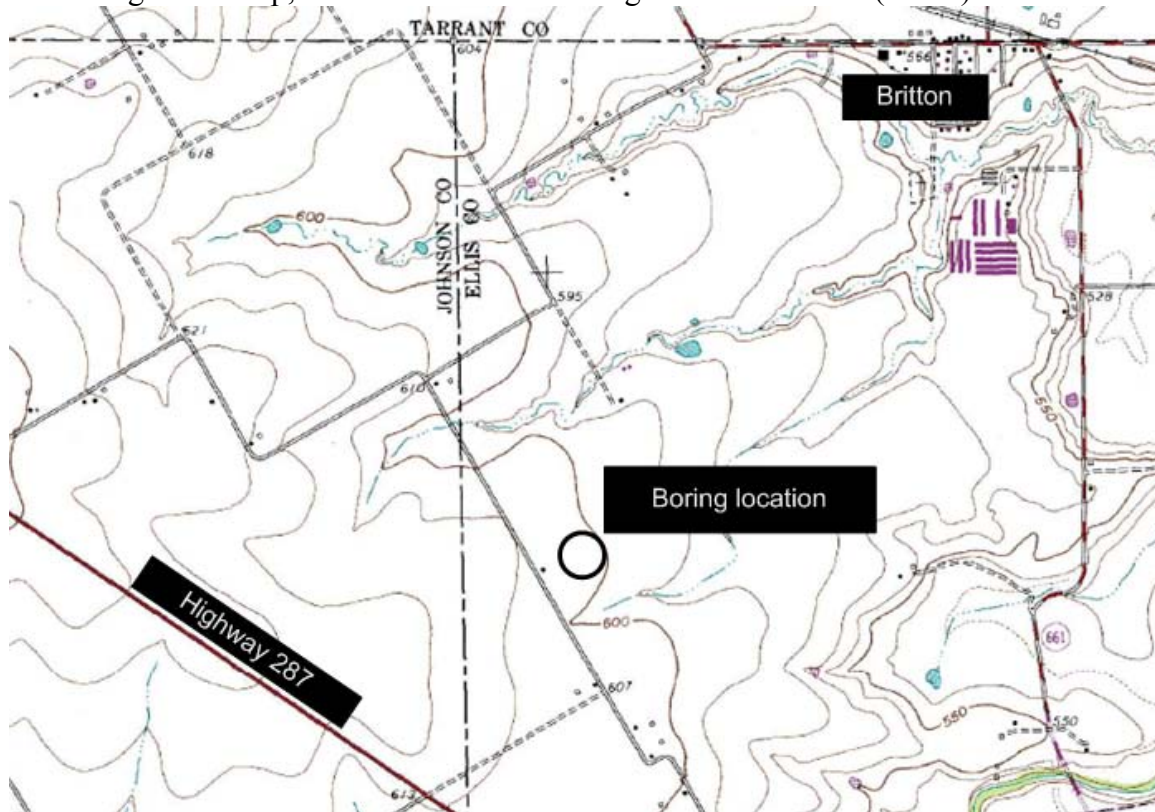
Figure 1.3.3 Boring location on topographic map near Mansfield, Texas

Austin Chalk

The Austin Chalk was named after the limestone outcropping near the City of Austin, which overlies Eagle Ford Shale (Nichols et al., 1968; Shumard, 1860). The Austin Chalk was deposited in a marine shelf setting as an upper Cretaceous rock unit (Chanchani et al., 1996). The chalk consists predominantly of light-gray, argillaceous, fossiliferous, white chalky limestone, and fine grained, dense microcrystalline, with intervening thin micaceous dark-gray shale units and commonly contains fossil oyster. (Hanson and Small, 1995; Nichols et al., 1968). The Austin Chalk unconformably overlies the Eagle Ford Shale and is unconformably overlain by the lower member of the Taylor Group (Ozan formation). The chalk is made up of three members: the lower chalk, the middle marl, and the upper chalk (Chanchani et al., 1996; Dawson and Reaser, 1996). The lower member (chalk) is marked by a layer of argillaceous chalk with abundant fossil detritus, pyrite and phosphate nodulues. The layer is locally called Transition Zone whose thickness ranges from 0 – 4 m (1 to 12 ft). The upper and lower chalk are lithologically similar and comprise 1 – 2 m (2 – 5 ft) beds of light gray to tan-weathered chalk interbedded with 0 – 1 m (1 – 2 ft) beds of marl. The middle member predominantly comprises 1 – 2 m (2 – 5 ft) beds of marl interbedded with 0 – 1 m (1 – 2 ft) beds of chalk. The maximum thickness of Austin Chalk is approximately 170 m (550 ft) in the City of Dallas, and 206 m (675 ft) in Dallas County (Allen and Flanigan, 1986).

Although the Austin Group is lithologically subdivided, the overall engineering properties of the Austin Chalk is considered to be homogeneous; therefore, the Austin Chalk is typically not subdivided into smaller formations for engineering purposes (Allen and Flanigan, 1986; Raney et al., 1987). The allowable bearing capacity of the unweathered Austin Chalk ranges from 3.5 MPa (35 tsf) to 5 MPa (50 tsf), and the settlement is expected to be less than 6.4 mm (0.25 in) when foundation rests on the chalk (Allen and Flanigan, 1986). The Austin Chalk used in this study was obtained on the Houston School Road of Red Oak, Texas. The boring location is marked in the topographic map of Lancaster, as shown in Figure 1.3.4. The cores are obtained at the elevation of approximately 177 m (580 ft)
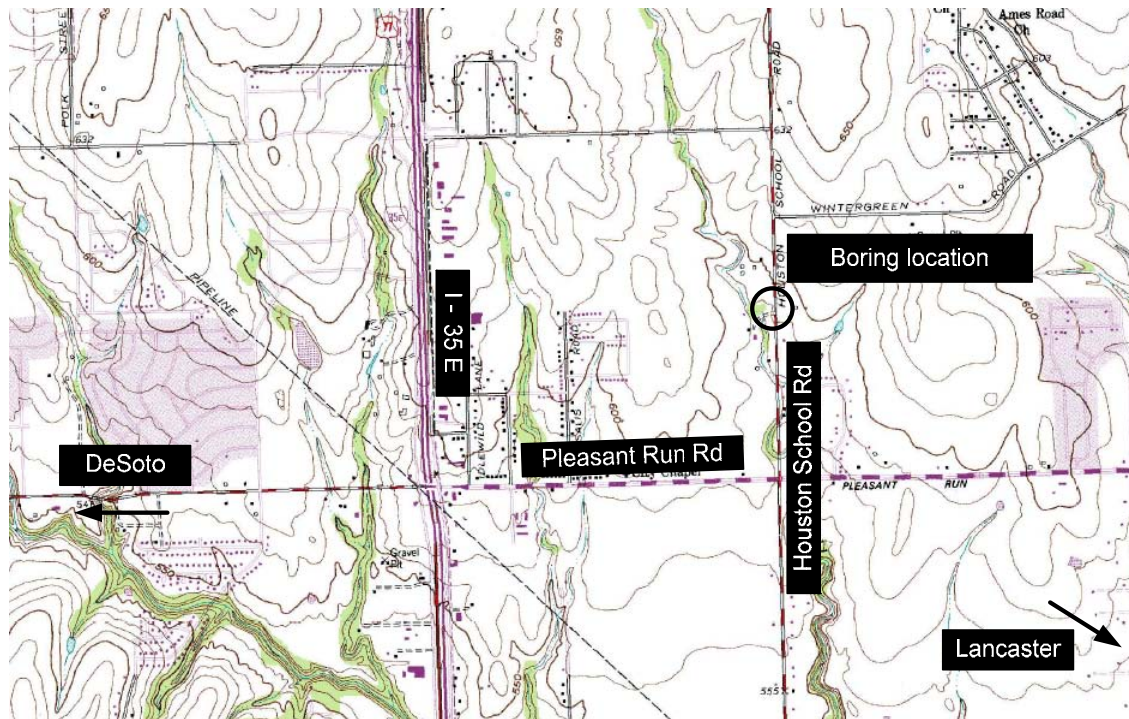
Figure 1.3.4 Boring location of Austin Chalk on topographic map of Lancaster

Taylor Marl

The Taylor Group was named after Taylor Prairie, Williamson County, Texas in 1892 (Nichols et al., 1968), and is comprised of chalky limestone that is sandwiched between the Austin Chalk and the Navarro Group. Deposition of the Taylor Marl took place during the upper Cretaceous (Gulfian) in a relatively shallow sea (Young, 1972). The Taylor Group is subdivided into four members, from the oldest to the youngest: 1) Ozan formation (Sprinkle formation in some locales), 2) Wolfe City formation, 3) Pecan Gap formation, and 4) Marl Brook Formation (Bergstrom formation in some locales). The Ozan formation is highly calcium carbonated, gray to greenish-gray, montmorillonitic, and slightly fissile, and contacts with upper member of Austin Chalk. The Wolfe City formation is sandstone overlying the Ozan formation. The Pecan Gap formation (chalk) is sandwiched between the Wolfe City and Marl Brook formations and consists of gray to gray-brown, soft, poorly bedded, compact, fossiliferous, marly chalk. The Marl Brook formation (marl) consists of a gray to greenish-gray, unctuous, montmorillonitic clay with slight fissility (Funk, 1975; Nichols et al., 1968). The typical Taylor Marl contains 60 to 70 percent illite and montmorillonite clay minerals interbedded with bentonite and chalk. Other non-clay minerals include calcite and feldspar (Lundin et al., 1990).

East of the City of Dallas, the Ozan formation is a surface deposit consisting of uniformly laminated, montmorillonitic, calcareous marine clay shale. The thickness of the Ozan formation near the City of Dallas is estimated to be 15 m – 30 m (50 – 100 ft). Most Ozan marl encountered in the city during construction is found to be weathered, and the variation of material properties is considerable (Allen and Flanigan, 1986). The Taylor Marl used in this study was obtained south of Princeton, near the intersection of local road 447 and 398. The name of the cored particular member is Ozan formation, the lowest member of the Taylor Group.
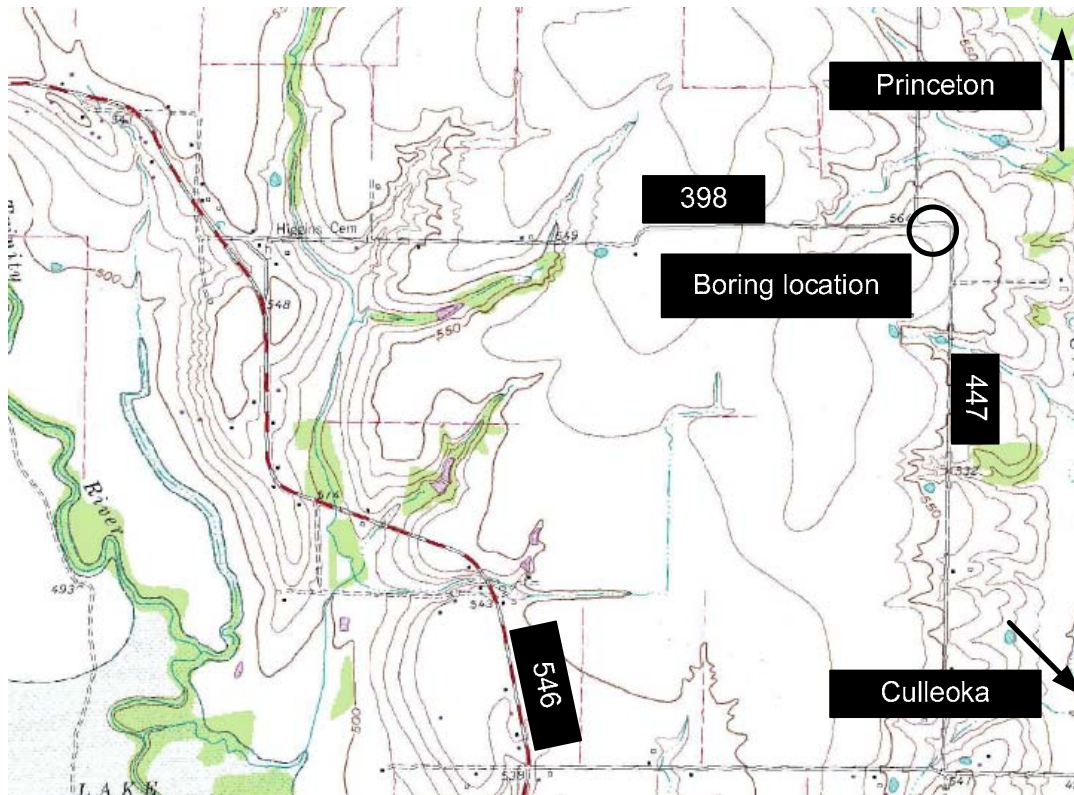
Figure 1.3.5 Boring location of Taylor Marl on topographic map near Princeton

Navarro Shale

The Navarro Group is the youngest Cretaceous formation overlying the Taylor Group and underlying the Midway Group. In northeast Texas, the Navarro Group is divided into three members in descending order: 1) Kemp Corsicana formation, 2) Nacatoch formation (sandstone), and 3) Neylandville formation (marl) (Adkins, 1933; Nichols et al., 1968). The Kemp Corsicana and Neylandville formations consist predominantly of light-gray microfossiliferous, micaceous, flaky shale interbedded with marly, calcareous, nonporous sandstone and very thin stringers of pale green white bentonite (Nichols et al., 1968). The Nacatoch formation is characterized by fossiliferous, calcareous quartz marine sandstone (Nichols et al., 1968). Lithologically, the Navarro formation is very similar to the Taylor Formation but is differentiated by the greater sand and glauconite content in the Navarro Formation (Chimene, 1983). The Navarro Shale used in this study was obtained northwest of Terrell, Texas, near the intersection of FM 1392 and 205 (See Figure 1.3.6). The available GPS reading of the location was N 32.78913 / W 96.32494, and the elevation of the site is approximately 160 m (525 ft). The obtained cores belong to the Kemp Corsicana member, which is the uppermost member of the Navarro Group.
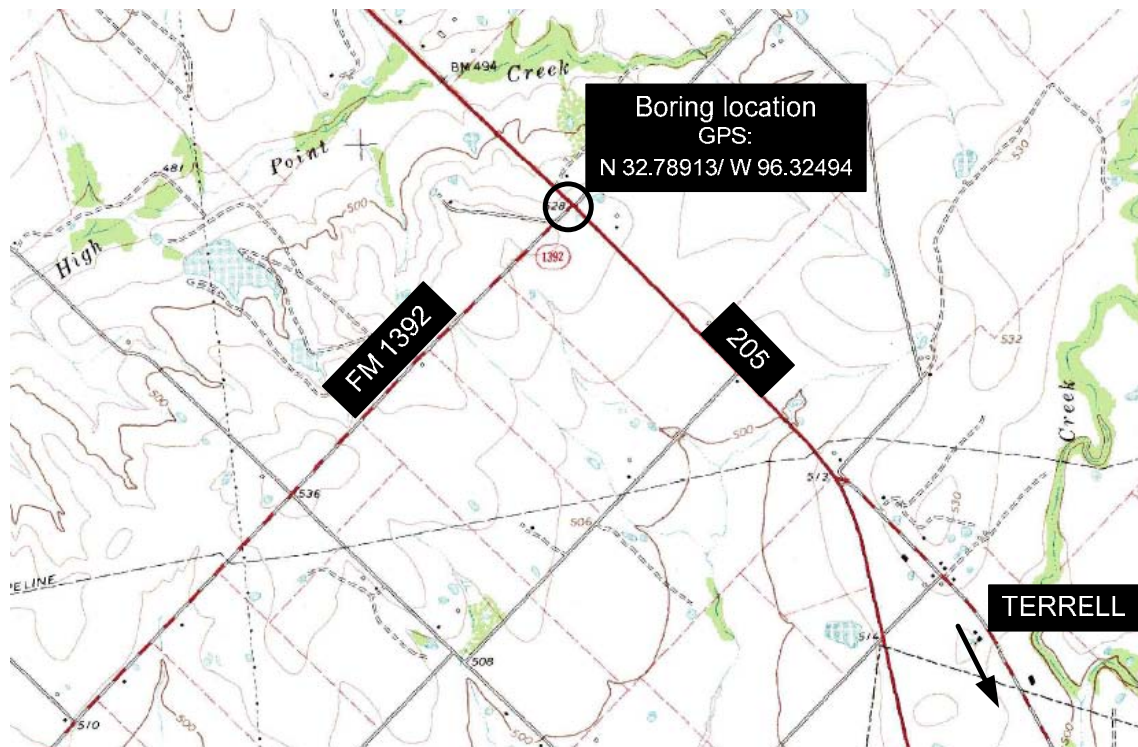
Figure 1.3.6 Boring location of Navarro Shale on topographic map near Terrell

Austin Area

    The City of Austin is located at the boundary between the Edwards Plateau to the west and the prairies of the coastal plain to the east (Nelson, 1987). Del Rio Clay and Edwards Limestone were obtained near the Austin area, so the geology of Austin is reviewed in this section.

Del Rio Clay

    Del Rio Clay contains bluish-green to yellow brown clay particles interbedded with thin beds of impermeable limestone, iron nodules, and oyster fossils. The clay contents of the units are predominantly kaolinite, illite, and a little smectite (Clark et al., 2006). The basal of Del Rio Clay is in contact with Georgetown Limestone with a transitional layer of several meters, and discomformably overlain by Buda Limestone. In the Austin area, the Del Rio Clay outcrops sporadically along Shoal Creek and Barton Springs Road and is approximately 23 m (75 ft) thick (Garner and Young, 1976). The Del Rio Clay used in this study was obtained near the Chandler Road, north of Round Rock, Texas (See Figure 1.3.7). The elevation of the site is approximately 235 m (770 ft).
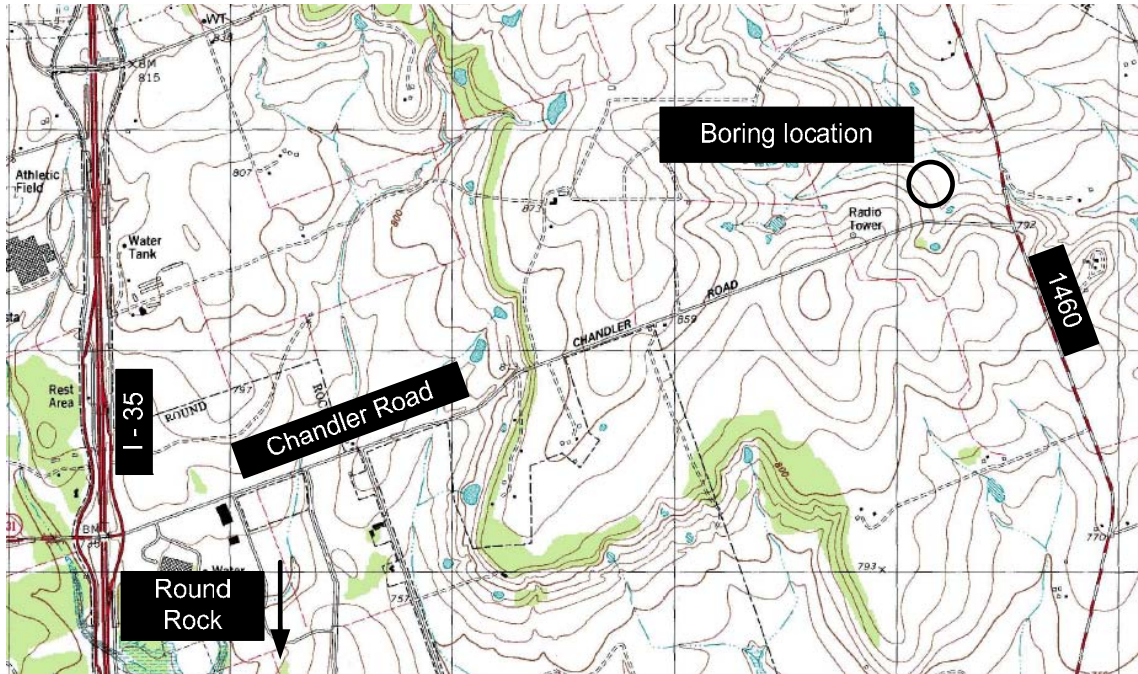
Figure 1.3.7 Boring location of Del Rio Clay on topographic map near Round Rock

Edwards Limestone

Edwards Limestone of the Austin area is approximately 100 m (300 – 340 ft) thick and is lithologically divided into four members. The lowest member of Edwards Limestone, mostly encountered in the Austin area, is about 104 m (200 ft) thick and consists of dolomite, dolomitic limestone, and hard gray limestone with gray to black chert. The third member consists of 12 m (40 ft) thick fine-grained dolomitic limestone and fine-grained flaggy limestone with common nodular chert. The second member is 3 – 4 m (10 – 15 ft) thick and mostly soft burrowed limestone. The uppermost Edwards Limestone is about 12 m (40 ft) thick and consists of flaggy limestone beds (Garner and Young, 1976). Edwards Limestone was deposited during Lower Cretaceous time in a carbonate environment. The limestone conformably contacts above with Georgetown and below with Walnut formations (Nichols et al., 1968). Unfortunately, the details of the boring location are unavailable for this rock unit.

1.3.3 Engineering Properties Available in the Literature

The engineering properties of clay shales and limestone published in the literature are summarized and discussed in this section. The clay shales summarized include Del Rio Clay, Navarro Shale, Taylor Marl, and Eagle Ford Shale, and the limestone included is Austin Chalk. Unfortunately, engineering properties of Edwards Limestone are unavailable.

The engineering properties will be provided in terms of an average value (if not a single value) and the ranges of the property are given in parentheses. A majority of the available data was obtained from extensive laboratory tests for the Superconducting Super Collider (SCC) tunnel project near Dallas, Texas in the early 90's. During the design and construction of this tunnel, three weathered and unweathered formations were of interest: Eagle Ford Shale, Austin Chalk, and Taylor Marl. Therefore, rigorous laboratory and field tests were performed on those formations. However, it should be noted that the existing sources for the project seem to share

similar database; thus, the obtained engineering properties are similar although the references are different. All available values are provided in this literature review with original references. Unfortunately, information for Navarro Shale and Edward Limestone is scant. The purpose of this section is to establish quick reference lists of the engineering properties of the Texas formations used in this study.

Index Property

Index properties of five formations are discussed in this section. Engineering properties of Edwards Limestone is unavailable. The index properties discussed include water content, specific gravity, Atterberg limit, carbonate content, and clay mineralogy.

Water content

The water content of four clay shales collected from various references are summarized in Table 1.3.1. The water content of the clay shales in Texas generally ranges between 15 and 20%. When the formation is bentonitic or weathered, the water content has been measured as high as 30%.

Table 1.3.1 Water content of the formations used in this study

Formation	Description	Water Content (%)	Reference
Del Rio Clay	Waco Dam	18 (16-23)	(Stroman and Feese, 1984)
	Waco, Texas	16	(Auken, 1963)
Eagle Ford Shale	Dallas, SSC project	16 (4-25)	(TECT, 1990a)
	Dallas, SSC project	17 (12-22)	(Lai, 1997)
	Dallas, SSC project	17	(Laughton et al., 1991)
	Dallas, SSC project	15 (11-19)	(Nelson and Lundin, 1990)
	Waco, Texas	16	(Auken, 1963)
Austin Chalk	Dallas, SSC project	13	(Laughton et al., 1991)
	Dallas, SSC project	12 (5-20)	(Nelson and Lundin, 1990)
	Austin, Tunnel	4.7-11	(Nelson, 1987)

Taylor Marl	Dallas, SSC project, Weathered	25 (16-47)	(TECT, 1990b)
	Dallas, SSC project	16 (3-38)	(Hsu, 1989; TECT, 1990b)
	Dallas, SSC project, Bentonitic Shale	30 (24-40)	(Hsu, 1989)
	Dallas, SSC project	17	(Laughton et al., 1991)
	Dallas, SSC project	16 (11-22)	(Nelson and Lundin, 1990)
	Austin, Texas	3.1-21.8	(Nelson, 1987)

Specific gravity

The specific gravity of the formations is approximately 2.70, which is commonly used in geotechnical practice. The specific gravity of Eagle Ford Shale is slightly higher than that of Taylor Marl or Austin Chalk.

Table 1.3.2 Specific gravity of the formations used in this study

Formation	Description	Specific Gravity	Reference
Eagle Ford Shale	Dallas, SSC project Oven dried samples. Pyrite	2.78	(Brouillette et al., 1993)
	Dallas, SSC project	2.78	(Lai, 1997)
	Dallas, SSC project	2.72	(Laughton et al., 1991)
Austin Chalk	Dallas, SSC project	2.67	(Laughton et al., 1991)
Taylor Marl	Dallas, SSC project	2.71	(Laughton et al., 1991)

Atterberg limit

Atterberg limit tests are feasible when stiff clay shales are ground to fine particles; and the liquid limit and plastic limit obtained from the tests may be used to determine the plasticity of such formations. The objectives of the test are to find the liquid limit that is the boundary between the plastic state and the liquid state, and to find the plastic limit that is the boundary between the semi-solid state and the plastic state. The moisture content at each limit refers to liquid limit and plastic limit, and the gap between the two limits refers to plasticity index (PI). The liquid limit and plasticity index may be used to classify the soil based on Casagrande's plasticity chart.

The test results of the Atterberg limit on Del Rio Clay, Eagle Ford Shale, Austin Chalk, and Taylor Marl are listed in Table 1.3.3. The liquid limit and plasticity index of Del Rio clay was measured to be about 60 and 40 respectively, which falls in highly plastic clay (CH) or highly plastic organic soil (OH) according to Casagrande's plasticity chart (see Figure 1.3.10).

The test results for Eagle Ford Shale and Taylor Marl are similar to those of Del Rio Clay, but the liquid limit of bentonite shale is much higher than that of other formations.

Table 1.3.3 Atterberg limit of the formations used in this study

Formation	Description	LL	PI	Reference
Del Rio Clay	Waco, Texas	68 (56-74)	47 (39-51)	(Stroman and Feese, 1984)
	Waco, Texas	60	42	(Auken, 1963)
Eagle Ford Shale	Dallas, SSC project	87 (39-140)	58 (16-113)	(TECT, 1990a)
	Dallas, SSC project	72 (59-88)	42 (31-58)	(Brouillette et al., 1993)
	Dallas area	60-80	34-48	(Font, 1979)
	Dallas, SSC project	75 (50-94)	47 (31-65)	(Lai, 1997)
	Dallas, SSC project	81	52	(Laughton et al., 1991)
	Dallas, SSC project	93 (76-104)	63 (46-73)	(Nelson and Lundin, 1990)
	Waco, Texas	65	45	(Auken, 1963)
Austin Chalk	Dallas, SSC project	30 (25-51)	10 (0-28)	(Nelson and Lundin, 1990)
Taylor Marl	Dallas, SSC project Weathered	84 (46-149)	62 (19-116)	(TECT, 1990b)
	Dallas, SSC project	65 (34-151)	43 (17-112)	(TECT, 1990b)
	Bentonitic Shale	126 (108-149)	98	(Hsu, 1989)
	Dallas area	50-70	35-49	(Font, 1979)
	Dallas, SSC project	81	51	(Laughton et al., 1991)
	Dallas, SSC project	80 (5.8-97)	51 (33-70)	(Nelson and Lundin, 1990)

Carbonate content

Calcium carbonate ($CaCO_3$) is a type of cementation between clay particles, frequently leading to higher strength and good durability over the service life of engineering structures. The calcium carbonate originates from the skeletons of floating marine organisms of the upper ocean. In a shallow sea, the organisms settle slowly to the sea floor after their death, and the sediments are compacted and/or cemented to stiffer materials. The sediments containing skeletons of marine organisms become carbonate clay shales after a geologically long time. Also, such

carbonate shales indicate that the deposition took place under a shallow sea because the skeleton of the organisms would dissolve to water if it takes long for them to settle to deep sea.

The carbonate content of Eagle Ford Shale, Austin Chalk, and Taylor Marl is shown in Table 1.3.4. The carbonate content of the Austin Chalk was measured to be the highest (65) and followed by Taylor Marl and Eagle Ford Shale according to the available data,. This finding seems natural because the high carbonate content results in high strength (Hsu, 1996).

Table 1.3.4 Calcium carbonate of formation used in this study

Formation	Description	Carbonate Content (%)	Reference
Eagle Ford Shale	Dallas, SSC project	10 (2-39)	(TECT, 1990a)
	Dallas area	2-30	(Font, 1979)
	Dallas, SSC project	8	(Laughton et al., 1991)
Austin Chalk	Dallas, SSC project	65	(Laughton et al., 1991)
Taylor Marl	Dallas, SSC project	25 (5-83)	(TECT, 1990b)
	Dallas area	58	(Font, 1979)
	Austin, Sprinkle	42	(Funk, 1975)
	Austin, Pecan Gap	42	(Funk, 1975)
	Austin, Bergstrom	20	(Funk, 1975)
	Dallas, SSC project	24	(Laughton et al., 1991)

Clay mineralogy

Table 1.3.5 displays the percentage of clay fraction, activity, and the percentage of smectite. The percentage of smectite means the ratio of the amount of smectite to the clay-sized fraction, which was determined by particle size (<0.002 mm). The activity is defined as the ratio of the plasticity index to the clay fraction, and they are well correlated with the type of clay mineral. In other words, high activity indicates that the sample tends to contain more montmorillonite. Clay content of Eagle Ford Shale and Taylor Marl is similar, and higher than that of Del Rio Clay. Specifically, the components of clay minerals of the five formations are tabulated in Table 1.3.6. Navarro Shale and Taylor Marl contain a large amount of montmorillonite, whereas the amount of montmorillonite in Del Rio Clay and Eagle Ford Shale is relatively low. The percentage of montmorillonite is a good indicator to determine the swelling potential as the clay mineral adsorbs water significantly.

Table 1.3.5 Percentage of clay mineral, activity, and percentage of smectite

Formation	CLAY %	Activity	Smectite	Reference
Del Rio Clay	36-50	1.61	10-15	(Stroman and Feese, 1984)
Eagle Ford Shale	38-88	0.3-1.2	14-74	(TECT, 1990a)
	70	n/a	n/a	(Font, 1979)
Taylor Marl	28-90	n/a	41-75	(TECT, 1990b)
	70	n/a	n/a	(Font, 1979)

Table 1.3.6 Components of clay minerals of the formations used in this study

Formation	% clay minerals	Illite (%)	Kaolinite (%)	Smectite/ montmorill onite (%)	Reference
Del Rio Clay	40	38	38	25	(Auken, 1963)
Eagle Ford Shale	86	35 (13-54)	26 (15-48)	40 (18-69)	(Lai, 1997)
	69	27 (6-54)	23 (3-44)	49 (14-74)	(Lai, 1997)
	55	36	27	36	(Auken, 1963)
Austin Chalk (Waco)	n/a	0	0	84	(Raney et al., 1987)
Taylor Marl (Waco)	n/a	8-16	1-10	66-82	(Raney et al., 1987)
Navarro (Waco)	n/a	2-5	1-4	89-93	(Raney et al., 1987)

Strength Parameters

The strength parameters of the formations used in this study are listed in this section. The discussed strength parameters include effective strength parameters, the unconfined compressive strength test, and the Brazilian tensile strength test.

Effective strength parameters

The shear strength of the formations is represented by the internal friction angle, φ, and cohesion, c. The internal friction angle is obtained from the slope of the failure envelope, and the cohesion is obtained from the y-axis intercept of the envelope. The drained (effective) shear strength parameters of the formations are listed in Table 1.3.7. As shown in the table, the cohesion and friction angle differ significantly from study to study, indicating that the obtained

values are highly dependent on the testing procedure, sample conditions, in situ confining stress, and, probably, on the skills of test performers. Particularly, in highly anisotropic rock, the loading direction is critical to the overall strength of intact rock. The existing fissures and the depositional direction dominate the strength; yet the loading direction in research literature is not particularly specified. Thus, the effective strength parameters shown in Table 1.3.7 are obtained, presumably, by loading axially to the bedding plane. Unlike index properties, the strength parameters are key to the design of structure; thus independent tests are recommended whenever strength of the formation is required at a specific site and under specific conditions.

Table 1.3.7 Effective strength parameters for formations used in this study

Formation	Description	c' (kPa)	φ'	Reference
Del Rio Clay	Weathered, Austin	10	16.5	(Fox, 1979)
	Waco, Texas	40-70	19-28	(Stroman and Feese, 1984)
Eagle Ford Shale	Dallas, SSC project Direct shear	0-200	32	(Brouillette et al., 1993)
	Dallas, SSC project Drained Triaxial	0-300	30 (20-47)	(Brouillette et al., 1993)
	Dallas, SSC project	170-660	17-31	(Hsu, 1996)
	Dallas, SSC project	370	17	(Olson et al., 1993)
	Dallas, CD test	n/a	18	(Font, 1979)
	Dallas, CU test with pore pressure measurement	65	51	(Lai, 1997)
	Dallas, CD test	352	33	(Lai, 1997)
Taylor Marl	Dallas, SSC project	600	31	(Olson et al., 1993)
	Dallas, SSC project	100-330	18.5-21	(Olson et al., 1993)
	Dallas area, CD	n/a	25.5	(Font, 1979)

Shear strength along the bedding planes

The only available source for the shear strength of the bedding planes is tabulated in Table 1.3.8. Direct shear test was performed along the bedding planes to obtain the cohesion and friction angle of the bedding planes. The cohesion and friction angle of the bedding plane is lower than those of regular samples, which is reasonable as the failure plane is developed along a fissility plane.

Table 1.3.8 Effective strength parameters of bedding planes of Eagle Ford Shale

Formation	Description	c' (kPa)	φ'	Reference
Eagle Ford Shale	Direct shear test/ peak	165	22	(Lai, 1997)
	Direct shear/ residual	55	14	(Lai, 1997)

Unconfined compressive strength (UCS)

      Test measuring unconfined compressive strength (UCS), also called uniaxial compressive strength, is frequently used to estimate rock strength. The test is relatively quick and easy; usually results in conservative design because the increase in strength by confining pressure is not accounted for. Table 1.3.9 shows the UCS of Eagle Ford Shale, Austin Chalk, and Taylor Marl. The loading direction to the specimen is unavailable from literature, but is believed to be perpendicular to the bedding planes because cores are typically obtained perpendicular to the planes. The UCS of Austin Chalk was beyond 10 MPa, and the values for Eagle Ford Shale and Taylor Marl range between 1.0 MPa to 3.2 MPa.

Brazilian tensile strength test

      The Brazilian tensile strength test is an indirect method to measure tensile strength of rock. The obtained tensile strengths of three formations are shown in Table 1.3.10. The tensile strength of Eagle Ford Shale and Taylor Marl is less than half UCS whereas that of Austin Chalk is about one-tenth of UCS. The relatively high tensile strength of clay shales is likely due to the fissure of the formation. The loading direction and failure patterns are not specified in the references. It is thought that the test results of clay shales were discarded when tensile failure occurs along the fissures; therefore the tensile strength was measured to be higher than that predicted from UCS.

Table 1.3.9 Uniaxial compressive strength of the formation used in this study

Formation	Description	UCS (MPa)	Reference
Eagle Ford Shale	Dallas, SSC project	2.1 (0.4-5.82)	(TECT, 1990a)
	Dallas, SSC project	3.4	(Laughton et al., 1991)
	Dallas, SSC project	2.0	(Lundin et al., 1990)
	Dallas, SSC project	2.1 (0.1-4.6)	(Nelson and Lundin, 1990)
Austin Chalk	Dallas, SSC project	18	(Laughton et al., 1991)
	Dallas, SSC project	14.5	(Lundin et al., 1990)
	Dallas, SSC project	15.4 (4.4-26.3)	(Nelson and Lundin, 1990)
	Austin, Texas	10.6-18.9	(Nelson, 1987)
Taylor Marl	Dallas, SSC project Weathered	0.8 (0.2-1.8)	(TECT, 1990b)
	Dallas, SSC project	3.2 (0.5-127)	(TECT, 1990b)
	Bentonitic Shale	1.4	(Hsu, 1989)
	Dallas, SSC project	4.8	(Laughton et al., 1991)
	Dallas, SSC project	2.8 (0.8-7.8)	(Nelson and Lundin, 1990)
	Austin, Texas	0.9-5.9	(Nelson, 1987)

Table 1.3.10 Brazilian tensile strength of formations used in this study

Formation	Description	Tensile strength (kPa)	Reference
Eagle Ford Shale	Dallas, SSC project	931 (717 – 1124)	(Lai, 1997)
Austin Chalk	Dallas, SSC project	1700	(Lundin et al., 1990)
Taylor Marl	Austin, Texas	1100	(Nelson, 1987)

Other Tests

Clay Shales embrace several problematic characteristics because their clay minerals are very sensitive to water. Hence, other engineering properties such as durability, swelling, consolidation, and permeability need attention in addition to the strength of the formation. This section summarized existing literature for slake durability, swelling pressure, consolidation coefficients, and permeability tests.

Slake durability test

The durability of weak rock may be measured by the standardized slake durability test, or jar slake test. Detailed procedures of such tests will be discussed in Section 1.4. The slake durability tests were carried out for the SSC project near Dallas and several tunnel projects in Austin. The Eagle Ford Shale and Taylor Marl are likely to degrade severely upon drying and wetting, according to the slake durability index (SDI) values, while the Austin Chalk appears to be durable.

Table 1.3.11 Slake durability index of the formations used in this study

Formation	Description	SDI	Reference
Eagle Ford Shale	Dallas, SSC project	21	(Laughton et al., 1991)
	Dallas, SSC project	25	(Lundin et al., 1990)
	Dallas, SSC project	9 (3-22)	(Nelson and Lundin, 1990)
Austin Chalk	Dallas, SSC project	95	(Laughton et al., 1991)
	Dallas, SSC project	96	(Lundin et al., 1990)
	Dallas, SSC project	91 (46-97)	(Nelson and Lundin, 1990)
	Austin, Texas	73-85	(Nelson, 1987)
Taylor Marl	Dallas, SSC project	52	(Laughton et al., 1991)
	Dallas, SSC project	23 (0-55)	(Nelson and Lundin, 1990)
	Austin, Texas	29-54	(Nelson, 1987)

Swelling pressure

Clay Shales containing a high percentage of smectite (montmorillonite) tend to swell significantly by absorbing water. Pressure that builds during swelling is responsible for structural damage due to many factors: e.g. cracks result from differential settlement and tensile failure of foundation results from uplifting. The swelling pressure of Eagle Ford Shale and Taylor Marl is shown in Table 1.3.12. The swelling pressure of Eagle Ford Shale is about 300 – 2000 kPa, which is slightly higher than Taylor Marl, but both formations lead to significant swelling pressure in the presence of water.

Table 1.3.12 Swelling properties of the formations used in this study

Formation	Description	Pressure (kPa)	Reference
Eagle Ford Shale	Dallas, SSC project	1054 (431-2060)	(Brouillette et al., 1993)
	Upper Eagle Ford Dallas area	239-1197	(Font, 1979)
	Dallas, SSC project	300	(Lundin et al., 1990)
Taylor Marl	Dallas area	192-862	(Font, 1979)

Consolidation coefficients

The compression and rebound indices from consolidation tests are shown in Table 1.3.13. The obtained indices for Taylor Marl and Eagle Ford Shale are alike for fresh formations.

Table 1.3.13 Consolidation coefficients of Eagle Ford Shale and Taylor Marl

Formation	Description	C_c	C_r	Reference
Eagle Ford Shale	Dallas, SSC Project	0.08-0.12	0.02-0.07	(Olson and Brouillette, 1990)
Taylor Marl	Compacted	0.3	0.1	(Cuenca, 1989)
	Dallas, SSC Project	0.05-0.11	0.01-0.07	(Olson and Brouillette, 1990)

Permeability coefficient

The permeability coefficients of three formations are shown in Table 1.3.14. The permeability of Eagle Ford Shale is the smallest and that of Taylor Marl is the largest. However, all three formations are practically impervious in the fresh condition. The difference arises when those formations are subject to weathering. While Austin Chalk is not susceptible to weathering, the clay shales (both Eagle Ford Shale and Taylor Marl) deteriorate considerably upon weathering. The permeability of clay shales subject to weathering tends to increase by allowing water flows through open fissures. Furthermore, the direction of water flow is critical to the permeability coefficient calculation in anisotropic materials. Unfortunately, the direction of water flow and the permeability of weathered formation are not available in the literature.

Table 1.3.14 Permeability of the formations used in this study

Formation	Description	Permeability (cm/sec)	Reference
Eagle Ford Shale	Dallas, SSC project	$5 \cdot 10^{-8}$	(Laughton et al., 1991)
Austin Chalk	Dallas, SSC project	$3 \cdot 10^{-7}$	(Laughton et al., 1991)
Taylor Marl	Dallas, SSC project	$2 \cdot 10^{-7}$	(Laughton et al., 1991)

1.3.4 Cation Exchange Capacity

Clay Mineralogy

Clay minerals comprise silicate tetrahedral and alumina octahedral sheet (gibbsite or brucite). The silica tetrahedron has the chemical composition of SiO_4 and shares three oxygen atoms among them, forming two dimensional layer sheets $(Si_4O_{10})^{4-}$, which can extend indefinitely. Alumina octahedron contains six hydroxyls with aluminum at the center and the composition is $Al_2(OH)_6$. When aluminum is at the center, the alumina sheet is also called gibbsite. If magnesium substitutes aluminum, the composition changes to $Mg_3(OH)_6$, and the magnesium sheet is called brucite.

The characteristics of clay minerals are determined by the way those sheets are stacked and by the bonding characteristics between silicate sheets and alumina sheets. The smectite is composed of a sandwiched alumina octahedral sheet (gibbsite) by silicate tetrahedral sheets. The neighboring silicate sheets are bonded together by van der Waals force. Another similar structure is observed in illite, except that the bonding between silicate sheets is potassium instead of van der Waals force. On the other hand, kaolinite consists of repeating alternate silicate with alumina sheets with hydrogen bonding between silicate and alumina.

Even though, ideally, the silicate tetrahedral sheets contain silicons, and octahedral sheets contain aluminum, those ideal cations are easily substituted with other cations. Such substitution does not affect clay structure and is called isomorphous substitution. For example, silicon (Si^{4+}) in the tetrahedron is replaced with aluminum (Al^{3+}) without changing the clay structure but with changing the surface charge. The aluminum (Al^{3+}) can be replaced by magnesium (Mg^{2+}) or iron (Fe^{2+}). In real clay structure, therefore, clay minerals are negatively charged and attract cations on their surfaces. Those cations are exchangeable with other types of cations, and the amount of exchangeable cations of clay minerals are called cation exchange capacity (CEC).

The hydrogen bonding of kaolinite is very strong such that interlayer separation does not take place. Hence, the exchangeable cations do not exist between inter-layers, but may exist at the surface of particles; consequently, the negative charge of the clay particles consisting predominantly of kaolinite is weak compared to other clay minerals such as smectite (montmorillonite) and illite. Illite, which is the most common clay mineral on earth, comprises sandwiched gibbsite by two silicates. Negative charges induced by isomorphous substitution are balanced by non-exchangeable potassium between inter-layers. On the other hand, the unit layers of the smectite group is bonded by weak van der Waals force and by existing exchangeable cations adsorbed to balance the negative charges of unit layers. Therefore, the bonding of unit

layers of the smectite group is easily broken by adsorption of water, and the cations developed by isomorphous exist between unit layers as well as at the surface of clay particles. Because there is a large amount of isomorphous substitution, the smectite minerals present high CEC.

Methylene Blue Adsorption Test

Cation exchange capacity may be a good indicator of swelling characteristics since the high cation exchange capacity of the clay shales are evidence of a high content of smectites. In order to measure CEC, the Methylene blue adsorption test was used in this study. This method fundamentally measures how many exchangeable cations are available in the clay particles by using Methylene blue dye ($C_{16}H_8N_3SCl \cdot 3H_2O$). The Methylene blue dye is dissociated into Methylene blue cation ($C_{16}H_8N_3S^+$) and chloride anion (Cl^-). The Methylene blue cation replace base cations (Na^+, Ca^{++}, K^+ and Mg^{++}) of clay minerals in an irreversible manner, and the amount of consumed Methylene blue dye is used to estimate the amount of the base cations around the clay minerals that is attracted to negatively charged clay particles.

Test Procedure

In order to carry out Methylene blue adsorption test, processed shale (ground powder) is mixed with water to form a slurry. The clay shales are ground to powder until more than 95% of the total weight of specimens passes the No.40 sieve and 100% pass through the No. 30 sieve. Table 1.3.15 provides the percentage passing through the No.40 sieve for each formation. Thirty grams of the processed clay shale is mixed with 1 gram of XC polymer and 350 ml of water using a high speed mixer for 20 mins. The XC polymer makes the processed clay shale suspend in the slurry. The slurry is kept overnight in order to ensure hydration of each clay shale particle.

After sufficient time elapses, 11.7 ml of prepared slurry is added to a flask with 3.3 ml of water. The amount of added slurry contains 1 gram of solid, which allows easy calculation of CEC in the end. Then using syringe, 0.5 ml of Methylene blue solution is inserted into the flask, and swirled for more than 30 seconds. Using a glass rod, suspended slurry mixed with Methylene blue solution is dropped on filter paper, which is observed for whether a light-blue ring appears around the heavy-blue dyed solid. The procedure is repeated by adding methylene blue solution stepwise (0.5 ml each time) until the light-blue ring is observed, which is called the "end point" of the Methylene blue adsorption test. The detailed procedure is described by the American Petroleum Institute (API) as recommended practice (API RP 13B-2, 1991). Each test was performed until the two consecutive readings of added methylene blue solution were obtained.

The cation exchange capacity is calculated by dividing the amount of added Methylene blue solution by the weight of solid. For example, if the added Methylene blue solution is 41 ml for one gram of Navarro shale, the CEC is 41 Meq/100grams. The mathematical representation of this derivation is as follows:

41 ml /gram* 10 Meq/liter (=0.01N) = 0.41 Meq/gram = 41 Meq/100gram

where the concentration of Methylene blue solution is 0.01N per one liter of solution. The concentration of the solution will change the calculation.

Table 1.3.15 powder used to make slurry of clay shales

Formation	#40 retained (g)	#40 passing (g)	Percent passing #40 (%)
Taylor Marl	1.3	44.7	97.2
Navarro Shale	1.0	30.4	96.8
Del Rio Clay	1.3	35.9	96.5
Eagle Ford Shale	1.9	37.2	95.1

Results and Discussion

The amount of adsorbed cations to 100 grams of processed dry clay shale is called CEC, and is expressed in Meq/100grams. A higher value of CEC indicates that the clay shales consist of larger amounts of montmorillonite, which significantly swells in the presence of water. The CEC obtained is shown in Table 1.3.16. The CEC is the largest for the Navarro Shale among the four clay shales, followed by Taylor Marl, Del Rio Clay, and Eagle Ford Shale, in order. The CEC of Navarro Shale was measured to be 41 Meq/100grams. In addition to the CEC of four clay shales, the CEC of bentonite and Rev Dust are listed in the table for comparison; their values are 70 and 2 Meq/100grams respectively. Rev Dust is a compound of very small particles and is usually used to simulate mud cutting fines in petroleum engineering. Bentonite is composed predominantly of montmorillonite, thus the high CEC of Bentonite is reasonable. Typical CEC of clay minerals is shown in Table 1.3.17, and the CEC of bentonite falls between 70 – 130 Meq/100grams. The used bentonite hits the lower limit of the range. As compared to bentonite, the CEC of Rev Dust was measured to be very low. In fact, the value is even lower than kaolinite. Typical mineral components of Rev Dust are 50% quartz, 25% kaolinite, 16% smectite, 5% illite, and 4% cristobilite. However, the mineralogy of the Rev Dust used is not analyzed.

Based on the test results, Navarro Shale is likely to present the severest reaction to water among the four clay shales. Hence, the swelling and degradation potential would be the largest for the Navarro Shale. On the contrary, the swelling and degradation potential would be the smallest for the Eagle Ford Shale. From the limited information, it is not clear that the numbers can be correlated with related with the magnitude of swelling and the degree of degradation.

Table 1.3.16 Cation exchange capacity of six materials

Name	Bentonite	Rev Dust	Taylor Marl	Del Rio Clay	Navarro Shale	Eagle Ford Shale
Cation Exchange Capacity (Meq/100g)	70	2	29	23	41	20

Table 1.3.17 Cation exchange capacity of typical clay minerals (Gray et al., 1980)

Clay Minerals	Meq/100g of dry clay
Montmorillonite	70 – 130
Vermiculite	100 – 200
Illite	10 – 40
Kaolinite	3 – 15
Chlorite	10 – 40
Attapulgite-Sepiolite	10 – 35

1.3.5 Adsorption Isotherm Test

The adsorption isotherm test quantitatively defines hydration tendency of argillaceous rocks, and the amount of adsorbed water can be used to estimate rock durability (Chenevert, 1970; Dunn and Hudec, 1965; Richardson and Wiles, 1990). In this section, the adsorptive property of the formations used in this study is investigated using the adsorption isotherm test.

The adsorption isotherm test allows us to determine the adsorption potential of shale at a given environment. For example, the formation tends to adsorb more water when the formation is dryer and when the formation is placed in a higher relative humidity environment. Besides environmental influence, the adsorption potential varies significantly depending on components of clay minerals. Hence, the adsorption potential of clay shales may be used to predict the degradation and swelling potential.

Test Procedure

The adsorption isotherm test starts by placing different clay shales in controlled relative humidity desiccators until equilibrium is achieved. At a specific relative humidity, the vapor pressure of salt solution is in equilibrium with water tension within capillaries of the clay shale specimens. The water contents of stabilized clay shales are plotted against the relative humidity of the desiccator chamber, and the plot is called the adsorption isotherm curve. These curves are used to predict the adsorptive potential of the argillaceous rocks.

In this study, four clay shales (Del Rio Clay, Eagle Ford Shale, Taylor Marl, and Navarro Shale) and two other materials (Bentonite and Rev Dust) were tested using the adsorption isotherm test. The four clay shales were cut into half inch cubes and dried in a 220° F oven for a day for complete dried samples (See Figure 1.3.8). Bentonite and Rev Dust were tested in dust form. The oven-dried specimens are then placed in desiccators whose relative humidity is maintained at 56, 86, 92, 96, and 98% respectively. Each target relative humidity is obtained using salt solution (Winston and Bates, 1960), and the chemicals composition of which are tabulated in Table 1.3.18. The dried specimens start adsorbing water and gaining weight when they are placed in the desiccators. The weight changes are recorded daily until equilibrium is reached, typically after 7 – 10 days of placement, and the amount of gained water is used to calculate the water content of the shale specimens.

Figure 1.3.8 Half inch cubic shale samples of Eagle Ford Shale

Table 1.3.18 Chemicals used to maintain relative humidity

Relative Humidity (%)	Chemical symbols of salt
56	Manganese dchloride ($MnCl_2$)
86	Pottasium chloride (KCl)
92	Na tatrate ($Na_2C_4H_4O_62H_2O$)
96	Potassium Di-hydrogen phosphate (KH_2PO_4)
98	Potassium dichromate ($K_2Cr_2O_7$)

Results and Discussion

Table 1.3.19 presents the equilibrium water content of the tested materials under a specific relative humidity. The adsorbed water content is the highest for the bentonite, and the lowest for the Rev Dust. The dry bentonite adsorbs 25.8% water at 98% relative humidity while the Rev Dust adsorbs a negligible amount of water in the same high relative humidity. This observation coincides with the results from the previous CEC test, which predicts the highest value for bentonite and the lowest value for the Rev Dust. Both the cation exchange capacity test and the adsorption isotherm test present similar and reasonable prediction for the water reactivity of clay shales. Among clay shales, Navarro Shale displayed the highest water reactivity; the weight of adsorbed water is 11.6% of the solids. It is worth noting that the degradation of clay shales by one cycle of drying and wetting was found to be severe in the triaxial testing performed on Navarro Shale (See Section 1.5 of this report).

The adsorption isotherm curves are created as shown in Figure 1.3.9. The amount of adsorbed water increases rapidly at high relative humidity. The saturated condition (100% relative humidity) was not attainable by a given salt solution, thus the drastic increase of adsorbed water was not fully traced. However, the drastic increase of water content at high water content can be extrapolated from the trend line drawn in the figure. The table and figure indicate different clay shales own different adsorptive potential, but similar trends in their behavior. It was also observed that the natural water content of the clay shales are greater than the equilibrium water content at 98% relative humidity. Table 1.3.1 indicates that the average water contents for Del Rio Clay, Eagle Ford Shale, and Taylor Marl are approximately 17, 16, and 19%

respectively. This is important to note since the natural moisture content of clay shales may evaporate even under high relative humidity values.

Table 1.3.19 Water content of test formations and corresponding relative humidity

Formation	Water content in equilibrium (%)				
	RH(56%)	RH(86%)	RH(92%)	RH(96%)	RH(98%)
Del Rio Clay	2.2	5.2	5.2	6.2	9.1
Eagle Ford Shale	2.3	4.3	4.3	4.6	6.2
Taylor Marl	2.0	4.8	4.8	5.6	7.4
Navarro Shale	4.4	8.1	8.0	9.6	11.6
Bentonite	7.8	17.7	17.8	19.3	25.8
Rev Dust	0.05	0.05	0.1	0.15	0.2

* RH indicates relative humidity in desicattor chamber

1.3.6 Atterberg Limits

The Atterberg limits are one of the most practical and widely used measures in geotechnical engineering to classify fine-grained soils. In fact, the typical use of the Atterberg limits is for clays or silts, but not for rocks. However, the frequency of use of the Atterberg limits test may be attributed to the fact that clay shales behave very similarly to highly over-consolidated clay.

The Atterberg limit test on the clay shales differ from typical one in terms of sample preparation because the clay shales are stiff solid, not powder. Therefore, the clay shales are physically ground to powders without slaking process, and the powders passing through No. 40 sieve are used for the test. Figure 1.3.10 displays the test results plotted on the Casagrande's plasticity chart along with the Atterberg limit test results from research literature. The values obtained from literature review are averaged and plotted for comparison. It can be seen from the figure that Del Rio Clay, Taylor Marl, and Navarro Shale are highly plastic, whereas Eagle Ford Shale is in the low plastic range. The high liquid limit indicates high potential of slaking (Morgenstern and Eigenbrod, 1974); therefore, Navarro Shale is expected to slake the most.
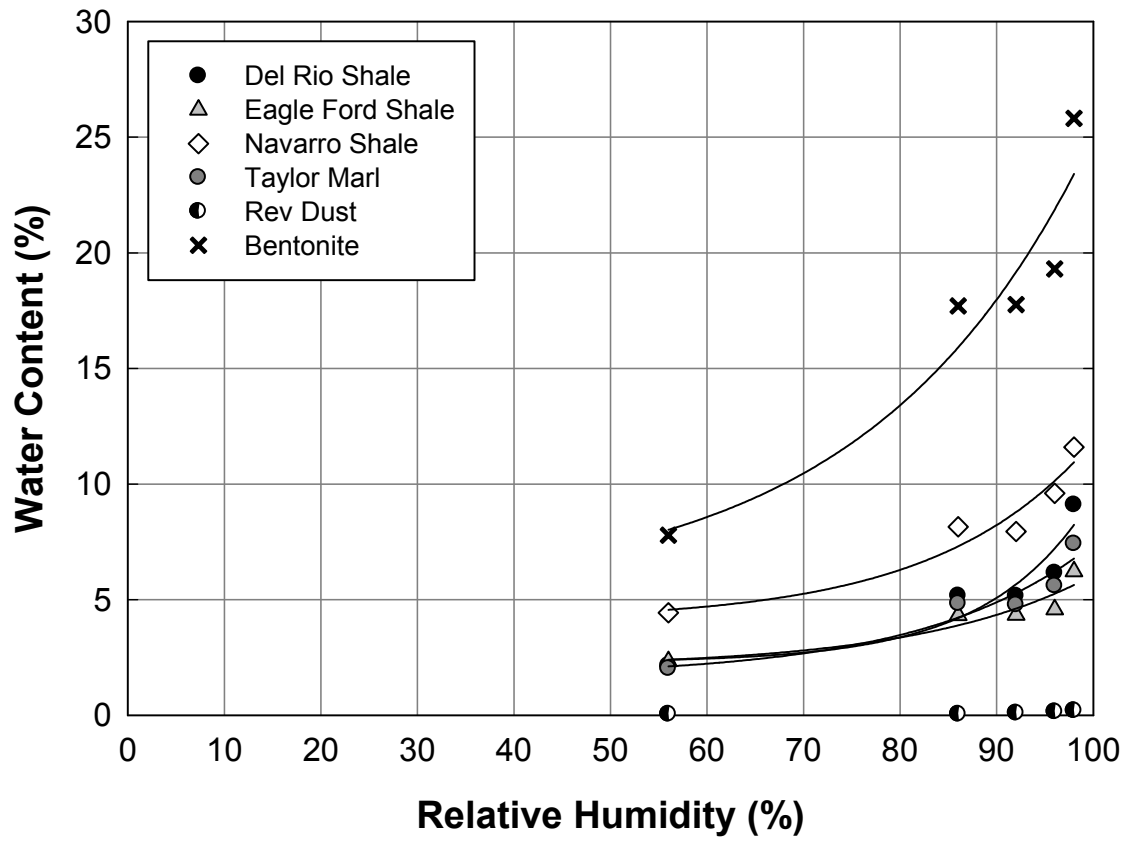
Figure 1.3.9 Adsorption isotherm curves
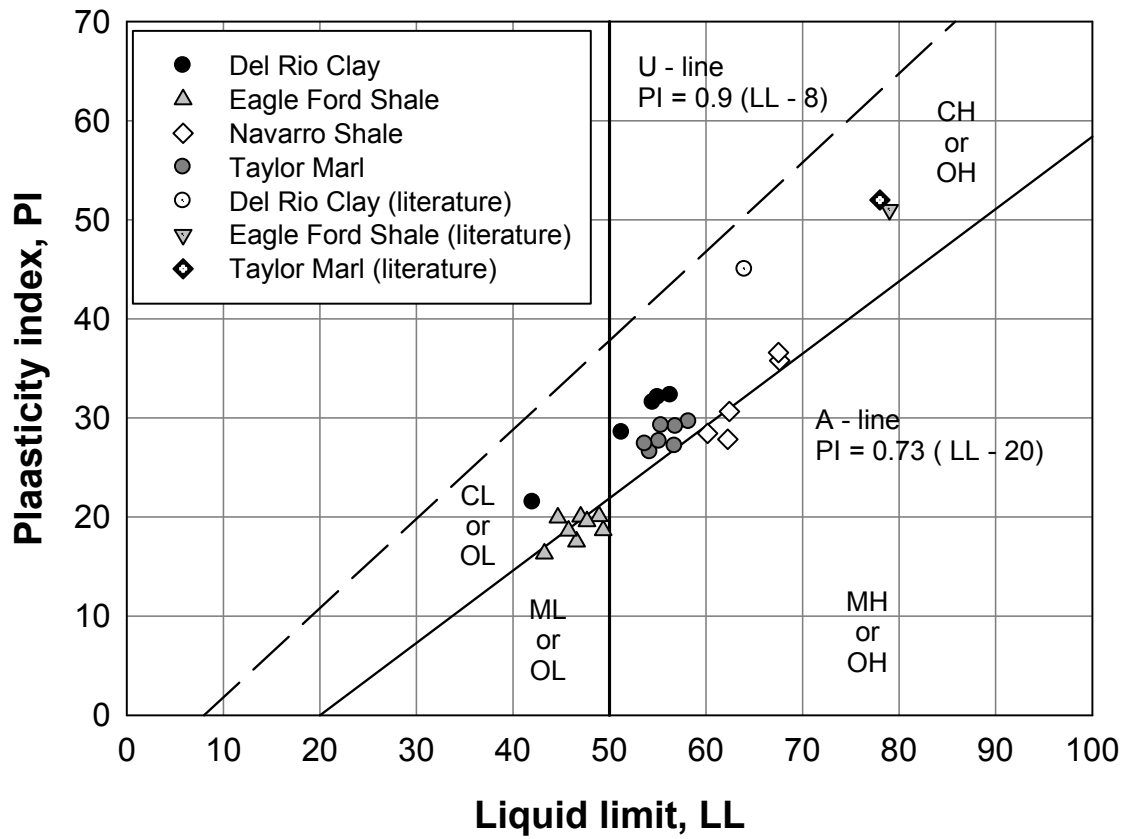
Figure 1.3.10 Atterberg limits of clay shales plotted on plasticity chart

1.4 LABORATORY TEST METHODOLOGY

1.4.1 Introduction

As discussed in Section 1.2, clay shales can be highly sensitive to water, and the engineering properties of clay shales are easily degraded upon weathering. Moreover, these formations are notorious to laboratory technicians due to the difficulty of sample preparation. Hence, ongoing study of clay shale requires specially standardized procedures for both sample preparation and laboratory testing.

Five kinds of laboratory tests are described in this section: 1) the triaxial compression test, 2) the unconfined compressive strength (UCS) test, 3) the point load test, 4) the slake durability test, and 5) the jar slake test. Among these tests, attention should be given to the triaxial compression test because the sample preparation for the test is not simple. Firstly, the test formations are fissile, which makes cutting and grinding a specimen difficult because specimens split easily along existing fissures. Secondly, the specimen must be dried and re-wetted for experimental purposes because the objective of this study is to estimate the degraded strength of clay shales through one cycle of air drying and wetting. It is also necessary to point out that both the multi-stage triaxial test (Kovari et al., 1983) and the single-stage conventional triaxial test were employed. Thus, the concept and applications of the multi-stage triaxial test are described. Brief explanations for other accompanying tests such as the uniaxial compressive strength test, the point load test, the slake durability test, and the jar slake test are provided.

1.4.2 Triaxial Compression Test

The triaxial compression test is intended to measure the stress-strain behavior of clay shales under specific confining pressure which simulates the *in situ* stress of clay shales. The triaxial test is considered a more sophisticated and accurate testing method than the unconfined compression test because geomaterials are pressure dependent. In other words, geomaterials present higher strength under higher confinement, which is not achieved in the unconfined compression strength test. In a typical triaxial test, the test specimen is subject to isotropic confining pressure, then axial stress or strain is gradually increased to failure. The information on confining pressure and corresponding peak strength is then used to estimate the parameters for a failure criterion, such as the Mohr-Coulomb model, which is the basic and most common criterion in geotechnical engineering. In this section, details of the triaxial test are introduced in the following order: 1) test apparatus, 2) test procedure, 3) the multi-stage triaxial test, and 4) the radial strain controlled test.

Test Apparatus

The testing machine used for this study was built by Geotechnical Consulting and Testing Systems (GCTS) and was installed at The University of Texas at Austin in 2006. The machine is a computer-controlled system using servo-valves, which enables the user to control the machine by continuously communicating with implemented sensors. Figure 1.4.1 displays the test specimen assembly for the triaxial test. Three linear variable differential transformers (LVDT) are installed to measure axial and radial strains; two for axial strain and one for radial strain, as

shown in Figure 1.4.1 (b). The LVDTs for axial strain are directly fixed to the specimen, thus the axial strain calculation does not include the deformation of top platen and loading piston. Axial strain was obtained by averaging the two values obtained from the LVDTs. Two layers of Latex membranes, secured by two sets of O-rings (top and bottom), cover the specimen to prevent hydraulic oil infiltration.

<div align="center">(a)   (b)</div>
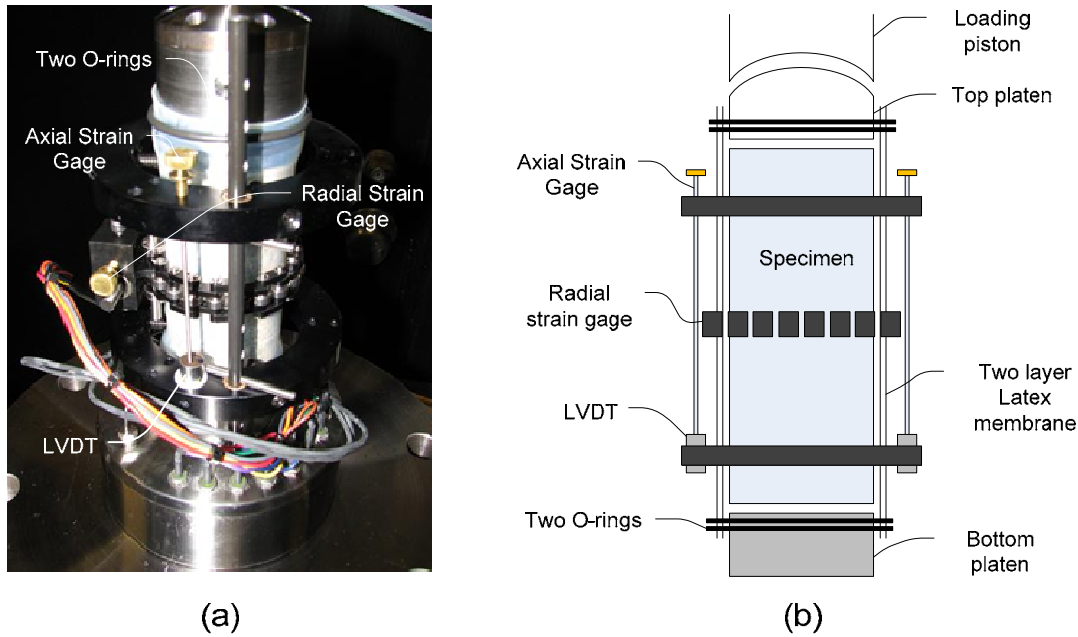
<div align="center">*Figure 1.4.1 Triaxial test set up (a) real view (b) schematic view*</div>

Figure 1.4.2 shows the circumferential strain gage used to measure radial strain of specimens in this study. The circumferential strain gage adopted in this study measures real average radial strain by utilizing a chain that surrounds the specimen. Axial loading to the specimen causes the specimen to expand laterally, which produces the displacement of LVDT attached to the specimen in Figure 1.4.2. The displacement is then used to calculate average radial strain of the specimen as axial load increases. The radial strain using the circumferential strain gage is calculated using the following equation (GCTS manual, 2007)

$$\varepsilon_r = \frac{\Delta C}{C_i}$$

where

$$C_i = 2\,\pi\,R_i: \text{ initial specimen circumference}$$

$$\Delta C = \frac{\pi \cdot \Delta X}{\sin\left(\dfrac{\theta_i}{2}\right) + \left(\pi - \dfrac{\theta_i}{2}\right)\cos\left(\dfrac{\theta_i}{2}\right)} \quad : \text{change in specimen circumference}$$

and

$$\Delta X = X_i - X_f : \text{change in LVDT reading}$$

$$\theta_i = 2\pi - \frac{L_c}{R_i + r} \text{ : initial chord angle}$$

L_c : change length measured from center of one end roller to center of other end roller

r: roller radius

R_i : initial specimen radius.

The calculations are implemented into GCTS software, CATS (GCTS manual, 2007).
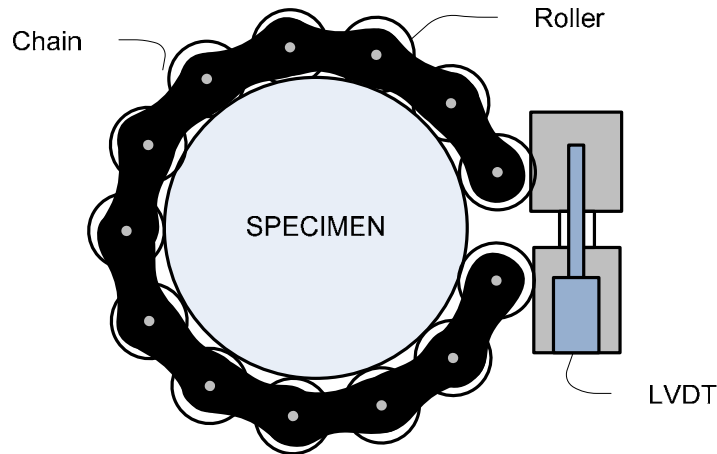
Figure 1.4.2 Top view of circumferential strain gage

Test Procedure

Sample Storage

      Sample preparation plays a key role in determining shear strength of clay shales. Careless preparation may cause a wide variation of engineering properties; thus, reliable sample preservation is essential to reliable test results. The samples are considered in fresh condition when they arrive at the laboratory, and they are preserved to maintain their condition. In this study, cored samples were delivered to the laboratory wrapped in thin plastic film covered by aluminum foil in heavy-duty plastic covering. The cores were then placed in wax-coated cardboard boxes, which reduced exposure of clay shales to atmospheric condition. Upon arrival, the boxes were stored in the moisture room whose relative humidity and temperature are maintained at 100% and about 73˚F, respectively. Figure 1.4.3 shows the core boxes stored in the moisture room to prevent air drying of clay shales.

Figure 1.4.3 Moisture room to preserve cores at 100% relative humidity and 73˚F

Sample Preparation

Triaxial test specimens were prepared in accordance with ASTM Standard D4543, 2007. The cores taken from the moisture room were cut into specimens with a height-to-diameter ratio of two or more using a slab saw (See Figure 1.4.4), which resulted in approximately 100 mm or more height and 50 mm diameter (NX size core). Typical hard rock core generated appreciable heat at the contact between the saw blade and rock. Hence, coolant oil was used to cool down the hard rock specimen to prevent it from overheating or the blade from deteriorating. The use of coolant is unavoidable when hard rock is cut. However, cutting clay shales using a saw does not create heat around the contact, as the clay shales are relatively soft. The coolant was removed from the slab saw to maintain the clay shales in their original state and to prevent the coolant oil from penetrating the specimen.

About 10 minutes was required to cut one side of the specimen using the slab saw, and the cut specimens were immediately wrapped in thin plastic film to prevent further exposure to atmosphere. Usually, 10 minutes of exposure to air does not result in significant open fissures during cutting, but sometimes specimens split along horizontal fissures (orthogonal to core axis), which leads to waste of time and samples. It is possible to cut the specimen with a knife or other sharp tool to obtain the desired size; specimens are usually split along existing closed fissures. This approach expedites the sample preparation and eliminates 10 minutes of air drying. However, the attempt is not always successful and often results in waste of long cores when the core is broken along undesired fissures. Clearly, both preparation methods result in some core loss.

After the cores were cut, both ends of each specimen were leveled and ground to meet the ASTM standard (ASTM D4543). The prepared specimen had to satisfy three criteria: 1) parallelism 2) perpendicularity, and 3) smoothness. Top and bottom faces of the specimen must be parallel to each other and perpendicular to the upright specimen, and the faces must be flat to prevent possible stress concentration. The left picture in Figure 1.4.4 shows the grinder that was used. Grinding clay shales requires extreme care because the specimens easily chip out along existing fissures. Therefore, grinding proceeded slowly, requiring about 10 minutes for each side of the specimen. The clay shales were sprayed with water as necessary to retard moisture loss. Moisture is provided not only to maintain the strength but also to prevent development of new fissures. Indeed, short periods of air drying (e.g. 4 hours) does not induce significant change in shear strength (Botts, 1986).

Figure 1.4.4 Slab saw (left) to initially cut the specimen to diameter to height ratio of 1:2, and the used grinder (right)

Drying and wetting

The research requires one cycle of drying and wetting of specimens to study the effect of drying duration on shear strength of clay shales. This cyclic event is to simulate what happens at the bottom of drilled shafts during construction. There are two possible cases that may result after drying: 1) the verification core hole dries and concrete is poured without wetting, and 2) the verification core hole dries but becomes wet due to water inflow before concrete is poured. The case of interest is case 2 since the wet-dry-wet cycle results in significant deterioration of clay shales.

The drying conditions of the clay shale test specimens must simulate the relative humidity near the bottom of drilled shafts. Relative humidity governs the evaporation rate and retained moisture in the specimen. The relative humidity inside the drilled shaft excavator is dependent on many factors such as season, rainfall, subsurface conditions, and the depth of drilled shafts. Therefore, the effect of different degrees of relative humidity on the change in water content was first studied.

Figure 1.4.5 presents Eagle Ford Shales placed in a relative humidity controlled desiccator (98% for this desiccator). The weight of the Eagle Ford Shale specimen had been continuously recorded under 67%, 80%, and 98% of relative humidity until equilibrium was reached. Figure 1.4.6 displays the change in water content against elapsed time in three different relative humidity desiccators and indicates that Eagle Ford Shale loses water content even in high relative humidity (98%). This finding coincides with the results of section 1.3.5, implying that the verification core hole wall of drilled shafts would dry out even in the possibly high relative humidity condition near the shaft bottom. It is clear that water evaporation is greater in a lower relative humidity environment. For example, a higher relative humidity (98%), the water content of the specimen stabilized near 16.5%, while the water content stabilized at 6% at a lower 67% relative humidity. It was observed that the water evaporation from specimens occurred mainly in the first 150 hrs after drying in all three cases. In spite of the different evaporation rate and magnitude for different relative humidity, the specimens were dried in a laboratory relative humidity because covering all relative humidity possibilities is practically infeasible and because comparatively extreme conditions can be simulated in the laboratory. The typical relative humidity and temperature of the laboratory is approximately 40% and 72°F, but varies slightly.

70

Figure 1.4.5 Eagle Ford Shale in a humidity controlled desiccators
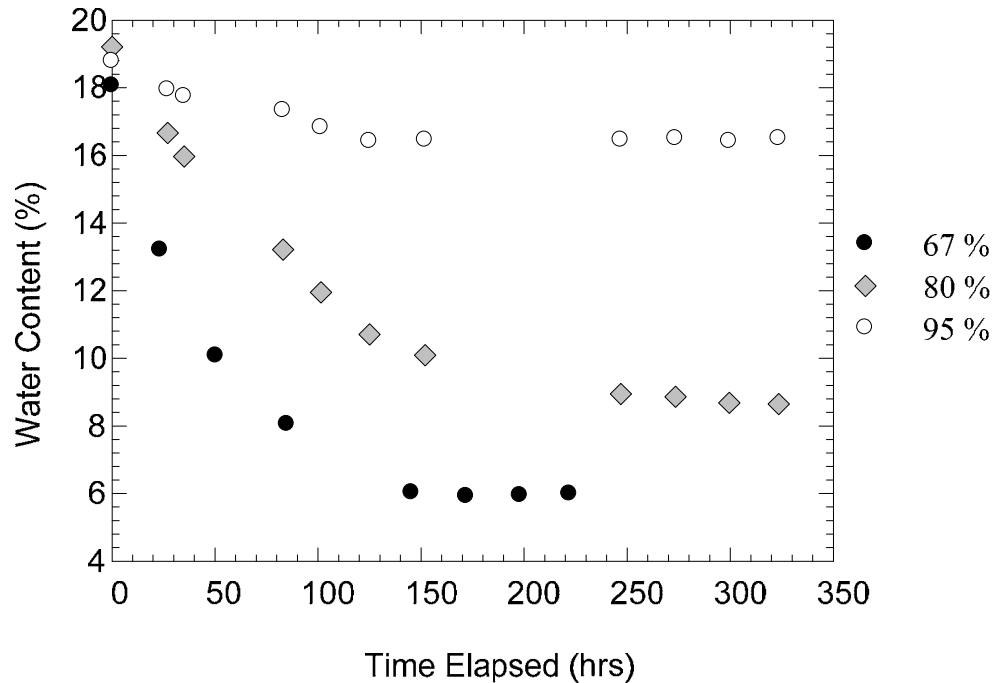
Figure 1.4.6 Water content variation with drying time in controlled humidity chamber

Visual inspection of four clay shales (Del Rio Clay, Eagle Ford Shale, Taylor Marl, and Navarro Shale) indicated that the fissures start developing within 10 to 30 minutes of air drying. The mature of developed fissures is different from formation to formation. Eagle Ford Shale and Taylor Marl tend to open horizontal fissures during air drying whereas Navarro Shale exhibits an irregular pattern of fissures. Del Rio Clay does not present any significant fissures. The fissures of Eagle Ford Shale and Taylor Marl are very tight, appearing as thin lines, and the shape of prepared specimens does not alter appreciably. However, the cracks of Navarro Shale specimens widen considerably as drying continues (see Figure 1.4.7). High deterioration is likely due to large amount of expansive clay minerals, as discussed in Section 1.3. All specimens had to be handled carefully because many fissures and cracks. In several specimens, portions of them just collapsed under their own weight.

The clay shales along the perimeter of the verification core hole may come in contact with water, and re-saturation of the clay shales will result in degradation. In this study, water was gently sprayed on the specimen until the weight of the specimen recovered to the original value.

In fact, it seems that saturating the clay shale specimens in the triaxial test cell under confinement properly mimics field conditions because the clay shale specimens in the cell are subject to all around confinement during wetting. However, the clay shales surrounding core hole will not be restrained in a radial direction indicating that wetting under confinement is not a proper approach. Water spraying technique, on the other hand, simulates the free swelling condition of clay shale in radial direction upon direct contact with water contact at the surface. Thus, water spraying technique is used to rehydrate clay shales as shown in Figure 1.4.8. Dried specimens were placed in high relative humidity desiccators during rehydration to isolate the specimens from atmospheric conditions. Water spraying continued until the weight of the specimens became similar to the initial value before drying.

Figure 1.4.7 Developed fissures of dried Navarro Specimens

Figure 1.4.8 Water spraying to restore water content

When a specimen was ready for a triaxial test, the specimen was axially loaded to failure under confining pressure of 1, 2, and 3 MPa. Usually, multi-stage triaxial tests were carried out concurrently with several single-stage triaxial tests that were used to support the validity of the multi-stage triaxial test. After trixial testing, the failed specimens from the triaxial test were used to measure the water content and determine the slake durability index (SDI).

Hole and Slurry

During sample preparation, several test specimens were "holed" at the center or soaked under slurry instead of drying and wetting. The purpose of drilling a hole is to mimic the verification core hole in the test specimen and to check its effect. The specimen immersed under slurry simulates the materials in contact with slurry during drilled shaft construction. Slurry is often used to stabilize the shaft excavation. Test specimens are prepared according to Section "cutting and grinding," and are drilled at the top-center using a 9.5 mm (3/8 inch) drill bit to 50.8 mm (2 inch) depth. To simulate the slurry soaked specimen, the test specimen is placed under slurry for 12 hours without any drying.

In order to make slurry, Soda Ash was first added to raise the pH of "make-up" water to between 8.5 and 9.5. About 1.8 grams of Soda Ash was added to fresh water of 1000 mL, and then 48 grams of finely ground Wyoming sodium bentonite was mixed together using a jet mixer. Both products are provided by Baroid Industrial Drilling Products.

Multi-stage Triaxial Test

The multi-stage triaxial test (multiple failure states test) has been adapted as an alternative for a series of single-stage triaxial tests to determine failure criterion. Whereas at least three single-stage triaxial tests are required to obtain a material strength envelope, one multi-stage triaxial test determines complete material parameters such as cohesion, c, and internal friction angle, φ, in the Mohr-Coulomb model. The multi-stage triaxial test concept was first introduced in the mid '70s (Kovari and Tisa, 1975) and has been validated by comparing multi-stage triaxial test results with several single-stage triaxial tests (Kim and Ko, 1979). It is reported that the multi-stage triaxial test produced a reasonable estimation of material parameters on shale but not on sandstone (Kim and Ko, 1979). The International Society for Rock Mechanics (ISRM) documented suggested methods for multi-stage triaxial tests (Kovari et al., 1983).

The concept of multi-stage triaxial tests is exactly the same as the conventional single-stage triaxial test, except that only one test specimen is used for different confining pressures. Figure 1.4.9 (a) exhibits the stress paths of a single-stage triaxial test and Figure 1.4.9 (b) and (c) presents those of a multi-stage triaxial test. In the single-stage triaxial test, the specimen is hydrostatically loaded to the desired level of confining pressure and is axially loaded to failure. Other independent tests are carried out to obtain the shear strength at different confining pressures. On the other hand, confining pressure acting on the specimen varies stepwise in the multi-stage triaxial test. Two different methods are available for the multi-stage triaxial test. The first method proposed by Kovari et al. (1983) shows stress paths of Figure 1.4.9 (b) indicating that the confining pressure increases at the imminent failure point sustaining axial stress. Imminent failure refers to the status of the specimen which is about to fail. The imminent failure point may be defined by the region of the stress strain curve where tangent elastic modulus approaches zero. The point is also called the termination point because at that point the test halts and confining pressure increases to the next level. The axial stress is then increased to the second imminent failure point, and the same procedure is repeated for the rest of the tests. The second method, on the other hand, is a slight modification of the first one, as shown in Figure 1.4.9 (c) (Crawford and Wylie, 1987). The axial stress after the first imminent failure point is released completely and the confining pressure hydrostatically increases to the next level at which the axial stress is increased to the second imminent failure point, and so on. The advantage of the second method is the full development of stress strain relation for three different confining pressures, while the first method only provides one stress strain relation (see Figure 1.4.10).

Three confining pressures and three corresponding peak stresses are obtained, which are used to develop strength parameters. In this study, the second testing method shown in Figure 1.4.9 (c) was adopted for the multi-stage triaxial test.

(a) single stage triaxial test

(b) multi stage triaxial test

(c) modified multi stage triaxial test
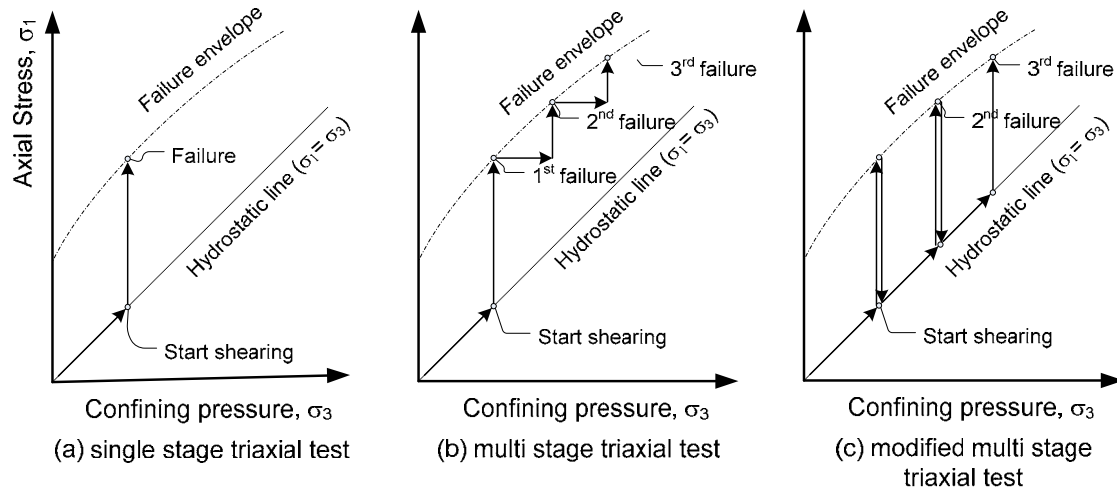
Figure 1.4.9 Stress paths of (a) single-stage triaxial test, (b) multi-stage triaxial test, and (c) modified multi-stage triaxial test

(a) single stage triaxial test

(b) multi stage triaxial test I

(c) modified multi stage triaxial test
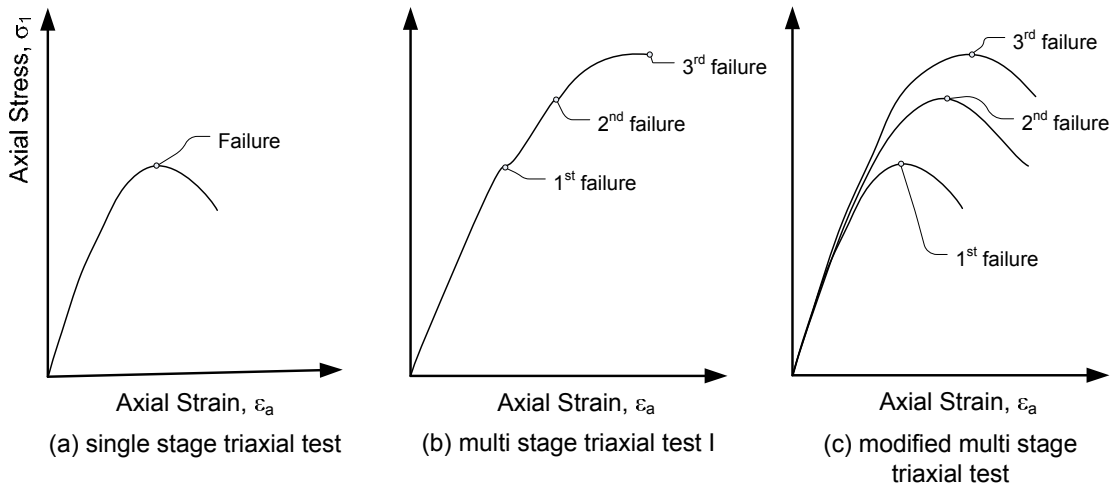
Figure 1.4.10 Stress strain relation of (a) single-stage triaxial test, (b) multi-stage triaxial test, and (c) modified multi-stage triaxial test

The multi-stage triaxial test has strong advantages in that it requires only a single specimen to estimate strength parameters: 1) a limited number of specimens is needed, 2) running time is reduced, and 3) budgets are saved. However, the basic assumption of the test is that the test specimen, after the first imminent failure point, is as fresh as the original specimen. The specimen near its imminent failure point would contain micro cracks that are connected together and that generate continuous failure planes when it is loaded further. Hence, the strength of the specimen that experienced such imminent failure may decrease compared to the strength of fresh specimen. In order to check if the specimen after imminent failure could be reloaded to

show the load path is similar to an unfailed specimen, one specimen was loaded to failure and unloaded and re-loaded to failure. The stress strain curves of the fresh specimen and the failed specimen are plotted in Figure 1.4.11. The applied confining pressure was 3 MPa and the formation used is Eagle Ford Shale. It should be noted that the fresh specimen was sheared to failure sufficiently after a peak stress to ensure complete failure. The specimen that underwent this failure is weaker than the specimen that underwent imminent failure. The specimen was unloaded and reloaded to failure under the same confinement (3 MPa). Figure 1.4.11 indicates that the peak strength of the fresh specimen is approximately 3.2 MPa and that of the failed specimen is approximately 2.9 MPa indicating that the difference between the two peak principal stress differences is less than 10%. Considering the fact that the specimen was sheared sufficiently past the peak, the specimen at the imminent failure point is likely to be practically as strong as the original specimen. Therefore, the peak principal stress difference obtained from the multi-stage triaxial test is believed to be reliable.

Figure 1.4.12 provides comparison between the results from single-stage triaxial tests and a multi-stage triaxial test for three clay shales. The test results of Navarro Shale were excluded because the multi-stage triaxial test on the formation was not possible. For more information on Navarro Shale, refer to Section 1.5. The figure indicates that the results from the single-stage triaxial test are not significantly different from the multi-stage triaxial test. Del Rio Clay presents an increase in principal stress difference as confining pressure increases, which implies that the material is pressure dependent. On the other hand, the principal stress difference of Taylor Marl is nearly independent of confining pressure, which implies that the internal friction angle approaches zero. The test results from single-stage triaxial tests of Eagle Ford indicate that the principal stress difference at 2 MPa of confining pressure was measured to be lower than that at 1 MPa confinement Shale (Figure 1.4.12 b). This is due to the rock spatial variability which exceeds the effect of confining pressure.
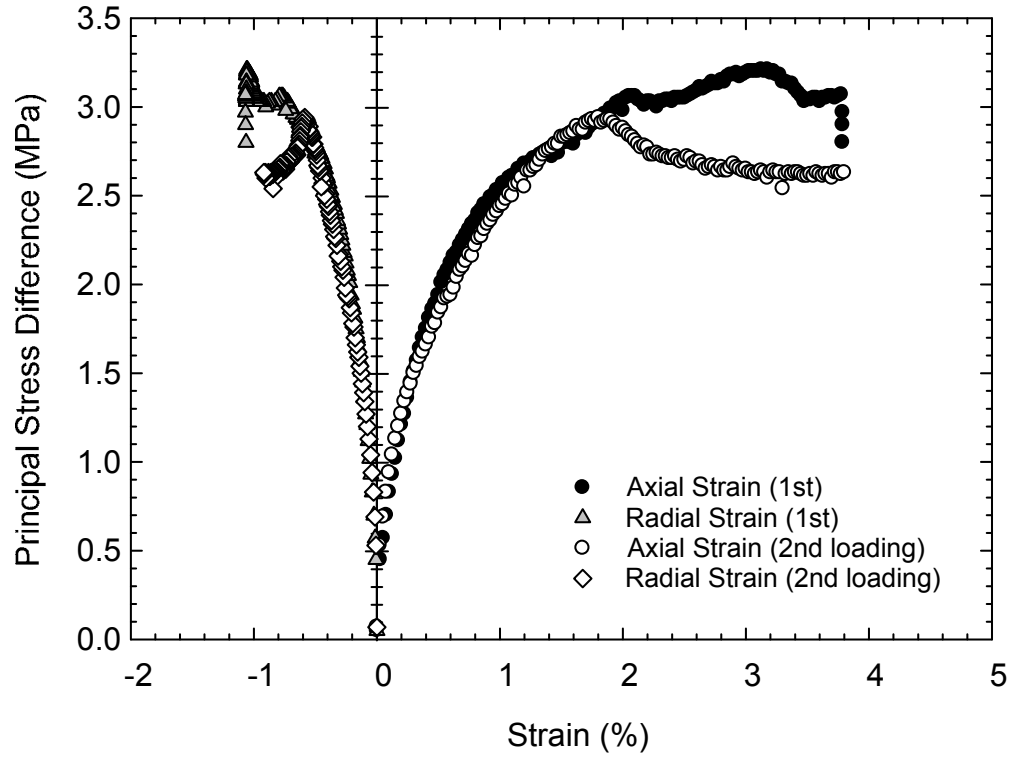
Figure 1.4.11 Stress strain curve of multi-stage triaxial test at same confining pressure (3 MPa)
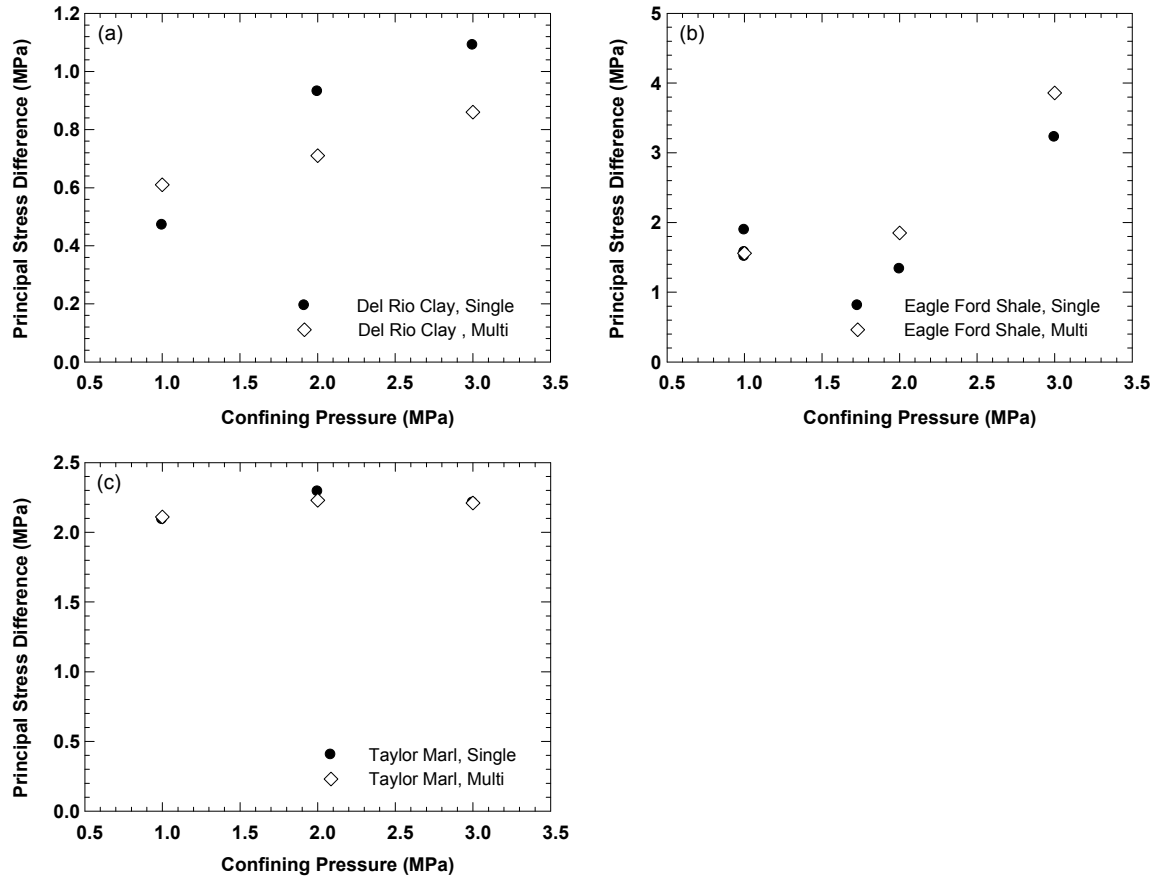
Figure 1.4.12 Comparison between multi-stage triaxial test and single-stage triaxial test on (a) Del Rio Clay, (b) Eagle Ford Shale, and (c) Taylor Marl

Radial Strain Control in Brittle Rocks

A typical multi-stage triaxial test is performed controlling axial strain, that is, the specimen is loaded to the imminent failure point by increasing axial strain. However, a significant drawback of this method is determining the imminent failure point of brittle rocks. Brittle rock typically exhibit abrupt failure without signifying yielding prior to failure. Edwards Limestone was found to be highly brittle such that the conventional multi-stage triaxial test is not suitable; thus radial strain control was adopted to avoid sudden failure. The merits of radial strain control in performing the multi-stage triaxial test on brittle rocks are explained in this section. However, it is important to note that the radial strain control is not likely to be suitable to clay shales such as Eagle Ford Shale because local failure frequently occurred.

Axial strain control

Axial strain was used as a feedback signal to control loading rate in the system, which is typically adopted in most triaxial testing standards. However, during testing of brittle rocks, snap-back behavior may occur due to large energy release at the peak principal stress difference. In order to obtain post-peak behavior, radial strain control is appropriate to carry out the multi-stage triaxial test on such rocks. Axial strain control does not capture snap-back behavior

77

because axial strain is set to increase continuously. Yet, the radial strain monotonically increases even as axial strain decreases after peak (Hudson et al., 1971; Hudson et al., 1972).

Edwards Limestone, which is encountered in the Central-Texas area, was tested using both the multi-stage triaxial test and the single-stage triaxial test. At the beginning of this study, a multi-stage triaxial test was carried out using axial strain control. The imminent failure point selected was the tangential elastic modulus was lower than the pre-determined value (typically close to zero). This criterion was not very successful because the tangential modulus did not reach even close to zero before failure and because the failure occurred drastically. Figure 1.4.13 presents the result of the axial strain rate (0.05%/sec) controlled triaxial test under 1 MPa confining pressure, which was supposed to be the multi-stage triaxial test but failed. The Edwards Limestone exhibited brittle behavior and the test specimen broke suddenly after it had passed the peak stress, which is not observable in the graph because failure occurred in a moment. It was practically infeasible to terminate the test right before the sudden failure of the specimen. Because successive increase in confining pressure is the key factor in conducting the multi-stage triaxial test, applying axial strain rate to the specimen was determined to be inappropriate for the Edwards Limestone. However, both volumetric strain and radial strain changed significantly near the peak load, whereas axial strain changed slightly by which one may conclude that the axial strain control is highly insensitive near the peak but the radial and volumetric strain is sensitive. Therefore, radial strain rate was used to shear the specimen, and both radial strain and volumetric strain were used to determine the apparent imminent failure point.
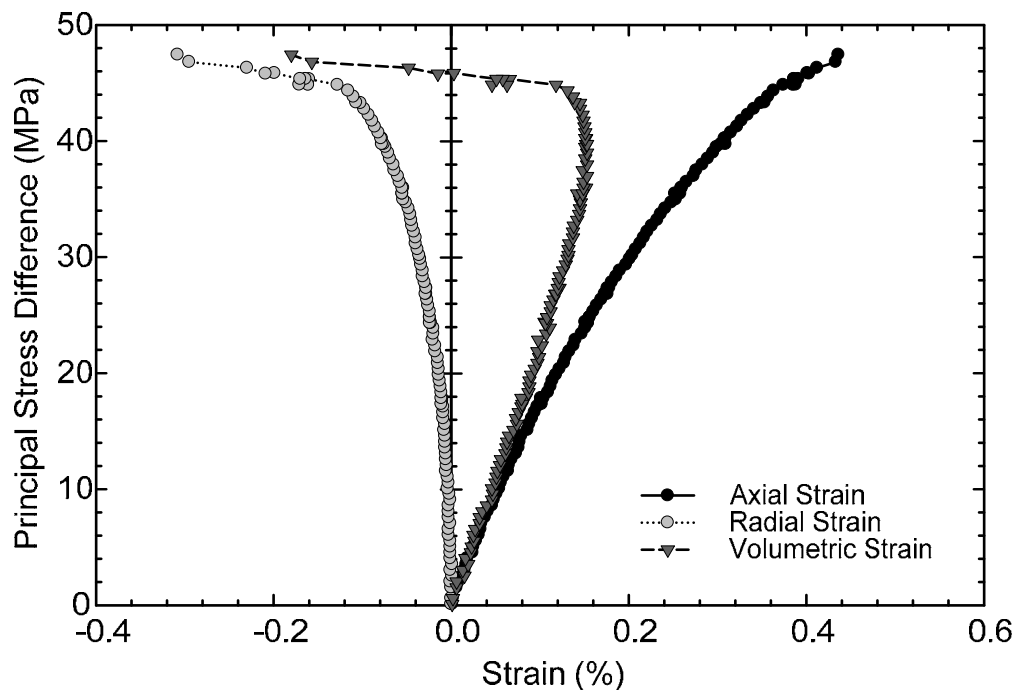
Figure 1.4.13 Stress-strain relationship from triaxial compression test using axial strain control for Edwards Limestone

Radial strain control

A result of the single-stage triaxial test using radial strain control on Edwards Limestone is shown in Figure 1.4.14. The specimen was sheared at -0.002%/sec radial strain rate with 1 MPa confining pressure. From the axial strain vs. stress relationship in the figure, it is apparant that the Edwards Limestone is in an elastic range immediately prior to failure. On the other hand, the radial strain or volumetric strain vs. principal stress difference curve indicates that the specimen started yielding appreciably before the peak principal stress difference. Advantages to using radial strain instead of axial strain as a feedback in a servo-controlled system and as a monitoring criterion in brittle rocks are: 1) Axial strain becomes very sensitive (more data points) in the vicinity of the peak load when radial strain control is used. As the specimen approached the failure state, axial strain did not vary as much as radial strain. 2) The radial strain curve displays yielding before it reaches peak stress; therefore, it is convenient to determine the imminent failure point. 3) Post peak behavior of the brittle rocks is available.

With the tested Edwards Limestone, it was found that the peak strength was not reached at either zero or maximum volumetric strain, whereas both criteria seem to be applicable in the axial strain controlled test (see Figure 1.4.13). Indeed, the behaviors of the axial strain controlled test and the radial strain controlled test are considerably different, especially where the radial strain – principal stress difference curve starts flattening out. The cause of the two different behaviors between axial and radial strain control is due to the large variation of radial strain using radial strain control compared to the radial strain using axial strain control. However, it is clear that neither maximum nor zero volumetric criteria is applicable as an imminent failure point when radial strain control is employed. By controlling the radial strain, the specimen approaches failure much more slowly than by controlling the axial strain; this gives the operator sufficient time to detect flattening of the principal stress difference – axial strain curve and move to the next stage. From the technical point view, it is recommended that an operator determines when the specimen started yielding rather than program a stopping criterion in the computer software, because of the variability of rock characteristics. For example, the person conducting the test can halt the test and continue to the next confining pressure when principal stress difference is not expected to increase considerably in order to preserve the specimen in as fresh a condition as possible.
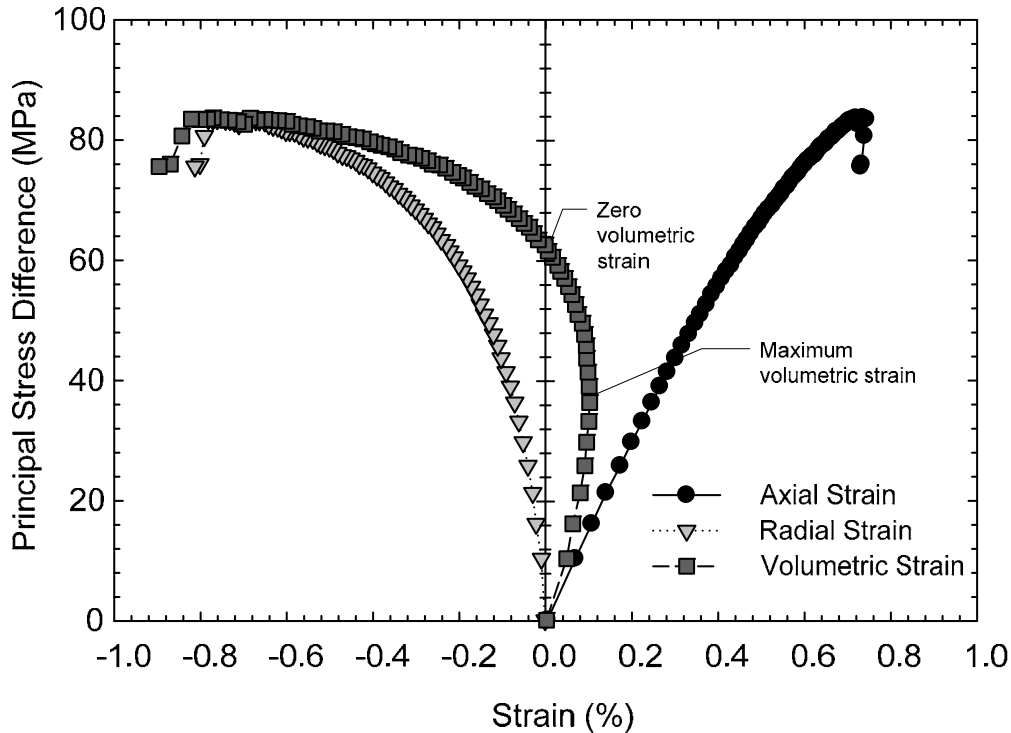
Figure 1.4.14 Stress-strain relationship from triaxial compression test using radial strain control for Edwards Limestone

Several multi-stage triaxial tests were carried out to validate the radial strain controlled multi-stage triaxial test. The specimens sampled at the depth between 20 ft and 22 ft were used to minimize the effect of rock core variability with depth. Test results of three single-stage triaxial tests were shown in Figure 1.4.15 (a) with three different confining pressures. As shown in the figure, volumetric strain and radial strain vs. principal stress difference curves approach plateau when the specimen approaches the peak stress. A multi-stage triaxial test was carried out on a specimen and the test result is shown in Figure 1.4.15 (b). The first imminent failure occurred at an elastic-looking region in the axial strain vs. principal stress difference curve; then the test was halted and confining pressure was increased to the next level. The peak strength of the multi-stage triaxial test and three single-stage triaxial tests are tabulated in the Table 1.4.1. The peak strength of the multi-stage triaxial test was predicted slightly higher than conventional triaxial test results; but, the difference appears to be trivial.

The Hoek – Brown failure criterion (Hoek, 1990) is often used to represent the failure of intact rock. The equation is empirically drawn and expressed as:

$$\sigma_1 = \sigma_3 + (m\sigma_c\sigma_3 + s\sigma_c^2)^{0.5}$$ Equation 1.4-1

where σ_1 is the major principal stress, σ_3 is the minor principal stress, σ_c is the uniaxial compressive strength of intact rock, and *m* and *s* are constants for a specific rock type. The constant *s* approaches 1 for completely intact rock and reduces as the rock contains fractures. The UCS and constant *m* can be back-calculated using the Hoek-Brown criterion assuming s = 1 (intact rock). Adopting the single-stage and multi-stage triaxial test results shown in Table 1.4.1,

80

the UCS and constant *m* were calculated and tabulated in Table 1.4.2. The measured UCS from the multi-stage triaxial test was 65.7 MPa, which is lower than both calculated values.

Table 1.4.1 Comparison between multi-stage triaxial test vs. conventional single-stage triaxial test

	Single-stage triaxial test			Multi-stage triaxial test		
	1MPa	**2MPa**	**3MPa**	**1MPa**	**2MPa**	**3MPa**
Principal stress difference at failure (MPa)	83	84	93	83	91	97

Table 1.4.2 Back calculated UCS, and constant *m*

	σ_c **(MPa)**	*m*	*s*
Single-stage	76.0	11.6	1
Multi-stage	75.3	16.7	1
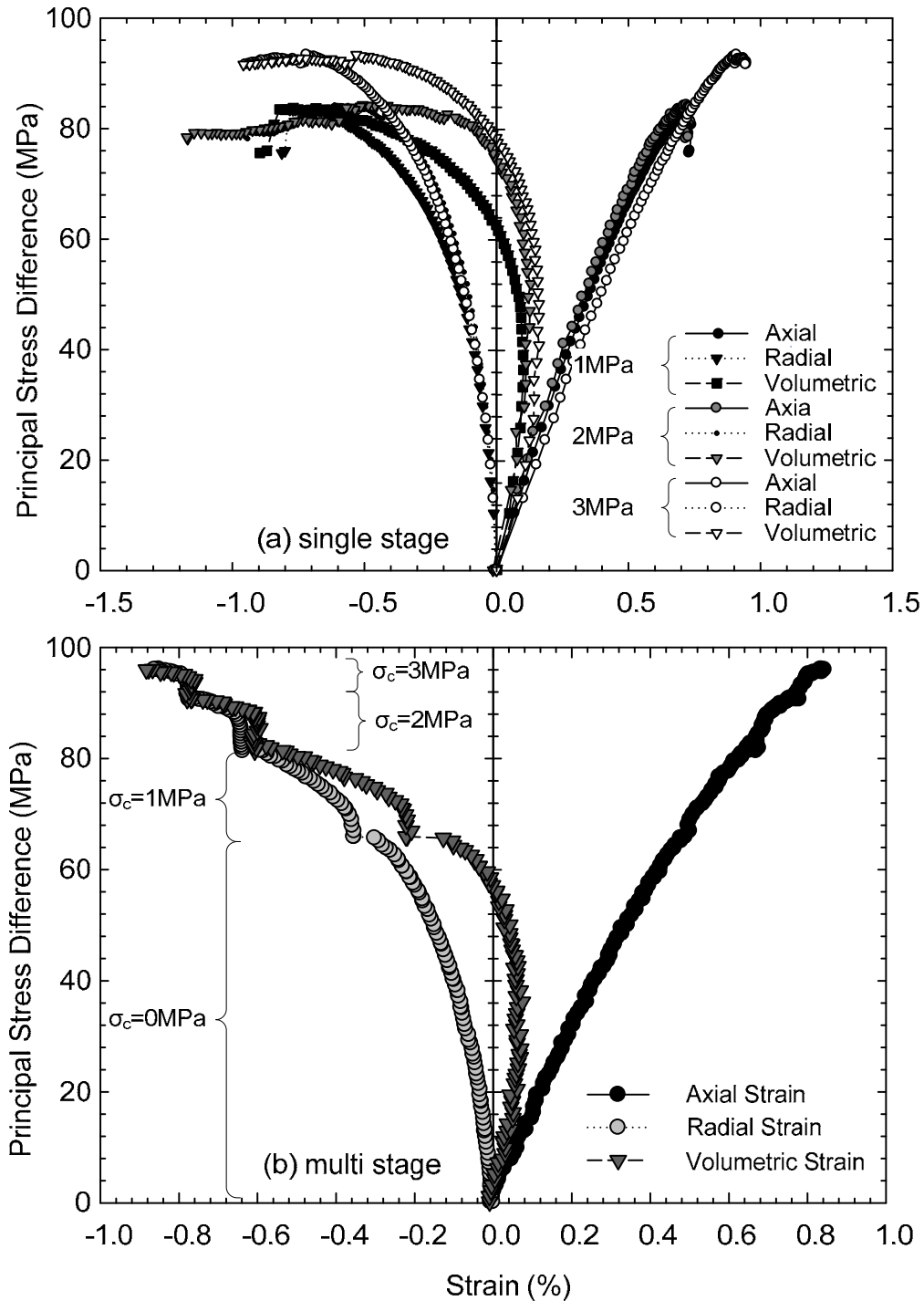
Figure 1.4.15 Stress strain relation of Edwards Limestone obtained from (a) single-stage triaxial test, and (b) multi-stage triaxial test using radial strain control

1.4.3 Unconfined Compressive Strength Test (UCS)

The UCS test is commonly used to measure the strength of rock even though the test does not simulate the *in situ* stress condition; therefore, the obtained strength is less than real value resulting in conservative estimation for most cases. The specimens were prepared using a

diamond blade cutter and grinder, as introduced in Section 1.4. In order to decouple testing and increase production, the apparatus used for the UCS test is different from the apparatus used for triaxial testing. The UCS test device consists of a loading frame, two steel platens (model PLT-110), and a load measuring system. The UCS apparatus is manufactured by GCTS, and it is able to record the peak load at failure but unable to measure axial strain. The peak load is then used to calculate the UCS by dividing the peak load by the cross sectional area of the test specimen. The cross sectional area was not corrected for the axial and radial strain of the specimen as they are not available, thereby resulting in slightly larger UCS. However, the difference was expected to be negligible because the triaxial test results in Section 1.5 suggest that the axial strain of Eagle Ford Shale at failure is typically around 1%.

A friction reducer (WD 40) was sprayed around the loading cylinder to minimize the friction between the steel cylinder column and the ram. Figure 1.4.16 demonstrates the complete process of UCS from the specimen placement to the failure. The specimens were properly prepared and then placed on the bottom platen. The specimen was lifted until the top of the specimen seated with the top platen, and then was loaded to failure. The loading duration generally ranged from 3 to 7 minutes. The failed specimen was then used to determine water content by oven-drying whole broken specimens.

Failure modes of UCS tests for specimens were found to be greatly diverse for Eagle Ford Shale, as shown in Figure 1.4.17. Two failure patterns were predominant: 1) a vertical tensile failure and 2) a diagonal shear failure. Sometimes, solely tensile or shear failure modes were clearly observed, but combinations of the two modes were the most common. Local bursting is another failure mode but rarely observed. Interestingly, the failure surface does not appear to propagate through the horizontal cracks that might develop during sample preparation. This observation suggests that the horizontal fissures are not likely to affect the overall strength of Eagle Ford Shale loaded in the vertical direction.
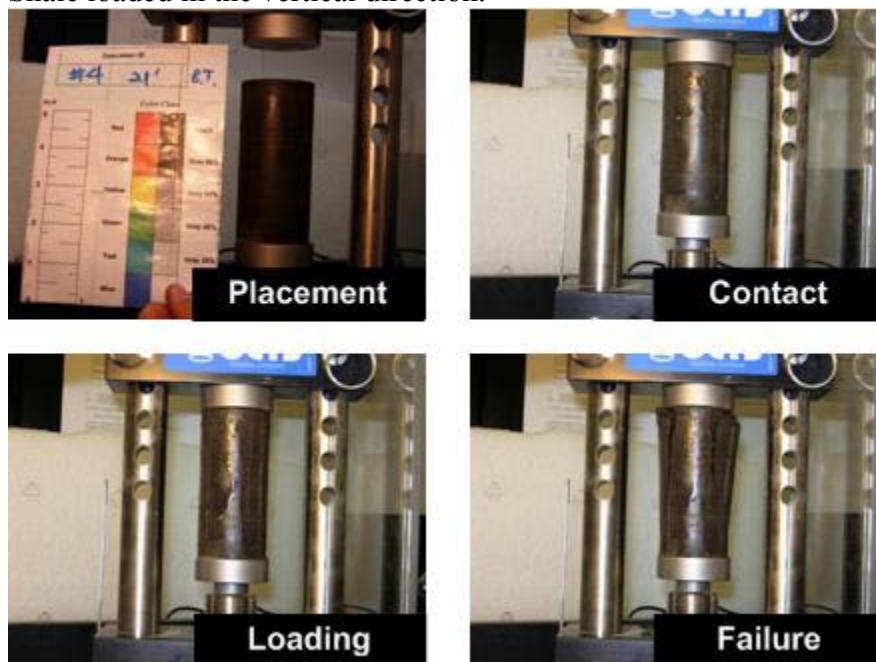
Figure 1.4.16 Uniaxial compressive strength test without strain measurement
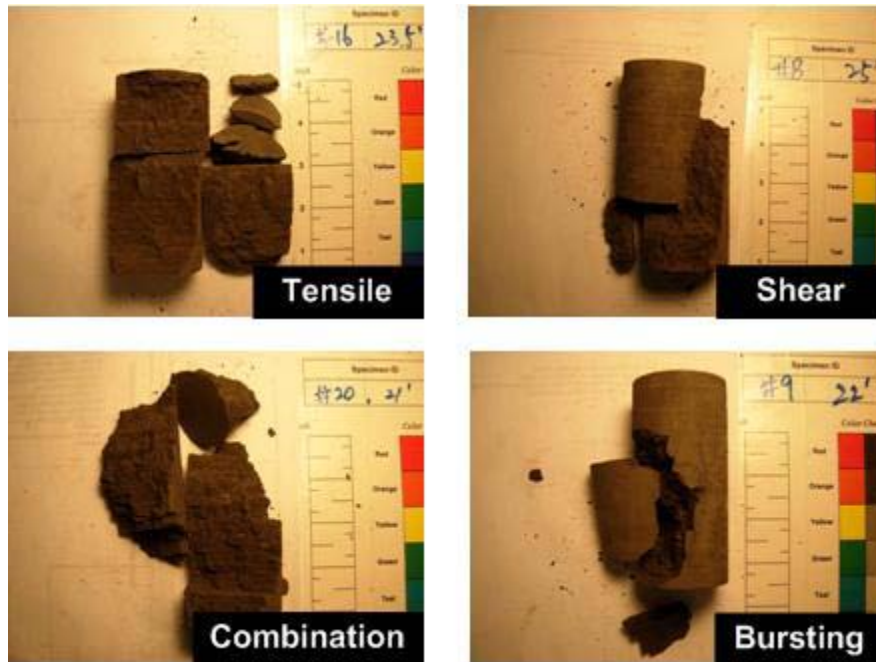
Figure 1.4.17 Several failure modes of Eagle Ford Shale

1.4.4 Point Load Test

The initial concept of the point load test is outlined by (Reichmuth, 1963) and detailed by (Broch and Franklin, 1972). As common rocks require a high capacity measuring system, the point load test is widely accepted to approximate the strength in an efficient manner. The point load index (PLI) obtained from the point load test is used to estimate UCS by pre-developed correlation factors. The method is very popular in the field, especially because there is no need for sample preparation.

Point load tests were carried out on the remaining shales from the UCS tests to obtain correlation factors between PLI and UCS. The results are presented in Section 1.6. Figure 1.4.18 shows the point load test device used in this study. It mainly consists of a loading frame, a load measuring system, and 60˚ conical platens. The apparatus used for the point load test is manufactured by GCTS (PLT-110). To calculate PLI, the dimensions of test cores and the maximum load at failure were recorded.
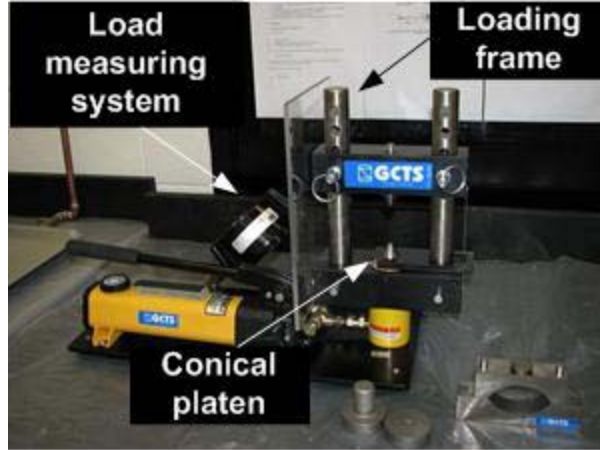
Figure 1.4.18 Point load test apparatus

      Four types of specimen shapes are satisfactory for the point load test (see Figure 1.4.19). The diametral test (Figure 1.4.19 (a)) or the axial test (Figure 1.4.19 (b)) were determined to be adequate because all test specimens had an identical diameter (NX size). However, the innate horizontal fissures of the cores disqualified the diametral test since the location of the fissures significantly affected the results of diametral point load. It was repeatedly observed that failure surfaces did not propagate through the loading point, indicating that fissures were the main sources of failure rather than overall strength of the shales. Figure 1.4.20 presents a failed specimen by the diametral point load test by which failure planes passed through apart from the loading point. The existence of fossils was another inherent failure surface regardless of the location of loading as can be seen on the right picture of Figure 1.4.20. Therefore, the specimens were loaded axially, i.e. perpendicularly to the bedding. Indeed, the axial point load test was recommended for highly anisotropic rock such as shales or other sedimentary rocks (Greene and Schaffer, 1997). In addition, the height of cylindrical specimens was limited to from 20 mm to 30 mm for maintaining consistency of dimensions. After measuring the maximum load, PLI was calculated using a following equation:

$$I_s = \frac{P}{D_e^{\,2}} \ (MPa) \qquad\qquad\qquad \text{Equation 1.4-2}$$

where *P* is a failure load (*N*), D_e is an equivalent core diameter, and the D_e is obtained by:

$$D_e^{\,2} = D^2 \ \text{ for diametral tests (mm}^2\text{), or}$$

$$D_e^{\,2} = \frac{4 \cdot A}{\pi} \ \text{for axial, block, and lump tests (mm}^2\text{)}$$

where $A = W{\cdot}D$ = minimum cross-sectional area of a vertical plane through the conical platen contact points. The PLI (I_s) is then corrected by the size correction factor since the PLI increases as the core diameter increases. Thus, PLI, I_s, is normalized to 50 mm diameter core by multiplying by the size correction factor. The size correction factor used in this study is expressed as follows (ASTM Standard D5731, 2007):

$$F = \sqrt{\frac{D_e}{50}} \qquad\qquad\qquad \text{Equation 1.4-3}$$

UCS is frequently correlated with PLI by the conversion factor, *C*. According to ASTM D5731, the recommended conversion factors, *C*, range from 17.5 to 24.5, depending on core size. On the other hand, it was reported that conversion factors of intact sedimentary rocks also varied depending on rock strength (Tsiambaos and Sabatakakis, 2004). Figure 1.4.21 exhibits the proposed conversion factors for sedimentary rocks, suggesting the conversion factors changing from 13 for limestones, 220 for marlstones, and 28 for sandstones. When the conversion factor is established, the UCS of rocks is simply estimated by multiplying the conversion factor by the obtained PLI. The specimens that failed axially to the bedding plane are shown in Figure 1.4.22. Either splitting into two pieces or three pieces was accepted as proper failure modes.

Two to four specimens were tested per one UCS specimen, and both water content of each test specimen and PLI values were averaged to one value to compare with information obtained from UCS tests.
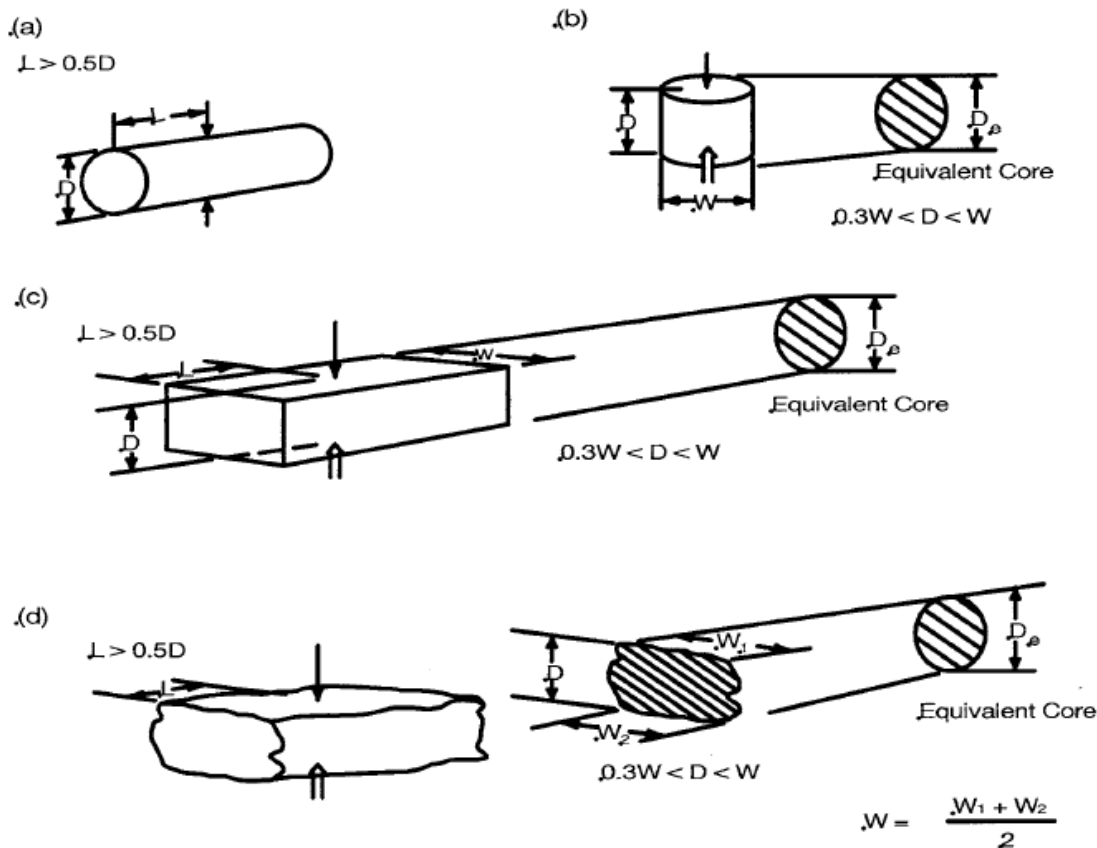
Figure 1.4.19 Load configurations and specimen shape requirement for (a) the diametral test, (b) the axial test, (c) the block test, and (d) the irregular lump test (after ASTM D 5731)

Figure 1.4.20 Failed specimen by diametral point load test
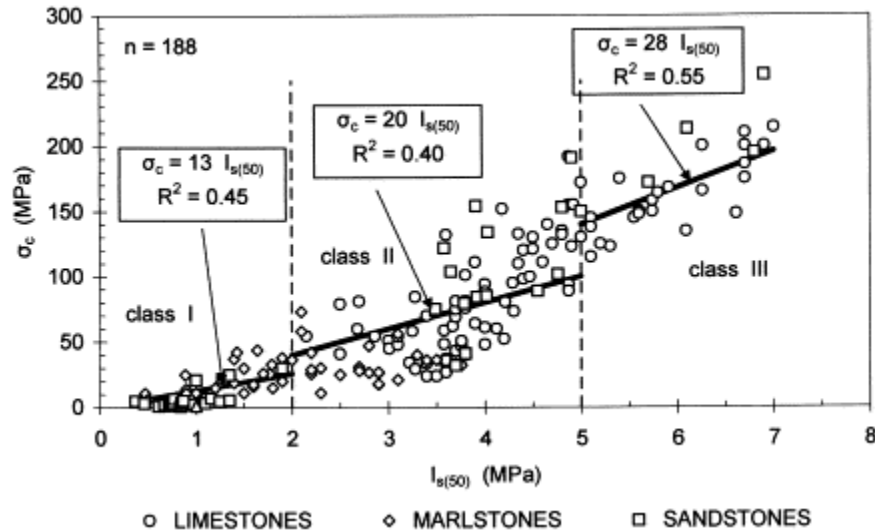
Figure 1.4.21 Conversion factors correlating PLI and UCS for soft to strong sedimentary rocks (Tsiambaos and Sabatakakis, 2004)

Figure 1.4.22 Failed specimens by axial point load test

1.4.5 Slake Durability Test

Unlike static slaking measurement such as the jar slake test, the slake durability test imposes dynamic weathering process. The slake durability test was first introduced by (Franklin and Chandra, 1972) in order to quantify the durability of weak rocks, and was later accepted by ISRM as a suggested method. Suitable weak rocks include mudstones, shales, or other weak rocks. About 50 g of ten lumps split from rocks were oven-dried, typically for 24 hours at 110˚C,

87

and were placed in a steel mesh drum with 2 mm screening size. The drum rotates at a rate of 20 revolutions per minute for 10 minutes submerging the rocks in distilled water. Remaining weak rocks are oven-dried and the final oven-dried weight is compared to the initial oven-dried weight; the ratio of final to initial oven-dried weight is called the slake durability index (SDI). The slake durability test can be repeated as many times as the tester desires, but two cycles of tests are recommended by ISRM.

1.4.6 Jar Slake Test

The jar slake test (USBR, 2006) is a simple and rapid test to evaluate durability of weak rocks such as clay shales when they are exposed to atmosphere. A typical jar slake test requires complete drying of test specimens prior to immersion under water. In this study, however, the clay shales are dried for different durations and immersed under water. Figure 1.4.23 shows the step-by-step pictures of the jar slake test on cubical Eagle Ford specimens before and immediately after immersion, 30 minutes and 24 hours after immersion. Prepared cubical specimens of Eagle Ford Shales were dried for a specific time, 48 hours for this particular sample, and placed in distilled water. Then the slaking patterns of cubic were described at 30 minutes and 1 day after placement, and the description is used to categorize the durability of the specimen based on jar slake charts shown in Figure 1.4.24. It should be noted that the specimens used in the jar slake tests were air dried in the laboratory for specific time periods; while the typical jar slake tests require that specimens be oven-dried before being placed in water. Eagle Ford Shales disintegrated along horizontal cracks for the first 30 minutes after placement and considerable changes were not subsequently observed. Indeed, most disintegration for the most tested rock types occurred within 30 minutes after submersion.
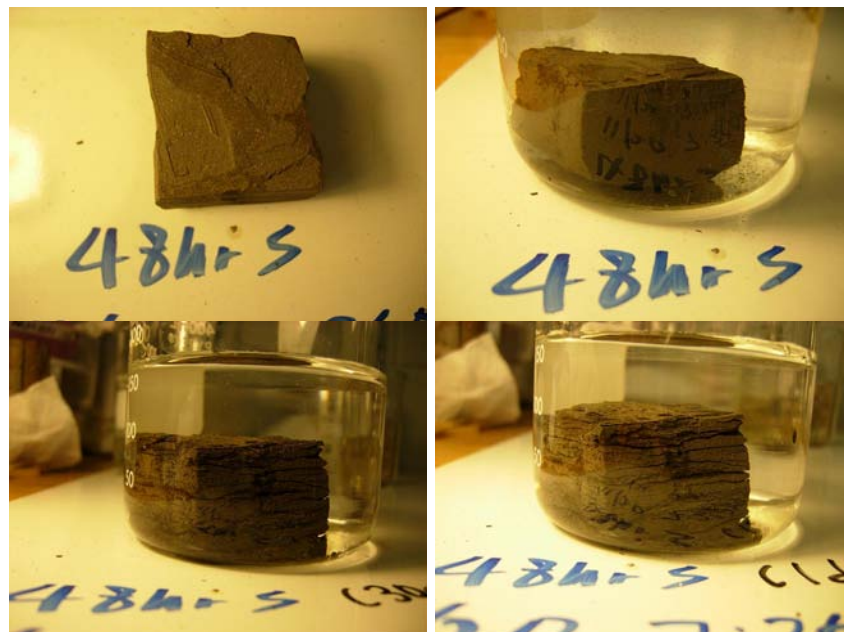
Figure 1.4.23 Slaking of the Eagle Ford Shale (before drying, soaking, 30 minutes after soaking, 1 day after soaking, in order)
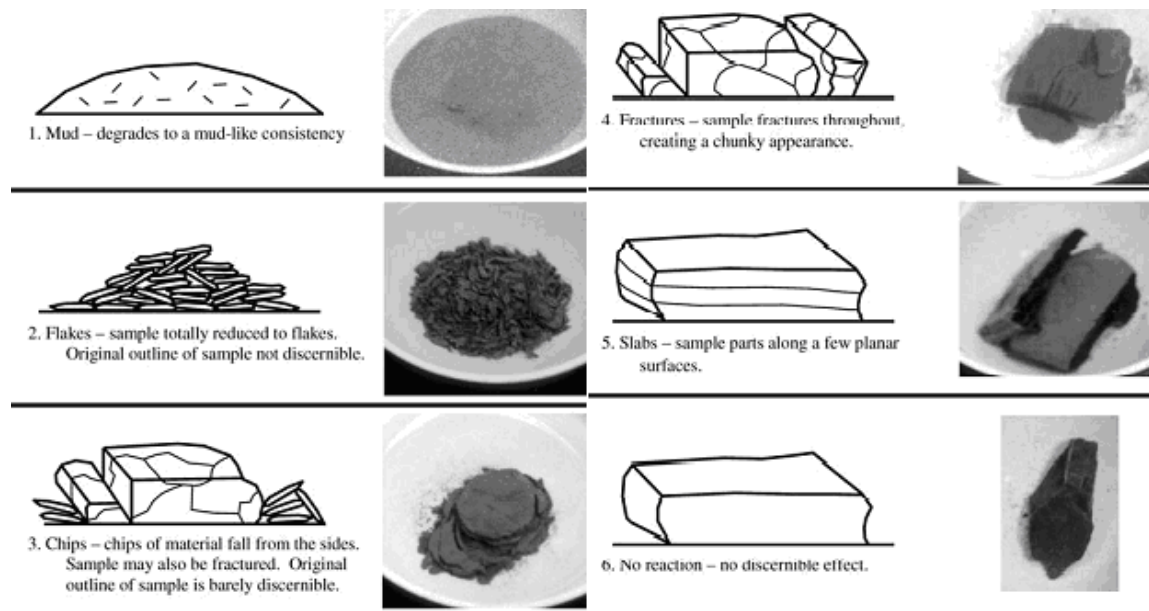
Figure 1.4.24 Six slake modes of jar slake test (Walkinshaw and Santi, 1996)

1.5 ENGINEERING PROPERTIES OF TEXAS ROCKS

1.5.1 Introduction

In this section, engineering properties of six different rock formations in Texas are presented based on the results of three different laboratory tests: (1) the multi-stage triaxial test, (2) the slake durability test, and (3) the jar slake test. The study was designed to investigate the change in principal stress difference, the slake durability index (SDI), and the qualitative durability of test formations when they are dehydrated. The test results were then used to ascertain how much the foundation material degrade as a result of allowing air drying. The wall of the verification core is likely to be dehydrated during the time interval between augering shaft holes and pouring concrete, but will eventually be re-wetted by ground water inflow. One cycle of drying and wetting, therefore, was imposed on the test specimens to simulate the field conditions. Besides the main topic tests, several specimens were holed at the center and triaxially tested to gain an insight into the effect of the verification core hole itself. In addition, a few specimens were placed under slurry for 12 hours and tested to check if the use of slurry expedites degradation. Slurry, typically either polymer or bentonite, is used to prevent water from penetrating towards hollow-drilled shaft holes where water inflow is considerable.

Tested formations included two relatively hard rock formations (Edwards Limestone and Austin Chalk) and four weak rock formations (Del Rio Clay, Eagle Ford Shale, Taylor Marl, and Navarro Shale). The tested formations were obtained by the commercial laboratory Fugro Consultants Inc. and transferred to the Rock Mechanic Laboratory located at The University of Texas at Austin. All test specimens were prepared and tested in accordance with the procedures introduced in Section 1.4. It should be also noted that principal stress differences displayed through this study are the peak value, the elastic modulus is the secant modulus obtained at 50% peak strength, and water content indicates value as received. The results differ among tested formations, so each specific test results is presented later. The results and observations provided in this section will be further discussed in Section 3.1. Laboratory and full-scale condition test results described in Section 1.6 and interpretation in Section 3.1 will then be used to quantify the effect of the verification core on the point bearing capacity of drilled shafts using numerical simulation in Section 3.2.

1.5.2 Specimen Labeling

The tested specimens were labeled by; their formation, drying-duration, adopted test type, and applied confining pressure. The first two letters of the specimen name denote the abbreviation of the tested formations: ED=Edwards Limestone, AC=Austin Chalk, DR=Del Rio Clay, EF=Eagle Ford Shale, TA=Taylor Marl, and NA=Navarro Shale. The third letter denotes either: S=single-stage triaxial test, or M=multi-stage triaxial test. The fourth letter denotes imposed drying-duration: N=natural, numerals=drying-duration, and S=slurry. The fifth letter represents the physical shape of the specimens: N=Solid, and H=Holed. Several specimens tested with the single-stage triaxial test have a sixth number which denotes confining pressure in MPa. For example, EDSNN1 indicates that: 1) the tested specimen is Edwards Limestone, 2) the single-stage triaxial test was used, 3) the test specimen was tested without dehydrating, 4) the specimen has no hole, and 5) the confining pressure is 1 MPa. As an another example, DRM33N

indicates that solid Del Rio Clay specimen was dehydrated for 33 hours and was tested using multi-stage triaxial tests.

1.5.3 Hard Rocks

The material properties of the two relatively hard rock formations (Edwards Limestone and Austin Chalk) were investigated to establish reference properties, by which one can compare the behavior of degradable clay shales. The test results on the two formations indicate that both formations are highly durable and are not subject to deterioration by allowing one cycle of drying and wetting. Hence, using these formations as references is believed to be acceptable. The following sections include the test results and the interpretations on Edwards Limestone and Austin Chalk.

Edwards Limestone

The Edwards formation was deposited during the Cretaceous Age underlying the Georgetown formation and is composed of fine-grained gray limestone with common nodular chert. Detailed geological features of the limestone are explained in Section 1.3.2. The material properties of Edwards Limestone were evaluated using both the multi-stage triaxial test and the slake durability test. The principal stress difference (deviator stress) was obtained from a series of multi-stage triaxial tests after drying the specimens for different time durations. The slake durability index (SDI) was obtained from the slake durability test and used to define the durability of the rocks. An attempt was made to quantify the effect of drying-duration on the durability of limestone by measuring SDI, but it was found that the SDI does not vary significantly after one cycle of drying and wetting. The jar slake test was not carried out because the limestone was found to be unchanged under the water in preliminary tests.

Figure 1.5.1 shows the Edwards Limestone obtained from 18 ft to 28 ft depth. The tested Edwards cores are ivory white in color with thin, dark gray clay seams which were not parallel to each other. The clay seams may play a key role in determining strength of intact Edwards Limestone because the failure of rock tends to propagate through the weak portion. The water content of obtained cores ranges from 0.4% to 4.0%, which is much less than that of four clay shales tested. Figure 1.5.2 presents a typical stress-strain curve of Edwards Limestone using radial-strain control. For this particular case, the stress-strain curve was obtained under 1 MPa confining pressure, and the axial-and radial-strain at failure was about 0.8 and -0.8%.

Figure 1.5.1 Edwards limestone cores before specimen preparation
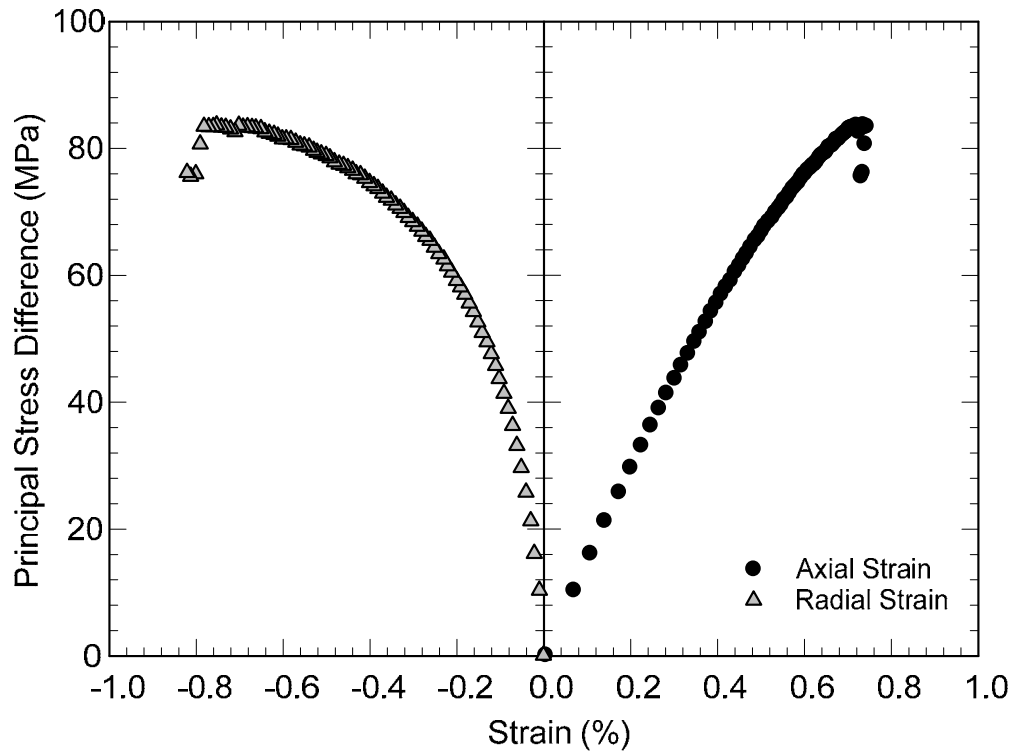
Figure 1.5.2 Typical stress-strain curve of Edwards Limestone from the single-stage triaxial test under 1 MPa confining pressure (EDSNN1)

Prepared Edwards specimens were dried from 0 hours to 48 hours in the laboratory conditions before being soaked in water for 2 days. Then, multi-stage triaxial tests were conducted on the specimens. Several prepared Edwards specimens became unusable after soaking because of the cracks developed through the weak clay seams. The effect of drying-duration on the principal stress difference and the slake durability index are shown in following

sections. In addition, the other relationships between parameters such as SDI, dry density, elastic modulus, water content, and principal stress difference are discussed afterwards.

Effect of drying-duration on material properties

Figure 1.5.3 presents the effect of drying-duration on the principal stress difference and the SDI showing that neither the principal stress difference nor SDI is affected by drying-duration. The principal stress difference of Edwards Limestone scatters between 30MPa and 140MPa depending on inherent specimen characteristics (Figure 1.5.3 (a)). The strength can differ by more than a factor of two between the weakest and the strongest for the non-dried specimens, which indicates that the strength is strongly influenced by spatial variability rather than drying-duration. Indeed, the specimen obtained at 9 ft depth appeared to be very different from other specimens, whose strength solely exceeded 130 MPa. Figure 1.5.4 presents several failure modes of tested limestone: 1) vertical tensile failure, 2) shear failure, and 3) cracks along clay seams.

In addition to solid specimens, holed specimens and slurry-soaked specimens are tested and results are shown in Figure 1.5.3 (b) through (d). The test result of the slurry-soaked specimen was plotted at 60 hours of drying-duration to prevent confusion with other test results, although the specimen was soaked under slurry for 12 hours. It appears that the use of slurry does not significantly affect the strength of Edwards Limestone. The strength of the slurry-soaked specimens is found to be approximately the median of non-slurry affected specimens.

However, the existence of a hole at the top half of the tested specimen may have reduced the strength. Because the effect of a hole is not a main concern of this research, only one or two specimens were tested per formation. The holed specimen indicates the specimen that was drilled to 50.8 mm (2 inches) depth with 9.5 mm (3/8 inch) diameter at the center. The slurry-soaked specimen indicates that the specimen was placed under the slurry for twelve hours prior to testing. While drying the specimen is intended to simulate the drying effects induced by the time difference between augering and concrete pouring, the specimen soaked under the slurry is intended to simulate the effect of usage of slurry. In other words, the dried specimen represents the material status around the verification core when the "dry method" is used, and the slurry-soaked specimen represents the material when the "wet method" is used during the construction of drilled shafts.

The durability of Edwards Limestone was measured by running slake durability tests on the broken specimen after multi-stage triaxial tests. Figure 1.5.5 displays the Edwards Limestone specimens after two cycles of a slake durability test. Ten lumps of Edwards Limestone have maintained their initial weights after the test. Overall durability of Edwards Limestone is between medium high to very high, according to slake durability classification proposed by Gamble (1971). The classification chart is shown in Table 1.5.1. It is very likely that rocks with this durability would not be degraded by one cycle of drying and wetting. Figure 1.5.3 (e) supports such a finding by showing that SDI does not decrease with 48 hours of drying. SDI did not increase with increasing drying-duration. Because it is durable through one cycle of wetting and drying, drilled shaft capacity in Edwards Limestone is likely to be unaffected when verification core holes are drilled at the bottom of drilled shafts. Furthermore, the difference in durability among specimens is thought to be negligible. Slight differences in SDI may result from the soft clay seam, which is easily washed away during the slake durability test, leading to slightly lower SDI.
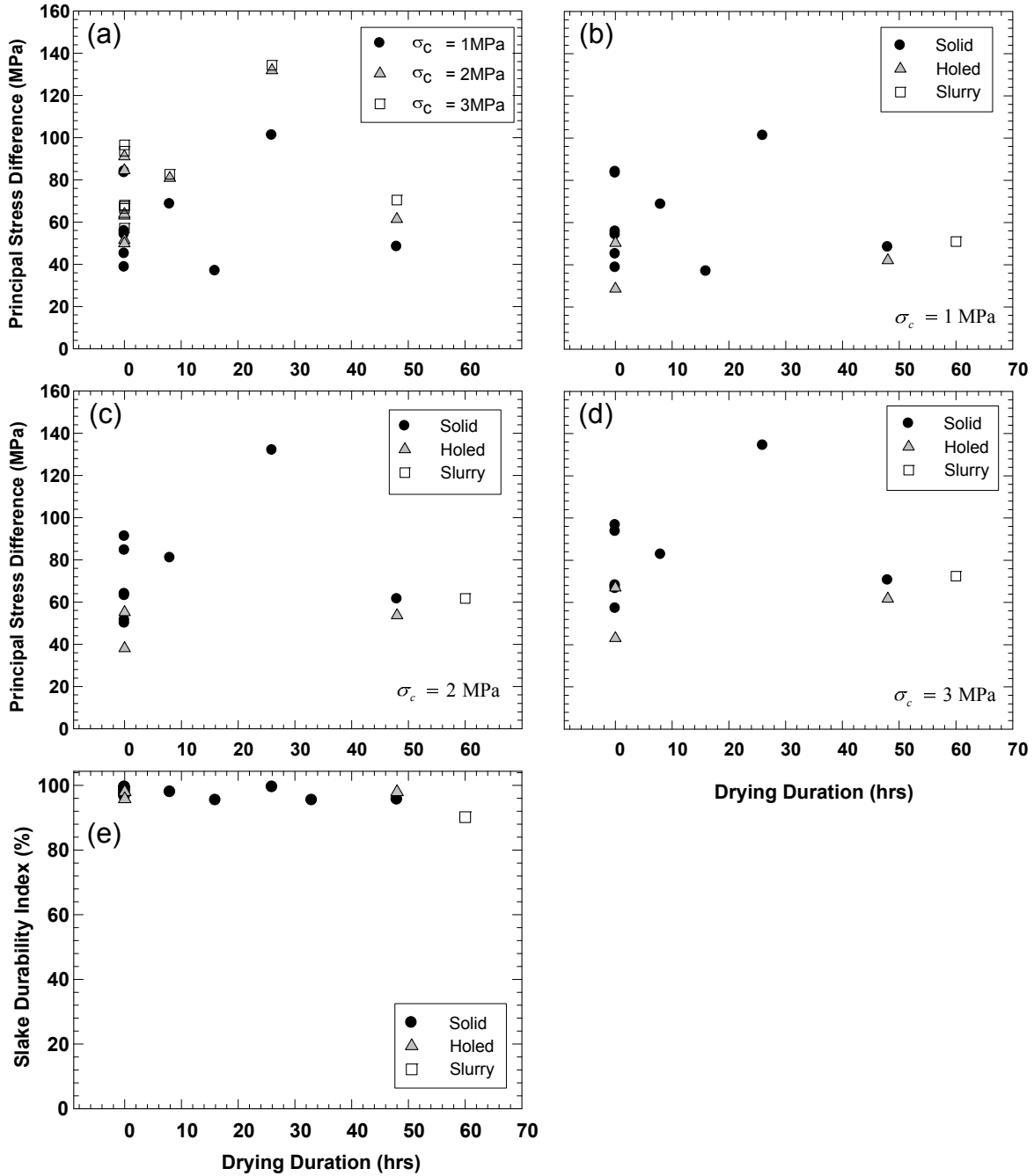
Figure 1.5.3 Edwards Limestone: effect of drying-duration on: (a) principal stress difference at three confining pressure, (b) principal stress difference of solid, slurry-soaked, and holed specimen at 1MPa, (c) principal stress difference of solid, slurry-soaked, and holed specimen at 2MPa, (d) principal stress difference of solid, slurry-soaked, and holed specimen at 3MPa, and (e) slake durability index (SDI)

Figure 1.5.4 Failure modes of Edwards Limestone
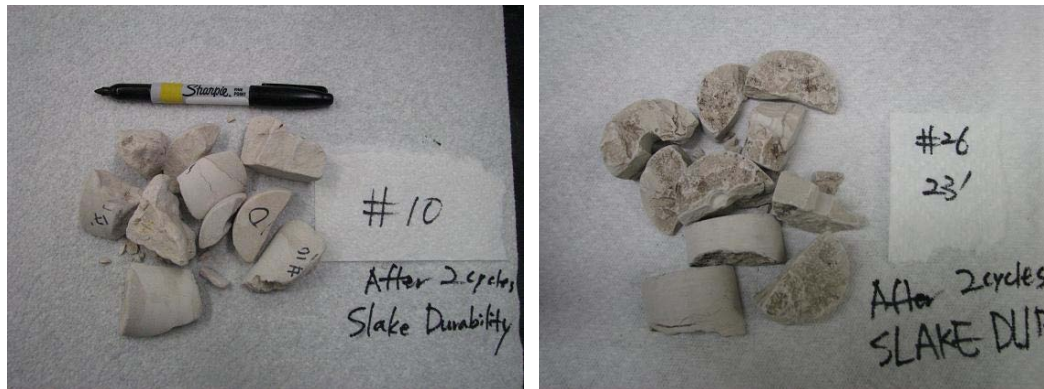
Figure 1.5.5 Edwards Limestone specimens after slake durability tests

Table 1.5.1 Gamble's Slake Durability Classification (Gamble, 1971)

Group Name	% Retained after one 10-min cycle (dry weight basis)	% Retained after two 10-min cycles (dry weight basis)
Very high durability	> 99	> 98
High durability	98 – 99	95 – 98
Medium high durability	95- 98	85 – 95
Medium durability	85 – 95	60 – 85
Low durability	60 – 85	30 – 60
Very low durability	< 60	< 30

Effect of water content on material properties

The effect of water content on the strength of soft rocks and shales has been outlined by a number of researchers (Ghafoori et al., 1993; Greene and Schaffer, 1997; Lashkaripour, 2002). Accordingly, the test results of Edwards Limestone exhibit similar trends as can be seen in Figure 1.5.6. Figure 1.5.6 (a) shows the variation of principal stress difference with water content at three confining pressures. The samples containing a higher moisture content tended to yield lower strength. Interesting observations are that the principal stress differences of the holed and slurry-soaked specimens are not significantly different from other test results. Figure 1.5.6 (e) provides the change in SDI with water content showing that the SDI of limestone is measured to be greater than 90%, and the difference in SDI with water content is none to minimal. The elastic modulus of Edwards Limestone tends to increase as water content decreases.
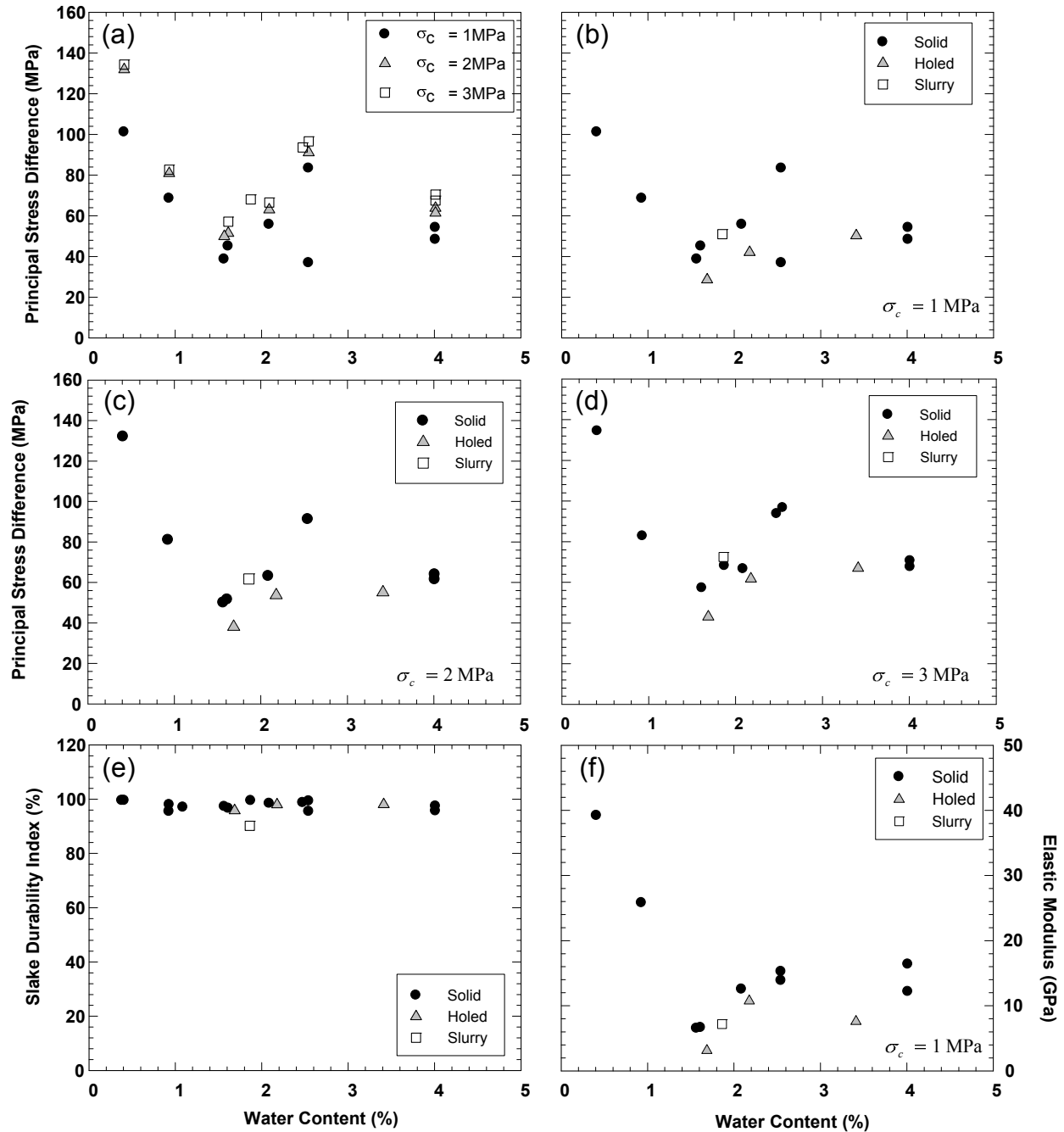
Figure 1.5.6 Edwards Limestone: effect of water content on: (a) principal stress difference at three confining pressures, (b) principal stress difference of solid, slurry-soaked, and holed specimen at 1MPa, (c) principal stress difference of solid, slurry-soaked, and holed specimen at 2MPa, (d) principal stress difference of solid, slurry-soaked, and holed specimen at 3MPa, and (e) slake durability index (SDI), and (f) elastic modulus

Other relationships

Other relationships of interest are correlations between properties such as principal stress difference, dry density, SDI, elastic modulus, and drying-duration. Specifically, the relationship

97

between elastic modulus and drying-duration offers important information since the elastic modulus of foundation material of drilled shafts is closely related to the stiffness of drilled shafts. Higher elastic modulus of founding material may result in stiff response of drilled shafts. Figure 1.5.7 (a) through (d) shows the relationship between (a) dry density and principal stress difference, (b) slake durability index and principal stress difference, (c) principal stress difference and secant modulus obtained at 50% peak strength, and (d) drying-duration and secant modulus at 50% peak strength. Figure 1.5.7 (a) to (c) shows tendency among variables, while Figure 1.5.7 (d) displays little to no correlation. The relationship between dry density and principal stress difference is consistent with earlier findings; principal stress difference increases as water content decreases. On the other hand, Figure 1.5.7 (b) describes the increasing trend of principal stress difference with increasing SDI. It is highly likely that durable and dense rocks tend to be strong.

Figure 1.5.7 (c) presents the relationship between principal stress difference and elastic modulus of Edwards Limestone. Deere's classification of intact rock utilizes both UCS and modulus ratio; the classification system is shown in Table 1.5.2 and Table 1.5.3 (Deere, 1968). Visualization of the two tables is provided in Figure 1.5.8 including data points for Edwards Limestone and Austin Chalk. The principal stress difference of Edwards Limestone ranges from D – low strength to C – medium strength, and most modulus ratios for the limestone fall into M-average modulus ratio. Modulus ratio indicates the ratio of tangent modulus at 50% ultimate strength to UCS, whose average was found to be 330 for tested Edwards Limestone belonging to average ratio (Class M). It should be noted that the classification tables use UCS instead of principal stress difference under confinement, thus the UCS might be slightly lower than the principal stress difference used for classification. The elastic modulus was found to be independent of drying-duration, as shown in Figure 1.5.7 (d).

Figure 1.5.7 Edwards Limestone: relations between: (a) dry density and principal stress difference, (b) SDI and principal stress difference, (c) principal stress difference and elastic modulus, and (d) drying-duration and elastic modulus

Table 1.5.2 Engineering classification of intact rock on the basis of UCS (Deere, 1968)

Class	Description	UCS (MPa)	Rock Type
A	Very high strength	> 220	Quartzite, diabase, and dense basalt
B	High strength	110-220	Most igneous rocks, most limestones, and dolomite, well-cemented sandstones and shales
C	Medium strength	55-110	Most shales, porous sandstones, and limestones
D	Low strength	28-55	Friable sandstones, porous tuff
E	Very low strength	< 28	Clay-shale, rock salt

Table 1.5.3 Engineering classification of intact rock on the basis of modulus ratio (After Deere, 1968)

Class	Description	Modulus ratio
H	High modulus ratio	> 500
M	Average (medium) ratio	200 – 500
L	Low modulus ratio	< 200
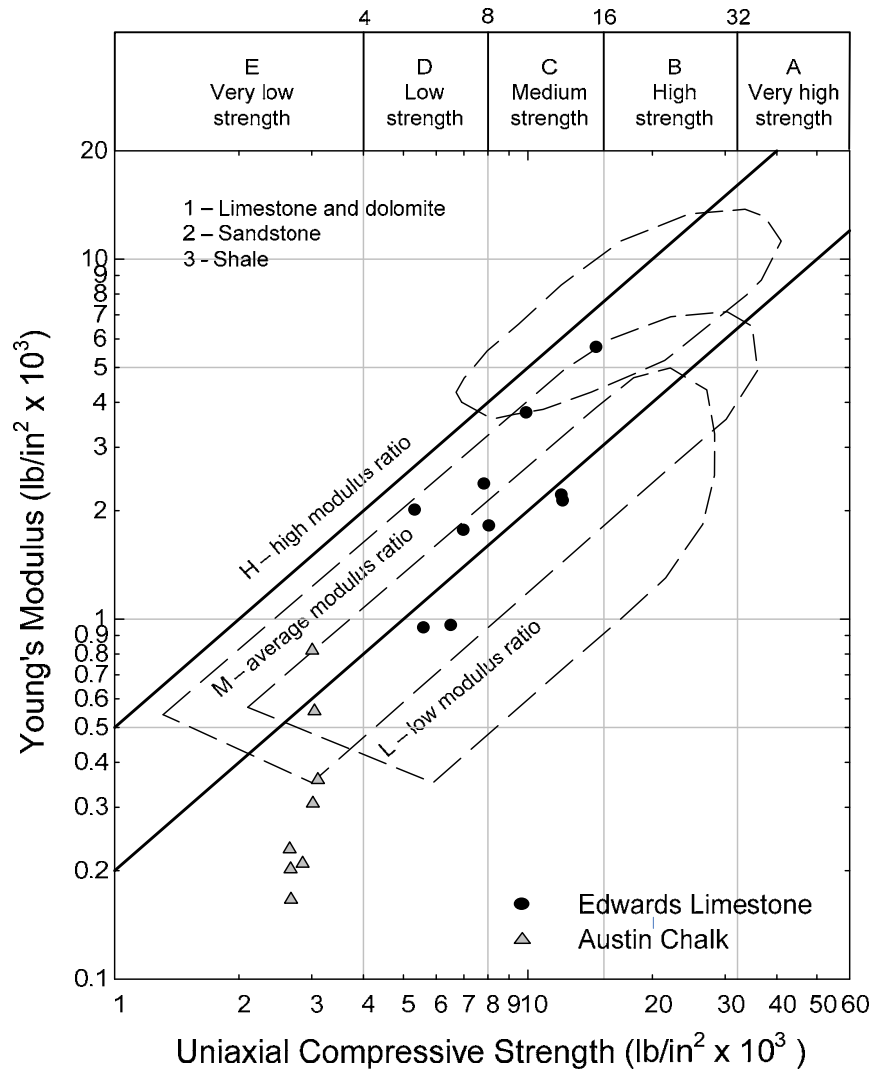
Figure 1.5.8 Engineering classification of Edwards Limestone and Austin Chalk on the classification chart (modified from Deere, 1968)

Austin Chalk

In this section, the laboratory test results of Austin Chalk are presented. Austin Chalk is composed of very fine grained carbonate mud that was deposited during the upper Cretaceous

and which is located across Texas, outcropping sporadically from southwest of Texas through central Texas to north central Texas (see Section 1.3.2 for details of geology). Figure 1.5.9 shows Austin Chalk cores wrapped in plastic bags as delivered to the laboratory; the core was light gray to gray, and was soft when classified in terms of the Mohs scale of hardness (easily scratched with the finger nail). The water content of the chalk was between 10% and 14%, which is high compared to that of Edwards Limestone, implying that the Austin chalk is weaker than Edwards Limestone.

Figure 1.5.9 Austin Chalk cores before specimen preparation

The Austin Chalk specimens were air dried in the laboratory for 0 to 48 hours, and were placed under water for two days prior to multi-stage triaxial testing. The relative humidity of the laboratory varied from 30% to 40% during air drying. The percent water loss is the ratio of loss in weight of water to the total weight of water of each specimen. Percent water loss with drying-duration was recorded and presented in Figure 1.5.10. It shows dramatic increase in water loss, up to 74% at 48 hours of drying (Figure 1.5.10). Percent water loss was adopted to study the evaporation rate, instead of change in water content, because the initial water content varied between each specimen. The amount of water loss of Austin Chalk is substantial compared to other formations. The multi-stage triaxial test on Austin Chalk was controlled by constant axial strain rate since the Austin Chalk failed in a ductile fashion unlike Edwards Limestone. A typical stress-strain curve of Austin Chalk using the single-stage triaxial test is shown in Figure 1.5.11.
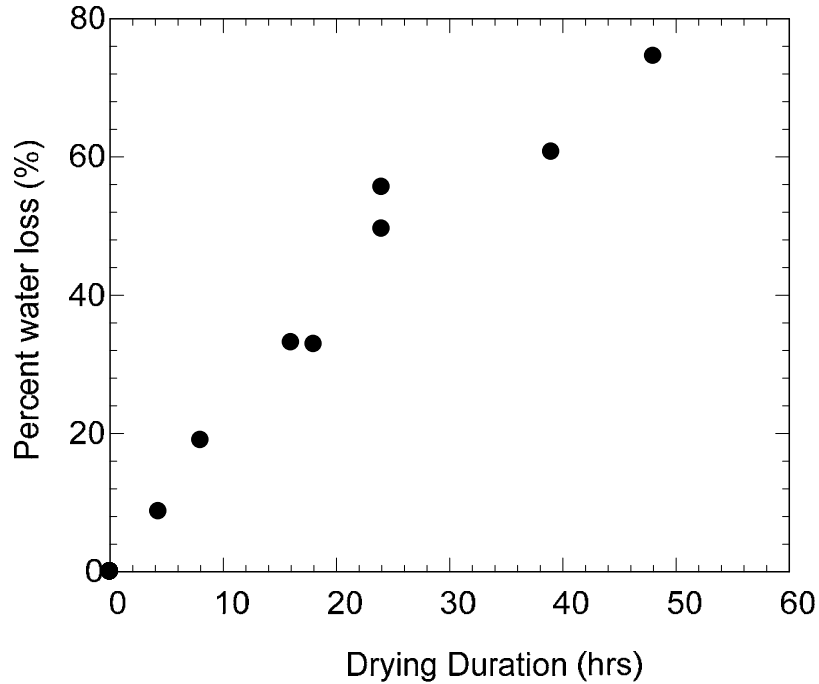
Figure 1.5.10 Percent water loss with drying-duration of Austin Chalk
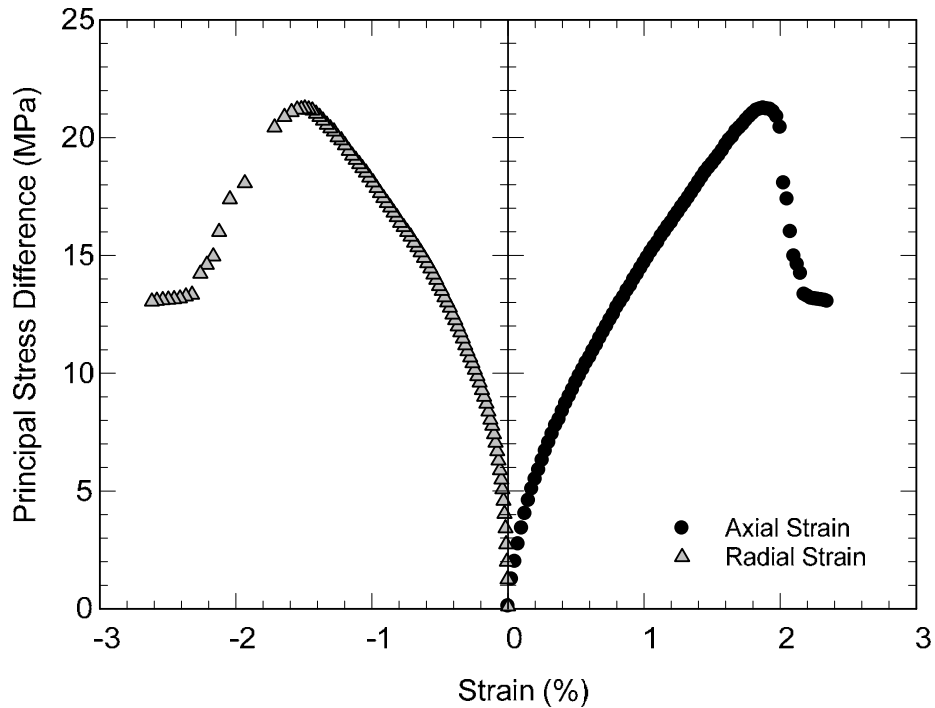
Figure 1.5.11 Typical stress-strain curve of Austin Chalk from the single-stage triaxial test under 3 MPa confining pressure

Effect of drying-duration on material properties

　　　　Figure 1.5.12 presents the effect of drying-duration on the principal stress difference and SDI of Austin Chalk. It is clear that drying-duration is not related to the strength of Austin Chalk

within 48 hours of drying. The principal stress difference of the Austin Chalk was measured to be approximately 20 MPa, regardless of drying-duration. The homogeneous properties of the chalk may contribute to less scatter in Austin Chalk than in Edwards Limestone. Several failure modes of Austin Chalk are shown in Figure 1.5.13: 1) clear shear failure, 2) vertical tensile failure, 3) local failure, and 4) combinations of the three.

Figure 1.5.14 shows an Austin Chalk sample removed after soaking in slurry for 12 hours. In addition to slurry-soaked specimens, one specimen with a hole at the center was tested in order to see the effect of the hole on the strength of the entire specimen. Only a few tests per each formation were carried out to gain an insight into the behavior of such a condition, rather than to draw a conclusion.

Figure 1.5.15 shows a holed Austin Chalk specimen before and after the multi-stage triaxial test. The failure plane passes through the end of the hole, which implies that the existence of a hole is not likely to affect the strength of the specimen significantly. The principal stress difference of the holed specimen and the slurry-soaked specimen is shown along with the results of solid specimens in Figure 1.5.12 (b) through (d). In these preliminary tests, the effect of the hole was measured to be nominal, possibly because the failure plane was not connected or extended through the hole. Conversely, the use of slurry was found to reduce the strength of Austin Chalk by as much as 30%. However, one cannot exclude the possibility that the spatial variability was the main reason for such a reduction. For example, the slurry-soaked specimen was obtained at 13 ft depth while other specimens were obtained at depths below 36 ft. Therefore, additional tests should be carried out to better understand the effect of slurry.

Durability of Austin Chalk was measured using the slake durability test in accordance with ASTM D4644. Figure 1.5.16 presents the Austin Chalk specimen before and after two cycles of the slake durability test, during which Austin Chalk broke and fragmented into smaller pieces. The fragmentation of Austin Chalk appears to be considerable compared to Edwards Limestone. From results of the slake durability test, it was found that drying-duration does not influence the SDI value, as is depicted in Figure 1.5.12 (e). The SDI values of the holed specimen and the slurry-soaked specimen does not noticeably differ from those of solid specimens. The SDI values range from 85% to 97%, and, accordingly, the rock is determined to be between medium high durable and high durable. The verification hole in Austin Chalk does not deteriorate in two days of drying.
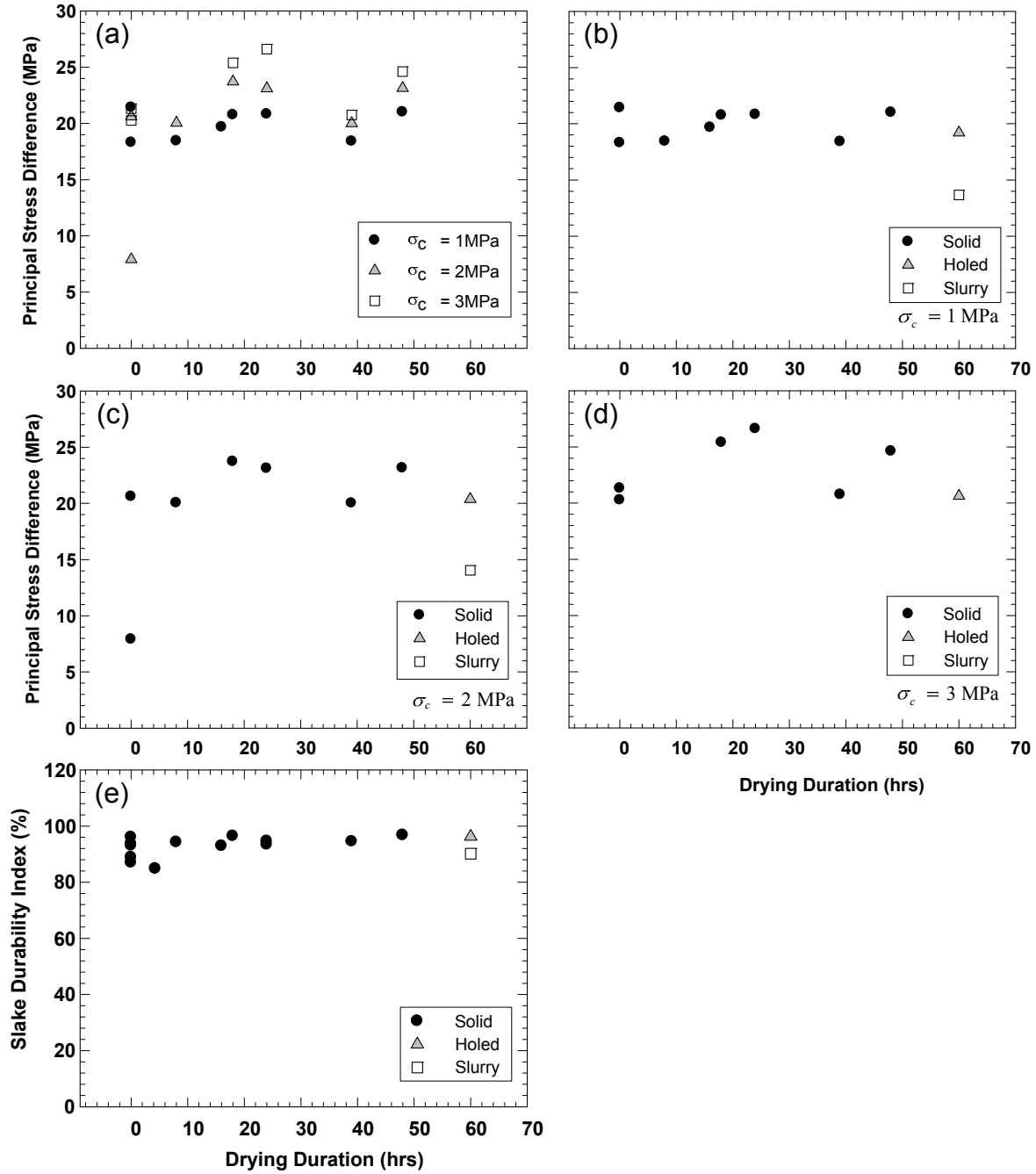
Figure 1.5.12 Austin Chalk: effect of drying-duration on: (a) principal stress difference at three confining pressure, (b) principal stress difference of solid, slurry-soaked, and holed specimen at 1MPa, (c) principal stress difference of solid, slurry-soaked, and holed specimen at 2MPa, (d) principal stress difference of solid, slurry-soaked, and holed specimen at 3MPa, and (e) slake durability index (SDI)

Figure 1.5.13 Failure modes of Austin Chalk after the multi-stage triaxial test

Figure 1.5.14 Slurry-soaked Austin Chalk
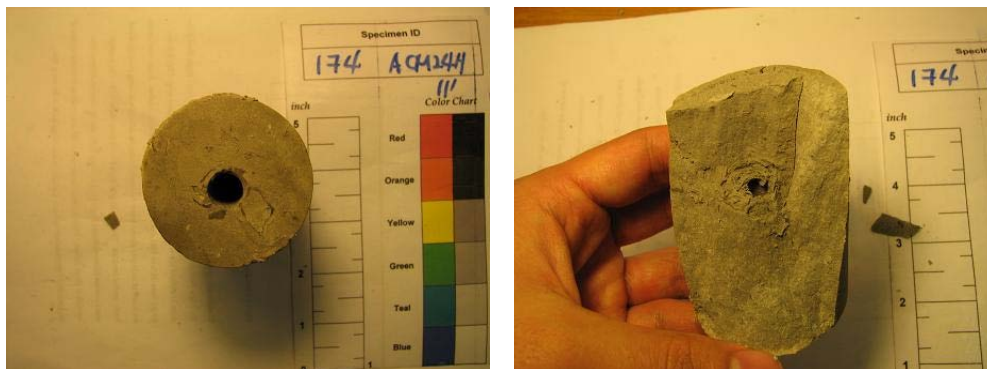
Figure 1.5.15 Austin Chalk specimen with hole before and after the triaxial test

Figure 1.5.16 Austin Chalk chunks before and after two cycles of the slake durability test

Effect of water content on material properties

The results of multi-stage triaxial tests are plotted against water content in Figure 1.5.17, indicating that the Austin Chalk strength is not sensitive in variation to water content. This finding does not imply that water content is an independent factor of rock strength but that the studied range of water content may be too narrow to determine a significant change in strength. Regardless of the water content, the principal stress differences were measured to be approximately 20 MPa. Moreover, the water content is not related to SDI, as shown in Figure 1.5.17 (e) which indicates no trend between the two factors. This observation agrees with the results of Edwards Limestone (See Figure 1.5.6). Hence, there is a strong possibility that water content does not affect SDI values in relatively hard rocks. However, in clayey shale formations, which are discussed in later sections, close relationships have been observed between water content and SDI.

Figure 1.5.17 Austin Chalk: effect of water content on: (a) principal stress difference at three confining pressures, (b) principal stress difference of solid, slurry-soaked, and holed specimen at 1MPa, (c) principal stress difference of solid, slurry-soaked, and holed specimen at 2MPa, (d) principal stress difference of solid, slurry-soaked, and holed specimen at 3MPa, (e) slake durability index (SDI), and (f) elastic modulus

Other relationships

       Controlling relationship plots of the following properties were developed to better understand the principal stress difference, dry density, SDI, elastic modulus, and drying-duration

107

(Figure 1.5.18). Of the four sub-figures, only Figure 1.5.18 (c) displays appreciable trend between principal stress difference and elastic modulus. The principal stress difference and elastic modulus of Austin Chalk was also plotted in Figure 1.5.8 together with Edwards Limestone. The modulus ratio of Austin Chalk was measured ranging from 60 to 280, and the measured strength indicates that the Austin Chalk belongs to the lowest strength category. Interestingly, the data points of Austin Chalk are off the range of proposed Deere's Classification, thus the y-axis extended from 0.3 to 0.1 ksi. No relationships are noticeable between dry density and principal stress difference, slake durability index and principal stress difference, and drying-duration and elastic modulus. For interpretation of the test results, the data whose principal stress difference is 8 MPa is excluded because the data seems to be the outlier of the tests.

1.5.4 Clay Shales

Engineering overall properties of four clay shales (Del Rio Clay, Eagle Ford Shale, Taylor Marl, and Navarro Shale) were characterized in terms of the multi-stage triaxial test, slake durability test, and jar slake test. It is unlikely that one variable (e.g., drying-duration or water content) governs the properties of all four formations. It has been discovered that the strength of clay shales such as Taylor Marl and Navarro Shale were influenced by drying-duration, whereas that of Del Rio Clay and Eagle Ford Shale were not. Instead, water content shows appreciable relationship with strength in Del Rio Clay and Eagle Ford Shale. On the other hand, it was commonly observed for all clay shales that SDI was controlled not by drying-duration, but primarily by original water content of the specimen. The insensitivity of SDI to drying-duration is inherent because all the tested specimens were completely dried in the oven at the beginning of the slake durability test. Hence, SDI of the specimen that dried for 48 hours in room conditions is not different from the SDI of the non-dried specimen, as long as such drying does not cause changes in the physical or chemical properties of shales. Following sections discuss the engineering properties of clay shales in geological order from oldest to youngest.
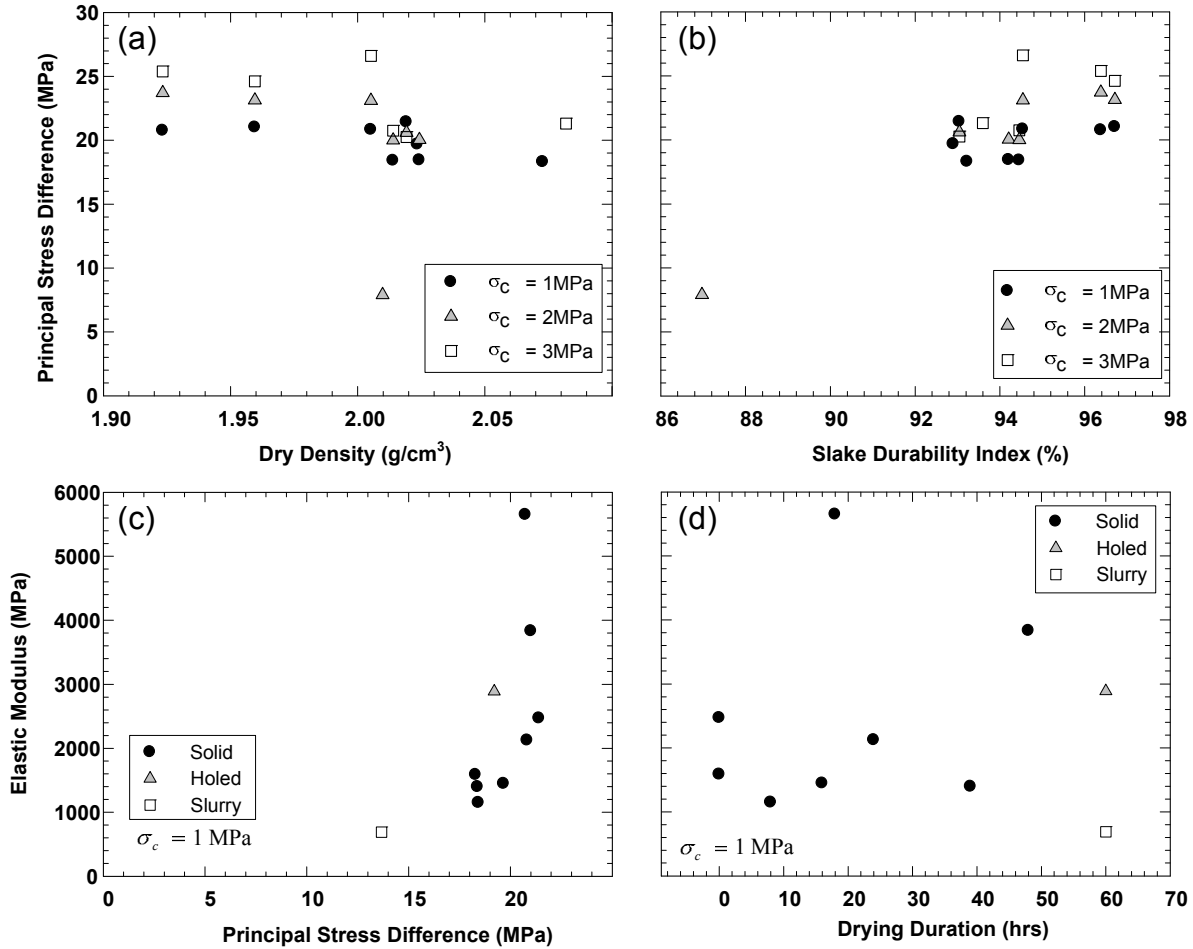
Figure 1.5.18 Austin Chalk : relationships between: (a) dry density and principal stress difference, (b) SDI and principal stress difference, (c) principal stress difference and elastic modulus, and (d) drying-duration and elastic modulus
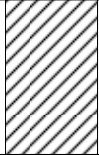
Del Rio Clay

The material properties of Del Rio Clay were measured using the multi-stage triaxial test, slake durability test, and jar slake test. The effects of drying-duration and water content on principal stress difference, durability (SDI), and elastic modulus were evaluated. It was found that both the strength and the SDI of Del Rio Clay are related to water content rather than drying-duration.

Del Rio Clay was deposited during the Cretaceous period, overlying Buda Limestone and underlying Georgetown Formation or Devils River Formation (see Section 1.3.2 for details of geology). Del Rio Clay cores were obtained at the project site of the Chandler Road Apartments located at Round Rock, Texas. According to the boring log in Figure 1.5.19, Del Rio Clay at the site underlies Buda Limestone, and is located 21.8 ft from the top of boring. The boring was terminated at 35 ft. The Del Rio Clay extended to this depth.. Water level at completion of drilling was measured at 2.7 ft below ground surface. The Del Rio Clay obtained is bluish green with low hardness and slightly fissile with shell fragments.

Figure 1.5.20 shows the container of Del Rio Clay cores and unwrapped cores. The cores were soft and had the feel of a stiff clay, but were not laminated as Eagle Ford Shale and Taylor

109

Marl. Judging by appearance, Del Rio Clay is quite different from Eagle Ford Shale and Taylor Marl in the sense that Del Rio Clay is rarely carbonated and much softer than other tested clay shales. Also, the grain size of Del Rio Clay is much finer than Navarro Shale. Indeed, the Del Rio Clay appears to be closer to stiff clay rather than clay shales. Nonetheless, Del Rio Clay is included in this study.

DEPTH, FT	SYMBOL	POCKET PEN, tsf / Blows/ft / Rec./ RQD, %	STRATUM DISCRIPTION SURF. ELEVATION: UNKNOWN	LAYER ELEV. DEPTH
			CLAY (CH), dark brown fat CLAY with sand, hard, w/abundant shell fragments and occasional rounded to subrounded chert gravel and limestone fragments (Alluvium)	
5			**Tan LIMESTONE**, weathered, moderately hard to hard, w/solution features, scattered marly seams and occasional pink zones. (Buda)	4.0
10			- 50% drilling fluid loss to termination depth -pink from 7.0 to 10.5ft w/clay filled solution features from 9.5 to 12.0ft	
15			**Gray LIMESTONE**, moderately weathered, hard, slightly nodular, moderately burrowd, glauconitic, w/numerous shell fragments and scattered dark gray discontinuities. (Buda) -tan from 12.5 to 13.0ft	12.0
20			-w/numerous dark gray clayshale seams from 19.7 to 21.8ft	
25			**CLAYSHALE,** bluish green, low hardness, slightly fissile, w/shell fragments. (Del Rio) -soft zone from 25.0 to 26.0ft	21.8
30			-limestone seam at 28.8ft	30.0

COMPLETION DEPTH: 35.0ft   WATER LEVEL / SEEPAGE: 5ft
DATE DRILLED: 10/09/06   UPON COMPLETION: 2.7 ft

Figure 1.5.19 Boring log of Del Rio Clay at project site of Chandler Road Apartments located at Round Rock, Texas (Provided by Fugro Consultants Inc.)

110

Figure 1.5.21 presents the relationship between drying-duration and percent water loss of each Del Rio Clay specimen. Percent water loss increases with increasing drying-duration, losing 46% of contained water after 48 hours of drying.

Figure 1.5.20 Del Rio Clay cores before sample preparation
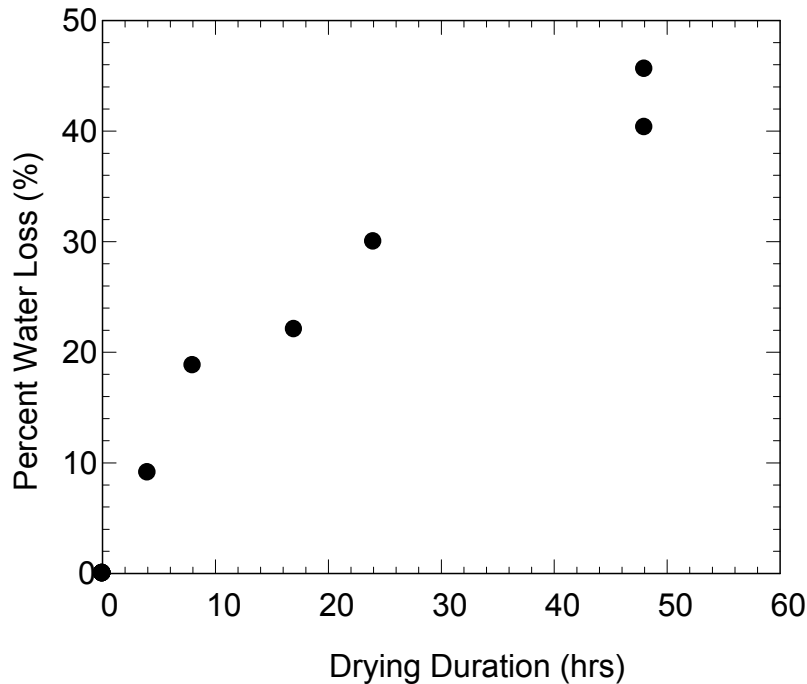
Figure 1.5.21 Percent water loss with drying-duration of Del Rio Clay

Effect of drying-duration on material properties

In Del Rio Clay, the principal stress difference decreases slowly with increasing drying-duration, as shown in Figure 1.5.22. One principal stress difference is measured to be near 1.2 MPa under 1 MPa confining pressure, far beyond the average trend. The specimen was found to contain the least water content, which results in the high strength (See Figure 1.5.27). Therefore, the data point was excluded and the principal stress difference declines slowly from 0.6 MPa for the non-dried specimen to 0.5 MPa for the 48-hour dried specimen. Nevertheless, the fact that

the specimen dried for 48 hours results in the highest strength because of the least water content indicates that the water content is a more crucial factor than drying-duration.

Del Rio Clay frequently shows ductile failure, which results in no failure plane but in bulging failure. Figure 1.5.23 presents a typical stress-strain relationship to Del Rio Clay, which was axially strained up to 6%. The specimen did not fail until that strain, but the resistance continued to increase indicating that bulging failure occurred (See Figure 1.5.23). Four failed specimens of Del Rio Clay are shown in Figure 1.5.24, displaying several cases of bulging failure. Bulging failure is typically represented by continuously increasing principal stress difference without reaching peak strength within the designed range of axial strain. Also, many bulging failures occurred locally at the middle, bottom, or top of the specimens without developing failure planes. In the calculation of principal stress difference, the area was corrected using volumetric and axial strain using the following equation (GCTS manual, 2007).

$$A_C = A_O \cdot \frac{1 - \varepsilon_V}{1 - \varepsilon_a} \qquad\qquad \text{Equation 1.5-1}$$

Where A_0 is the initial cross-sectional area of the specimen, ε_a is axial strain, and ε_v is a volumetric strain.
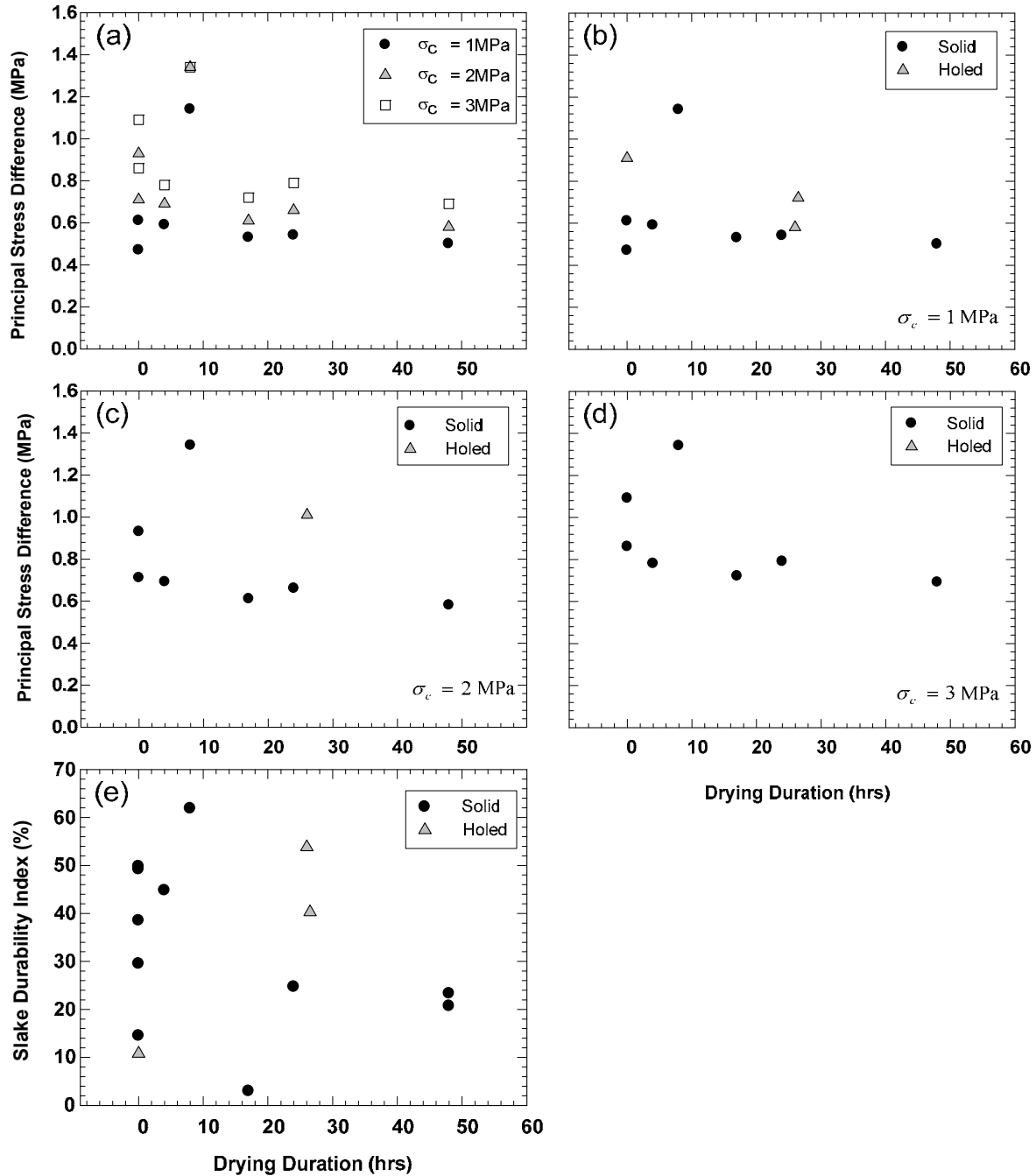
Figure 1.5.22 Del Rio Clay: effect of drying-duration on: (a) principal stress difference at three confining pressures, (b) principal stress difference of solid, slurry-soaked, and holed specimen at 1MPa, (c) principal stress difference of solid, slurry-soaked, and holed specimen at 2MPa, (d) principal stress difference of solid, slurry-soaked, and holed specimen at 3MPa, and (e) slake durability index (SDI)
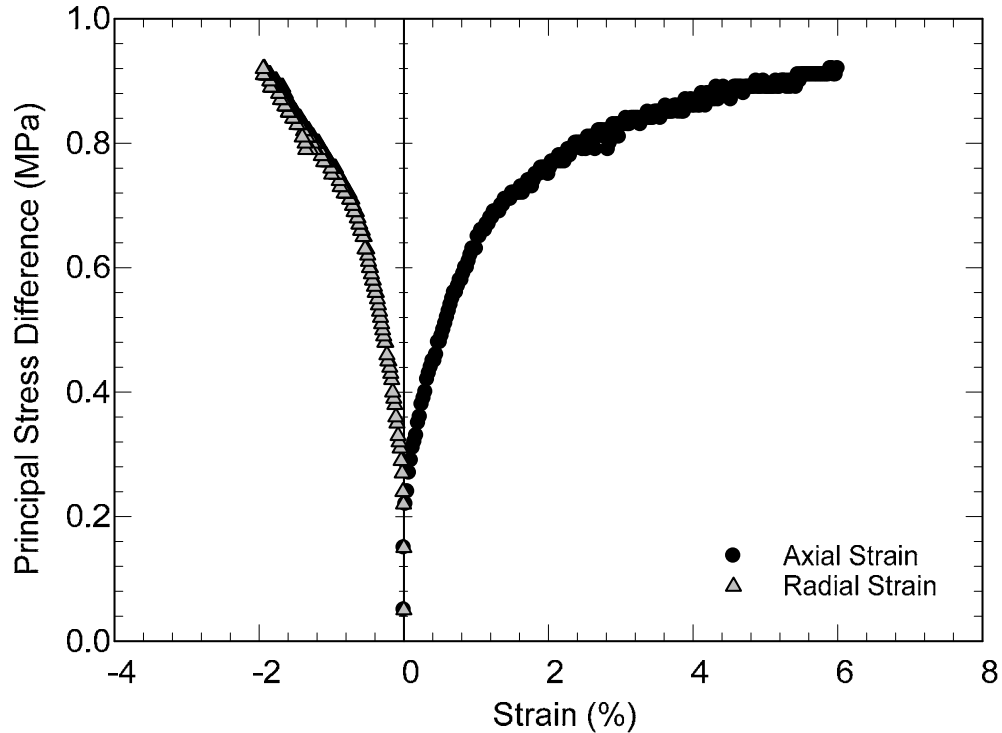
Figure 1.5.23 Stress-strain curve of Del Rio Clay (DRSNN2) which has not failed until 6% of axial strain

Figure 1.5.24 Failure modes of Del Rio Clay specimens

In addition to solid specimens, three holed specimens were tested to see the effect of the hole; holed specimens do not indicate any reduction due to the existence of the core hole. From these preliminary tests, it is determined that the existence of the hole does influence the strength of specimens over the effect of drying-duration or the effect of water content. Figure 1.5.25 displays a holed specimen that was dried for 24 hours, the hole of which was later clogged by collapsing surrounding shales under axial loading during triaxial tests.

A strength test on the slurry-soaked specimen was not possible due to the severe deformation of the specimen after soaking. Figure 1.5.26 presents Del Rio Clay before and after

the slake durability test. For this specific case, the tested specimen was dried for 48 hours, and the SDI of the specimen was measured to be 21%, indicating very low durability. Following the slake durability test, the Del Rio Clay degraded into several segments with high plastic clay at their surfaces. Figure 1.5.22 (e) presents the effect of drying-duration on SDI, and, again, the SDI was found to be independent of drying-duration in the Del Rio formation. The SDI of tested Del Rio Clay ranges from 14% to 61% and is generally classified as low durability.

Figure 1.5.25 Holed Del Rio Clay specimen before and after the multi-stage triaxial test

Figure 1.5.26 Del Rio Clay before and after two cycles of the slake durability test (DRM48N)

Effect of water content on material properties

Figure 1.5.27 presents the effect of water content on principal stress difference. Substantial decrease in principal stress difference is observed as water content rises. It is shown that the holed specimen displays higher strength due to relatively low water content. The strength tendency of holed specimens agrees well with solid specimens when principal stress difference is plotted against water content. This fact implies that water content, not drying-duration, is an important factor in the strength of Del Rio Clay. In addition, it is also shown that the SDI of Del Rio Clay is a function of water content. The measured SDI of Del Rio Clay ranges between 0% and 65%, with most test results falling below 50%, and the relationship is shown in Figure 1.5.27 (e). At water content as high as 22%, the SDI approaches zero after two cycles of slake durability tests. No relationship was found between water content and elastic modulus because the drying-duration critically affects the elastic modulus Figure 1.5.27 (f). This finding was duplicated for four clay shales.
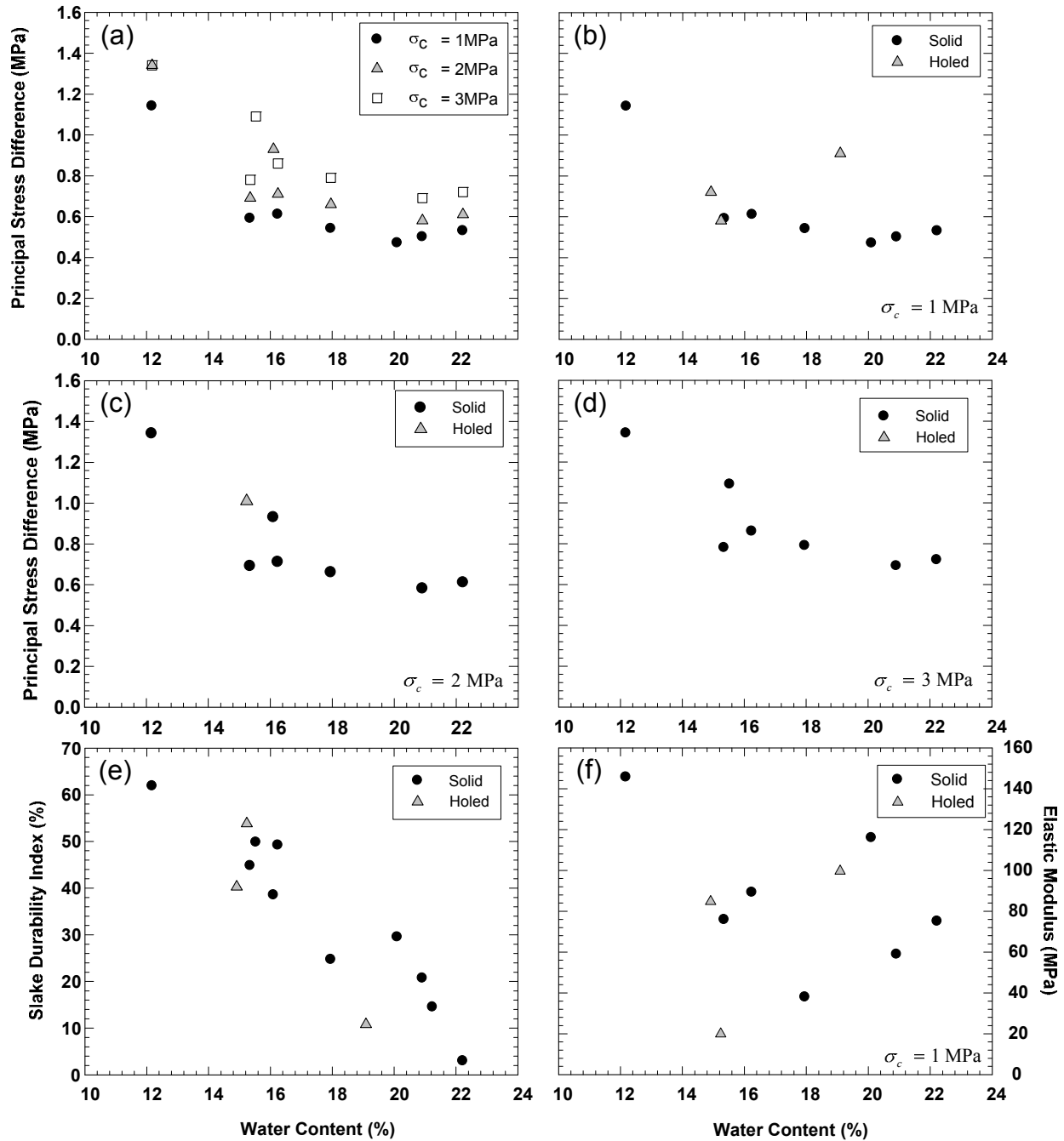
Figure 1.5.27 Del Rio Clay: effect of water content on: (a) principal stress difference at three confining pressures, (b) principal stress difference of solid, slurry-soaked, and holed specimen at 1MPa, (c) principal stress difference of solid, slurry-soaked, and holed specimen at 2MPa, (d) principal stress difference of solid, slurry-soaked, and holed specimen at 3MPa, (e) slake durability index (SDI), (f) and elastic modulus

Other relationships

Other relationships between parameters are shown in Figure 1.5.28 (a) through (d). The strength increases as the dry density of Del Rio Clay increases. The dry density of Del Rio Clay

116

varies extremely from 1.59 g/cm^3 to 1.95 g/cm^3, and the strength changes from maximum 1.1 MPa to minimum 0.5 MPa. The strength of the Del Rio formation was measured to be the lowest among tested shale formations. The SDI is likely to increase as principal stress difference increases, but the trend is not very clear. The elastic modulus variation of Del Rio Clay is shown in Figure 1.5.28 (c) and (d). It was expected that the elastic modulus increased with increasing principal stress difference, but several points are significantly off the trend line. An increase in drying-duration results in steep decrease in elastic modulus. The maximum elastic modulus of the specimen was observed at 8 hours of drying-duration, but this data point was excluded because the specimen contains much less water content. Excluding the data point, the plot follows a more logical declining trend (Figure 1.5.28 (d)). The structure of Del Rio Clay is believed to be destroyed by wetting and drying, resulting in low stiffness of the specimen. The destruction of the structure was not proven in this research. Decrease in elastic modulus with increasing drying-duration is a common finding in other tested shales (see Figure 1.5.28, Figure 1.5.40, Figure 1.5.52, and Figure 1.5.63).

Figure 1.5.29 presents slightly modified classification charts proposed by Deere (1968) showing the data points of the four tested clay shales. The range of Young's modulus and UCS were re-arranged to fit the data range because the measured UCS and Young's modulus of the four clay shales were very low. The test results of dried specimens were excluded to eliminate the effect of drying-duration; thus all plotted data points were from tests on fresh specimens. All four clay shales belong to Class E – very low strength; and the modulus ratio for Del Rio Clay was approximately 200, which falls in the boundary between average and low modulus ratio.
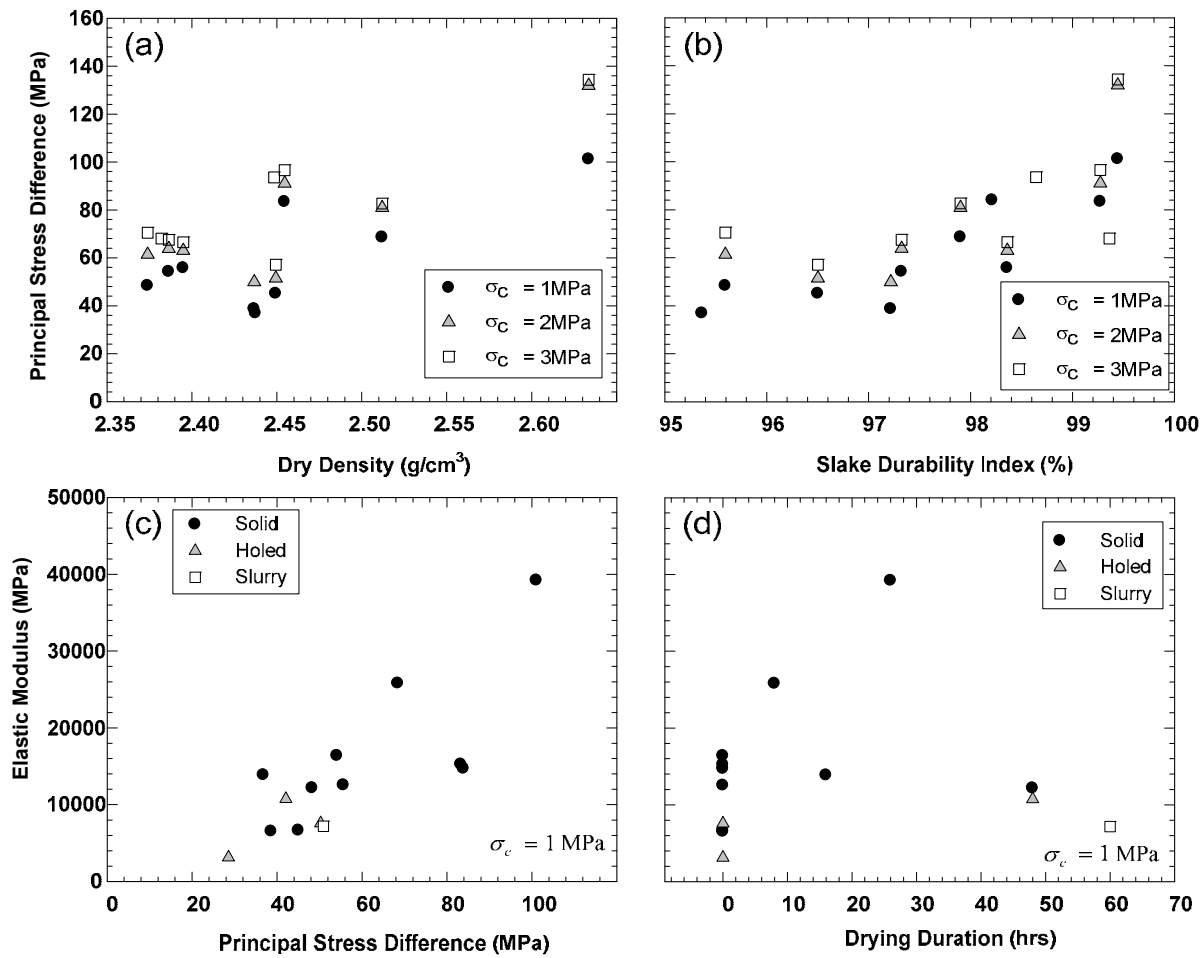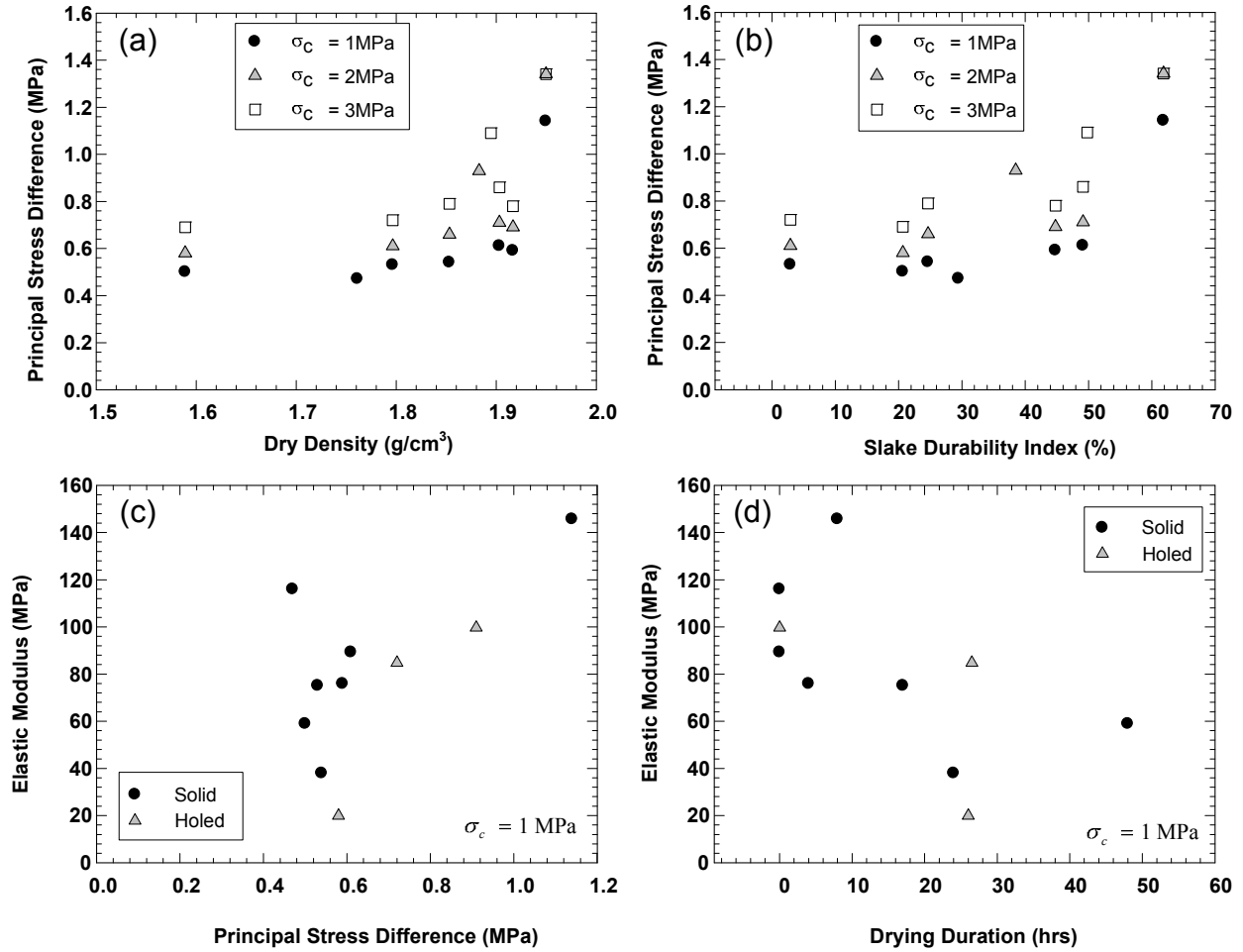
Figure 1.5.28 Del Rio Clay: relationships between: (a) dry density and principal stress difference, (b) SDI and principal stress difference, (c) principal stress difference and elastic modulus, and (d) drying-duration and elastic modulus
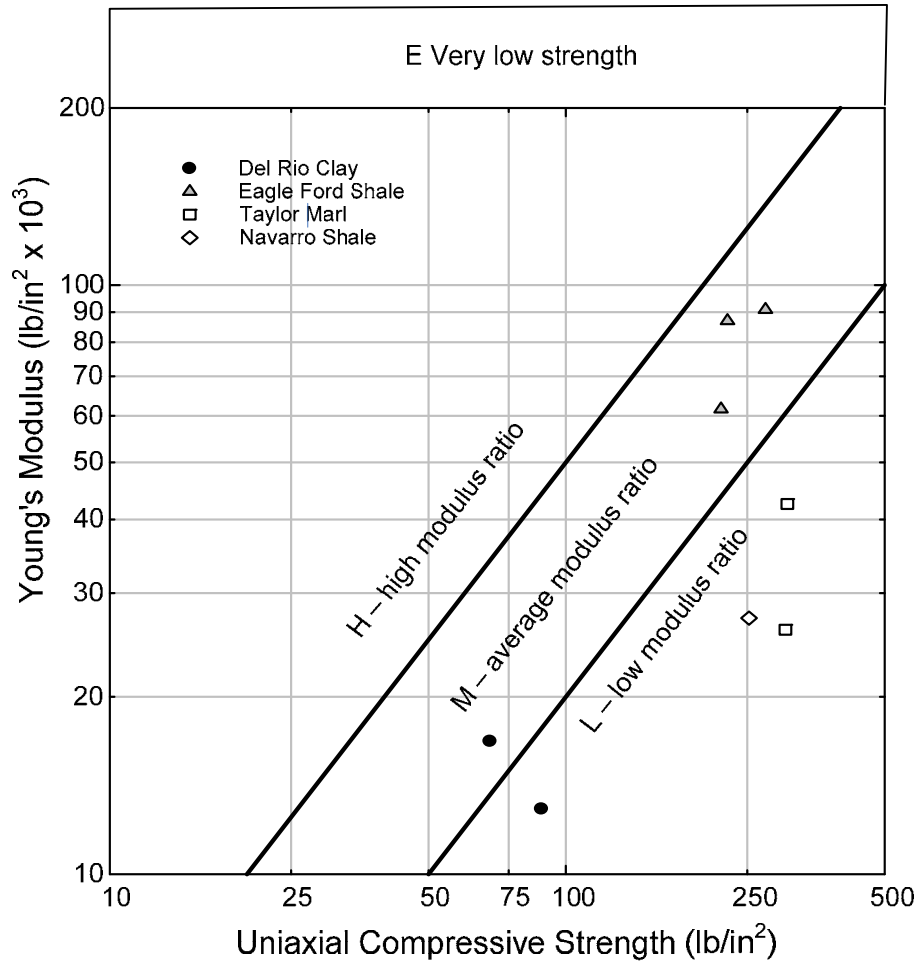
Figure 1.5.29 Engineering classification of Del Rio Clay, Eagle Ford Shale, Taylor Marl, and Eagle Ford Shale on the classification chart (modified from Deere, 1968)

Jar slake test

From Figure 1.5.30, it was discovered that Del Rio Clay degrades significantly if dried for 4 hours or more. The numbers shown in each figure represent slake modes of chart classification proposed by Walkinshaw and Santi (1996). Although the fresh specimen did not disintegrate under the water, considerable slaking started developing in the specimen dried for 4 hours. Eight hours of drying led to the state in which disintegration of the specimen is appreciable, and specimen crumbling is extreme. This observation indicates that drilled shafts constructed in this formation should be filled with concrete no later than 4 hours after drilling holes. Otherwise, the verification core wall may slake severely and collapse inward if water inflow is expected.

119
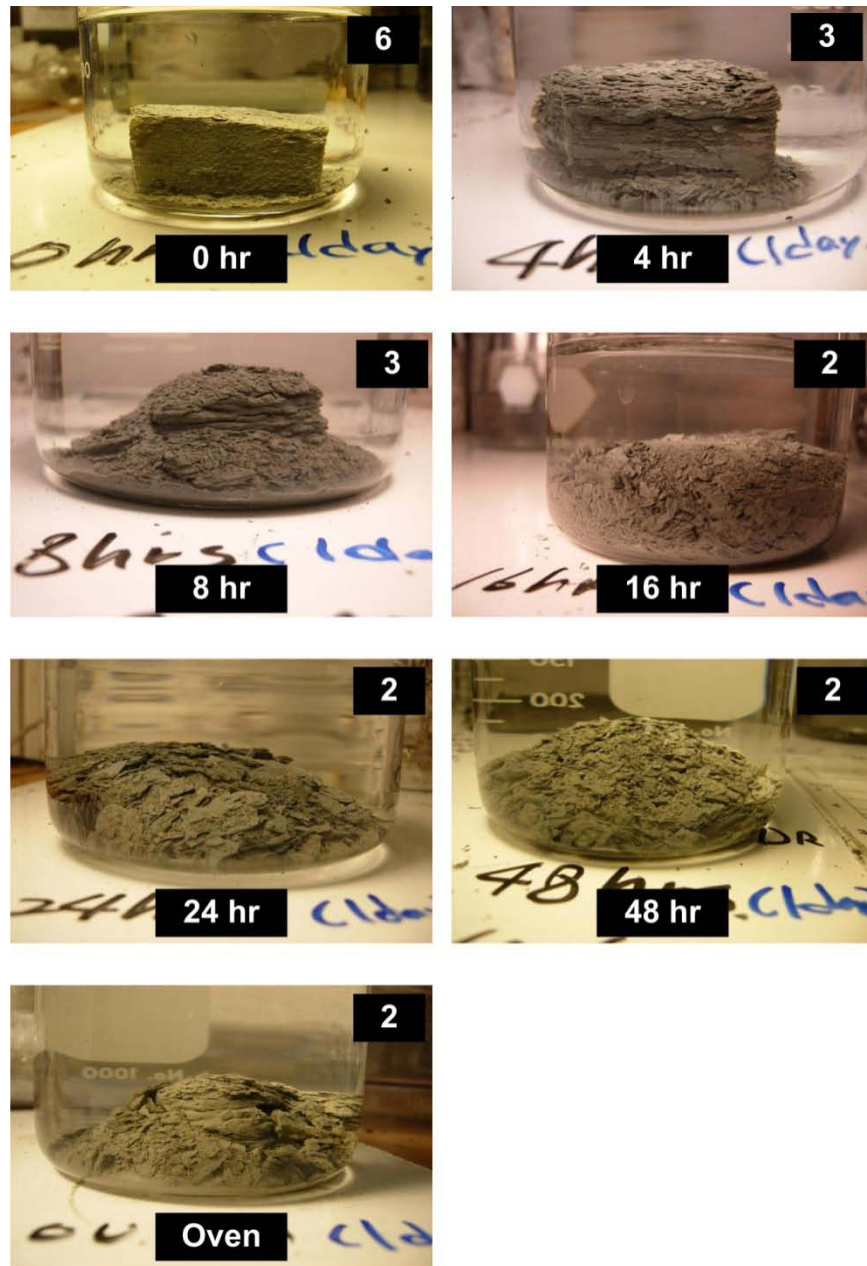
Figure 1.5.30 Jar slake test on Del Rio Clay after one day of soaking: numbers represent chart classification (Figure 4-24)

Eagle Ford Shale

Laboratory test results of Eagle Ford Shale are presented in this section. Eagle Ford Shales are upper Cretaceous clay shales, typically overlain by Austin Chalk or Taylor Marl, and underlain by Woodbine formation (see Section 1.3.2 for details of geology). Tested Eagle Ford Shale was obtained at State Highway 360 near Mansfield, Texas; the boring location is the same

site where the field scale condition test took place as described in Section 1.6. The boring log of the obtained cores is shown in Figure 1.5.31. Highly plastic clay overlies gray tan, shaly clay, which overlies Eagle Ford Shale. Ground water table was encountered at a depth of 17 ft during drilling. The cores prior to specimen preparation are shown in Figure 1.5.32. The Eagle Ford Shale was regarded as fresh at the moment the samples were unpackaged in the lab. The surface of the cores was moist, and no cracks were observed. However, horizontal cracks in the bedding plane started developing within a few hours of exposure to air drying.

Like other tested formations, Eagle Ford Shale was dried for 0 to 48 hours in the laboratory. Figure 1.5.33 presents the ratio of water loss to the total contained water at different drying-duration. This indicates that Eagle Ford Shale lost as much as 60% of its water content after 48 hours of air drying. The contained water evaporated rapidly upon exposure to air; the evaporation rate gradually decreased as drying-duration increased. Thus, approximately 32 % of water evaporated after 16 hours of drying and 60% after 48 hours of drying. It is expected that the moisture content of the specimen reaches equilibrium in laboratory conditions within a few days of exposure to air. The evaporation rate is the second highest of the tested formations, after Austin Chalk (See Figure 1.5.10). It should be pointed out that data points in the figure result from different dried specimens, not from a single specimen; hence the evaporation rate shown in the figure represents all the tested Eagle Ford Shale cores. Figure 1.5.34 presents a typical stress-strain curve of Eagle Ford Shale. The stress-strain curve was obtained from a single-stage triaxial test performed under 2 MPa confining pressure.

DEPTH, FT	SYMBOL	POCKET PEN, tsf / Blows/ft / Rec./RQD, %	STRATUM DISCRIPTION	LAYER ELEV. DEPTH
			SURF. ELEVATION: UNKNOWN	
5			**CLAY (CH)**, tan, soft to very stiff. moist. with few calcareous nodules	
10				13.0
15			**SHALY CLAY (CH)**, gray and tan, very stiff to hard moist to water bearing	
20		RC 1 20'-26' 100/100	**SHALE**, gray, soft, moist	17.0
25			Bentonite seam from 23.6 – 24.0 ft	

COMPLETION DEPTH: 36.0
DATE DRILLED: 1-18-07

WATER LEVEL / SEEPAGE: 17.0

Figure 1.5.31 Boring log of Eagle Ford Shale at State Highway 360 near Mansfield, Texas (provided by Fugro Consultants Inc.)

Figure 1.5.32 Eagle Ford cores prior to sample preparation

Effect of drying-duration on material properties
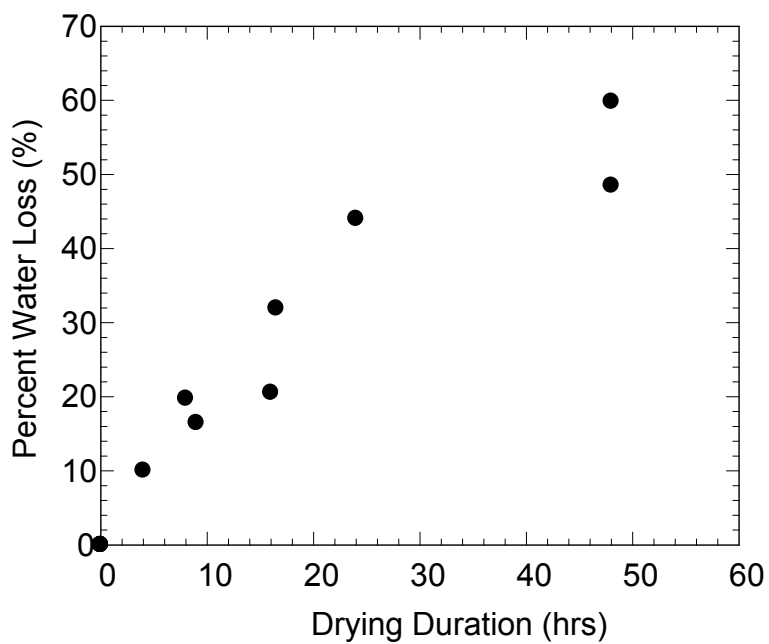
Figure 1.5.33 Percent water loss with drying-duration of Eagle Ford Shale
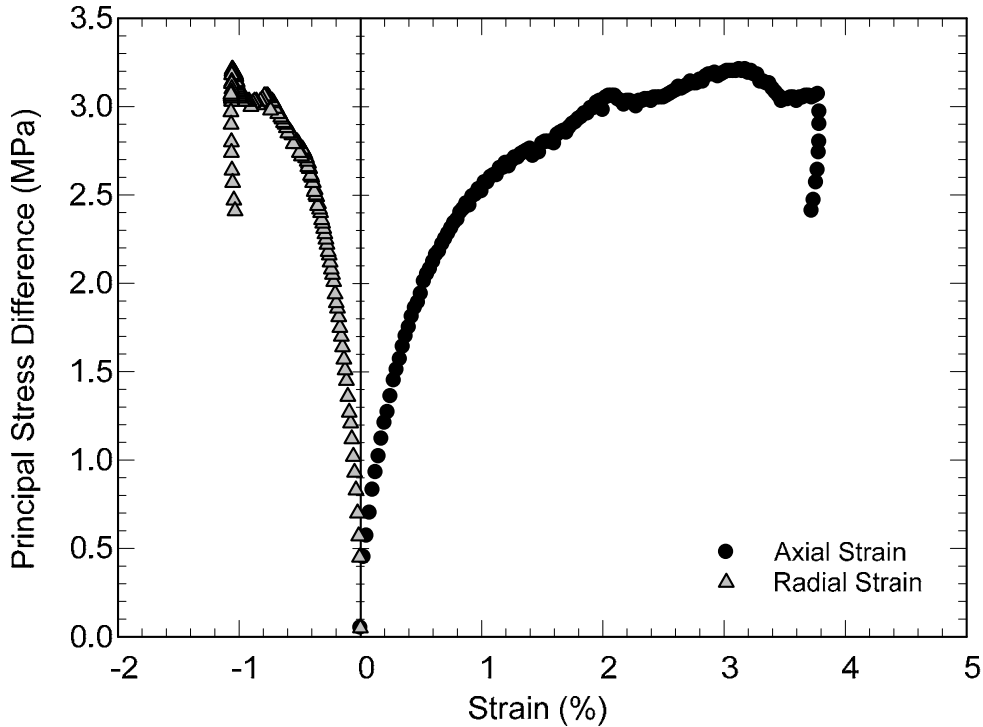
Figure 1.5.34 Typical stress-strain curve of Eagle Ford Shale (EFSNN2)

The drying-duration effect on both principal stress difference and SDI are displayed in Figure 1.5.35. Figure 1.5.35 (a) presents the principal stress difference of a solid specimen at three different confining pressures, which indicates that the principal stress difference of a dried specimen does not decrease as drying-duration increases. The strength of Eagle Ford Shale was not influenced by one cycle of drying and wetting, although outcropped Eagle Ford Shale at the site showed signs of weathering with time as a result of water and direct sunlight. In particular, the specimen that dried for 48 hours lost 60% of contained water, was re-wetted and no difference in strength was observed. Indeed, one cycle of drying and wetting resulted in observed horizontal cracks along specimens without notable weakening, but the failure modes of tested specimens were found to be either by vertical tensile failure or shear failure propagating in a diagonal direction in the specimen (Figure 1.5.36). Therefore, the horizontal cracks may have little effect on the compressive strength of Eagle Ford Shale when loading direction is perpendicular to cracks.

In addition to the solid specimen, a holed specimen and slurry-soaked specimen were tested to investigate the effect of hole and slurry use. Figure 1.5.35 (b) through (d) presents the variation of principal stress differences with drying-duration at 1MPa, 2MPa, and 3MPa confining pressures. For Eagle Ford Shale, unlike other formations, holed specimens were tested for various drying-durations. The results on the holed specimen indicate that the principal stress difference is independent of the drying-duration, like solid specimens. One holed specimen before and after testing is shown in Figure 1.5.37. Failure modes of the specimen appear to be a combination of tensile failure and shear failure. Similarly, placing the specimen under slurry for 12 hours did not impact the strength of the specimen. In fact, the slurry-soaked specimens has slightly higher strengths than solid specimens. Although it may be premature to conclude that slurry usage does not affect the strength of Eagle Ford Shale, this finding indicates that the expected reduction in strength is negligible compared to other factors such as spatial variability.

124

Figure 1.5.38 shows the Eagle Ford Shale fragments before and after the slake durability test. The ten representative chunks degraded into small and larger chips after two cycles of slake durability testing. It seemed that the clay matrix contained in the specimen was washed away during the test leaving the stiff portion of the sample. Although the figure indicates that the specimen disintegrated severely after the slake durability test, the SDI is calculated to be as high as 72.5% indicating that these fragmented and degraded shales are medium durable. This is due to the limitation of the slake durability test; the weight of all chips retained in the 2 mm screen size drum is included as the weight of durable rock. Thus, the SDI may not represent durability, especially when stiff lumps of clay shales are larger than 2 mm. As was expected, the SDI was independent of drying-duration (Figure 1.5.35 (e)).
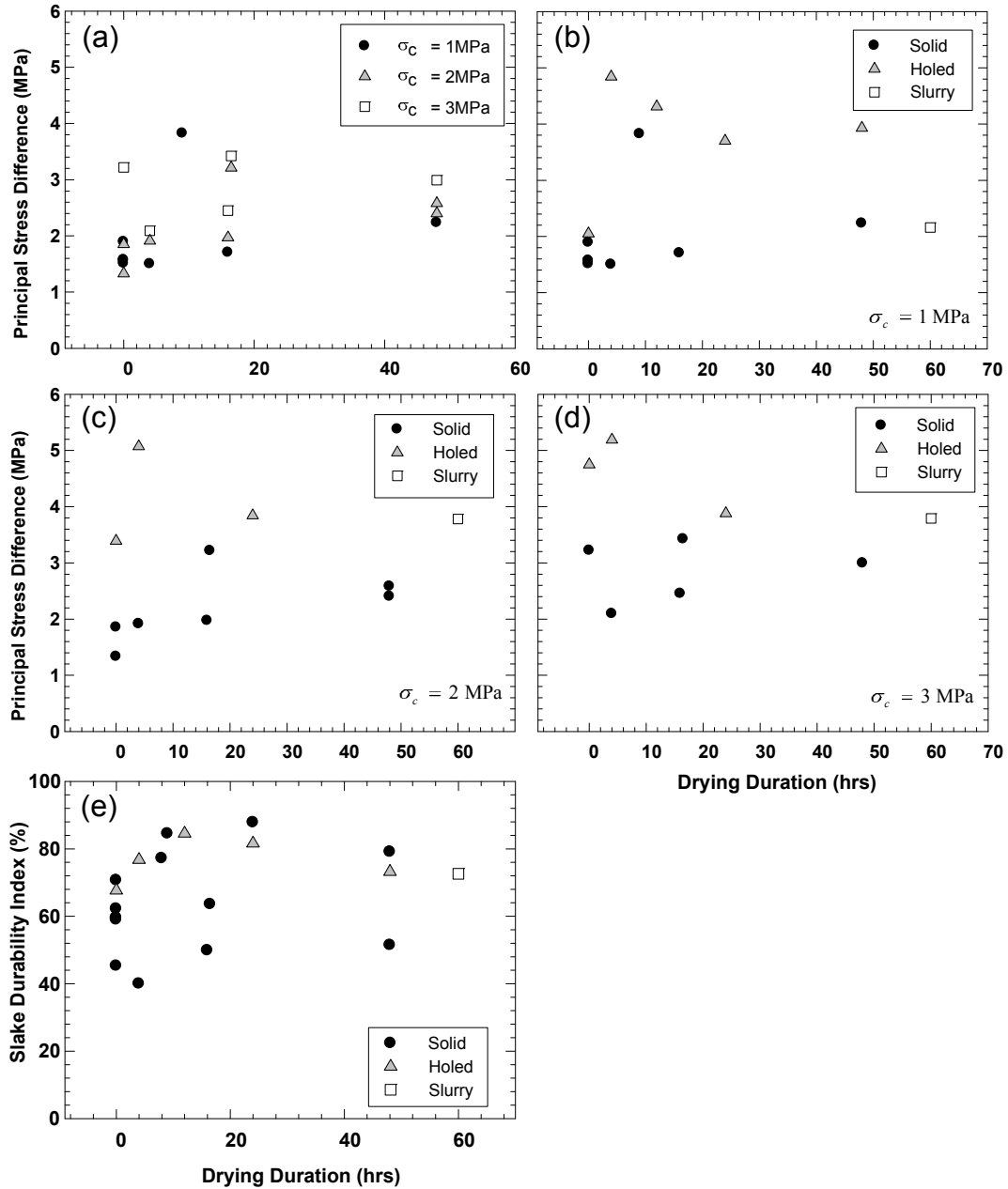
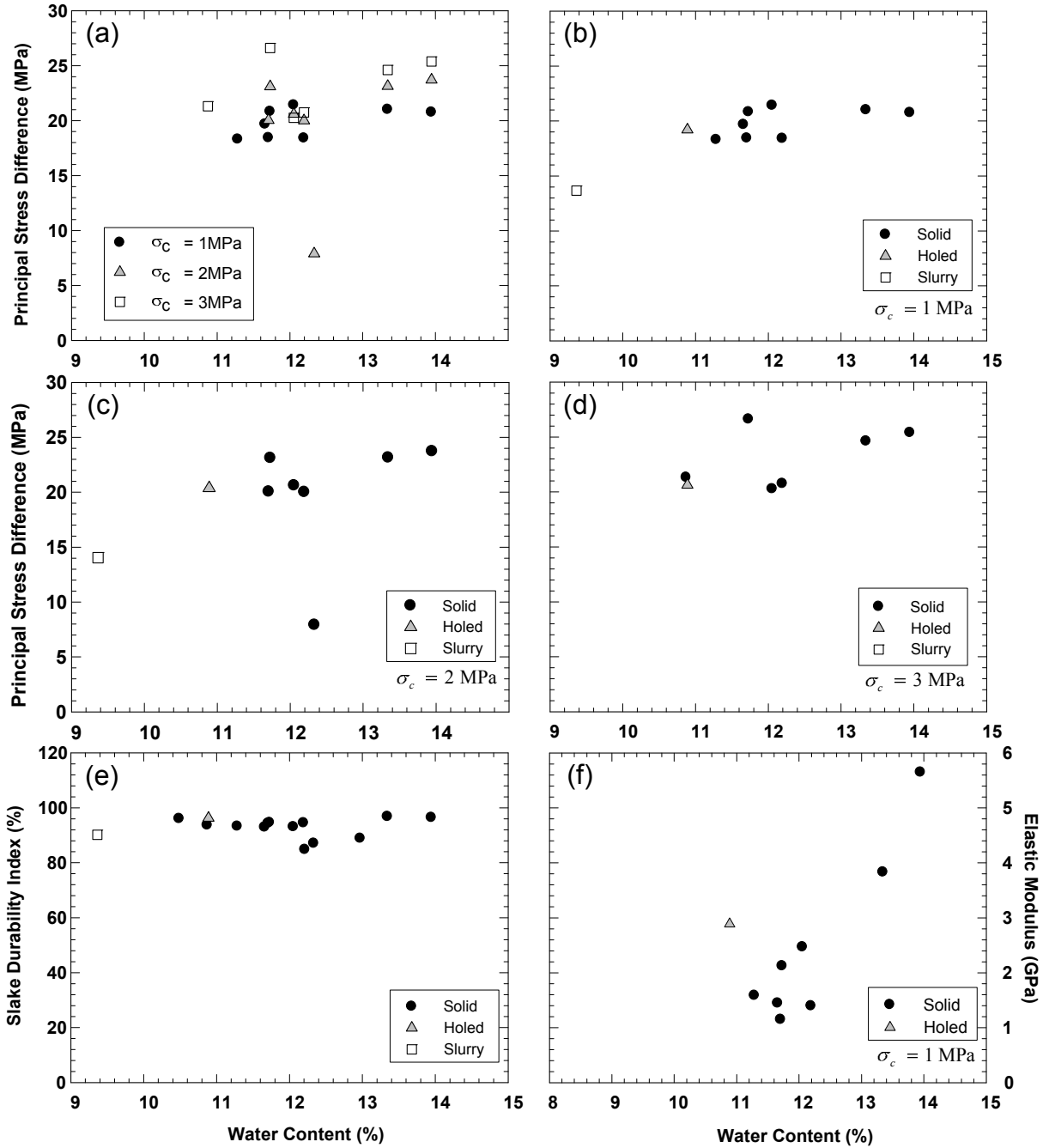*Figure 1.5.35 Eagle Ford Shale: effect of drying-duration on: (a) principal stress difference at three confining pressures, (b) principal stress difference of solid, slurry-soaked, and holed specimen at 1MPa, (c) principal stress difference of solid, slurry-soaked, and holed specimen at 2MPa, (d) principal stress difference of solid, slurry-soaked, and holed specimen at 3MPa, and (e) slake durability index (SDI)*

Figure 1.5.36 Failure modes of Eagle Ford Shale after multi-stage triaxial tests
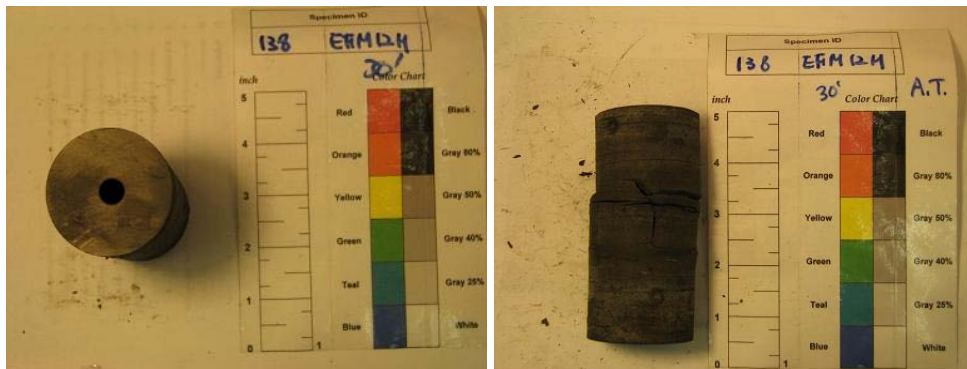
Figure 1.5.37 Holed Eagle Ford Shale specimen before and after the multi-stage triaxial test

Figure 1.5.38 Eagle Ford Shale before and after the slake durability test (EFMSN)

Effect of water content on material properties

Results of multi-stage triaxial tests and slake durability tests are plotted against measured water content in Figure 1.5.39. Interestingly, principal stress difference tends to decrease as water content rises from 15% to 21%. It is evident that the principal stress difference of Eagle Ford Shale is controlled by water content of tested specimens rather than drying-duration. The importance of water content in understanding the strength of Eagle Ford Shale is well-explained by the following example: physically, it is unlikely that the strength of a holed specimen is greater than that of a solid specimen, but it occurred in this study (Figure 1.5.35 (b) – (d)). This

127

phenomenon can be explained from Figure 1.5.39 (b) through (d), which displays that holed specimens contain less water, resulting in higher strength. It was found that, regardless of its being a solid, holed or slurry-soaked specimen, the strength of Eagle Ford Shale is significantly influenced by the water content of the tested specimens. Hence, the effect of water content compensates for possible degradation caused by drying and wetting, meaning that the influence of drying and wetting might be negligible compared to the effect of water content. However, the relationships between SDI and water content were found to be weak, as shown in Figure 1.5.39 (e). As pointed out previously, the mesh size of the rotating drum is likely to contribute to the scatter in the graph.

Other relationships

In this section, other relationships among parameters are discussed in addition to the effect of water content and drying-duration. In Figure 1.5.40 (a), dry density is plotted against principal stress difference. Typically, principal stress difference is directly related to dry density such that heavier rock tends to be stronger; however, this fact is not applicable to Eagle Ford Shale. The SDI is positively but weakly related to the principal stress differences.

Elastic modulus is a significant factor that affects the point bearing capacity of drilled shafts by influencing the axial displacements. Softer behavior of the founding material at the shaft tip results in larger displacement for the same axial load. Figure 1.5.40 (c) and (d) displays the relationship between (c) elastic modulus and principal stress difference and (d) elastic modulus and drying-duration. The figures reveal that the elastic modulus of Eagle Ford Shale plunges when the specimen undergoes even a short period of air drying, and the reduction rate rapidly flattens out as drying-duration increases. This finding may be attributed to the fact that wetting of the specimen and/or development of horizontal fractures significantly softens the once-dried region. The graphs include test results only of 1 MPa confining pressure because the elastic moduli of higher confining pressure are measured from the specimen that underwent unloading and reloading during multi-staged tests. The modulus of fresh Eagle Ford Shale without drying was measured to be near 400 to 600 MPa, but the modulus dropped drastically below 200 MPa when the clay shales were dried for 4 hours. This finding describes that drying the specimen for as short as 4 hours may reduce elastic modulus by one-fourth. This is quite important because drying-duration may affect the bearing capacity of the drilled shafts by limiting displacement, not by ultimate load. According to Deere's classification, Eagle Ford Shale classifies as an average modulus ratio. (see Figure 1.5.29).

A slurry-soaked specimen is excluded from this discussion because specimens exposed to slurry may cause changes in the specimen water content as well as affect chemical bonds among sample particles.

Jar slake test

To review the test procedure and durability classification, refer to "Jar Slake Test" in Section 1.4. Figure 1.5.41 exhibits Eagle Ford Shale specimens at the completion of jar slake tests when the specimens were dried for different durations. The numbers in the figure indicate the category of the specimens determined according to jar slake test charts. Severe disintegration starts occurring in the cubical specimens when they are dried for more than 8 hours. The converse was true for Eagle Ford Shale that was submerged for 1 day when the specimen had not been dried. Only one crack was observed at the face of the specimen that had been dried for 4 hours, and more cracks developed in the specimen with 8 hours of drying. Much debris flaked

off from the cubic sample and more severe slaking was observed when the specimen was dried longer than 8 hours. This finding implies that the degradation may be severe when the Eagle Ford Shale at the verification core hole is dried for more than 8 hours and is wetted even for as few as 30 minutes. In fact, the wetting duration does not affect the durability of clay shales significantly, as observed during the jar slake test.
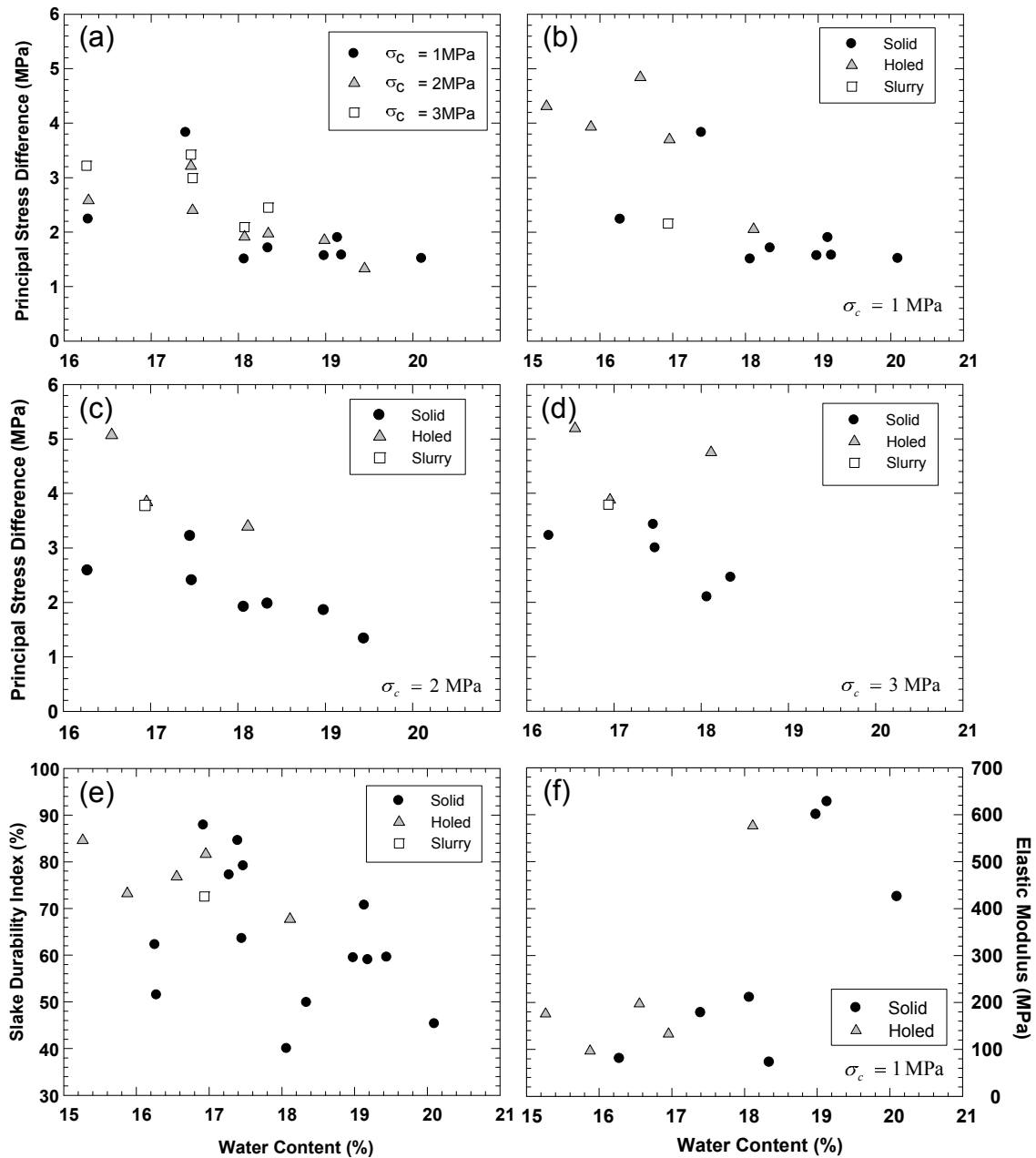
Figure 1.5.39 Eagle Ford Shale: effect of water content on: (a) principal stress difference at three confining pressures, (b) principal stress difference of solid, slurry-soaked, and holed specimen at 1MPa, (c) principal stress difference of solid, slurry-soaked, and holed specimen at 2MPa, (d) principal stress difference of solid, slurry-soaked, and holed specimen at 3MPa, (e) slake durability index (SDI), and (f) elastic modulus
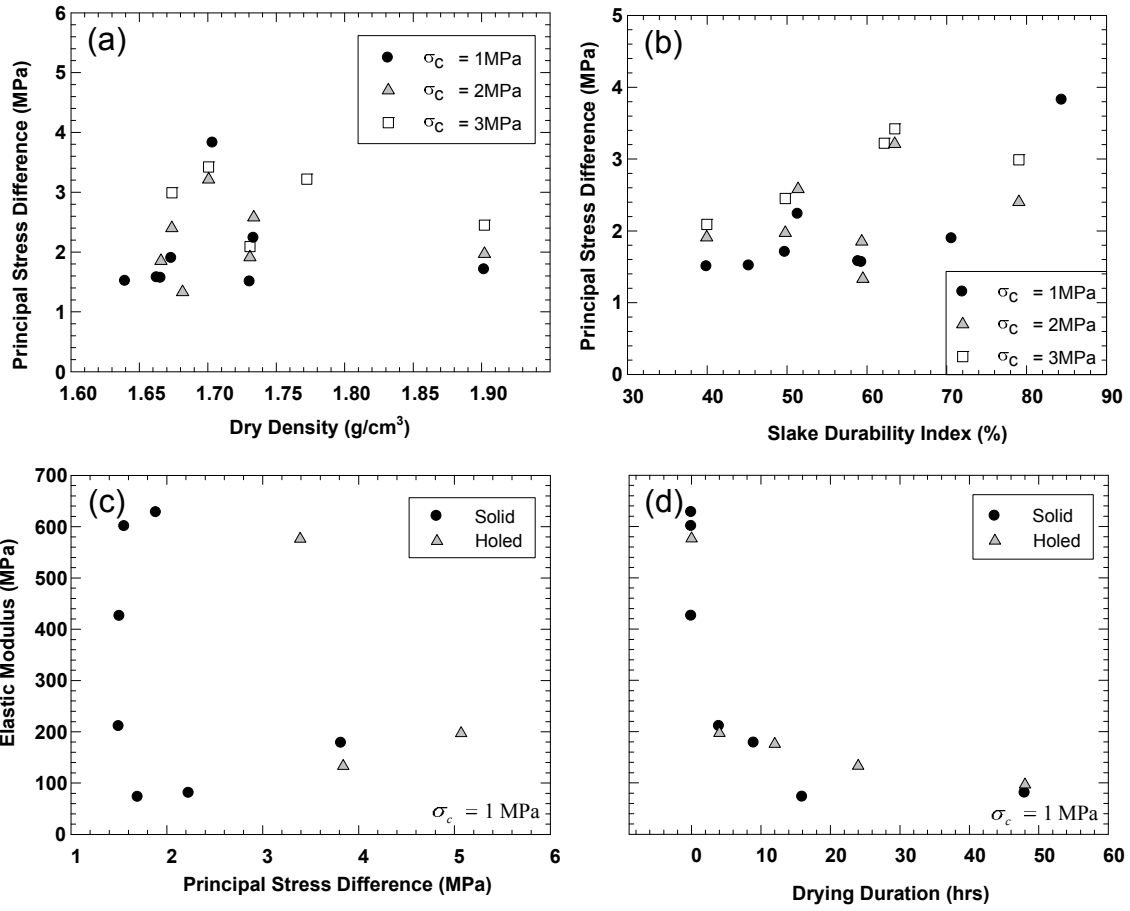
Figure 1.5.40 Eagle Ford Shale: relationships between: (a) dry density and principal stress difference, (b) SDI and principal stress difference, (c) principal stress difference and elastic modulus, and (d) drying-duration and elastic modulus
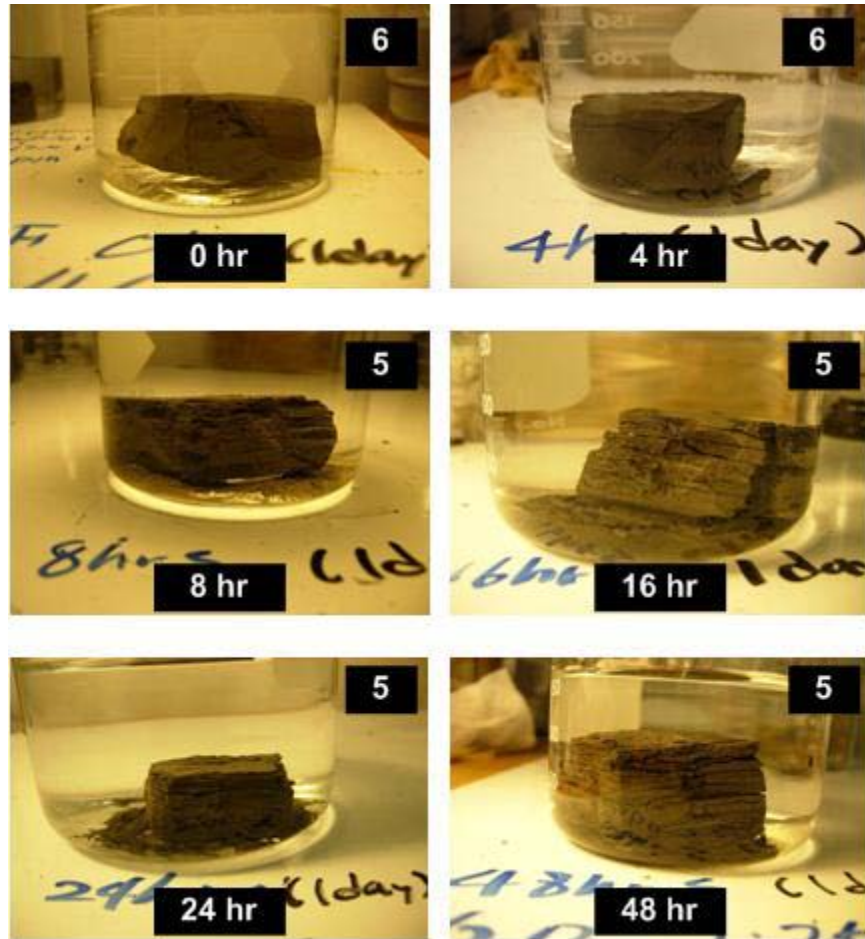
Figure 1.5.41 Results of the jar slake test on Eagle Ford Shale after one day of soaking: numbers represent chart classification (Figure 4-24)

Taylor Marl

Taylor Marl was deposited in the late Cretaceous era and is underlain by Austin Chalk and overlain by the Navarro group (see Section 1.3.2 for details of geology). A significant amount of carbonate content improves the strength properties of the marls. Figure 1.5.42 displays the preserved Taylor Marl cores in a container (left) and the core drawn out from a plastic bag (right). Taylor Marl looks slightly grayer than Eagle Ford Shale, but apparent characteristics such as hardness, touch, and fissility are very similar to Eagle Ford Shale. In this study, overall properties of Taylor Marl were found to be very different from those of Eagle Ford Shale. Specifics of test results are provided in this section.

131

Figure 1.5.42 Taylor Marl cores prior to sample preparation

The percent of water loss of each specimen is plotted against drying-duration in Figure 1.5.43. The evaporation of the contained water gradually increases over 24 hours, and the evaporation rate slightly flattens from 24 hours to 48 hours, showing that about 40 % of contained water evaporates during 48 hours of drying. Single and multi-stage triaxial tests were performed on Taylor Marl, and one typical stress-strain curve from the single-stage triaxial test under 1 MPa confining pressure is displayed in Figure 1.5.44. Figure 1.5.45 presents the boring log of Taylor Marl created by Fugro Consultants Inc. According to the boring log, Taylor Marl is found at a depth of 49.3 ft and is overlain by weathered shale.
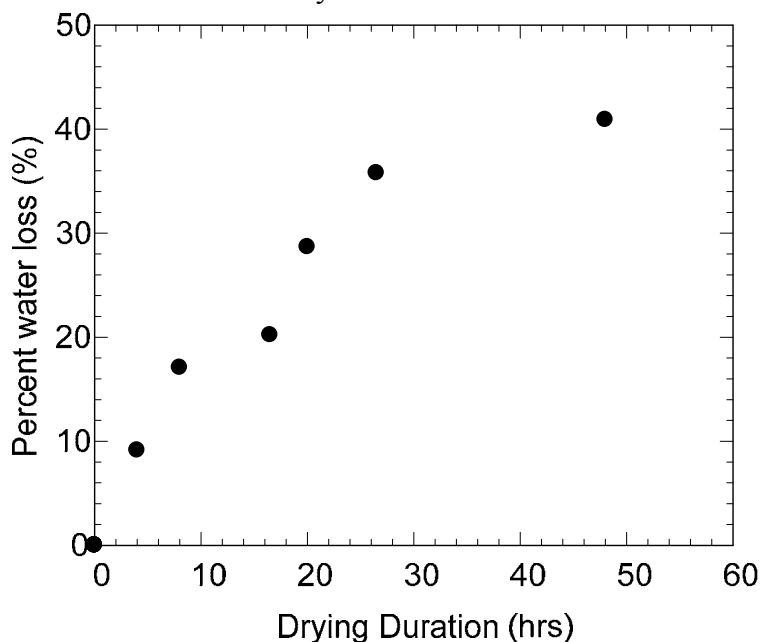
Figure 1.5.43 Percent water loss with drying-duration of Taylor Marl

132
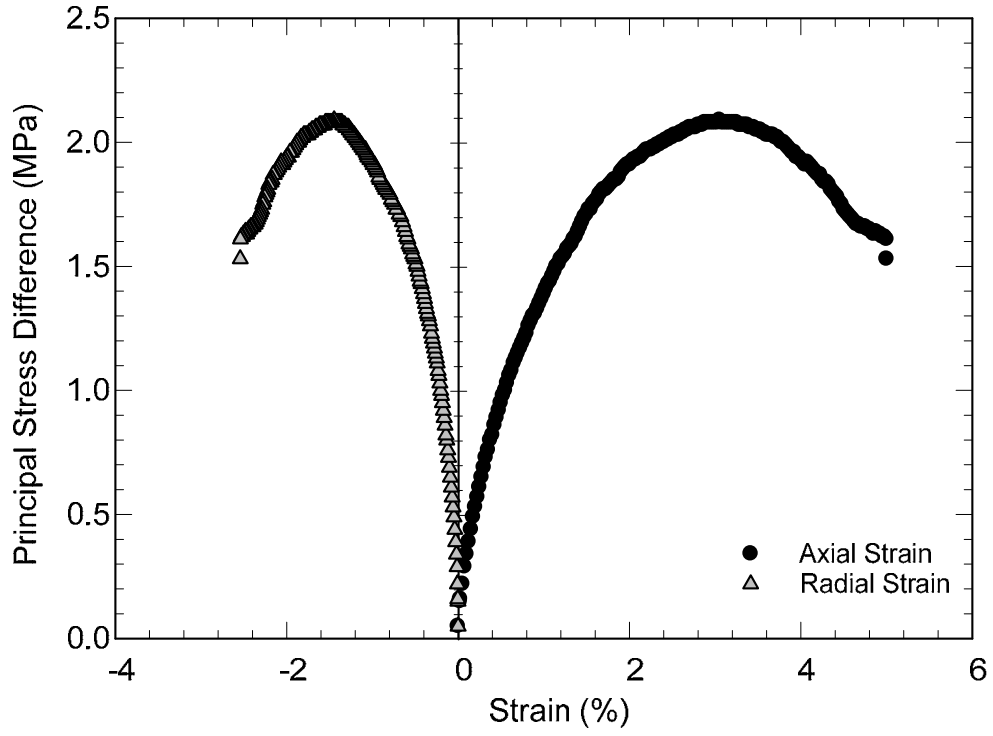
Figure 1.5.44 Typical stress-strain curve of Taylor Marl (TMSNN1)

DEPTH, FT	SYMBOL	POCKET PEN, tsf Blows/ft Rec./ RQD, %	STRATUM DISCRIPTION SURF. ELEVATION: UNKNOWN	LAYER ELEV. DEPTH
		P 2.0 - 4.0	**CLAY (CH),** medium stiff to very stiff, dark gray, gray, few organics	
				5.5
		P 2.0 - 2.5	**CLAY (CH),** stiff, brown, light brown	
				8.5
10		P 3.25	**WEATHERED SHALE,** highly to completely weathered, very soft, light brown, light gray, calcareous, fissile (locally known as SHALY CLAY)	
20		P 4.5+		
				29.0
30			**WEATHERED SHALE,** moderately to highly weathered, very soft, brown, gray, dark gray, calcareous, fissile	
40		P 4.5+		
				42.5
			WEATHERED SHALE, slightly to moderately weathered, very soft to soft gray, dark gray, brown, calcareous, fissile	
				49.3
50			**SHALE,** soft to medium hard, dark gray, calcareous, fissile	
60			Note: The shale core was obtained up to 71ft	

COMPLETION DEPTH: 71.0
DATE DRILLED: 12-6-06

WATER LEVEL / SEEPAGE: DRY
UPON COMPLETION: NOT MEASURED

Figure 1.5.45 Boring log of Taylor Marl at the intersection of County Road 398 and County Road 447, Princeton, Texas (provided by Fugro Consultants Inc.)

Effect of drying-duration on material properties

It was determined that the strength of Taylor Marl is significantly influenced by drying-duration. Figure 1.5.46 presents the effect of drying-duration on principal stress difference and on SDI at different confinement and specimen conditions. It is clearly shown that the strength declines the longer the specimens dry. The principal stress difference of solid specimens under 1 MPa confinement slightly exceeds 2 MPa, whereas the strength dropped down to 1.3 MPa at 24 hours of drying. The principal stress difference increases slightly to 1.5 MPa for 48 hours of drying, but the declination of the strength is obvious, as shown in Figure 1.5.46 (a). The dependency of strength on confining pressure does not appear to be considerable. Four representative failure modes for Taylor Marl specimens are displayed in Figure 1.5.47: 1) shear plane failure, which is likely to occur if the specimen is homogeneous such that local failure does not occur, 2) local bulging failure, and 3) the combination of vertical tensile failure, shear failure, and bulging failure.

Holed and slurry-soaked specimens were tested and the results are shown in Figure 1.5.46 (b) through (d). The effect of the hole was found to be negligible by comparing the strength of the holed specimen to that of solid specimens; yet the effect of drying-duration was determined to be significant in holed specimens as well. It should be noted that this preliminary conclusion on the holed specimen was made based on three test results. The slurry-soaked specimen that was submerged under water for 12 hours becomes weaker than fresh solid specimen. The results of slurry-soaked specimens were plotted at at 60 hours of drying-duration of the figure for comparison. The Figure 1.5.49 exhibits the slurry-soaked specimen for 12 hours, and the appearance of which was similar to other solid specimens, except for possible high moisture content near the specimen surface as a result of adsorbing water from slurry.
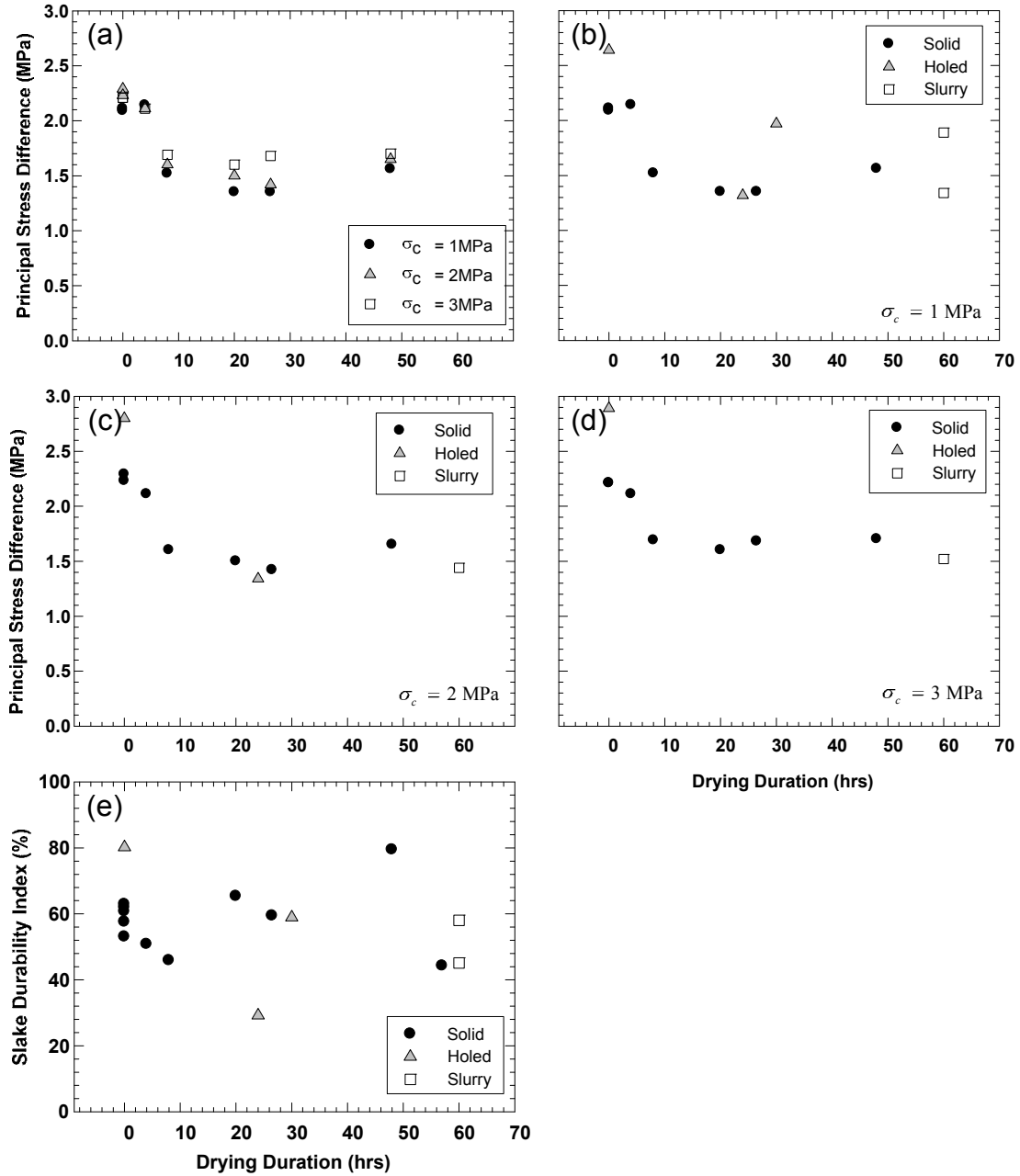
Figure 1.5.46 Taylor Marl: effect of drying-duration on: (a) principal stress difference at three confining pressures, (b) principal stress difference of solid, slurry-soaked, and holed specimen at 1MPa, (c) principal stress difference of solid, slurry-soaked, and holed specimen at 2MPa, (d) principal stress difference of solid, slurry-soaked, and holed specimen at 3MPa, and (e) slake durability index (SDI)

Figure 1.5.47 Failure modes of Taylor Marl after the multi-stage triaxial test

Figure 1.5.48 Holed Taylor Marl specimen after the triaxial test

Figure 1.5.49 Taylor Marl slurry-soaked for 12 hours

As observed in previous samples, the drying-duration was found not to impact the SDI of Taylor Marl, as shown in Figure 1.5.46 (e). Most Taylor Marl samples tend to have SDI between 40 and 70, indicating that Taylor Marl is low to medium-low durable. Figure 1.5.50 shows Taylor Marl before and after the slake durability test. Ten chunks fragmented into smaller-size pieces after the test, as observed in Eagle Ford Shale (Figure 1.5.38). The remaining fragments may appear to be similar to those of Eagle Ford Shale, but their slaking patterns differ slightly in

that the remaining Taylor Marl seemed to contain high clay content, whereas the remaining Eagle Ford Shale was very stiff. The SDI of this specimen was measured to be 50.8%, which would classify as low durability.

Figure 1.5.50 Taylor Marl before and after the slake durability test (TAM4N)

Effect of water content on material properties

The effect of water content of Taylor Marl on the strength and SDI is plotted in Figure 1.5.51. Unlike Eagle Ford Shale, Taylor Marl does not exhibit any relationship between water content and principal stress difference for the given range. Interestingly, Taylor Marl shows relation between drying-duration and principal stress difference, while Eagle Ford Shale does not; upon observation, the two formations presents exactly opposite of each other. In other words, Eagle Ford Shale is related to water content but not to drying duration, yet, Taylor Marl is related to drying duration but not to water content. The plots of the relationships are shown in Figure 1.5.51 (a) through (d). Natural water content of Taylor Marl ranges from 17.5% to 21% with two exceptions at around 23.5%, which are the holed, and slurry-soaked specimens. Even if the holed, and slurry-soaked specimens are included in interpretation, tendency of decreasing principal stress difference with increasing water content is still speculative. This observation is the opposite of both Del Rio Clay and Eagle Ford Shale, specimens of which exhibit slight to close relationship between water content and principal stress difference.

Obvious decrease in SDI was observed with increasing water content, as shown in Figure 1.5.51 (e). Holed specimens in addition to solid specimens were accounted for in creating trend because whether their being holed or solid does not affect SDI. It is known that the SDI of shales is closely related to the expandable clay content (Dick and Shakoor, 1997). Thus, there is a strong possibility that the expandable clay tends to contain more water, leading to low SDI. While drying-duration and SDI are not related at all, the close relationships between water content and SDI are common findings in both Taylor Marl and Del Rio Clay. The relationship was found to be weak in Eagle Ford Shale.
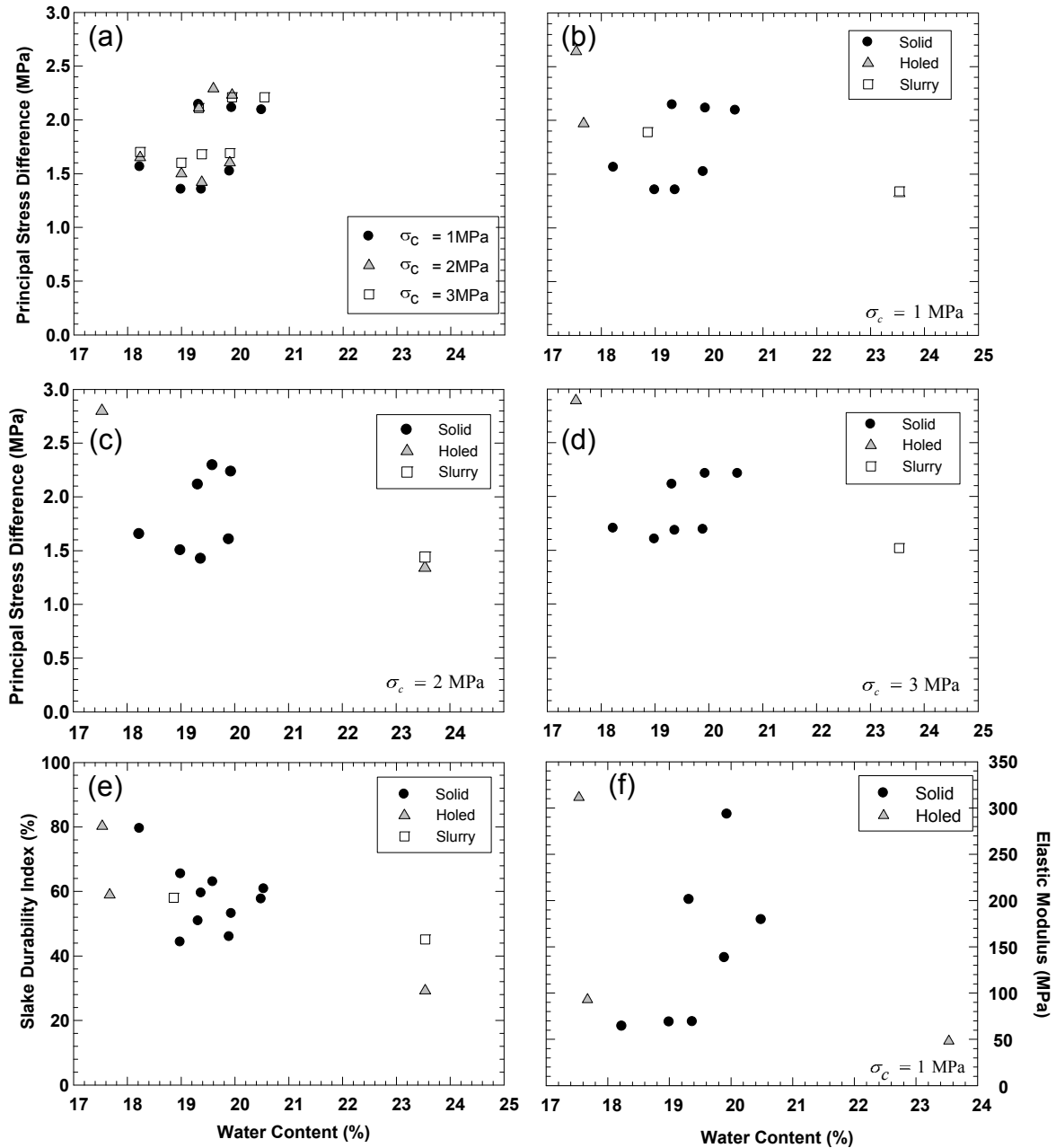
Figure 1.5.51 Taylor Marl: effect of water content on: (a) principal stress difference at three confining pressures, (b) principal stress difference of solid, slurry-soaked, and holed specimen at 1MPa, (c) principal stress difference of solid, slurry-soaked, and holed specimen at 2MPa, (d) principal stress difference of solid, slurry-soaked, and holed specimen at 3MPa, (e) slake durability index (SDI), and (f) elastic modulus

Other relationships

Figure 1.5.52 (a) through (d) provides the correlations among parameters; it was found that neither dry density nor SDI is related to principal stress difference. Indeed, the dry density is another way of representing water content, and typically either both or neither relates to other

properties. Therefore, it is natural that dry density of Taylor Marl is not related to principal stress difference in the same way as water content is not related to principal stress difference.

Figure 1.5.52 (c) and (d) present the relationships between elastic modulus and principal stress difference and drying-duration. Elastic modulus increases nearly proportionally as principal stress difference increases. It is important to note that drying-duration significantly influences the elastic modulus of the Taylor Marl. The reduction of elastic modulus is likely due to free swell of expandable clay minerals during the rewetting process. While a sudden drop in elastic modulus occurred after a few hours of drying in Eagle Ford Shale (see Figure 1.5.40 (d)), the gradual decaying curve is observed in Taylor Marl. The elastic modulus maximizes around 300 MPa for the fresh specimen and falls to as low as 48 MPa after 48 hours of drying. The modulus ratio obtained from fresh Taylor Marl specimens falls below 200, indicating that the marl is classified with a low modulus ratio. No substantial difference in behavior is found between the solid and holed specimens.

Jar slake test

Six cubes of Taylor Marl were dried for from 0 to 48 hours, one specimen was dried in the oven for a day, and all were submerged in distilled water for a day. Figure 1.5.53 provides the pictures taken one day after submerging, and the numbers in the figure indicate the categories of slaking modes. Taylor Marl starts to disintegrate severely when the specimen was dried for 4 hours. Conversely, the non-dried Taylor Marl specimen keeps its original shape even after being submerged for 1 day. Observable cracks developed in the specimen that was dried for 4 hours. At 8 hours of drying, the cube started disintegrating into small chips, and complete disintegration was observed in the specimen that dried for 24 hours or more. Therefore, the degradation process of Taylor Marl is quicker and more severe than Eagle Ford Shale. While Eagle Ford Shale disintegrates in a platy pattern but still keeps its initial shape after the jar slake test (See Figure 1.5.41), Taylor Marl degrades into an irregular shape.

Figure 1.5.52 Taylor Marl: relationships between: (a) dry density and principal stress difference, (b) SDI and principal stress difference, (c) principal stress difference and elastic modulus, and (d) drying-duration and elastic modulus
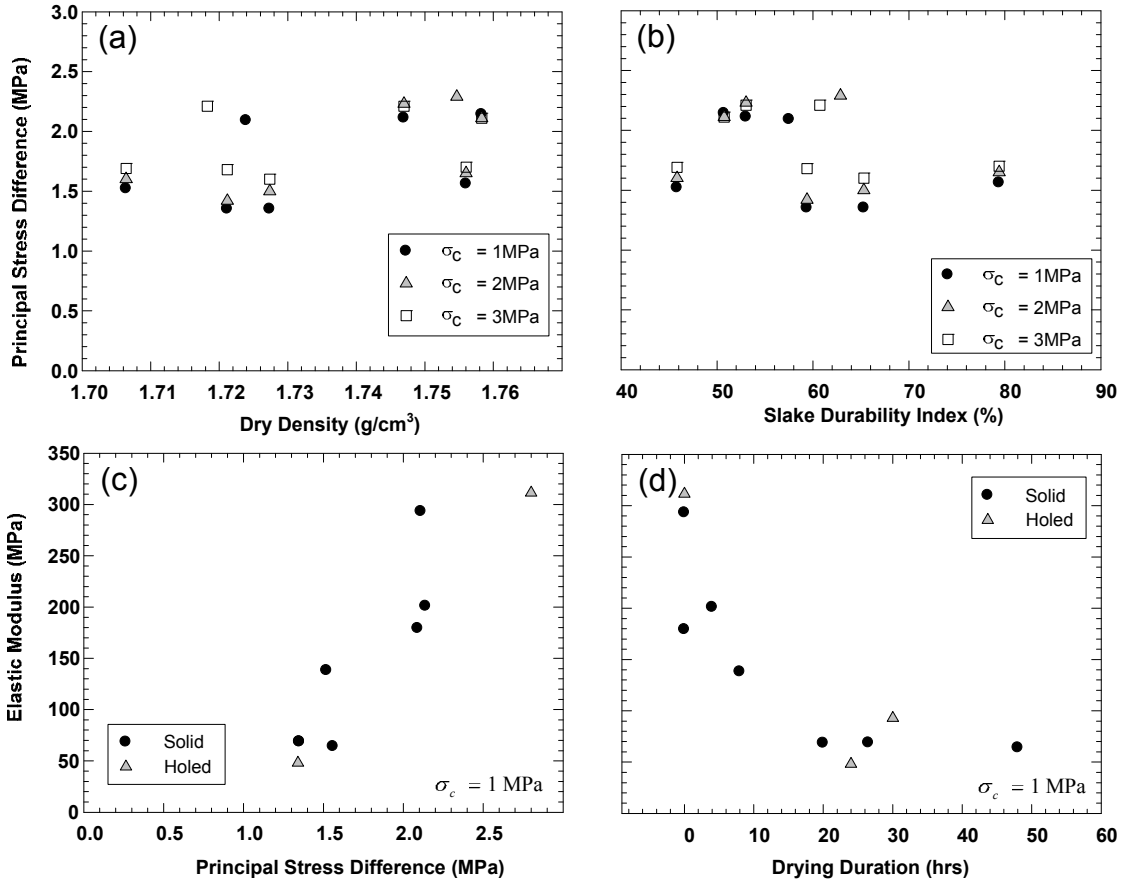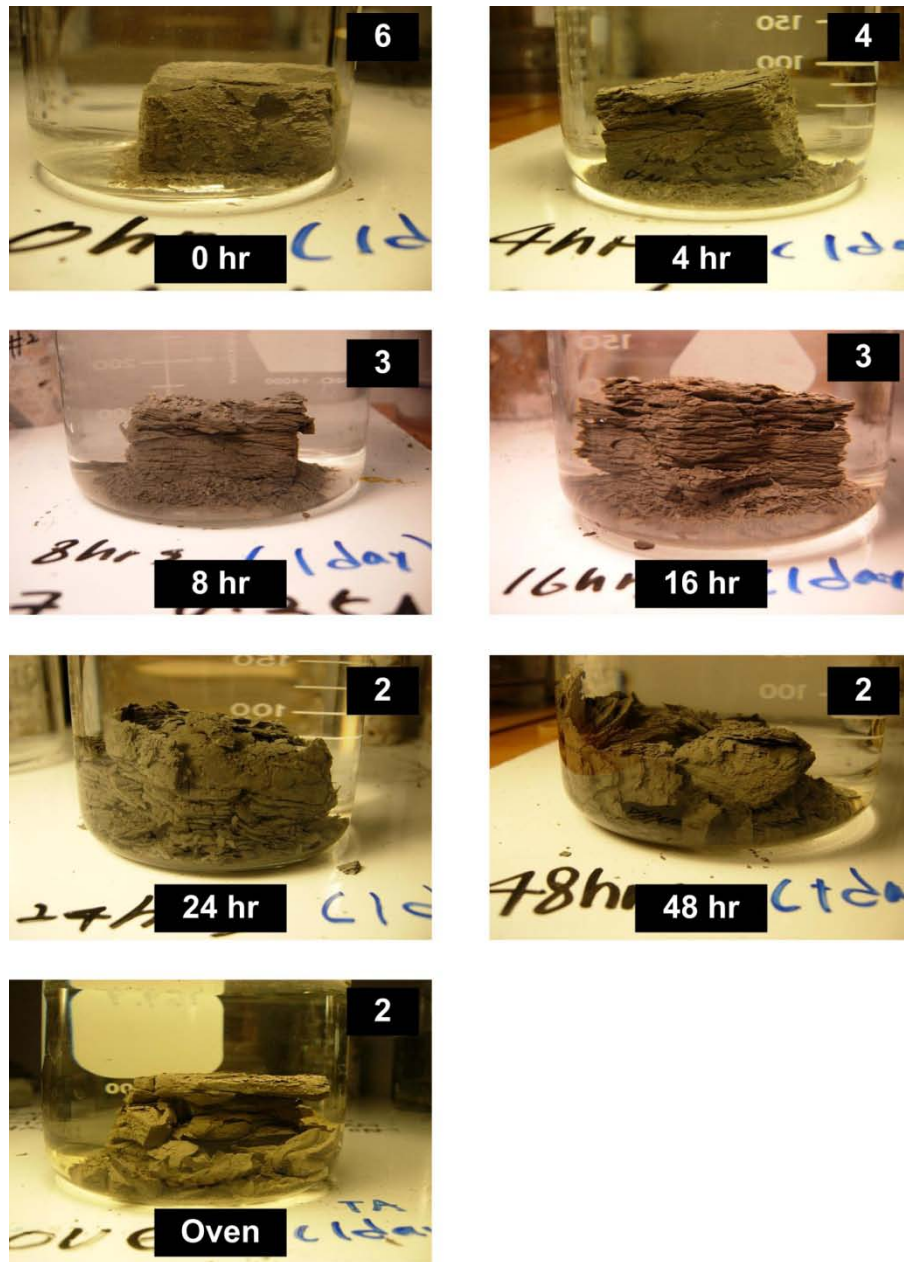
Figure 1.5.53 Results of jar slake tests on Taylor Marl after one day of soaking: numbers represent chart classification (Figure 4-24)

Navarro Shale

Navarro Shale is the youngest Cretaceous formation tested in this study. It overlies Taylor Marl and underlies the Midway group (see Section 1.3.2 for details of geology). Characteristics of Navarro Shale were evaluated using the single-stage triaxial test and jar slake test. Slake durability tests were also attempted, but all SDI were found to be zero because the Navarro Shale disintegrated completely. Thus, the durability of Navarro Shale is qualitatively

evaluated solely by the jar slake test. Navarro Shale samples that were tested were cored at Terrell, Texas, and the boring log is shown in Figure 1.5.54. High plasticity clay extends to 41.5 ft below the ground surface, and overlies shale which is described as soft to hard, moist, and gray with trace fossils. The coring was completed to a depth of 64 ft, and tested specimens were obtained between 52 ft and 62 ft. Figure 1.5.55 displays Navarro cores in the container as delivered. The fresh Navarro Shale appeared to be as strong as Eagle Ford Shale and Taylor Marl. However, the appearance of the specimen after drying is considerably different.

Figure 1.5.56 shows the specimens after a few hours of drying, displaying that drying Navarro Shale induces substantial numbers of horizontal and vertical cracks, which may be due to lack of cementation and compaction. Navarro Shale appears to be non-cemented whereas Eagle Ford Shale and Taylor Marl appear to contain appreciable amounts of calcium carbonate. Therefore, severe degradation was observed during the jar slake test, presenting virtual stacks of silts and clays after soaking specimens that had been dried for 16 hours or more. There is no doubt that the SDI of Navarro Shale reaches zero when it has been significantly dried.

In order to estimate how fast the water content decreases, the percent water loss is displayed in Figure 1.5.57. About 33% of water evaporated when Navarro Shale was dried for 48 hours in a laboratory condition. Navarro Shale loses little contained water within the designated drying-duration compared to the Eagle Ford Shale and Taylor Marl. Tested specimens disentigrated to silts rather than clay upon wetting after drying. Upon wetting, the specimens were found to effervesce under water, which suggests that the specimen was unsaturated. The dried specimens tend to break down upon contact with water. A typical stress-strain curve of fresh Navarro Shale is shown in Figure 1.5.58, which was obtained at 1 MPa confining pressure.

Figure 1.5.54 Boring log of Navarro Shale at Terrell, Texas (provided by Fugro Consultants Inc.)

Figure 1.5.55 Navarro Shale cores prior to sample preparation

Figure 1.5.56 Outlook of Navarro Shale specimen during drying
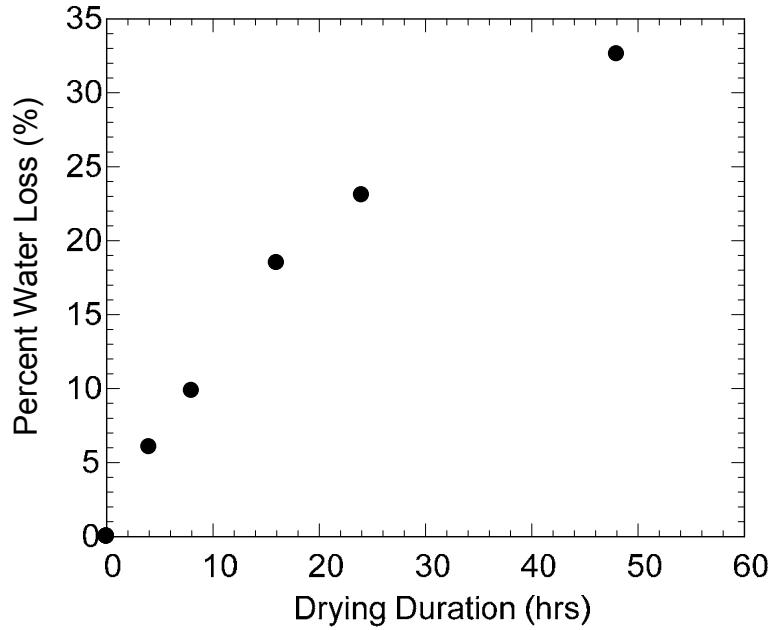
Figure 1.5.57 Percent water loss of Navarro Shale with drying-duration
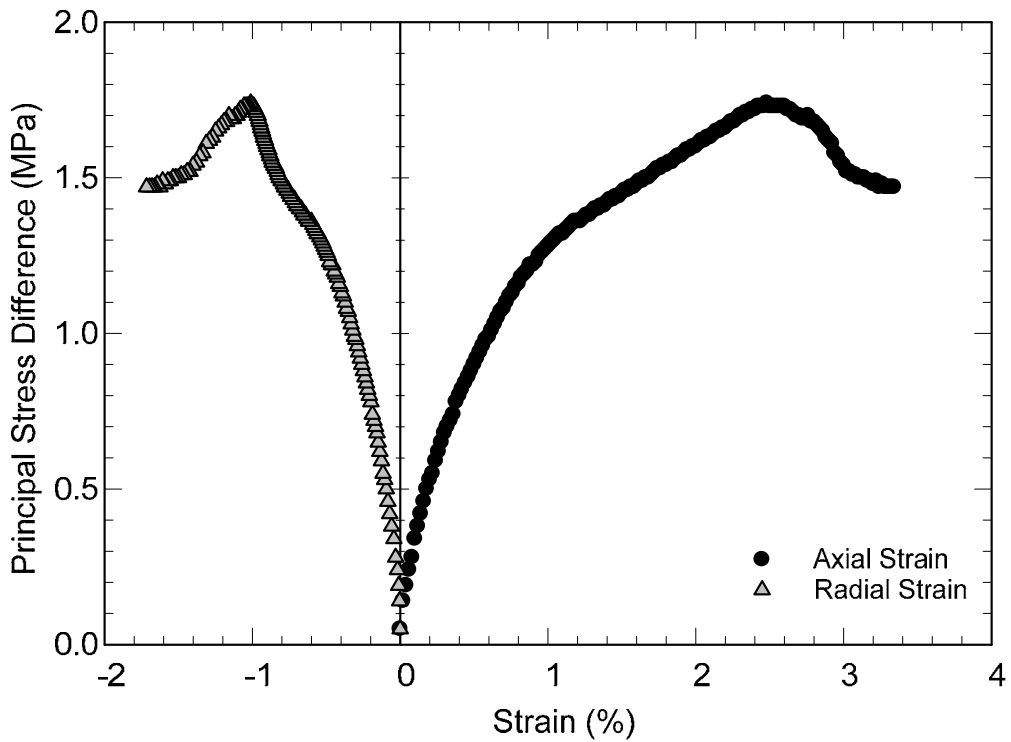
Figure 1.5.58 Typical stress-strain curve of Navarro Shale (NASNN1)

Effect of drying-duration and water content on material properties

      Results of triaxial tests are shown in this section. Prepared Navarro specimens displayed many cracks upon drying (Figure 1.5.56), which prevented the author from carrying out multiple stages of the triaxial test on one specimen. After the specimen was loaded to the imminent failure

point under the first confining pressure (typically 1 MPa), an attempt was made to unload the specimen to proceed to the next stage. However, the specimen appeared to fail at the moment of unloading, and the failed specimen did not reflect the original physical characteristics of the specimen. Moreover, radial strain decreased when confining pressure was applied, indicating that the specimen was extremely soft. Frequently, the radial strain variation was measured to be quite small when the specimen was loaded axially because softened Navarro Shale does not expand in radial direction. Radial strain information is, therefore, rarely obtained and meaningless even if obtained. Therefore, the decision was made to run the single-stage triaxial test under 1 MPa confinement. Two additional non-dried specimens were tested at 2 MPa, and 3 MPa to examine the effect of confining pressures. Interestingly, developed cracks that had been noticeable before triaxial tests were closed completely after applying triaxial loading (Compare Figure 1.5.56 and Figure 1.5.60). Thus, several cracks of specimens before tests tended to close during the triaxial test. Subsequent failure planes uncorrelated to existing cracks caused by drying developed in the specimens as shown in Figure 1.5.60. In most Navarro Shale specimens, shear failure surface developed starting from either the top or bottom of the specimen.

Figure 1.5.59 presents the effect of drying-duration and effect of water content on the principal stress differences. It was observed that drying for 24 hours reduced the principal stress difference by as much as about 30%. Testing the specimen that had dried for 48 hours was impossible because the specimen was not practically manageable due to severe degradation. It is inferred that the Navarro Shale among tested clay shales is the most susceptible to slaking upon exposure to air drying. Even water spraying on specimens dried 48 hours ruined the test specimen, and the surface literally slumped as the surface Navarro Shale adsorbed water. Severe degradation is also observed in the jar slake test. If the dried specimens were placed under water, the specimens inevitably disintegrated into silts and clays immediately. No strength test is feasible on such specimens. Bulging and tensile failure are rarely observed in Navarro Shale.

Figure 1.5.61 shows a Navarro specimen after soaking under slurry for 12 hours. The figure indicates that using slurry ruins specimens such that triaxial tests are not possible. Hence, no information of strength test is available for slurry-soaked Navarro Shale. Two holed specimens were tested after they had been dried for 0 and 24 hours. From the test, it was found that drying-duration affects the principal stress difference of holed specimens as well. However, the existence of the hole did not reduce the principal stress difference compared to solid specimens. This observation is consistent with all previous test results except for Edwards Limestone, which shows slight influence. It is likely that the narrow hole of relatively weak clay shales does not affect the strength of the specimen. Figure 1.5.62 represents the holed specimen at failure. It is observed that the hole wall collapsed slightly toward the center.
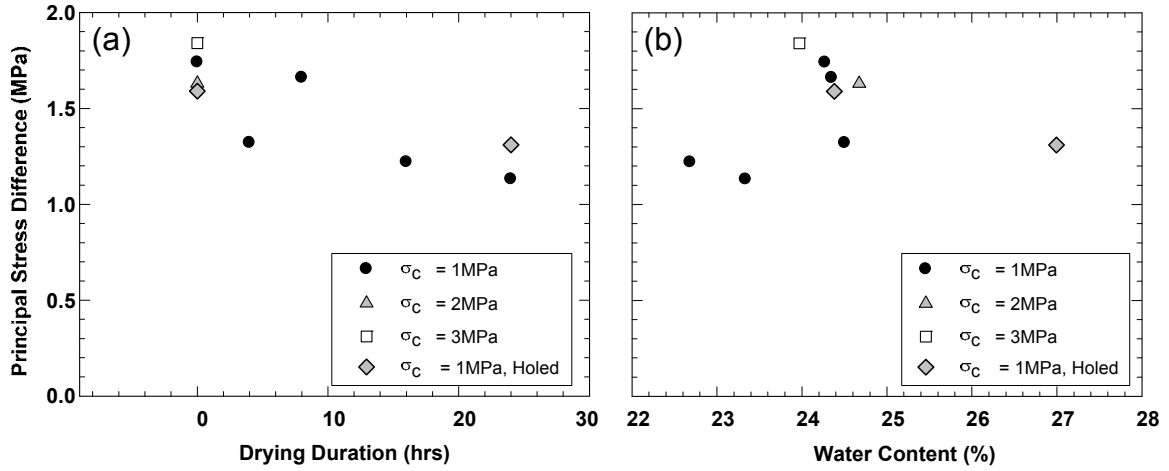
Figure 1.5.59 Navarro Shale: effect of (a) drying-duration, and (b) water content on principal stress difference

Figure 1.5.60 Failure modes of several Navarro Shale specimens

Figure 1.5.61 Slurry-soaked Navarro Shale specimen

Figure 1.5.62 Navarro Shale specimen with hole after the triaxial test

Other relationships

As slake durability tests were not run, only three figures are shown in Figure 1.5.63. The principal stress difference appears to be independent of dry density. However, as is noticeable in Figure 1.5.40 (Eagle Ford Shale) and Figure 1.5.52 (Taylor Marl), elastic modulus of Navarro Shale is strongly related to principal stress difference and drying-duration. The elastic modulus dropped gradually with increasing drying-duration from 190 MPa for the non-dried specimen to 43 MPa for the specimen dried 24 hours. In addition, the elastic modulus increased as the principal stress difference increased; the elastic modulus was measured to be 43 MPa at 1.1 MPa of principal stress difference, which corresponds to the data for the specimen dried 24 hours. The observation tells us that the long duration of drying resulted in low elastic modulus as well as low principal stress difference. Drying-duration plays a key role on both the strength and the elastic modulus of Navarro Shale. According to Figure 1.5.29, the modulus ratio of fresh Navarro Shale was calculated to be below 200, indicating the shale is classified with a low modulus ratio.

149
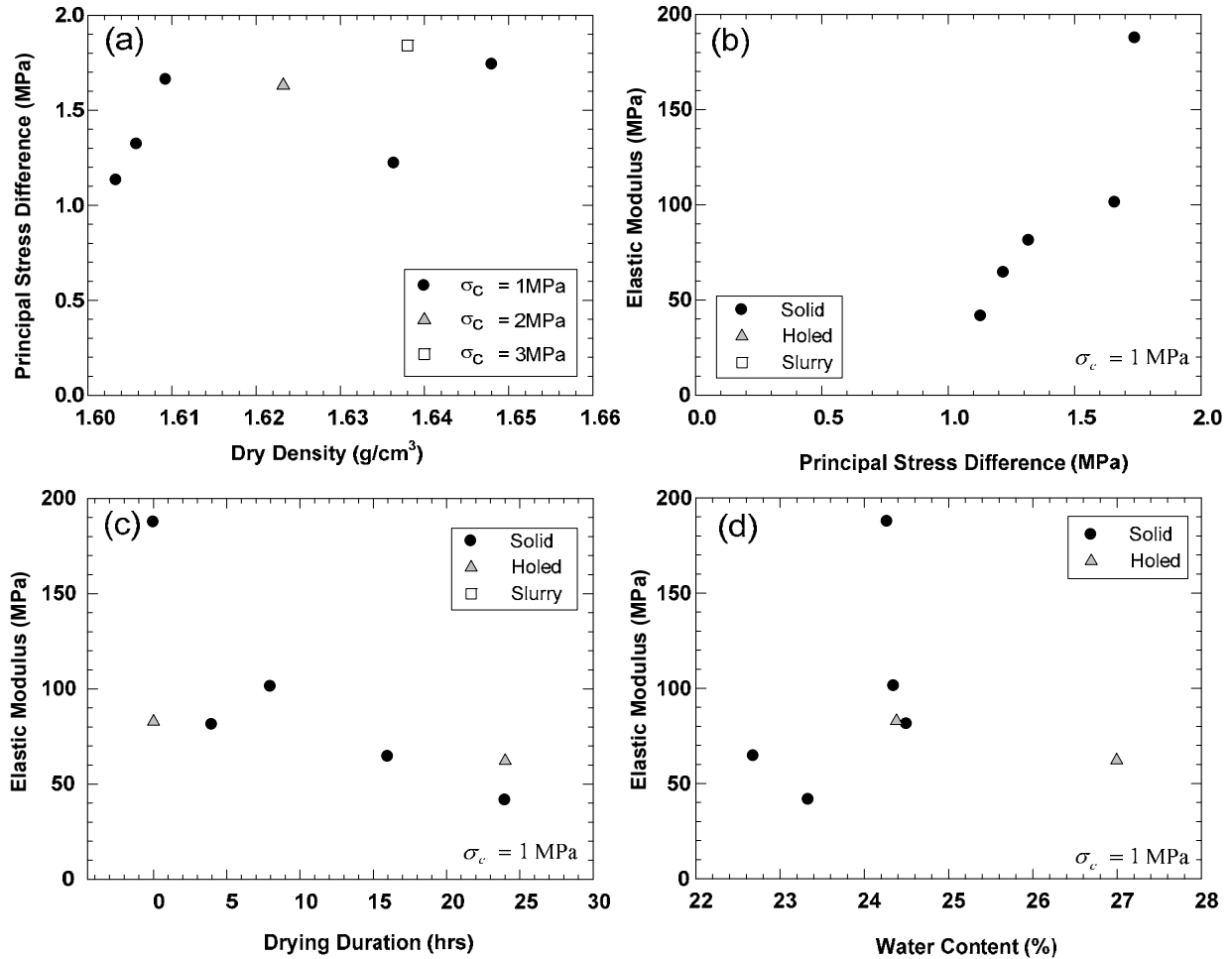
Figure 1.5.63 Navarro Shale: relationships between: (a) dry density and principal stress difference, (b) principal stress difference and elastic modulus, (c) drying-duration and elastic modulus, and (d) water content and elastic modulus

Jar slake test

The jar slake test provides significant information about Navarro Shale because quantification of durability was unattainable. Figure 1.5.64 shows specimens of different drying-durations one day after being submerged in distilled water. The fresh Navarro Shale specimen is practically undamaged except for little crumbs observed at the surface. The extent of degradation turned out to be severe when the specimen had been dried for 4 or more hours; the specimens, as identified, disintegrated into silts within 10-30 minutes after submergence. This finding suggests that drying the verification hole considerably impacts the engineering properties of Navarro Shale when the shale is dried for more than 4 hours.

150
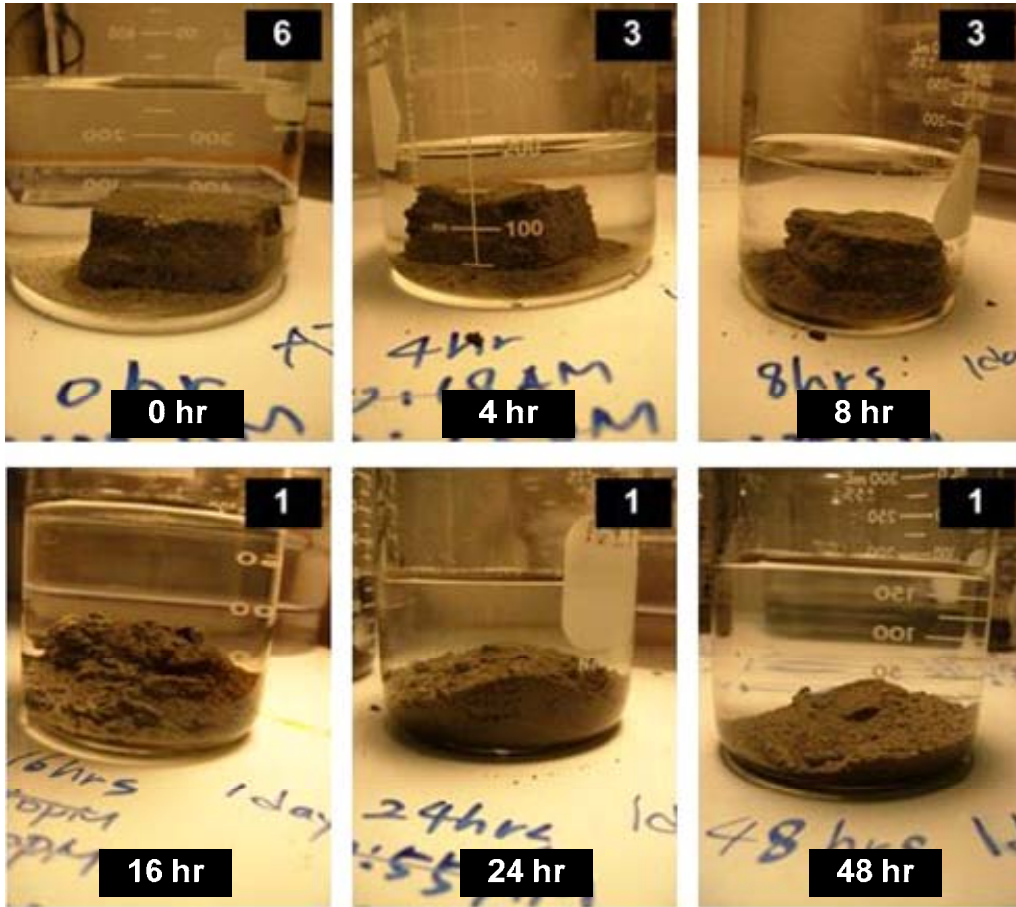
Figure 1.5.64 Jar slake test on Navarro Shale after one day soaking: numbers represent chart classification (Figure 4-24)

1.5.5 Summary

The main purpose of Chapter 1 is to investigate whether the existence of a verification core detrimentally affects the point bearing capacity of drilled shaft. The hypothesis is that the strength and durability of the founding materials at the shaft's tip may be influenced by one cycle of drying and wetting that results in the time gap between drilling and concrete placement. Laboratory tests were conducted on clay shales and limestones to investigate carefully controlled formation strength and durability. Tested formations include two limestones (Edwards Limestone and Austin Chalk) and four shales (Del Rio Clay, Eagle Ford Shale, Taylor Marl, and Navarro Shale) found in Texas. The findings in this section are subject to further analyses and interpretation in Section 1.7.

Three kinds experiments were performed: 1) the multi-stage triaxial test, 2) the slake durability test, and 3) the jar slake test. The material properties tested vary significantly from one formation to another; therefore, the overall results of the six formations are summarized in Table 1.5.4. The effects of both drying-duration and water content are negligible in two limestones, whereas the four clay shales are likely to be affected by either drying-duration or water content. It is an important finding that the elastic modulus is considerably influenced by drying-duration for all clay shales. It is also shown that the existence of the hole would not affect the strength of the five formations except for Edwards Limestone. This observation does not indicate that the

151

effect of the hole does not reduce the strength but that the effect is negligible compared to other effects such as drying-duration or water content. The effect of slurry use is inconclusive because of the lack of available data.

The critical time when slaking becomes severe has been based on a series of jar slake tests. The jar slake test was not performed on limestones since the test was designed for weak degradable rocks. Considerable slaking was observed if clay shale specimens were dried for a specific period and then submerged in water. Eagle Ford Shale appears to be most resistant to slaking among the four clay shales tested. Other clay shales disintegrated considerably after 4 to 8 hours of drying and slaking in water.

Table 1.5.4 Summary of laboratory test results

Formation	Effect of drying-duration on			Effect of water content on		Effect of hole	Effect of slurry	Severe slaking
	Principal stress difference	SDI	Elastic Modulus	Principal stress difference	SDI			
Edwards Limestone	None	None	None	None	None	Slight	None	None
Austin Chalk	None	None	None	None	None	None	N/D	None
Del Rio Clay	Slight	None	Clear	Clear	Clear	None	D	4-8hours
Eagle Ford Shale	None	None	Clear	Clear	Slight	None	None	8-16hours
Taylor Marl	Clear	None	Clear	None	Clear	None	None	4-8hours
Navarro Shale	Clear	N/A	Clear	None	N/A	None	D	4-8hours

Note: *N/D indicates the effect was not determined
* N/A indicates not available
* D indicates disintegration
* Effect of hole and slurry was determined based on strength.

1.6 EVALUATION OF THE THICKNESS OF THE WEATHERED ZONE AROUND VERIFICATION CORES

1.6.1 Introduction

This section focuses on full scale condition tests performed in the Dallas District and laboratory tests conducted on samples obtained from the test site. From the laboratory test results discussed in Section 1.5, several formations were found to degrade with increasing drying-duration, while others did not degrade significantly. It is repeatedly emphasized that the principal stress difference between Taylor Marl and Navarro Shale at failure and the elastic modulus of all four clay shales were found to decrease with increased drying time whereas the principal stress difference between Eagle Ford Shale and Del Rio Clay was not affected by the drying time. Although the deterioration of material properties of several formations was found to be distinct, the applicability of laboratory test results appears to be limited to the degraded region at the perimeter of the verification core hole. Shales far from the verification core wall may not be influenced by drying or wetting induced by the verification core. Hence, it is necessary to determine the extent of the degraded region around the verification core. Following sections provide the test site descriptions, field procedures for the full-scale condition test, laboratory test results, and interpretations of the laboratory results to determine the degraded area.

1.6.2 Site Investigation

The site chosen for the field test is located in the median of future State Highway 360 (SH 360) near Mansfield, Texas. The location of the test site is marked on the Texas geological map in Figure 1.6.1; the test site is located on the narrow band starting from Southeast through Central Texas and extending to Northeast Texas through Dallas. The geological map indicates that the Upper Cretaceous formations outcrop on the bands. Among the four common clay shales investigated in this study, the Eagle Ford Shale was chosen because it is known as the most problematic ground material causing significant damage to infrastructures and properties in Central Texas and because natural outcrops appear at the chosen site. The following were considered during the site selection phase: 1) accessibility of heavy equipment to the site, 2) the ownership of the property, and 3) highway traffic. Fortunately, we were able to locate a site beside SH 360 that is relatively uncrowded, owned by TxDOT, and has little traffic. The close-up views of the test site before testing are shown in Figure 1.6.2, which was photographed before augering the sites. The two lane road shown on the right side of Figure 1.6.2 (b) is SH 360. The yellow flag markers in the ground indicate the location to be augered.
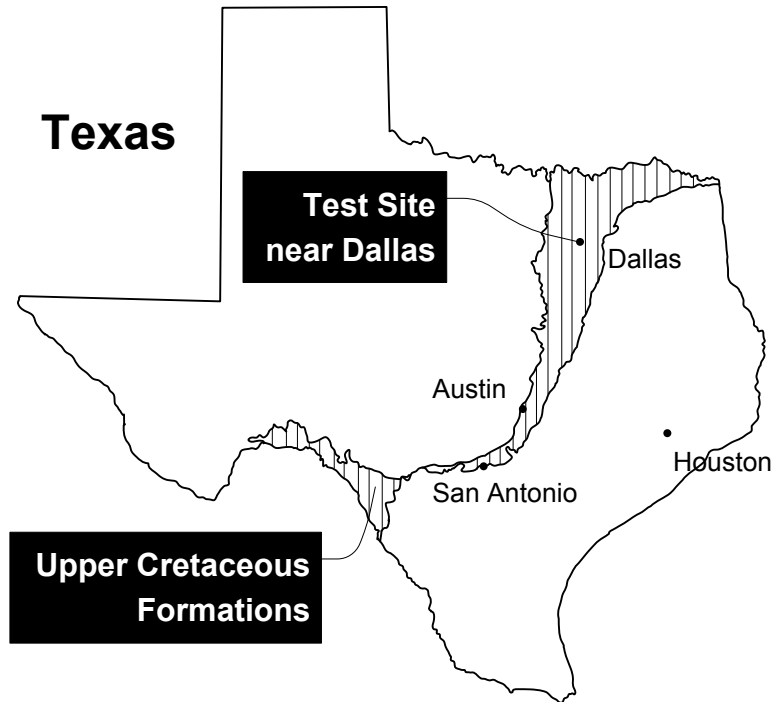
Figure 1.6.1 Location of the testing site on the geological map of Texas

Figure 1.6.3 exhibits an example of the boring log of the site that was generated by Fugro Consultants Inc. The site was covered by vegetation at the ground surface. High plastic clay overlies shaly clay that extends to 5.2 m (17 ft) until unweathered shale is encountered. The unweathered Eagle Ford Shale encountered is described as moderately hard and dark gray with an intervening bentonite seam. It was recorded in the boring log that ground water was encountered at 6.1 m (20 ft) below ground surface, but the author observed that, at the time the drilled shafts were excavated, the elevation of the water level was near the ground surface due to heavy rain falls near the test date (rainiest season ever recorded in Texas).

1.6.3 Field Test Procedures

The full-scale condition test is designed to determine the extent of the damaged zone at the perimeter of verification cores. Six groups of three different core lengths were to be drilled at the bottom of 18 non-production drilled shaft excavations. The plan view of the layout is shown in Figure 1.6.4. A rectangular area about 9 m × 21 m (70 ft × 30 ft) was used to drill three rows and six columns of non-production drilled shaft holes. The spacing between drill holes is 4.0 m (13 ft) from center to center to provide drilling and coring machines free access to the location. In the figure, the numbers below each shaft hole represent the order of drilling, starting from 1 to 18. A schematic vertical cross-section of the location of drill holes and verification cores is shown in Figure 1.6.5. The diameter of drilled shafts and verification cores are 0.9 m (3 ft) and 25.4 cm (10 in), respectively, which are commonly used sizes in Texas. The depth of the verification core holes ranges from 1.5 m (5 ft) to 3.0 m (10 ft). Over two days, 18 drilled shafts holes were drilled by three experienced drillers from Texas Shafts Inc.
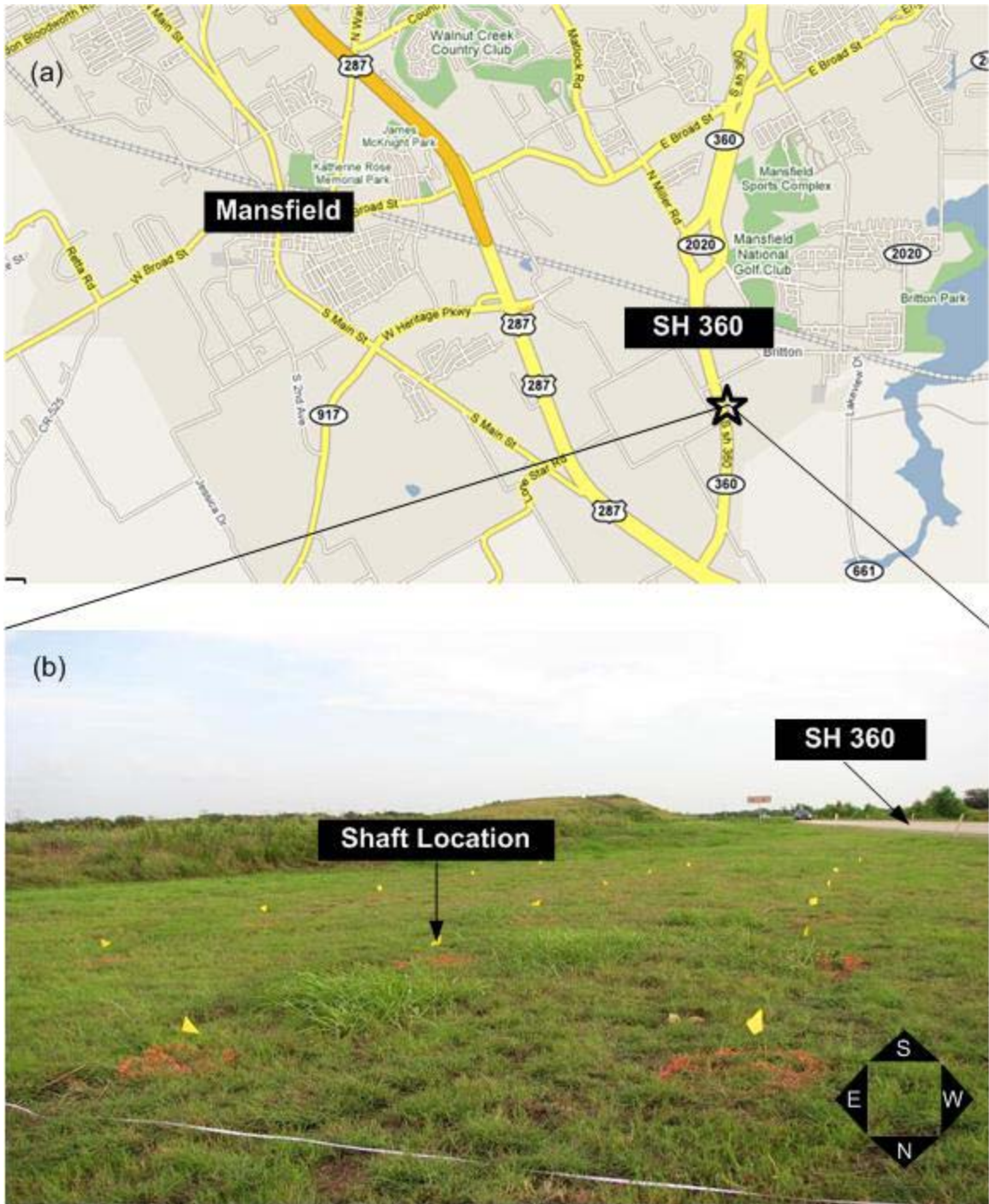
Figure 1.6.2 Testing location: (a) close up view of testing site and (b) photographed landscape prior to augering; the yellow flags indicate the location of shaft holes (Mansfield, Texas)

The boring log table contains the following columns: DEPTH, FT; SYMBOL; POCKET PEN, tsf / Blows/ft / Rec./RQD, %; STRATUM DISCRIPTION; LAYER ELEV. DEPTH

SURF. ELEVATION: UNKNOWN

CLAY (CH), tan, soft to very stiff. moist. with few calcareous nodules

(Depth markers: 5, 10)

13.0

SHALY CLAY (CH), gray and tan, very stiff to hard moist to water bearing

(Depth marker: 15)

17.0

SHALE, gray, soft, moist

(Depth markers: 20, 25)

RC 1
20'-26'
100/100

Bentonite seam from 23.6 – 24.0 ft

COMPLETION DEPTH: 36.0
DATE DRILLED: 1-18-07

WATER LEVEL / SEEPAGE: 17.0

Figure 1.6.3 Boring log at State Highway 360, Mansfield, Texas (provided by Fugro Consultants Inc.).

Figure 1.6.6 presents the schematic procedures of the full-scale condition testing. The verification holes were excavated in unweathered Eagle Ford Shale at the bottom of drilled shafts. The verification hole was kept dry to allow air drying for the designated period. Theoretically, the shales at the perimeter of the verification hole would crack through weakest bedding planes due to evaporating contained moisture. Shales in contact with the verification core hole may degrade significantly; but shales beyond the drying

front may not be influenced by drying the sides of the verification core hole. When water is introduced into the verification core hole, the clay shales that degrade by air drying are subject to free slaking in contact with water. In addition, if the developed cracks propagated to some distance, the shales containing such cracks might deteriorate significantly by allowing water migration through those open cracks. In the end, the investigation cores were taken at three different locations relative to the verification core hole to determine how large the degraded zone is.
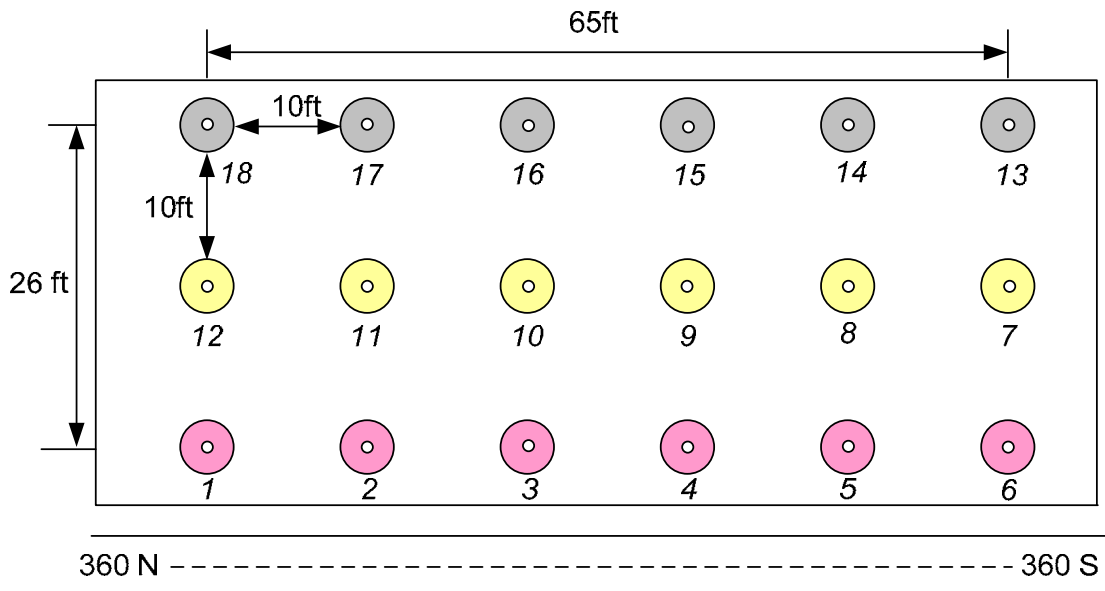
Figure 1.6.4 Layout of 18 non-production drilled shaft holes
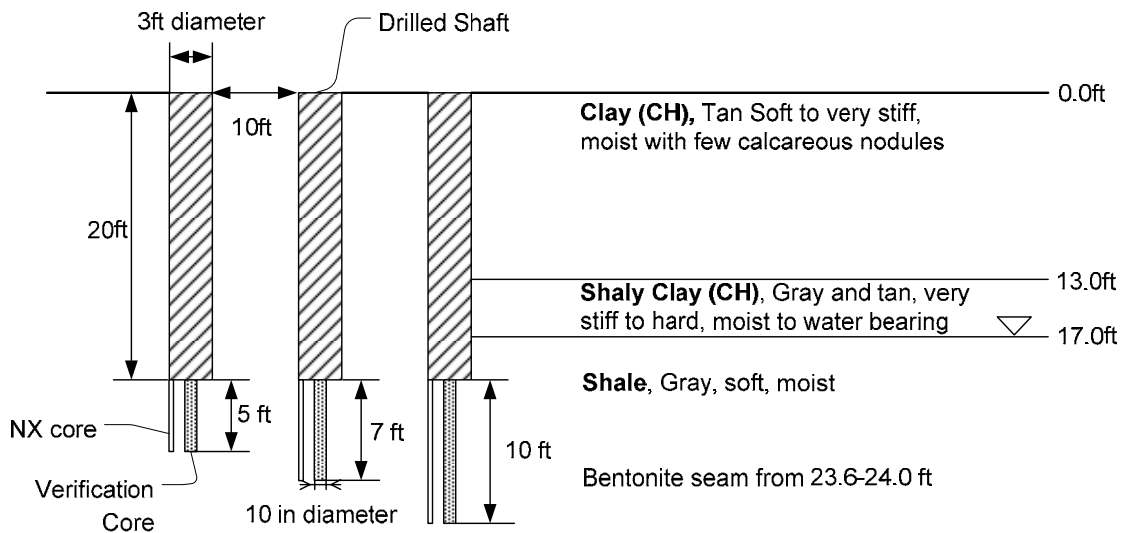
Figure 1.6.5 Side view of drill holes for three different core depths

158

It was expected that the water table would be lower than the shaft tip during the dry season (August) in the North Texas area, thereby permitting air drying conditions in the verification core holes. However, because of the unexpected, heavy rainfalls on the test date, the water level at the test site was found to be higher than expected. An observation well was installed to a 9.1 m (30 ft) depth near the site, several weeks before the field test (July 10, 2007), with the water levels monitored by Fugro Consultants, Inc. to determine a reasonable test elevation. The water table was equilibrated between 3.4 m (11 ft) and 3.7 m (12 ft) below the ground surface approximately 2 weeks after the well installation. Simple calculations were carried out to estimate water inflows with the following assumptions: 1) water inflows occur through weathered shales overlying fresh shales around 5.2 m (17 ft) below ground surface, 2) the permeability of weathered shale was 10^{-4}cm/s (4×10^{-4} in/s), which is higher than that of clay, 3) the thickness of water-bearing weathered shale is 61cm (2 ft), and 4) hydraulic gradient is unity. These values were chosen after discussion with a local geologist from Fugro Consultants Inc. and the values were expected to result in conservative predictions. The total inflow per day was estimated using Darcy's law:

$$q = k\,i\,A \qquad\qquad\qquad\qquad \text{Equation 1.6-1}$$

where q is total rate of flow, k is coefficient of permeability, i is hydraulic gradient, and A is the cross-sectional area. The cross sectional area for 61 cm (2 ft)-thick weathered shale was calculated to be 1.75 m^2 (18.85 ft^2); thus, the total rate of flow was calculated to be 151 L/day (40 gal/day). Therefore, it would take 12 hours to fill up a core 1.5 m (5 ft) long and 12.7 cm (5 in) diameter, and 24 hours to fill up core holes 3 m (10 ft) long and 12.7 cm (5 in) diameter by natural water inflows induced by a high ground water table. Hence, it was expected that the cores may not dry sufficiently due to natural water inflow. Therefore, a pump was used to keep the verification core hole dry and the project on schedule.
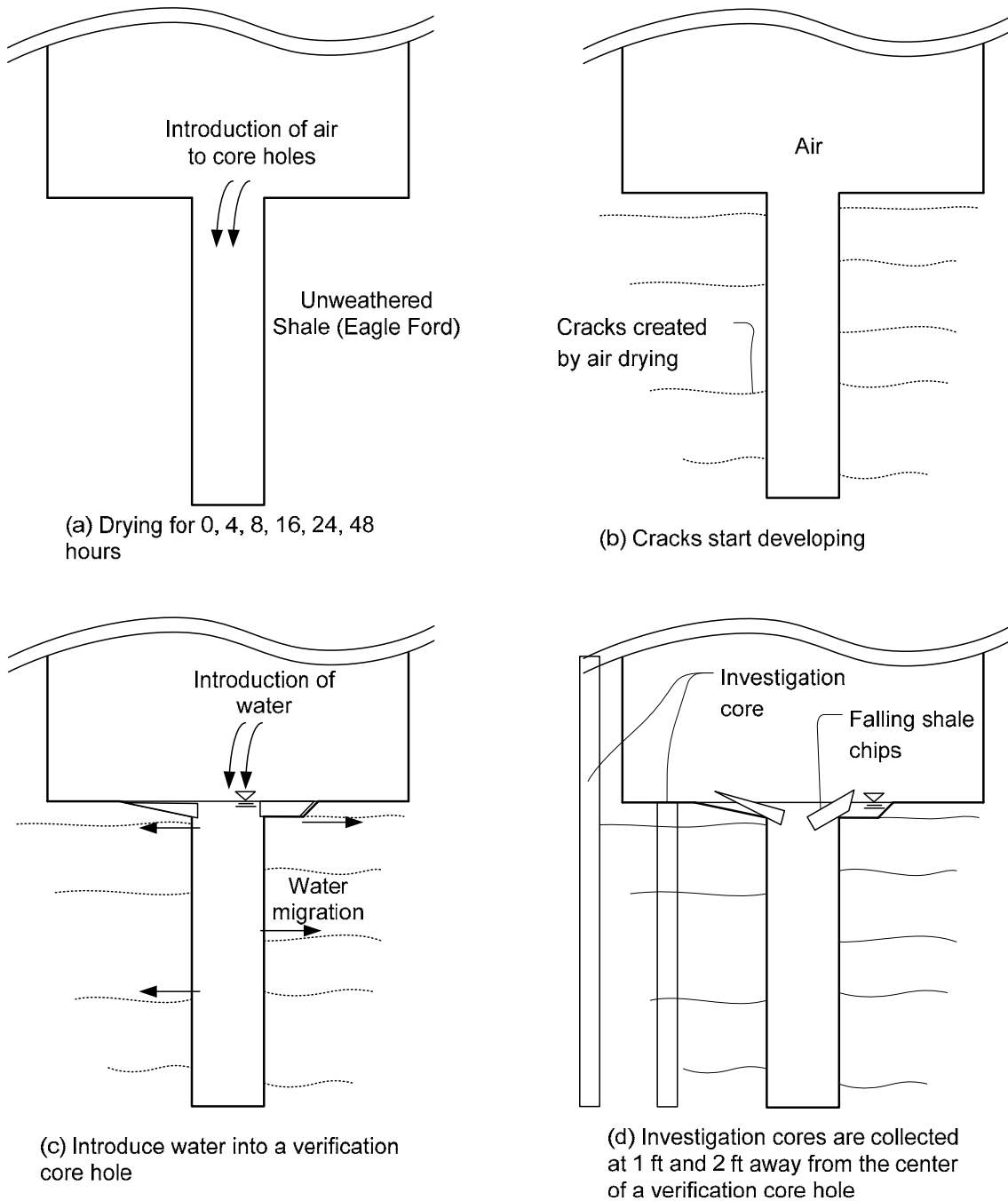
Figure 1.6.6 Schematic procedure of drying and wetting induced by a verification core hole

It was not possible to keep all core holes dry for 16-48 hours as planned because of limited pump capacity. In fact, it took less than 8 hours for most verification core holes to be filled with water, with the exception of shaft holes 16 and 17. The last two holes

were not affected by the rapid water infiltration due to the high water table; and it took approximately 20 hours for those holes to be filled up. In order to artificially impose long drying-duration (48 hours), three holes including #16, #17, and #15 were dried for 48 hours by pumping filled-in water out from the core holes. Then, all holes were filled with water for one week to allow sufficient time for clay shales at the perimeter of the verification core to deteriorate in the presence of water. Drying 48 hours and immersing under water for 1 week are unlikely to occur during construction; therefore, this test condition represents a worst-case scenario. Such a condition may occur when the verification core hole is not filled with any material, which is highly unlikely.

In order to assess the effect of drying-duration and wetting, NX-size investigation cores were obtained near verification cores by Fugro Consultants, Inc. The summary of the full-scale degradation test is tabulated in Table 1.6.1 showing the shaft number, drying-duration, and the location of the investigation core that provides the information of how far away the core was excavated from the center of the shaft hole. The "shaft bottom" in the table indicates that the NX-size investigation core was obtained at 1 ft away horizontally from the shaft hole center at the shaft bottom. The "ground surface" for the NX core location in the table indicates that the investigation cores were obtained 0.6 m (2 ft) horizontally away from the hole center at depth starting from 6.1 m (20 ft). One NX-size investigation core was obtained 3.0 m (10 ft) away from all shaft holes to eliminate any effects from shaft holes. A total of 14 cores were obtained at between 6.1 m (20 ft) and 9.1 m (30 ft) depth: ten investigation cores from the shaft bottom and four investigation cores from the ground surface. The reason such different coring locations were used was to investigate the change in strength with horizontal variation. In this specific study, no difference in strength was noticed, indicating that the damaged zone did not extend to the outer perimeter of the shaft holes. Details of this conclusion are presented later in this section.

1.6.4 Field Observation

The study site after augering (left) was completed and the verification cores (right) were extruded from the ground are shown in Figure 1.6.7. The site was secured by enclosing the area with barricades and by covering each shaft with wooden safety covers. The verification cores were extruded with a 25.4 cm (10 in) diameter core tube using hydraulic pressure. Normally, friction between tubes and cores seems to be higher than the applied hydraulic pressure, which may result from the expansion of Eagle Ford Shale upon being released from the confining pressure at deep depth.

Table 1.6.1 Summary of the full-scale degradation test

Shaft number	Verification core depth (ft)	Drying-duration (hours)	Location of NX investigation core
1	n/a	n/a	n/a
2	5	8	n/a
3	7 (20 – 27 ft)	7	Shaft bottom (1 ft)
4	10 (20 – 30 ft)	7	Shaft bottom (1 ft)
5	5 (20 – 25 ft)	3	Shaft bottom (1 ft)
6	7	2	n/a
7	10 (20 – 30 ft)	2.5	Ground surface (2 ft)
8	5 (20 – 25 ft)	3	Ground surface (2 ft)
9	7 (20 – 27 ft)	3.5	Shaft bottom (1 ft)
10	10	22	n/a
11	5	n/a	n/a
12	7	n/a	n/a
13	10 (20 – 30 ft)	4	Shaft bottom (1 ft)
14	5 (20 – 25 ft)	4.5	Shaft bottom (1 ft)
15	7 (20 – 27 ft)	48	Shaft bottom (1 ft)
16	10 (20 – 30 ft)	48	Shaft bottom (1 ft)
			Ground surface (2 ft)
17	5 (20 – 25 ft)	48	Shaft bottom (1 ft)
18	10 (20 – 30 ft)	8	Shaft bottom (1 ft)
20	10 (20 – 30 ft)	0	Ground surface (10 ft)

* All investigation cores were obtained starting from 20 ft deep either at shaft bottom or ground surface.
* n/a indicates "not available"
* 1 ft = 0.3 m

The sample tubes were tapped on the top and sides to release the contained cores. Significant impact was required to dislodge the core samples. This resulted in the opening of already present horizontal fissures. This process caused significant fracturing along horizontal weakness planes in the core samples. Moreover, rotating the coring tube into the stiff layer during coring generated notable heat around core samples, which appears to have changed the physical characteristics of the shale. Visual inspection of the verification cores implied that the Eagle Ford shale at the bottom of the shaft hole is fresh without appreciable fractures immediately after augering.

Figure 1.6.7 Site landscape after finishing drilling 18 non-production shaft holes (left) and the verification cores obtained (right)

On the other hand, the clay shales at the perimeter of the verification core hole become soft and weak as a result of air drying and slaking. Figure 1.6.8 displays a retrieved core from the Shelby tube pushed adjacent to the edge of the verification core after completion of the drying and wetting process. The Shelby tube core shown in Figure 1.6.8 was obtained from the verification core hole that was dried for 3 hours (#5) and then allowed to fill with water. The core was very soft in that the surface of the sample was easily dented and scratched with fingers, and the entire core crumbled in a platy pattern when grabbed firmly. The surface of the investigation core was jagged with numerous horizontal open fissures. It is obvious that the shales weaken depending on the duration of drying and slaking for a week. This finding contradicts the laboratory results of Section 1.5, which show that the principal stress difference is not influenced by drying and wetting for Eagle Ford Shale. The difference may result from the wetting method; water was gently sprayed in the laboratory, whereas the clay shale was submerged under water for a week. It is unclear that the wetting duration significantly affects the strength, but the degree of swelling and slaking effects is considerable at the contact between water and clay shales. The reduction in elastic modulus may be due to many open cracks upon weathering, as shown in Figure 1.6.8.

Visual inspection indicates that the shale at the core wall was severely weathered and behaved very differently from fresh shale. However, the Eagle Ford Shale exhibits practically no degradation in the jar slake test when the clay shales are dried for 4 hours and submerged in water. The difference in observations between the laboratory jar slake test and the field condition test may be due to overheating and disturbance by the rotating core sample tube. The contact between the sample core tube and shale were severely

163

sheared and overheated as the tube was advanced. This is believed to turn the fresh shale into crushed clay particles. Therefore, the shale of the verification core hole wall was found to slake more severely than the shales used in the laboratory test. Because the shale adjacent to the verification core hole was too weak to sample, and because the softening behavior of the shales might occur only near the edge of the verification core wall, NX-size investigation cores were obtained 0.3 m (1 ft) away from the edge of verification core holes.

Figure 1.6.9 shows the top view of a shaft hole a week after drilling of the verification cores had been completed and when the NX-size investigation core was obtained. The ground water table was measured to be approximately 1 m (3 – 4 ft) below the ground surface. The verification core was dewatered using a submersible pump to determine the location to auger the NX-size investigation core. All cores were obtained approximately 0.3 m (1 ft + 1 in) away from the center of the verification core holes.

Figure 1.6.8 Extruded sample from the side wall of the verification core (#5)
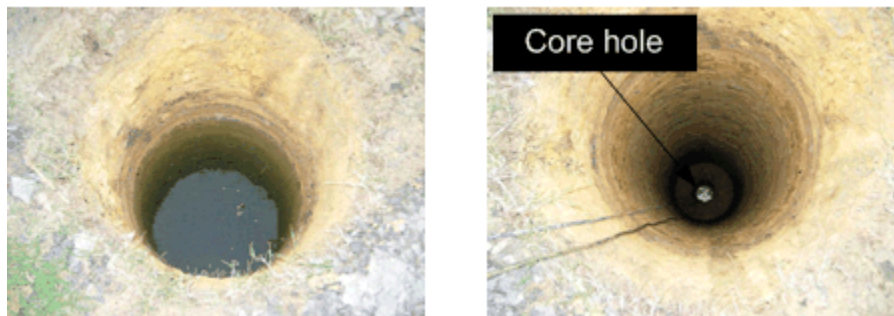
Figure 1.6.9 Shaft hole filled with water by natural inflow (left) and the shaft holes which were dewatered using a water pump.

1.6.5 Results and Interpretation of Laboratory Tests

Two different laboratory tests were conducted on the NX-size investigation cores obtained from the full-scale degradation test site: 1) uniaxial compressive strength (UCS) test and 2) point load test (PLT). UCS test results were used to provide the strength variation among shaft holes that were dried for different periods of time, to determine the effect of drying-duration on the strength of Eagle Ford Shale. The PLT was conducted to establish a correlation between the UCS and the PLT. Details of test procedures are described in Section 1.4.3 (UCS) and Section 1.4.4 (PLT).

In this section, the results of UCS tests and the PLI tests are provided and are interpreted to approximate the degraded zone at the verification core holes. Furthermore, correlations between water content, UCS, PLI, and dry density were established as index properties of Eagle Ford Shale.

The Extent of Degraded Zone

The main finding of this section is that the probable degraded zone is unlikely to extend further than 0.3 m (1 ft) from the center of shaft holes. The degraded zone was estimated by comparing the UCS of investigation cores that were not affected by drying with that of investigation cores obtained from the dried verification core hole. A total of nine specimens were prepared along an investigation core per each shaft hole, and the specimens were axially loaded to failure using UCS test apparatus.

Figure 1.6.10 (a) exhibits the results of the UCS test plotted for each shaft hole, and Figure 1.6.10 (b) shows the change in UCS with drying-duration. Three symbols are used: solid circles, gray triangles, and hollow rectangles. Solid circles represent that tests were carried out on the investigation cores obtained at the shaft bottom and 0.3 m (1 ft) away from the center of each shaft hole. The gray triangles indicate that the investigation cores were obtained from the ground surface that was 0.6 m (2 ft) from the center of shaft holes. The hollow rectangles represent the investigation cores obtained far away (3 m (10 ft)) from the shaft hole, where cores were believed to be completely isolated from any of the verification core holes. The cores were obtained between 6.1 m (20 ft) and 9.1 m (30 ft) deep from ground surface in where Eagle Ford Shale (see Table 1.6.1). It was found that all cores have similar strength but widely varying between 2 MPa and 6 MPa. The maximum UCS was measured to be as much as three times the minimum for each shaft hole. Because of such wide rock variability, the effect of drying-duration shown in Figure 1.6.10 (b) is inconclusive.
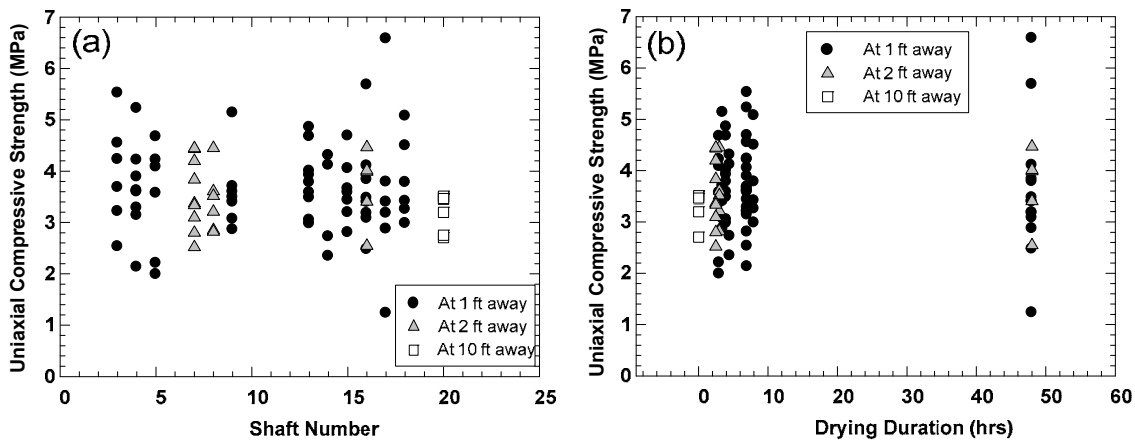
Figure 1.6.10 The results of UCS tests of Eagle Ford Shales: a) the UCS per shaft hole and b) the effect of drying-duration on UCS

Because variability of core strength makes it difficult to analyze the effect of drying-duration, the test results of each shaft hole were averaged into a representative value for each shaft hole (see Figure 1.6.11). The error bars on each point indicate a range of one standard deviation for each shaft hole. The standard deviation generally

measured to be less than 1 MPa, but for the cores taken from Shaft 17 it was 1.7 MPa. It is clearly that the UCS results obtained from each shaft are similar regardless of both drying-duration and the coring location. The average UCS ranges between 3 and 4 MPa. The resulting UCS values were, unfortunately, nested around 4 hours to 8 hours of drying-duration with only three data points at 48 hours of drying. This was due to the inability to control water inflow in the field. It should be noted, however, that the UCS values at 48 hours of drying are very similar to those of other cores, which assures that the intermediate data points are likely to be in a similar range. Also, it is shown that the UCS of the investigation cores obtained at shaft bottoms are not lower or higher than that of the investigation cores obtained 0.6 m (2 ft) and 3 m (10 ft) away from the center of the shaft hole. This critical observation implies that the clay shale at 0.3 m (1 ft) distance is as fresh as that at 0.6 m (2 ft) and 3 m (10 ft) distance.

Figure 1.6.12 displays the variation of UCS and water content with depth that was measured from the investigation cores of Shaft 16. One series of cores was obtained from the shaft bottom, 0.3 m (1 ft) away from the hole center (at shaft bottom), and the others were obtained at 0.6 m (2 ft) away from the hole center (at ground surface) at 6.1 m (20 ft) depth. Both the UCS and water content scatter within similar ranges for both investigation cores, and the average UCS of the two was measured to be practically identical (3.7 MPa). The variation of water content with depth is also similar at 0.3 m (1 ft) and 0.6 m (2 ft) from the center. The similarity in the UCS of those cores from the same shaft but from different distance strengthens the finding that the effects of air drying or wetting do not reach the cores augered at 1 ft from the shaft hole center.

The schematic side view of the verification core is displayed in Figure 1.6.13 showing the location of the NX size investigation core, the diameter of the shaft, and the conceptual degraded zone resulting from air drying. As discussed earlier in this section, the degraded zone does not extend over the location of the NX-size investigation core. However, the clay shales at the perimeter were observed to be highly deteriorated from contact with air and water (See Figure 1.6.8). Therefore, the degraded zone is located between the NX-size investigation core and the verification core hole wall, even though the transition pattern is unclear.
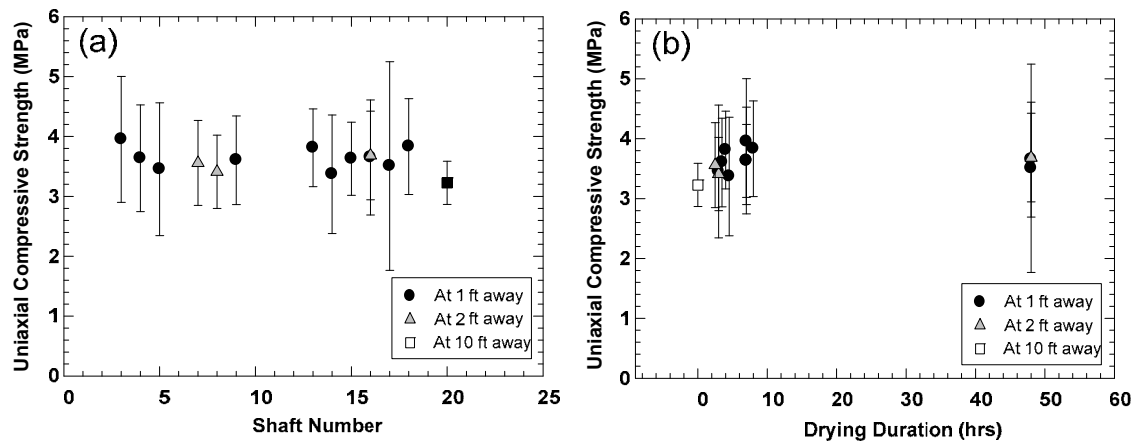
Figure 1.6.11 The results of UCS tests of Eagle Ford Shales by averaging values per shaft hole: (a) variation of UCS per shaft hole and (b) the effect of drying-duration on the averaged UCS
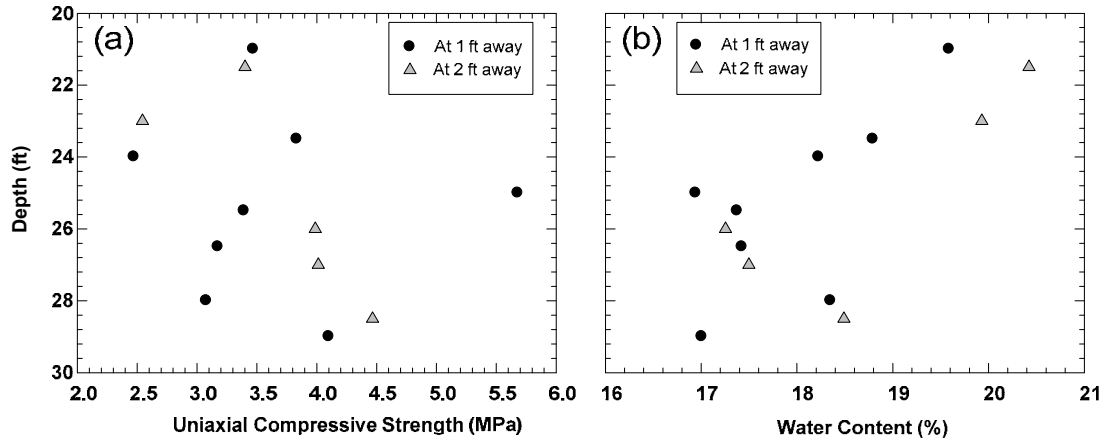
Figure 1.6.12 The variation of (a) UCS and (b) water content with depth measured from investigation cores obtained at 0.3 m (1 ft) and 0.6 m (2 ft) away from the center of Shaft Hole #16

Figure 1.6.14 shows the probable configuration of the degraded zone. The bases of this conclusion are as follows:

- The entire clay shales between the verification core hole and the investigation coring location are degraded.

- The NX-size investigation core is located 0.3 m (1 ft) away from the center, indicating the distance from the core hole wall to the center of the NX-size investigation core is 17.8 cm (7 in).

- 2.5 cm (1 in) is subtracted because half the NX-size (1 in) investigation core is fresh.

- One additional inch is subtracted because of the difficulty of placing the core bit at exactly 0.3 m (1 ft) away from the center. Hence, one inch of variation is accounted for.

Even though the fourth conclusion seems to be imprecise, the shale right next to the NX-size investigation core is not likely to degrade entirely. Therefore, these assumptions are still thought to result in a conservative estimation. The thickness of the degraded zone from the verification core to the fresh zone is proposed to be 12.7 cm (5 in) from the verification core wall in an extreme case such as long drying-duration in arid conditions. The degraded zone is minimal when concrete is poured immediately after the verification core is augered, in which case drying is not introduced. The vertical thickness of the degraded zone at the bottom of drilled shafts was not investigated specifically; however, we can draw a conclusion based on the estimation of the radial directional degraded zone. To test for an extreme case, a 12.7 cm (5 in)-thick degraded zone vertically from shaft bottom may lead to a conservative and reasonable assumption.

167

Table 1.6.2 summarizes what might happen to the clay shales at the bottom of drilled shafts during construction within an eight-hour time frame. The eight hours of construction is selected because construction of drilled shafts is planned, ideally, to be completed within one day, which allows the maximum eight hours of drying. The eight-hour time gap between augering and concrete pouring was divided into five sub-groups depending on the drying and wetting duration. For example, if the verification core wall is dried for six hours, the Eagle Ford Shale is subject to wetting for two hours. In the table, the jar slake test results are shown in order to understand how the clay shales react to the water in the free-swelling condition. The status of concrete filled in the verification core is also stated for reference.
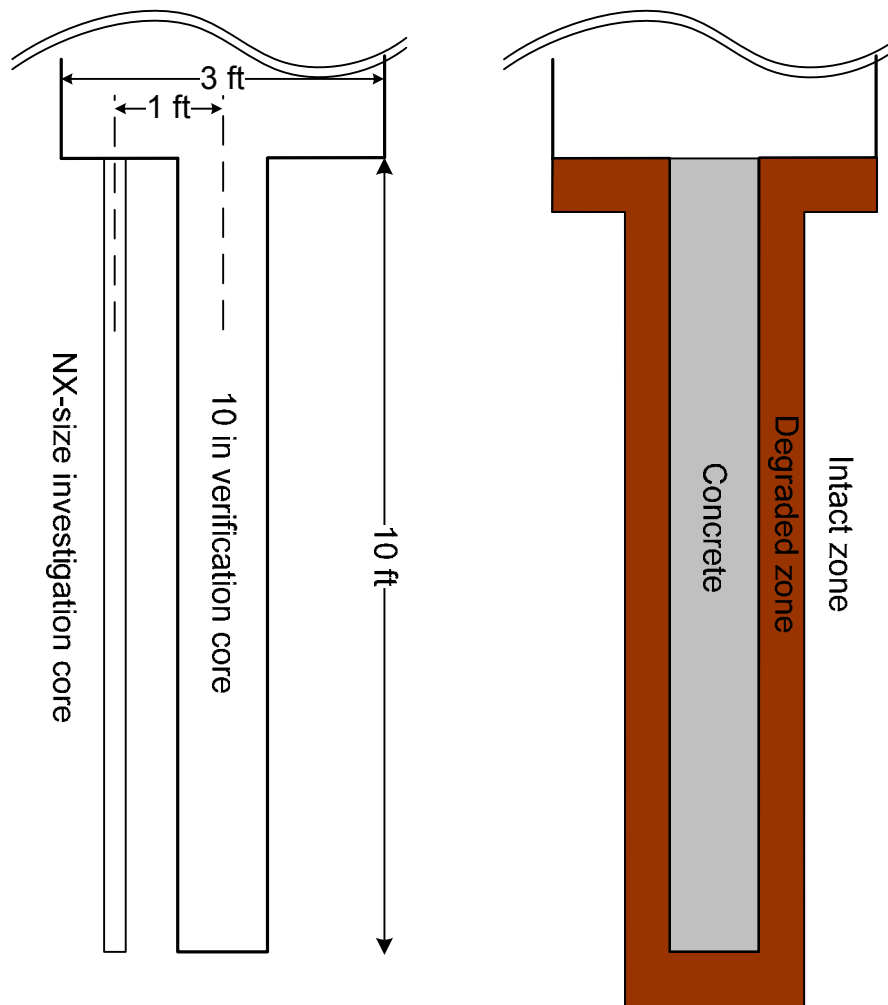
Figure 1.6.13 Scaled conceptual model of degraded zone and non-degraded zone

When the shales are dried for eight hours, meaning the shales were entirely dried without wetting, the core-filled concrete should be solid. In this case, the drying would not affect the strength of clay shales. On the other hand, if the clay shales are dried, the shales start degrading upon contact with water. The degradation extent depends on the drying-duration, thus the results of the jar slake test provided in Section 1.5 are used to define the required drying-duration that results in 12.7 cm (5 inch)-thick degraded zone.

As discussed in Section 1.5, the test specimens used for jar slake tests were dried for 0 – 48 hours and were immersed under water. The durability of all clay shales are qualitatively classified, and the severe degradation threshold was defined as 8 hours for Eagle Ford Shale and 4 hours for the other clay shales (Del Rio Clay, Taylor Marl, and Navarro Shale: refer to Section 1.5.5). Therefore, the clay shales dried for 0 hours are regarded as fresh or near fresh; those dried for more than the proposed threshold are regarded as severely degraded; and those dried for intermediate duration are regarded as slightly degraded. When the jar slake test results indicate that the clay shale exhibits severe degradation, the maximum thickness of the degraded zone (12.7 cm, 5 in) is assigned. However, the degraded zone would not extend significantly when the lab test specimens of clay shales are slightly degraded, because the dimension of the test specimens is roughly 2.5 cm × 2.5 cm × 1.3 cm (1 in × 1 in × 0.5 in) and those do not severely degrade under water. Assigning the maximum thickness of 12.7 cm (5 in) appears to be overly conservative when the specimen of that dimension is slightly degraded. Therefore, the specimens that were defined as slightly degraded in jar slake test are also considered fresh or near fresh when the degraded zone thickness is determined.

Based on the foregoing discussion and Table 1-2, the thickness of degraded zone around the verification core is determined as shown in Table 1.6.3. When the jar slake test results indicate the formation is severely degraded, the thickness of the degraded zone is assumed to be 12.7 cm (5 in), which implies that the entire clay shales between the NX size investigation core and the verification core wall are degraded. For other cases within an 8-hour time frame, the clay shales are not likely to degrade severely; consequently, the thickness is set to zero. It should be pointed out that the thickness of the degraded zone (12.7 cm, 5 in) is developed based on the full-scale condition test of Eagle Ford Shales, not of the other three clay shales. Therefore, further investigation of other formations is necessary to confirm the thicknesses for other clay shales. The vertical thickness of the degraded zone at the bottom of drilled shafts is assumed to be identical to the horizontal thickness (12.7 cm, 5 in).

The time frame may extend to 48 hours, which is the upper limit of this research. We observed from numerous jar slake tests that the clay shales slaked within 30 minutes of when the specimens were submerged in water. The difference between the samples soaked for 30 minutes and those soaked for 24 hours is negligible when the samples are dried for the same period. Hence, the thickness of the degraded region is a function of drying-duration, not of wetting duration. Based on this conclusion, a 16-hour, or longer, time frame may be developed (see Table 1.6.4). The critical points are: 1) how long the clay shales dry and 2) whether water flows into and fills in the verification core prior to the pouring of concrete. The thickness of the degraded zones of Del Rio Clay, Taylor Marl, and Navarro Shale are 12.7 cm (5 in) when those formations are dried for more than 4 hours and are subsequently in contact with water. On the other hand, the thickness of the degraded zone of Eagle Ford Shale is the maximum 12.7 cm (5 in) when it is dried for more than 8 hours. Degradation is not likely to occur when water is not present in the verification core.

The degraded zone has been proposed depending on the formations, drying-duration, and existence of water. In Texas, the clay shales at the bottom of drilled shafts that disintegrate severely before casting concrete are typically reamed out (personal conversation with TxDOT representative, 2008). Thus, the top degraded zone is

eliminated for final configuration of the degraded zone such that the shaft tip is in direct contact with fresh shales. The proposed degraded zone around the verification core is shown in Figure 1.6.14 (a), and the final configuration after reaming the vertical 12.7 cm (5 in)-thick degraded zone at the shaft bottom is shown in Figure 1.6.14 (b).

Table 1.6.2 Drying and wetting in the field within 8 hours of construction

Time gap	Drying (hrs)	Wetting (hrs)	Concrete in V.C.	Jar Slake test observation (core hole wall status)			
				Eagle Ford	Del Rio	Taylor Marl	Navarro
8	8	0	Solid	n/p	n/p	n/p	n/p
	6	2	Aggregate	Slight deg	Severe deg	Severe deg	Severe deg
	4	4	Aggregate	Near Fresh	Severe deg	Severe deg	Severe deg
	2	6	Aggregate	Near Fresh	Slight deg	Slight deg	Slight deg
	0	8	Aggregate	Fresh	Near Fresh	Near Fresh	Near Fresh

* n/p means not problematic, deg means degradation

Table 1.6.3 Thickness of the degraded zone at the bottom of drilled shafts (in an 8-hour time frame)

Time gap	Drying (hrs)	Wetting (hrs)	Concrete in V.C.	Thickness (in)			
				Eagle Ford	Del Rio	Taylor Marl	Navarro
8	8	0	Solid	0	0	0	0
	6	2	Aggregate	0	5	5	5
	4	4	Aggregate	0	5	5	5
	2	6	Aggregate	0	0	0	0
	0	8	Aggregate	0	0	0	0

Table 1.6.4 Drying and wetting in the field within 16 hours of construction

Time gap	Drying (hrs)	Wetting (hrs)	Concrete in V.C.	Jar Slake test observation (core hole wall status)			
				Eagle Ford	Del Rio	Taylor Marl	Navarro
16	16	0	Solid	n/p	n/p	n/p	n/p
	12	4	Aggregate	Severe deg	Severe deg	Severe deg	Severe deg
	8	8	Aggregate	Severe deg	Severe deg	Severe deg	Severe deg
	4	12	Aggregate	Slightly deg	Severe deg	Severe deg	Severe deg
	0	16	Aggregate	Fresh	Near Fresh	Near Fresh	Near Fresh

Index Properties of Eagle Ford Shales

In this section, material parameters of Eagle Ford Shale and the relationships among these parameters are provided. Since the strength of Eagle Ford Shales was found to be independent of drying-duration and coring location, the tested cores were believed to be fundamentally identical. The test results were analyzed to establish correlations.
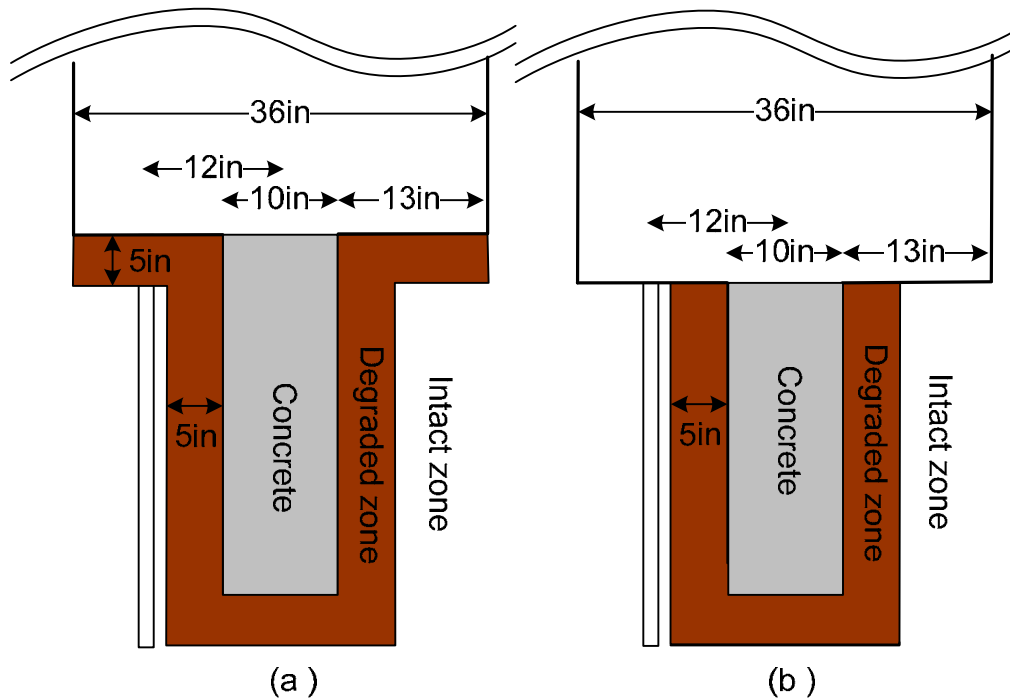
Figure 1.6.14 Configurations of the degraded zone (a) before the degraded shales were rimmed out and (b) after the degraded shales were reamed out

The histograms of four different material properties of Eagle Ford Shales are presented in Figure 1.6.15. Both the UCS and PLI appear to be subject to normal distribution whereas dry density and water content do not. The average values of dry density, water content, the UCS, and the PLI were calculated to be 1.7 g/cm^3, 18.41%, 3.6 MPa, and 0.22 MPa, respectively.

Figure 1.6.16 presents the effect of: (a) water content on UCS, (b) dry density on the UCS, (c) water content on the PLI, and (d) the PLI on UCS. The PLI in the figure was obtained by averaging the test results of several samples per one UCS test. The correlation coefficients of each graph were calculated to be small indicating the correlation is relatively weak due to spatial rock variability. The UCS tends to decrease as water content increases with r^2 equaling to 0.17. This finding coincides with the observation from laboratory controlled tests on Eagle Ford Shales, which shows that the effect of water content is related to principal stress difference whereas the effect of drying-duration is minimal (See Figure 1.5.35 and 1.5.39).
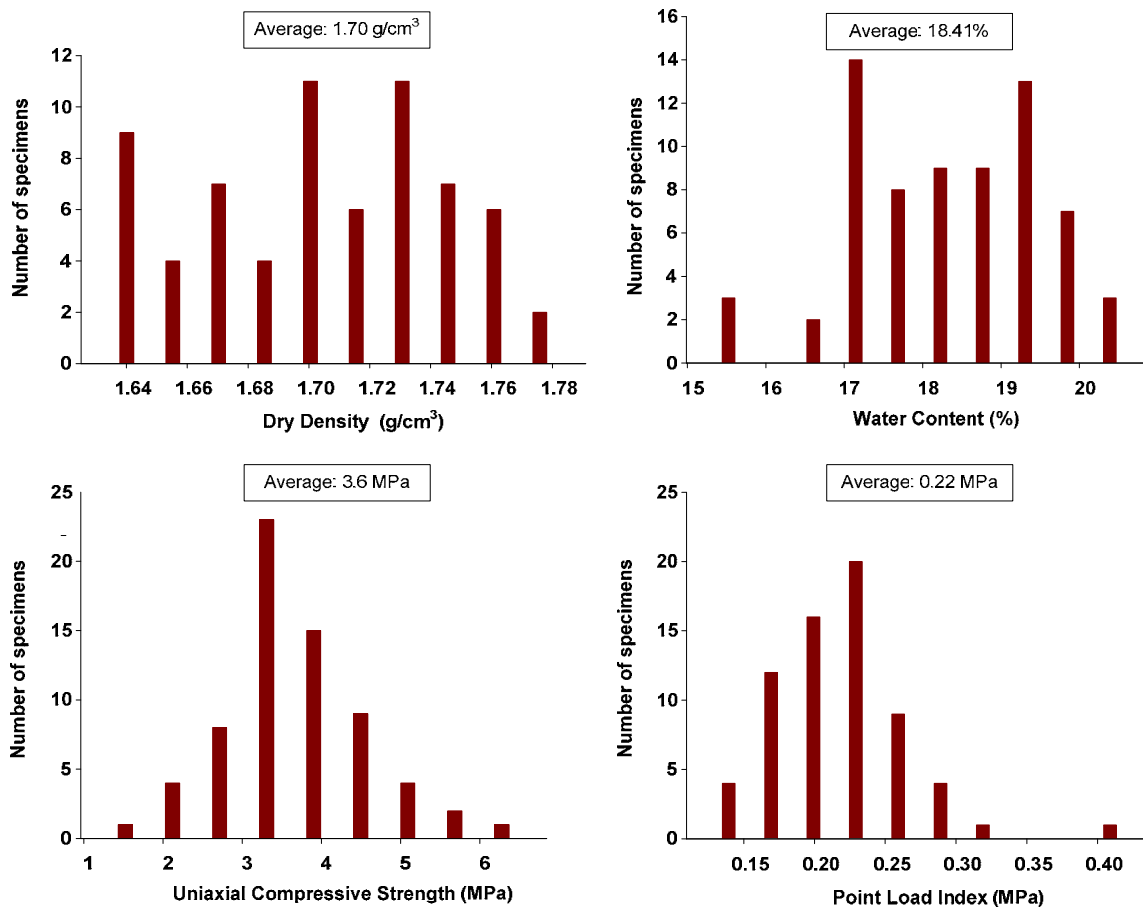
Figure 1.6.15 Distributions of the material properties of Eagle Ford Shales

Linear regression analysis was conducted to find correlations among material parameters. The line was drawn through a series of data points such that the square of the deviation from the line to data points converges to the minimum. The regression line best

173

fits the data sets when the correlation coefficient, r, approaches a unity. The UCS increases as dry density increases, but the r^2 is calculated to be as low as 0.08. As water content increase, the PLI decreases with r^2 equaling to 0.37, which is the largest value in all trend lines of raw data in Figure 1.6.16. The effect of water content on the PLI is clearer than that of the UCS, which may be because the PLI values were the averages of several tests, resulting in elimination of spatial variability. The correlation between the PLI and UCS is shown, in Figure 1.6.16 (d), with a conversion factor of 16.1. Even if the r^2 is as low as 0.13, the conversion factor may be of interest to engineers, because point load tests are the most frequently and easily conducted tests in the field.

Table 1.6.9 presents the conversion factors from the PLI to UCS for sedimentary rocks (Tsiambaos and Sabatakakis, 2004). The conversion factors of sedimentary rocks are divided into three classes depending on PLI values. Strong sedimentary rock tends to result in a high conversion factor. The average PLI of Eagle Ford Shale was found to be 0.22 MPa, which belong to Class I in the table, yet the conversion factor obtained for Eagle Ford Shale was 16.1, which is higher than the proposed value in the literature. The literature established the conversion factors for limestone, which may result in a different conclusion. Therefore, the conversion factor for clay shales must be separately established because the different conversion factor would lead to significant difference in estimation of the UCS. The rule-of-thumb number for the conversion factor is around 25, which is fundamentally applicable to hard rock. This high value for the conversion factor will lead to unconservative design for clay shales such as Eagle Ford Shale.

Rock variability might be eliminated by averaging these values. Hence, raw data shown in Figure 1.6.16 were reduced to fewer data points by averaging obtained properties according to the following standards: 1) shaft hole, 2) depth, and 3) water content. For example, all raw test results are averaged per each shaft hole to obtain representative value for the shaft hole. The reduced data obtained from averaging are shown from Figure 1.6.17 through Figure 1.6.19. The information of each approach is provided in the next paragraph. It was found that averaging significantly eliminates the effect of rock variability, resulting in a higher correlation coefficient.
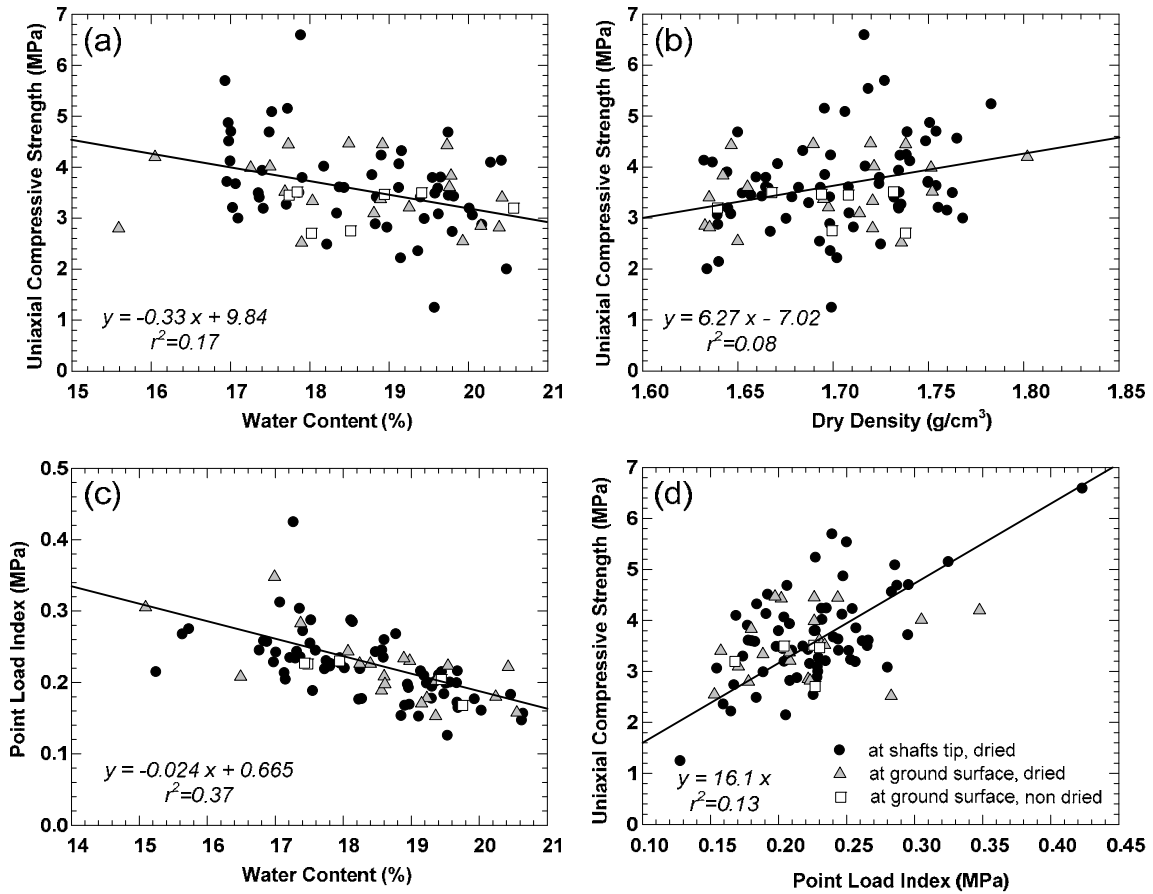
Figure 1.6.16 Correlations among parameters: (a) water content and UCS, (b) dry density and UCS, (c) water content and PLI, and (d) PLI and UCS.

175

Table 1.6.5 Conversion factors between uniaxial compressive strength (UCS) and the point load index (PLI, I$_{s(50)}$) for sedimentary rocks (after (Tsiambaos and Sabatakakis, 2004))

Class	Point Load Strength (I$_{s(50)}$) (MPa)	Conversion Factor
I	< 2	13
II	$2 - 5$	20
III	> 5	28

Firstly, the material properties were averaged by grouping properties per each shaft hole, and the results are presented in Figure 1.6.17. The error bars represent one standard deviation. Using averaged values, the correlation coefficients of all correlations were calculated to be considerably higher than those shown in Figure 1.6.16 (See Table 1.6.9). Averaging values reduce rock-variability effects although the standard deviation of UCS is more than 1 MPa for a few cases. The measured standard deviation per shaft hole is tabulated in Table 1.6.6; and the largest of the standard deviations was observed in Shaft Hole #17 that was dried for 48 hours. The correlation coefficient between dry density and UCS, and water content and the PLI were found to be 0.85 and 0.56. However, the relationship between UCS and the PLI was not reasonably captured by the trend line that passes through origin.

Secondly, test results are averaged per cored depths, as shown in Figure 1.6.18, assuming shales from similar depth are physically similar. Cores were classified into nine groups based on cored depths (0.3 m (1 ft) intervals from 6.4 m (21 ft) to 9.1 m (30 ft)), and the results were plotted with one standard deviation bar. The explanation for reducing the number of specimens at deeper elevation is that several investigation cores were obtained only from the top five ft (6.1 m (20 ft) to 7.6 m (25 ft) below the ground surface). Compared to Figure 1.6.17, the standard deviation appears to decrease, indicating that the rock cores tend to be relatively similar material at similar depth (see Table 1.6.7). In other words, the horizontal variation of rock properties is smaller than the vertical variation. The average of the standard deviations obtained is 0.76 MPa for the second method, whereas that of the first method is 0.85 MPa.

The third method adopted in this study is averaging values based on water content because water content is generally known as a significant factor affecting the strength of shales (Ghafoori et al., 1993; Greene and Schaffer, 1997; Lashkaripour, 2002). The test results were re-arranged into six groups based on water content, and the averaged values were plotted in Figure 1.6.19. The correlation coefficient, r^2, was measured to be 0.78, 0.83, 0.59, and 0.73, respectively. The standard deviation per each range of water content is shown in Table 1.6.8 along with the number of averaged specimens. Most test specimens have water content ranging from 17% to 20%; 78 out of 94 test specimens belong to this range.

The correlation equations and correlation coefficients are tabulated in Table 1.6.9. Even though the trends among parameters were estimated to be similar, the equation of the trend lines and the correlation coefficients were found to be significantly different

from each other. Therefore, the engineer's judgment is required to select proper representative values among these three methods.
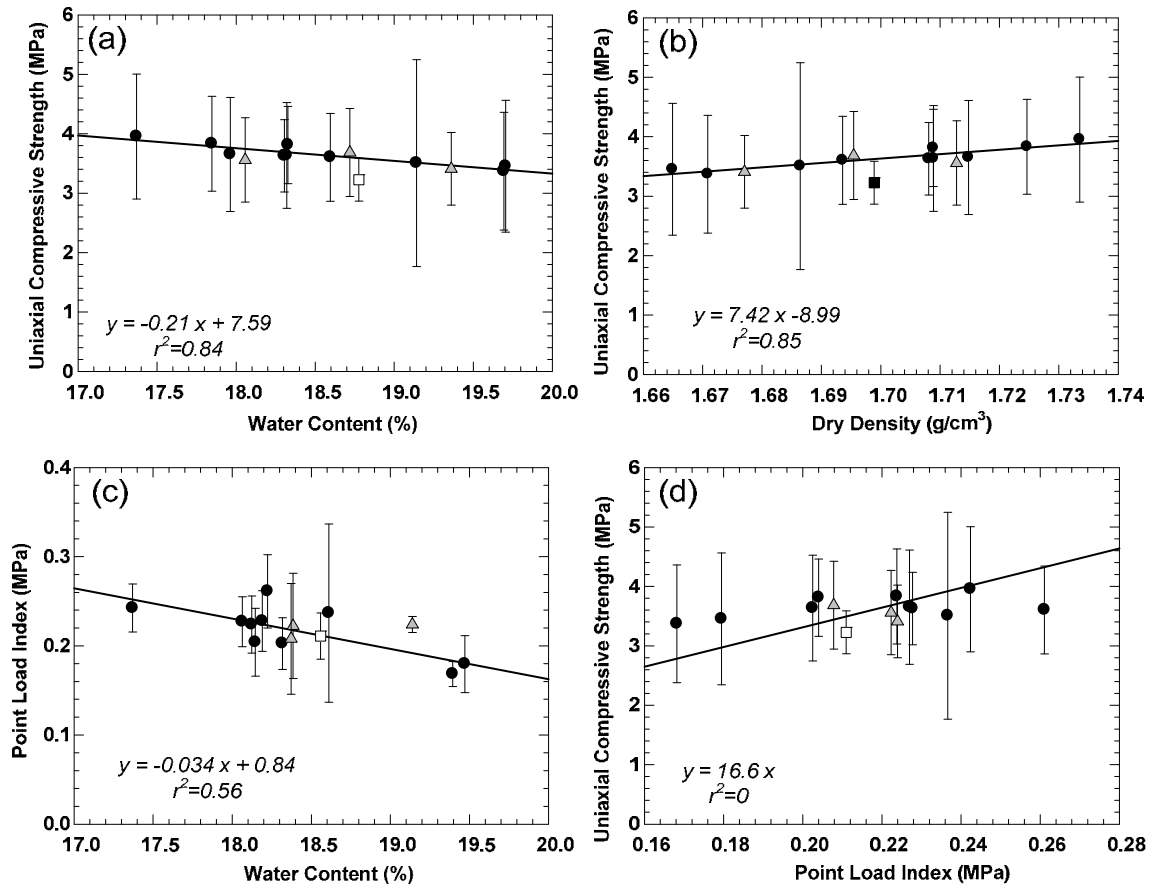
Figure 1.6.17 Correlations among parameters by averaging values per each hole: (a) water content and UCS, (b) dry density and UCS, (c) water content and PLI, and (d) PLI and UCS.

Table 1.6.6 Standard deviation of the UCS results averaged per shaft hole

Shaft Number	Standard Deviation (MPa)	Number of Specimens	Shaft Number	Standard Deviation (MPa)	Number of Specimens
3	1.05	6	14	0.99	4
4	0.89	8	15	0.61	7
5	1.11	6	16	0.96	8
7	0.71	9	16-1	0.74	5
8	0.61	6	17	1.74	6
9	0.74	7	18	0.80	6
13	0.65	9	20	0.36	7
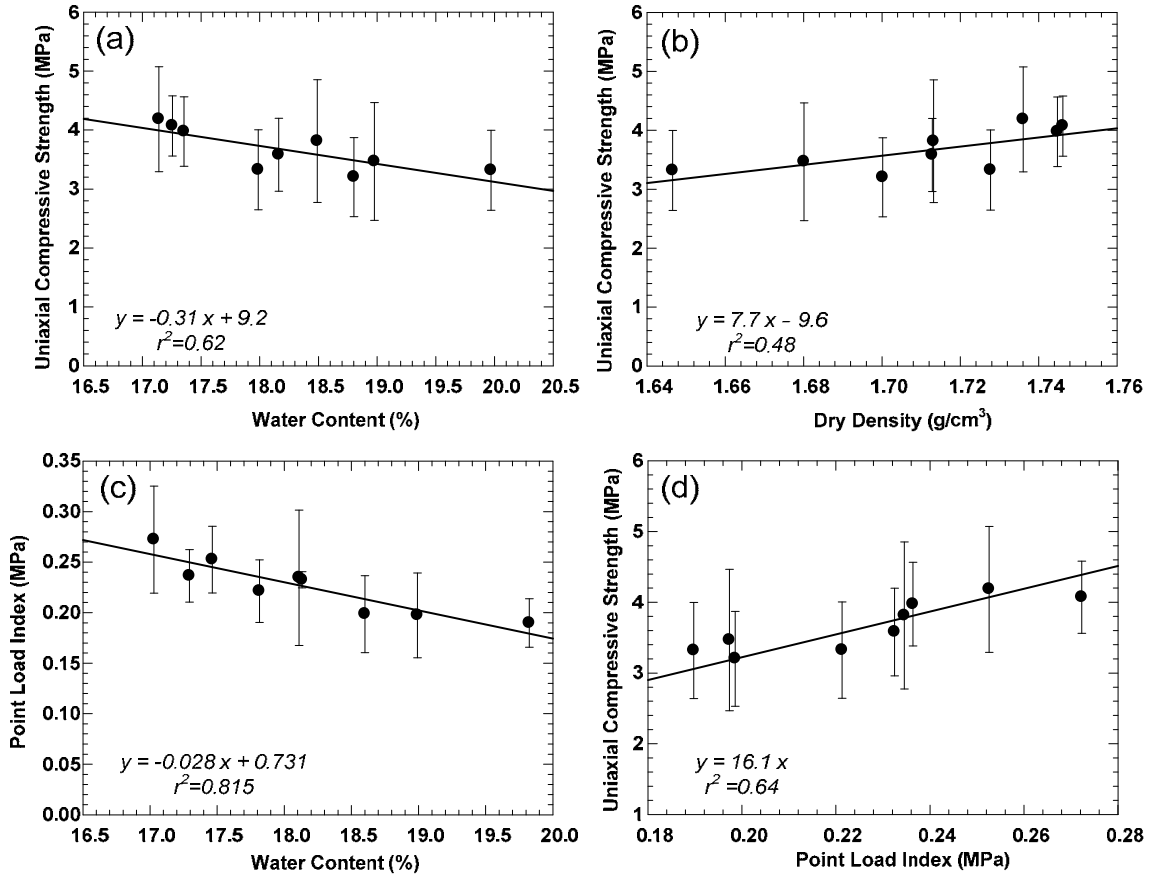
Figure 1.6.18 Correlations among parameters by averaging values per each depth: (a) water content and UCS, (b) dry density and UCS, (c) water content and PLI, and (d) PLI and UCS.

Table 1.6.7 Standard deviation of the UCS results averaged per depth

Depth (ft)	Standard Deviation (MPa)	Number of Specimens	Depth (ft)	Standard Deviation (MPa)	Number of Specimens
20-22	0.68	19	22-23	1.00	13
23-24	0.67	14	24-25	1.04	12
25-26	0.89	12	26-27	0.59	8
27-28	0.51	5	28-29	0.68	7
29-30	0.62	4			
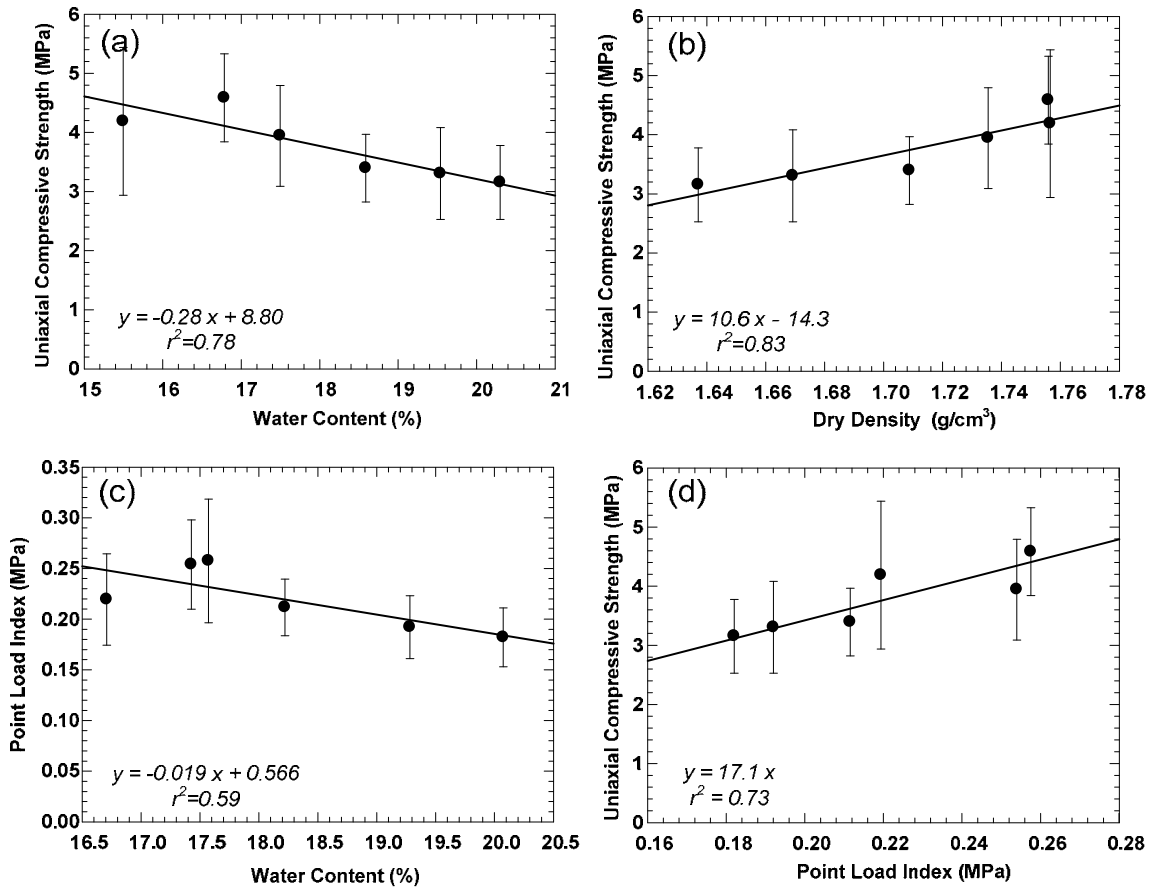
Figure 1.6.19 Correlations among parameters by averaging values per water content: (a) water content and UCS, (b) dry density and UCS, (c) water content and PLI, and (d) PLI and UCS.

Table 1.6.8 Standard deviation of the UCS results averaged per water content

Water Content (%)	Standard Deviation (MPa)	Number of Specimens
15-16	1.25	3
16-17	0.74	5
17-18	0.85	29
18-19	0.57	20
19-20	0.78	27
20-21	0.62	10

Table 1.6.9 Correlation equations and correlation coefficients of trend lines

Averaging method	Relationship	Correlation equation	R^2
Raw Data	Water content vs UCS	y = - 0.33 x + 9.84	0.17
	Dry density vs. UCS	y = 6.27 x – 7.02	0.08
	Water content vs. PLI	y = -0.024 x + 0.665	0.37
	PLI vs. UCS	y = 16.1 x	0.13
Shaft Hole	Water content vs UCS	y = - 0.21 x + 7.59	0.84
	Dry density vs. UCS	y = 7.42 x – 8.99	0.85
	Water content vs. PLI	y = - 0.034 x + 0.84	0.56
	PLI vs. UCS	y = 16.6 x	0
Depth	Water content vs UCS	y = - 0.31 x + 9.2	0.62
	Dry density vs. UCS	y = 7.7 x – 9.6	0.48
	Water content vs. PLI	y = - 0.028 x + 0.731	0.82
	PLI vs. UCS	y = 16.1 x	0.64
Water Content	Water content vs UCS	y = -0.28 x + 8.8	0.78
	Dry density vs. UCS	y = 10.6 x – 14.3	0.83
	Water content vs. PLI	y = - 0.019 x + 0.57	0.59
	PLI vs. UCS	y = 17.1 x	0.73

1.6.6 Summary

A total of eighteen non-production shaft holes were drilled, and 25.4 cm (10 in) verification cores were augered at the center of each shaft hole. In order to research the drying-duration effect on shale strength, verification cores were dried for 0 to 48 hours, and NX-size investigation cores were consequently obtained 0.3 m (1 ft) away from the verification core holes. From 94 UCS tests for each core hole, we concluded that drying-duration does not result in shale strength at 0.3 m (1 ft) away from verification cores in Eagle Ford Shale. Based on this finding, the degraded region was conservatively estimated, and the extent was assumed to be 25.4 cm (10 in) from the center of the verification core hole, meaning 12.7 cm (5 in) from the core wall for extreme conditions (48 hours of drying and 1-week submerging). It was expected that the thickness of the degraded zone maximizes up to 12.7 cm (5 in) when Del Rio Clay, Taylor Marl, Navarro Shales were dried for 4 or more hours. For Eagle Ford Shale, the thickness increases as much as 12.7 cm (5 in) for an 8-hour or more drying-duration. No degradation is expected if water is not present in the verification core at the time of concrete placement. In addition to the definition of the degraded zone, the correlations among the index

properties of Eagle Ford Shales were provided. It was found that averaging material properties significantly reduces the rock spatial variability.

REFERENCES

Abu-Hejleh, N. M., M. W. O'Neill, D. Hanneman, and W. J. Attwooll (2003). "Improvement of the geotechnical axial design methodology for Colorado's drilled shafts socketed in weak rocks," *CDOT-DTD-R-2003-6*. Denver: Department of Transportation.

Adkins, W. S. (1933). "The geology of Texas, part 2, The Mesozoic systems in Texas," *University of Texas Bulletin*, pp 239-518.

Akai, K. (1993). *Testing methods of indurated soils and soft rock - suggestions and recommendations*: Kinki Shupan Insatsu Co., Ltd. Press Inc.

Allen, P. M., and W. D. Flanigan (1986). "Geology of Dallas, Texas, United States of America," *Bulletin of the Association of Engineering Geologists*, Vol. 23, No. 4, pp 359-418.

API RP 13B-2 (1991). "API recommended practice standard procedure for field testing oil-based drilling fluids," *American Petroleum Institute*, pp pp. 9.32-39.36.

ASTM Standard D4543 (2007). "Standard practices for preparing rock core as cylindrical test specimens and verifying conformance to dimensional and shape tolerances," *American Society for Testing and Materials*.

ASTM Standard D5731 (2007). "Standard test method for determination of the point load index of rock," *American Society for Testing and Materials*.

Auken, F. M. V. (1963). "Shear strength of clay-shales found in the southwestern USA," *Proceedings of the Second Panamerican Conference on Soil Mechanics and Foundation*, pp 255-287.

Aurora, R. P., and L. C. Reese (1976). "Behavior of axially loaded drilled shafts in clay-shales," *Research Report 176-4*. Austin: Center for Highway Reserach, The University of Texas at Austin.

Baker Jr., C. N. (1985). "Comparison of caisson load tests on Chicago hardpan," In: C. N. Baker Jr., Ed., *Drilled Piers and Caissons II*. Reston, Va: ASCE, pp 99-113.

Barton, N., R. Lien, and J. Lunde (1974). "Engineering classification of rock masses for the design of tunnel support," *Publikasjon - Norges Geotekniske Institutt*, No. 106, p 48.

Bieniawski, Z. T. (1973). "Engineering classification of jointed rock masses," *Trans S Afr Inst Civ Eng*, Vol. 15, No. 12.

Bieniawski, Z. T. (1993). "Classification of rock masses for engineering: the RMR system and future trends," *Comprehensive Rock Engineering*, Vol. 3, pp 553-573.

Blatt, H. (1982). *Sedimentary Petrology*, New York, NY: William H. Freeman and Company.

Botts, M. E. (1986). "The effects of slaking on the engineering behavior of clay shales." *Ph.D. Dissertation*, Civil Engineering, University of Colorado.

Botts, M. E. (1998). "Effects of slaking on the strength of clay shales: A critical state approach," *The Geotechnics of Hard Soils--soft Rocks: Proceedings of the Second International Symposium on Hard Soils, Soft Rocks: Naples, Italy, 12-14 October 1998*.

Broch, E., and J. A. Franklin (1972). "Point-Load Strength Test," *International journal of rock mechanics and mining sciences*, Vol. 9, No. 6, pp 669-697.

Brouillette, R. P., R. E. Olson, and J. R. Lai (1993). "Stress-strain characteristics of Eagle Ford Shale," *Proceedings, International Symposium on Hard Soils-Soft Rocks*, pp 397-404.

Carrubba, P. (1997). "Skin friction of large-diameter piles socketed into rock," *Canadian Geotechnical Journal*, Vol. 34, No. 2, pp 230-240.

Chanchani, J., R. R. Berg, and C. I. Lee (1996). "Pressure solution and microfracturing in primary oil migration, Upper Cretaceous Austin Chalk, Texas Gulf Coast," *AAPG Bulletin*, Vol. 80, No. 9.

Chenevert, M. E. (1970). "Shale control with balanced-activity oil-continuous muds," *Journal of Petroleum Technology*, Vol. 22, pp 1309-1316.

Chimene, J. B. (1983). "Ostracode biostratigraphy and depositional environments of the Upper Taylor Group (Campanian, Upper Cretaceous) in Central Texas." Department of Geosciences, University of Houston-University Park.

Clark, A. K., J. R. Faith, C. D. Blome, and D. E. Pedraza (2006). "Geologic map of the Edwards aquifer In Northern Medina and Northeastern Uvalde Counties, South-central Texas."

Coates, D. F. (1964). "Classification of rocks for rock mechanics," *International Journal Rock Mechanics and Mining Science*, Vol. 1.

Crawford, A. M., and D. A. Wylie (1987). "A modified multiple failure state triaxial testing method," *28th US Symposium on Rock Mechanics*. Tucson, pp 133-140.

Cuenca, F. A. (1989). "Stability of reinforced embankments constructed of high plasticity clays." *Ph.D. Dissertation*, Department of Civil Engineering, The University of Texas at Austin.

Dawson, W. C. (2000). "Shale Microfacies: Eagle Ford Group (Cenomanian-Turonian) North-Central Texas Outcrops and Subsurface Equivalents," *Transaction Gul Coast Association of Geological Societies*, pp 607-622.

Dawson, W. C., and D. F. Reaser (1996). "Austin Chalk (Uppermost Santonian) Discontinuity Surface, North-Central Texas," *Transaction-Gulf Coast Association of Geological Societies*, pp 79-86.

Deen, R. C. (1981). "The need for a schema for the classification of transitional (shale) materials," *ASTM Geotechnical Testing Journal, GTJODJ*, Vol. 4, pp 3-10.

Deere, D. U. (1968). "Rock mechanics in engineering practice," In: K.G. Stagg, and O.C. Zienkiewicz, Eds. London: John Wiley Publishing.

Deere, D. U., and R. P. Miller (1966). "Engineering classification and index properties for intact rock. Air Force Weapons Lab," *Technical Report, AFWL-TR 65-116*. Kirtland Base, New Mexico.

Dick, J. C., and A. Shakoor (1992). "Lithologic controls of mudrock durability," *Quarterly Journal of Engineering Geology*, Vol. 25, pp 31-46.

Dick, J. C., and A. Shakoor, Eds. (1997) *The locations and engineering characteristics of weak rock in the US*, Denver, CO: Association of Engineering Geologist.

Dunn, J. R., and P. P. Hudec (1965). *The influence of clays on water and ice in rock pores*: Bureau of Physical Research.

Engeling, D. E., and L. C. Reese (1974). "Behavior of three instrumented drilled shafts under short term axial loading," *Research Report 176-3*. Austin: Center for Highway Research, The University of Texas at Austin.

Font, R. G. (1979). "Geotechnical properties of unstable clay shales in north-central Texas," *Texas Journal of Science*, Vol. 31, No. 2, pp 119-124.

Fox, T. J. (1979). "A study of slope stability in stiff-fissured clays in the Austin area, Texas." *M.S. Thesis*, Department of Civil Engineering, University of Texas at Austin.

Franklin, J. A. (1981). "A Shale rating system and tentative applications to shale performance."

Franklin, J. A., and R. Chandra (1972). "The slake durability test," *International Journal of Rock Mechanics and Mineral Science*, Vol. 9, pp 325-341.

Funk, A. C. (1975). "The relationships of engineering properties to geochemistry in the Taylor Group, Travis County, Texas." *Master of Art Thesis*, University of Texas at Austin.

Gamble, J. C. (1971). "Durability-plasticity classification of shales and other argillaceous rocks." *Ph.D. Dissertation*, University of Illinois at Urbana-Champaign.

Garner, L. E., and K. P. Young (1976). *Environmental geology of the Austin area: an aid to urban planning*: Bureau of Economic Geology, University of Texas at Austin.

GCTS manual (2007). "CATS Triaxial Test Mode 1.79: User's Guide and Reference." Tempe, Arizona.

Ghafoori, M., M. Mastropasqua, J. P. Carter, and D. W. Airey (1993). "Engineering properties of Ashfield shale, Australia," *Bulletin of the International Association of Engineering Geology*, No. 48, pp 43-57.

Glos, G. H., III, and O. H. Briggs, Jr. (1983). "Rock sockets in soft rock," *Journal of Geotechnical Engineering*, Vol. 109, No. 4, pp 525-535.

Goeke, P. M., and P. A. Hustad (1979). "Instrumented drilled shafts in clay-shale," In: E.M. Fuller, Ed., *Proceeding Sympoium on Deep Foundation*. Atlanta, GA: ASCE, pp 149-164.

Goodman, R. E. (1993). *Engineering geology: rock in engineering construction*, New York, NY: John Wiley and Sons.

Grainger, P. (1984). "The classification of mudrocks for engineering purposes," *Quarterly Journal of Engineering Geology and Hydrogeology*, Vol. 17, No. 4, pp 381-387.

Gray, G. R., H. C. H. Darley, and W. F. Rogers (1980). *Composition and properties of oil well drilling fluids*, Houston, London, Paris, Tokyo: Gulf Publishing Company.

Greene, B. H., and A. Schaffer, Eds. (1997) *Laboratory measurement of weak rock strength*, Denver, CO: Association of Engineering Geologists.

Gulla, G., M. C. Mandaglio, and N. Moraci (2006). "Effect of weathering on the compressibility and shear strength of a natural clay," *Canadian Geotechnical Journal*, Vol. 43, No. 6, pp 618-625.

Hanson, J. A., and T. A. Small (1995). "Geologic Framework and Hydrologic Characteristics of Edwards Aquifer Outcrop, Hay County, Texas," *Water-Resources Investigation Report 95-4265* Austin, Texas: U.S. Geological Survey.

Hinds, G. A., and R. R. Berg (1990). "Estimating organic maturity from well logs, Upper Cretaceous Austin Chalk, Texas Gulf coast," *Texas Gulf Coast. Trans. GCAGS 40*.

Hoek, E. (1990). "Estimating Mohr-Coulomb friction and cohesion values from the Hoek-Brown failure criterion," *Int. J. Rock Mech. Min. Sci. & Geomach. Abstr.*, Vol. 27, pp 227-229.

Hoek, E. (1994). "Strength of rock and rock masses," *ISRM News Journal*, Vol. 2, No. 2, pp 4-16.

Hoek, E., and E. T. Brown (1997). "Practical estimates of rock mass strength," *Int J Rock Mech Min Sci*, Vol. 34, No. 8, pp 1165-1186.

Hopkins, T. C., and R. C. Deen (1983). "Identification of shales," *Geotechnical Testing Journal*, Vol. 7.

Horvath, R. G., T. C. Kenney, and P. Kozicki (1983). "Mmethods of improving the performance of drilled piers in weak rock," *Canadian Geotechnical Journal*, Vol. 20, No. 4, pp 758-772.

Hsu, S. (1996). "Stability and failure mechanisms of slopes in weak rock masses." *Ph.D. Dissertation*, Department of Civil Engineering, The University of Texas at Austin.

Hsu, S. C. (1989). "Material properties evaluation for the marly claystone and chalk for the Upper Cretaceous period in Central Texas," *Unpublished M.S. report*. Austin: The University of Texas at Austin.

Hudec, P. P. (1982). "Statistical analysis of shale durability factors," *Transportation Research Record*, pp 28-35.

Hudson, J. A., E. T. Brown, and C. Fairhurst (1971). "Optimizing the control of rock failure in servo-controlled laboratory tests," *Rock Mechanics and Rock Engineering*, Vol. 3, No. 4, pp 217-224.

Hudson, J. A., S. L. Crouch, C. Fairhurst, and M. T. S. S. Corporation (1972). *Soft, Stiff and Servo Controlled Testing Machines: A Review with Reference to Rock Failure*: MTS Systems Corp.

Hummert, J. B., and T. L. Cooling (1988). "Drilled pier test, Fort Collins, Colorado," In: S. Prakash, Ed., *Proceedings of the Second International Conference on Case Histories in Geotechnical Engineering*. Rolla, Missouri, pp 1375-1382.

ISRM (1979). "Suggested method for determining water content, porosity, density, absorption and related properties, and swelling and slake durability properties," *International Journal of Rock Mechanics and Mineral Science & Geomechanics Abstract*, Vol. 16, pp 141-156.

Jubenville, M. D., and R. C. Hepworth (1981). "Drilled pier foundations in shale - Denver, Colorado area," *Drilled piers and caissons, Proc., Session at the ASCE National Convention*. Reston, Va, pp 66-81.

Kim, M. M., and H. Y. Ko (1979). "Multistage triaxial testing of rocks," *Geotechnical Testing*, Vol. 2, pp 98-105.

Kovari, K., and A. Tisa (1975). "Multiple failure state and strain controlled triaxial tests," *Rock Mechanics and Rock Engineering*, Vol. 7, No. 1, pp 17-33.

Kovari, K., A. Tisa, H. H. Einstein, and J. A. Franklin (1983). "Suggested methods for determining the strength of rock materials in triaxial compression: revised version," *International journal of rock mechanics and mining sciences*, Vol. 20, No. 6, pp 283-290.

Lai, J. (1997). "Mechanical behavior of Eagle Ford shale." *Ph.D. Dissertation*, Department of Civil Engineering, The University of Texas at Austin.

Lashkaripour, G. R. (2002). "Predicting mechanical properties of mudrock from index parameters," *Bulletin of Engineering Geology and the Environment*, Vol. 61, No. 1, pp 73-77.

Laughton, C., P. P. Nelson, and T. K. Lundin (1991). "The adoption of mechanized excavation techniques for the Superconducting Super Collider," *High Level Radioactive Waste Management*. Las Vegas, Nevada, pp 1098-1104.

Lee, S. G., and M. H. de Freitas (1989). "A revision of the description and classification of weathered granite and its application to granites in Korea," *Quarterly Journal of Engineering Geology and Hydrogeology*, Vol. 22, No. 1, p 31.

Leung, C. F., and H. Y. Ko (1993). "Centrifuge model study of piles socketed in soft rock," *Soils and Foundations*, Vol. 33, No. 3, pp 80-91.

Lundin, T. K., C. Laughton, and P. P. Nelson (1990). "The first tunnel section of the Superconducting Super Collider project," *AGM and Conference*. Vancouver, British Columbia: Tunneling Association of Canada.

Lutton, R. J. (1977). *Design and construction of compacted shale embankments, volume 3*: Dept. of Transportation, Federal Highway Administration, Office of Research.

Marques, E. A. G., E. D. A. Vargas, and F. S. Antunes (2005). "A study of the durability of some shales, mudrocks and siltstones from Brazil," *Geotechnical and Geological Engineering*, Vol. 23, No. 3, pp 321-348.

Martin, R. P., and S. R. Hencher (1986). "Principles for description and classification of weathered rock for engineering purposes," *Geological Society, London, Engineering Geology Special Publications*, Vol. 2, No. 1, pp 299-308.

McVay, M., K. Ellis, M., J. Villegas, S.-H. Kim, and S. M. Lee (2003). "Static and dynamic fielding testing of drilled shafts: suggested guidelines on their use and for FDOT structures," *Report No. WPI No. BC354-08*: FDOT, Department of Civil and Coastal Engineering, University of Florida.

Mead, W. J. (1938). "Engineering geology of dam sites," *Transactions, Second*.

Morgenstern, N. R. (1979). "Geotechnical behaviour of clay shales - an overview," *Proceedings of the International Symposium on Soil Mech*. Mexico: Oaxaca, pp 29-52.

Morgenstern, N. R., and K. D. Eigenbrod (1974). "Classification of argillaceous soils and rocks," *American Society of Civil Engineers, Journal of the Geotechnical Engineering Division*, Vol. 100, No. 10, pp 1137-1156.

Nam, M. (2004). "Improved design for drilled shafts in rock." *Ph.D. Dissertation*, Department of Civil Engineering, University of Houston.

Nelson, P. P. (1987). "Performance comparisons for tunneling projects in weak rock," In: I.W. Farmer, J.J.K. Daemen, C.S. Desai, C.E. Glass, and S.P. Neuman, Eds., *Rock Mechanics: Proceedings of the 28th US Symposium*. Tucson, AZ.

Nelson, P. P., and T. K. Lundin (1990). "Geotechnical characterization and construction methods for SSC tunnel excavation," *Unique Underground Structures Symposium*. Denver, CO.

Nichols, P. H., G. E. Peterson, and C. E. Wuestner (1968). "Summary of subsurface geology of northeast Texas," In: B.W. Beebe, Ed., *A symposium: American Association of Petroleum Geologists memoir 9*, pp 982-104.

O'Neill, M. W. (1998). "Applications of large diameter bored piles in the United States," *Proceedings of the Third International Geotechnical Seminar on Deep Foundations on Bored and Auger Piles*. Ghent, Belgium.

Olivier, H. J. (1979). "A new engineering-geological rock durability classification."

Olson, R. E., and R. P. Brouillette (1990). "Laboratory testing, samples from Superconducting Super Collider project," *Final Report to The Earth Technology Corporation under Contract SP-3133*: The University of Texas at Austin.

Olson, R. E., J. R. Lai, and S. C. Hsu (1993). "Measurement of rock properties for the Superconducting Super Collider Project," *Final report to the PB/MK team under contract SC-A25-1077*: The University of Texas at Austin.

Orpwood, T. G., A. A. Shaheen, and R. P. Kenneth (1989). "Pressuremeter evaluation of glacial till bearing capacity in Toronto Canada," In: F.H. Kulhawy, Ed., *Foundation Engineering: Current Principles and Practices*. Reston, Va., pp 16-28.

Osterberg, J. O. (2001). "Load testing high capacity piles: What have we learned," *Proceedings of the 5th International Conference on Deep Foundation Practice*. Singapore.

Radhakrishnan, R., and C. F. Leung (1989). "Load transfer behavior of rock-socketed piles," *Journal of Geotechnical Engineering*, Vol. 115, No. 6, pp 755-768.

Raibagkar, A. (2008). "Simulation of concrete flow into verification core hole at the bottom of drilled shafts." *M.S. Thesis*, Department of Civil Engineering, University of Texas at Austin.

Raney, J. A., P. M. Allen, D. F. Reaser, and E. W. Collins (1987). "Geology and geotechnical considerations of the SSC site in Texas," *Underground Tunnelling Advisory Panel*.

Reese, L. C., and W. R. Hudson (1968). "Field testing of drilled shafts to develop design methods," *Research Report 89-1*. Austin: Center for Highway Research, University of Texas at Austin.

Reichmuth, D. R. (1963). "Correlation of force displacement data with the physical properties of rock for percussive drilling systems," *Proceedings of the 5th U.S. Symposium of Rock Mechanics*. University of Minnesota, pp 33-60.

Richardson, D. N., and T. T. Wiles (1990). "Shale durability rating system based on loss of shear strength," *Journal of Geotechnical Engineering*, Vol. 116, No. 12, pp 1864-1880.

Russell, D. J. (1982). "Controls on shale durability: the response of two Ordovician shales in the slake durability test," *Canadian Geotechnical Journal*, Vol. 19, No. 1, pp 1-13.

Santi, P. M. (1995). "Classification and testing of weak and weathered rock materials: model based on Colorado Shales." *Ph.D. Dissertation*, Colorado School of Mines.

Santi, P. M., and B. C. Doyle, Eds. (1997) *The locations and engineering characteristics of weak rock in the US*, Denver, CO: Association of Engineering Geologist.

Santos, H. M. R., A. Diek, J. C. Roegiers, and S. A. B. Fontoura (1996). "Investigation of the effects of sample handling procedures on shale properties," *Proc. Conference Rock Mechanics, Rotterdam*, pp 951-958.

Schmitt, L., T. Forsans, and F. J. Santarelli (1994). "Shale testing and capillary phenomena," *International journal of rock mechanics and mining sciences*, Vol. 31, No. 5, pp 411-427.

Seedsman, R. (1986). "The behaviour of clay shales in water," *Canadian Geotechnical Journal*, Vol. 23, No. 1, pp 18-22.

Sheikh, S. A., W. O. N. Michael, and K. J. Kapasi (1985). "Behavior of 45 underream footing in Eagle Ford Shale ", *Research Report 85-12*. Houston: University of Houston.

Shumard, B. F. (1860). "Observations upon the Cretaceous strata of Texas," *Transactions of the Academy of Science of Saint Louis*, pp 582-590.

Strohm, W. E. (1980). "Design and construction of shale embankments: summary," Department of Transportation Report No. FHWA-TS-80-219.

Stroman, W. R., and A. L. Feese (1984). "Engineering properties of clay shales. report 5. strength and deformation properties of Pepper and Del Rio clay shales from Waco dam," *Technical Report S-71-6*. Vicksburg, Miss.: U.S. Army Engineer and Waterways Experiment Station.

Taylor, R. K. (1988). "Coal measures mudrocks; composition, classification and weathering processes," *Quarterly Journal of Engineering Geology*, Vol. 21, No. 1, pp 85-99.

Taylor, R. K., and T. J. Smith (1986). "The engineering geology of clay minerals; swelling, shrinking and mudrock breakdown," *Clay Minerals*, Vol. 21, No. 3, pp 235-260.

TECT (1990a). "Geomechnical characterization of the Eagle Ford Shale at the Superconducting Super Collider site," *SSC Geotechnical Report GR-66*: The Earth Technology Corporation.

TECT (1990b). "Geomechnical characterization of the Taylor Marl at the Superconducting Super Collider site," *SSC Geotechnical Report GR-68*: The Earth Technology Corporation.

Texas Department of Transportation (2006). "Geotechnical manual."

Thompson, W. R. (1994). "Axial capacity of drilled shafts socketed Into soft rock." *M.S. Thesis*, Department of Civil Engineering, Auburn University.

Thorne, C. P. (1980). "The capacity of piers drilled into rock," *Proceedings of the International Conference on Structure and Foundations on Rock*. Rotterdam, The Nethelands, pp 223-233.

Tsiambaos, G., and N. Sabatakakis (2004). "Considerations on strength of intact sedimentary rocks," *Engineering Geology*, Vol. 72, pp 261-273.

Underwood, L. B. (1967). "Classification and identification of shales," *ASCE Journal of the Soil Mechanics and Foundations Division*, Vol. 93, pp 97-116.

USBR (2006). "Engineering geology field manual," *Engineering Geology*. Denver, CO: Technical Service Center, Bureau of Reclamation, U.S. Department of the Interior.

Vijayvergiya, V. N., W. R. Hudson, and L. C. Reese (1969). "Load distribution for a drilled shaft in clay shale," *Research Report 89-5*. Austin: Center for Highway Research, University of Texas at Austin.

Vipulanandan, C., A. Hussain, and O. Usluogulari (2007). "Parametric study of open core-hole on the behavior of drilled shafts socketed in soft rock," *Geotechnical Special Publication*, No. 158.

Vipulanandan, C., and N. Moon (2005). "Case Studies on Testing Drilled Shafts Socketed In Uncemented Clay Shales in Texas," *Proceedings, Geo3*, pp 259-270.

Walkinshaw, J. L., and P. M. Santi (1996). "Chapter 21- Shales and other degradable materials. ," *Landslides: Investigation and Mitigation, TRB Special Report*, pp 555-576.

Watters, R. J., Ed. (1997) *The effects of weathering on rock masses*, Denver, CO: Association of Engineering Geologists.

Webb, D. L. (1976). "The behavior of bored piles in weathered Diabase," *Geotechnique*, Vol. 26, No. 1, pp 63-72.

Welsh, R. A., L. E. Vallejo, L. W. Lovell, and M. K. Robinson (1991). "The US office of surface mining (OSM) proposed strength-durability classification system:: In Kane, WF and Amadei, B," *Detection of and Construction at the Soil/Rock Interface, ASCE Geotechnical Special Publication No. 28*, pp pp. 125-140.

Williams, A. F. (1980). "The design and performance of piles socketed into weak rock." *Ph.D. Dissertation*, Department of Civil Engineering, Monash University.

Wilson, L. C. (1976). "Tests of bored and driven piles in cretaceous mudstone at port Elizabeth, South Africa," *Geotechnique*, Vol. 26, No. 1, pp 5-12.

Winston, P. W., and D. H. Bates (1960). "Saturated Solutions For the Control of Humidity in Biological Research," *Ecology*, Vol. 41, No. 1, pp 232-237.

Wood, L. E., and P. Deo (1975). "A suggested system for classifying shale materials for embankments," *Bulletin of the Association of Engineering Geologists*, Vol. 12, No. 1, pp 39-55.

Yoshida, N., N. R. Morgenstern, and D. H. Chan (1991). "Finite-element analysis of softening effects in fissured, overconsolidated clays and mudstones," *Canadian Geotechnical Journal*, Vol. 28, No. 1, pp 51-61.

Young, K. (1972). "Mesozoic history, Llano region," In: V.E. Barnes, W.C. Bell, S.E. Clabaugh, P.E. Cloud, McGehee Jr., R.V., P.U. Rodda, and K. Young, Eds., *Geology of the Llano region and Austin area, field excursion: Austin*, p 77.

Zhang, L., and H. H. Einstein (1998). "End bearing capacity of drilled shafts in rock," *Journal of Geotechnical and Geoenvironmental Engineering*, Vol. 124, No. 7, pp 574-584.

Chapter 2. INVESTIGATION OF CORE FLOW INTO THE VERIFICATION CORES AT THE BOTTOM OF DRILLED SHAFTS

2.1 INTRODUCTION

2.1.1 Background

"The Texas Department of Transportation (TxDOT) is a major user of deep foundations to support transportation facilities, namely bridges [1]". Deep foundation systems mainly include piles and drilled shafts. Drilled shafts are typically used in regions where rock beds at shallow depths have insufficient bearing capacity and the rock type is not competent to support large loads such as bridge piers, abutments etc.

2.1.2 Research Motivation

Extraction of cores is perhaps the most common way of determining the in situ properties of rocks. Cores are taken at the bottom of the drilled shaft. The cores are cylindrical specimens of rock on which various lab tests can be performed to determine properties of the rock such as its strength, deformability and potential for degradation. In case of drilled shafts, the properties of rock at the bottom of the shaft are crucial in the verification of the drilled shaft tip capacity and the overall response of the shaft. The core taken at the top of the shaft is called a 'Verification Core.' A verification core is a core that varies from 6" to 18" in diameter. The depth varies from 5ft to 10 ft. The core is taken at the bottom of the shaft concentric to the shaft hole. Figure 2.1.1 shows the drilled shaft and the verification core. The requirements for the size and depth of the verification core are specified in contract documents for each project and are typically project specific [2].

These cores are important tools in ascertaining the condition and properties of the founding material at the bottom of drilled shafts. Even though there has been no evidence of any detrimental effect [2] of the verification core on the bearing capacity of the drilled shafts, this research was intended to investigate any potential problems that may arise due to the verification cores. The work contained in this chapter is part of the TxDOT sponsored research project 0-5825, "The Influence of Verification Cores on the Point Bearing Capacity of Drilled Shafts."
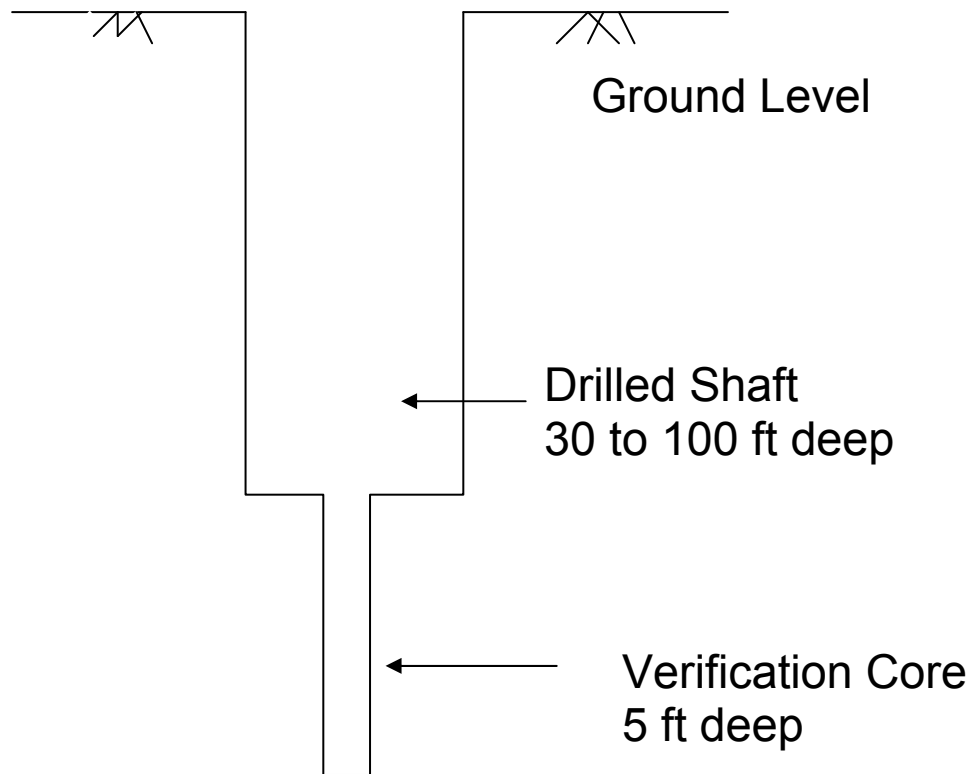
Figure 2.1.1 – Elevation of a Drilled shaft and verification core

TxDOT Research program 0-5825 has two objectives:

1) To study the degradation properties of certain rock formations around the verification core. This degradation of rocks is expected to occur in the time between the excavation of the drilled shaft and concreting. The degradation of rock can typically occur due to wetting and drying of the rock mass.

2) To investigate if the verification core hole fills with concrete when concrete is placed in the drilled shaft after excavation. The investigation also includes the determination of properties of material obtained (if any) in the core hole. This result is crucial in the estimation of the bearing capacity and the overall load-deformation response of the drilled shaft.

The work contained in this chapter deals with the second objective (TASK 4 in TXDOT 0-5825) and comprises of two subtasks:

1) Determine if the verification core hole of the drilled shaft is filled with concrete when concrete is placed in both the wet and dry conditions.

2) Determine the properties of material obtained in the core hole (if any) after the concrete is placed in the shaft.

The filling of verification core hole is significant from the following stand points –

1) If the verification core hole does not fill with concrete, then the degradation of the rock mass around the verification core hole may occur, causing reduction in bearing capacity.

2) If the verification core hole does not fill or the filling material is very weak or deformable as compared to the surrounding ground, then the bearing capacity may be reduced.

The work on the degradation of rock formations and estimation of bearing capacity is contained in Chapter 1 and 3.

2.1.3 Literature Review

Prior to this investigation, researchers have investigated the effects of minor anomalies on Axial Capacity of drilled shafts [3], [4]. However, the effect of the verification core alone on the bearing capacity of drilled shafts has never been investigated. This is one of the primary reasons that the research was initiated.

2.1.4 Outline of Chapter 2

The work contained in this thesis mainly addresses the issue of the properties of material obtained from the verification core hole. Details of the experiment that was conducted to simulate the flow of concrete in the drilled shaft are given in Section 2.2.2. Section 2.2.3 documents the design of the testing apparatus that was used to simulate the flow of concrete in the drilled shaft. Section 2.2.4 contains the detailed procedure adopted for testing the properties of the material obtained from the verification core hole and the test results.

2.2 EXPERIMENTAL SETUP FOR THE SIMULATION

2.2.1 Introduction

Verification cores are important tools in ascertaining the condition and properties of the founding material at the bottom of drilled shafts. However, the influence of verification core holes on the point bearing capacity of drilled shafts is still unknown. The key step in understanding the effect of core hole on the bearing capacity is to study the flow of concrete into the core holes during the concreting operation. The intent of this experiment is to simulate the flow of concrete into the verification core hole using a custom built apparatus.

2.2.2 Experimental Setup, Procedure.

Testing Apparatus

In order to simulate the flow of concrete into the verification core hole, the drilled shaft and the core hole were replicated. The apparatus was designed to satisfy the following requirements, i) the apparatus provides an exact geometry of the shaft and core hole and ii) the apparatus should have the ability to replicate the static pressure head that the concrete would exert at the bottom of the shaft.

To achieve these requirements, it was decided to build an apparatus that consisted of a steel pipe of 3' diameter and 13' length resting vertical on a steel frame. The diameter of the pipe was chosen to be 3' since 3' is the most common diameter for drilled shafts [1]. The pipe was built to simulate the vertical shaft. The bottom of the steel pipe was closed with a steel lid that could be used to attach a clear PVC (Polyvinyl Chloride) pipe of 5' length concentric to the shaft. The PVC pipe simulated the verification core hole at the bottom of the shaft. A PVC pipe of 6" or 12" diameter could be used depending upon the size of core hole that was to be tested. The vertical shaft (steel pipe) could be closed with a steel lid both at the top and bottom. Typical depth of a drilled shaft varies between 30 to 100 ft [1]. As a result, when the concrete is placed in the drilled shaft, it will exert a static pressure at the bottom of the shaft whose magnitude will vary with the depth. Considering the maximum depth equal to 100 ft, the static pressure head that would be required to simulate the actual field conditions was estimated to be 100 psi. This static pressure head of the concrete at the bottom of the drilled shaft was considered a factor that would assist the concrete flow into the verification hole. To simulate this condition, the steel cylinder was designed as a pressure vessel of capacity 100 psi. Figure 2.2.1 and 2.2.2 show the schematic elevation and plan of the testing apparatus respectively. Because of its shape, the apparatus was nicknamed "Rocket." The rocket was built at the Pickle Research Campus of The University of Texas at Austin. A valve was provided at the bottom of the steel pipe that enabled evacuation of concrete from the cylinder after each pour. A 22' tall scaffold as shown in Figure 2.2.3 was built all around the testing apparatus to access it from all the sides. A total of five students and two technicians (to operate forklift and backhoe) were required to carry out each pour. The apparatus also had two viewing ports placed diametrically opposite of each other and a foot above the bottom of the steel pipe. Viewing ports are shown in Figure 2.2.4. The

194

viewing ports, or "peep holes," were mainly provided for visual inspection of the concrete flow and to be able to record the flow while the experiment was in progress. Viewing ports, or "peep holes," were 6" diameter holes covered with an acrylic sheet of dimensions 15" x 15" and 1" thickness. The acrylic sheet was connected to the hole through a flanged connection with 8, ¾" bolts as shown in Figure 2.2.4. Two cameras were installed (one camera per hole) in front of each peep hole to videotape the concreting operation. As it can be seen in Figure 2.2.5, the whole assembly of steel cylinder was supported by four circular columns that were bolted to a reinforced concrete slab foundation. The total dead weight of the apparatus was about 13,000 lb. Approximately two cubic yards of concrete was placed into the cylinder during the experiment and added an additional 11,000 lb of weight. Appendix A gives detailed specifications of the components/materials used in the rocket.
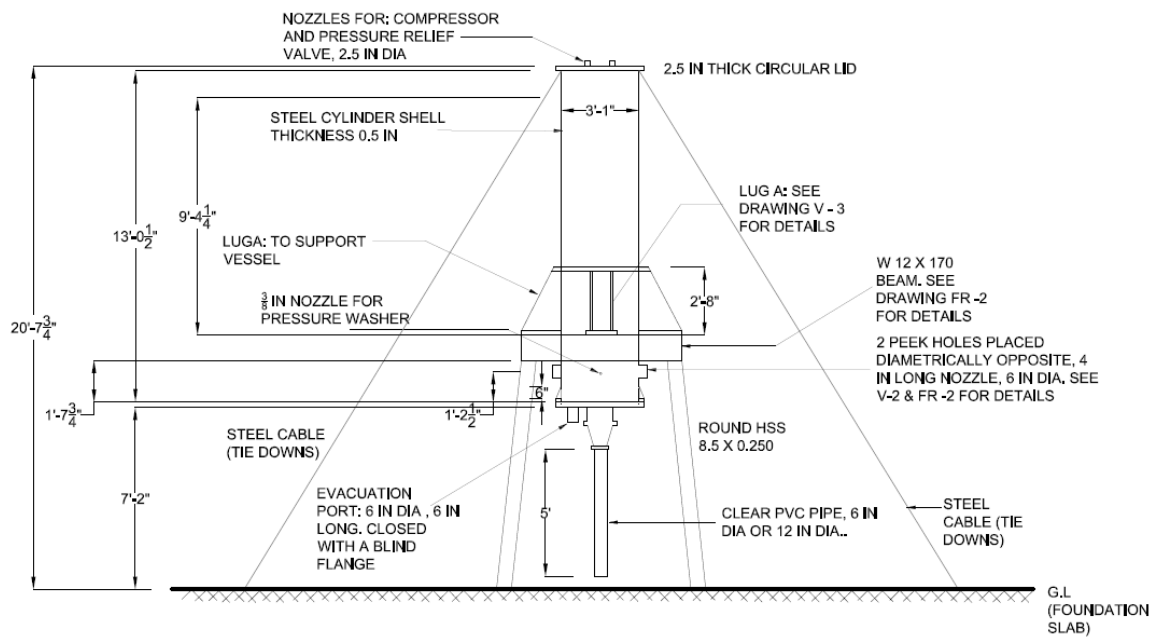
Figure 2.2.1   Schematic Elevation of the Rocket
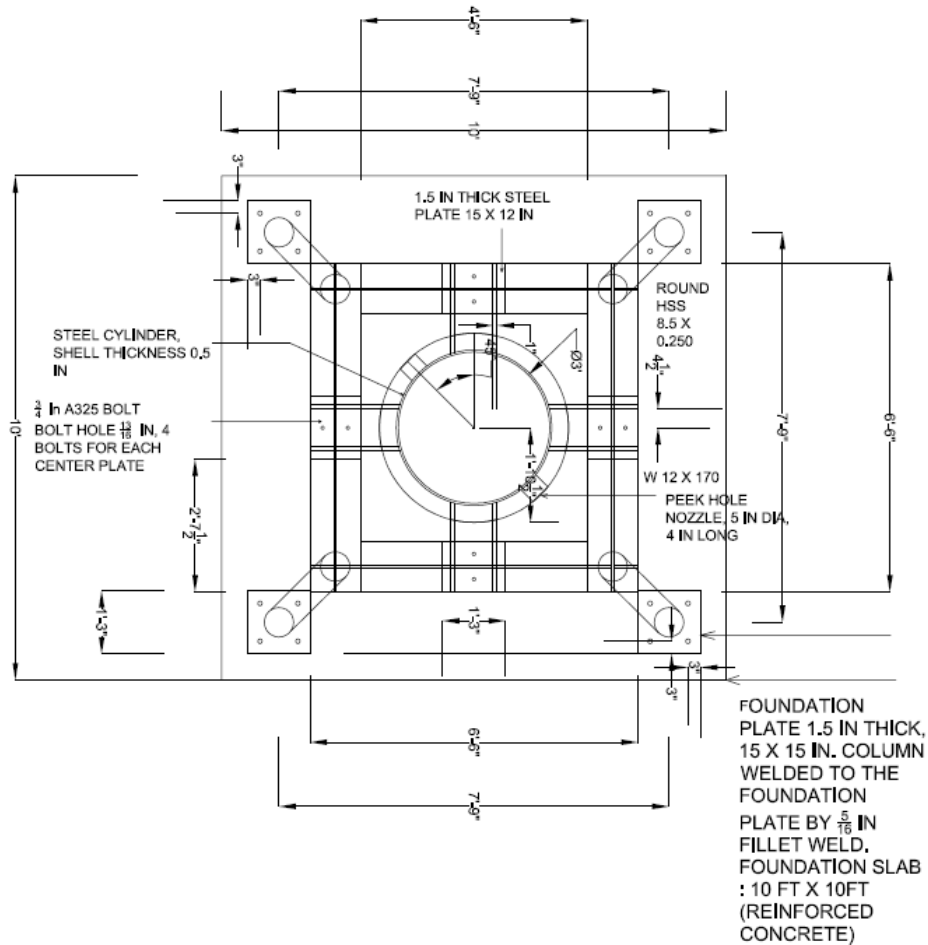
Figure 2.2.2 Schematic Plan of the Rocket

2.2.3 Procedure

The flow of concrete in a drilled shaft was simulated by pouring concrete into the testing apparatus (rocket) utilizing a concrete pump. The following parameters were varied in the testing program:

- Size of the Verification core – This parameter was changed by using 2 clear PVC pipe diameters i.e. 6" diameter to a 12".

- Slump of concrete – TxDOT requires certain specifications on the use of concrete in drilled shafts. The upper bound and lower bound of slump specified in the TXDOT specifications [5], [6], were used as extreme values in the investigation. Refer to Section 2.5 for detailed TxDOT specifications on concrete used in drilled shafts.

Figure 2.2.3 – Scaffold built around the rocket

Figure 2.2.4 – Viewing Port at the bottom of the rocket to monitor the flow of concrete

Figure 2.2.5 – Rocket

- Height of Pour – Drilled shafts vary in depth, mostly ranging from 30' to 100' [1]. It was not possible to replicate the length of the drilled shaft into the apparatus. To replicate the actual length of drilled shaft into the apparatus, a steel cylinder of 100' length would be required (as opposed to 13' which was actually used). This was not viable from both practical and economic stand point. Hence, the effect of the depth of the shaft was considered in an indirect way by using a concrete pump that could pump concrete from a height of 30' to 100'. The measured height was from the bottom of the drilled shaft (in this case, bottom of the steel cylinder of the rocket) to the top most point of the boom of the concrete pump. Effort was made to achieve a perfect straight drop by keeping the boom of the concrete pump exactly vertical. Figure 2.2.6 shows the configuration of the boom and also the height of the drop. The attempt was to produce the same effect at the bottom of the shaft that would occur in the field if the shaft was deeper. A total of three different heights, 30', 70' and 100' were tested in this experiment. To achieve this, concrete pumps with different boom lengths were used. Table 2.2.1 shows the specification of the concrete pump that was used to place concrete from different heights. Concrete pump was rented from Capital concrete Pumping, which is a company based in Austin Texas.

Table 2.2.1: Details of concrete pump used for different heights of drop

Height of drop ft	Length of Boom of the concrete pump (m)	Pump Manufacturer	Model Number
30	32	Schwing	S 32 XL
70	36	Schwing	S 36 SX
100	61	Schwing	S 61 SX

Height of drop
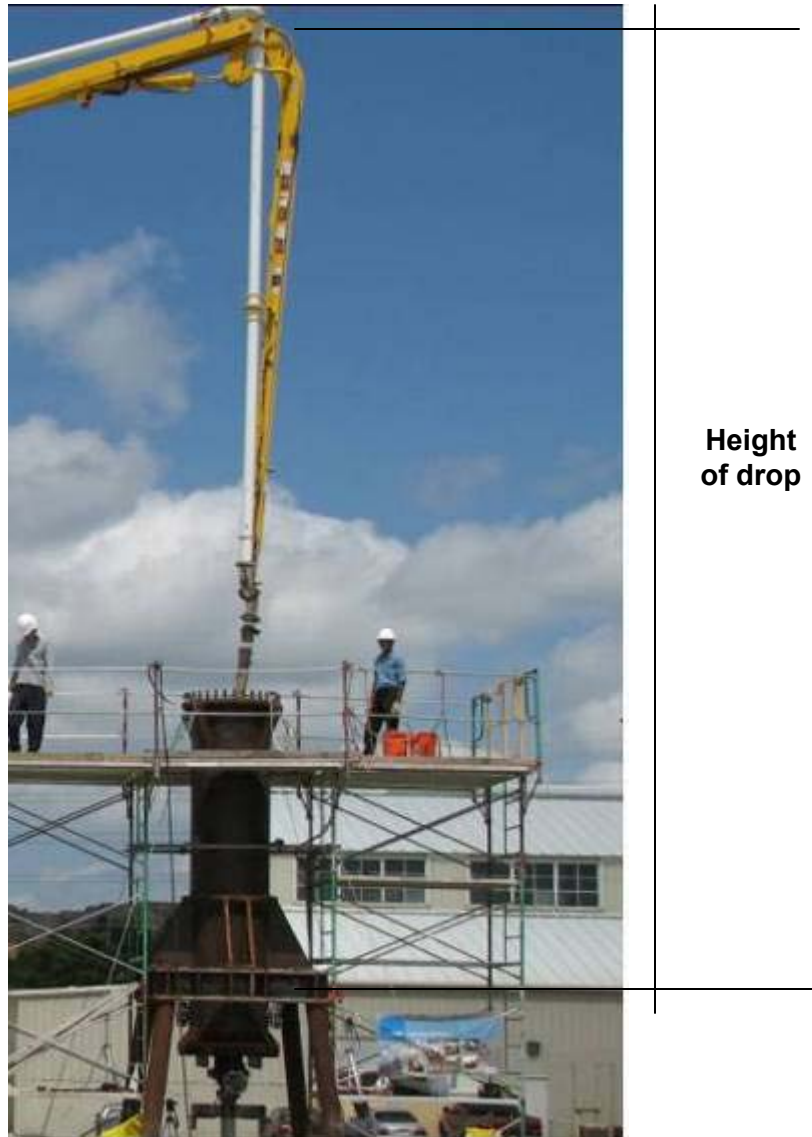
Figure 2.2.6 – Rocket

The experiment was carried out in the following 8 stages

1) Preparation of the testing apparatus

2) Pump set up

3) Add retardant to the concrete

4) Pump priming

5) Monitoring the Pump line

6) Pouring of concrete into the rocket.

7) Evacuation of concrete from the rocket

8) Post pour operation

Preparation of the testing apparatus

The rocket was prepared before pouring the concrete. Initially the top lid was opened by unscrewing the 32, 1-1/2" A325 bolts using a pneumatic impact wrench (see Figure 2.2.7). The pneumatic wrench delivered a torque close to 400 ft-lb. The weight of the top lid was approximately 1200 lb and hence a crane was used to lift it (see Figure 2.2.8). The clear PVC pipe was then bolted to the bottom steel lid of the rocket through a flanged connection (see Figure 2.2.9). The bottom steel lid had a 12" diameter opening with a flanged connection that could be used to attach either a 12" clear PVC pipe directly as shown in Figure 2.2.9 or a 6" clear pipe through a reducer shown in Figure 2.2.10.

Figure 2.2.7 – Ingersoll Rand pneumatic impact wrench

Figure 2.2.8 – Top lid hooked to crane.

Figure 2.2.9 – Flanged connection between the clear PVC pipe and the bottom lid

Figure 2.2.10– 6" Clear PVC pipe attached through a reducer

Pump set up

The concrete pump was set up in such a way that the boom of the concrete pump was exactly vertical and the desired height of the drop was achieved. As shown in Figure 2.2.6, the height of drop was calculated from the bottom of the steel cylinder (drilled shaft) to the top of the vertical section of the boom. Figures 2.2.15 – 2.2.18 show the complete setup of the concrete pump for different drop heights.

Figure 2.2.11 – Addition of retardant in the concrete truck

Figure 2.2.12 – Typical Slump Test

Add retardant to the concrete

The total duration of test, which included 2 pours (6" and 12" core), was between 5 and 6 hours. Hence we required that the concrete remained plastic during the entire testing process to meet TxDOT specifications and make removal and disposal of concrete easier. The total volume of concrete placed in the 'Rocket' during the experiment was approximately 2 yards. The ambient air temperature at the time of testing was 105◦ F. A retardant was essential to prevent the setting of concrete in the testing apparatus. Delvo, a commercially available stabilizer made by MASTER Builder (now BASF) was used. Tests were conducted to set the dosage of the stabilizer to achieve the desired setting time for the concrete that was used. A dose of 20 fl oz/ 100 lb weight of cement was used, which delayed the setting time up to 12 hours. The retardant was added directly into the mixing drum of the concrete truck and was allowed to mix in the truck with 60 revolutions of the mixing drum (see Figure 2.2.11). The dosage of Delvo was not varied according to the class of concrete as both class C and class SS concrete contained equivalent amounts of cement. The dosage corresponding to the larger cement content was used for both the mixes even though it was conservative for the Class C mix which contained less cement than the class SS concrete. The performance of the stabilizer was satisfactory and retarded the setting of concrete to provide adequate time for carrying out the entire experiment.

A slump test was conducted on the concrete to make sure that it met the required TxDOT specifications given in Table 2.2.7. A typical slump test is shown in Figure 2.2.12. The slump of the concrete was measured before adding the retardant and with the retardant. It was observed that the retardant increased the slump of the concrete. To compensate for the added slump, concrete was left longer in the concrete truck while being mixed by the rotating drum. In any case, the slump value did not exceed the maximum permissible value as specified in the TxDOT specifications for the use of concrete in drilled shafts.

Pump priming

Concrete pump was first primed and the primer concrete discarded as shown in Figure 2.2.13

Figure 2.2.13 - Priming of concrete pump.

Monitoring the Pump line

The concrete was poured into the drilled shaft in both wet and dry conditions. In the dry, the steel cylinder was completely dry and did not contain any water. This condition was considered to simulate the flow of concrete into the drilled shaft in the dry. In the wet condition, the steel cylinder was filled with water up to half of its depth (about 7 feet) and then concrete was pumped in with a steel tube. In the wet condition, a total of

9 pours were carried out. In the wet condition, three different procedures of underwater concreting were adopted. The three processes are explained below.

Wet Process 1: (WP 1)

For this process, the steel pipe was simply inserted into the water and the concrete was pumped. The bottom of the steel pipe was approximately two feet from the bottom of the drilled shaft.

Wet Process 2: (WP 2)

In this process, the steel tube was inserted into the water such that the tremie was approximately 2 to 3 inches above the bottom of the drilled shaft. Also, a plug or a piece of sponge (also called "pig") was first introduced into the pump line before the concrete was pumped. This process ensures that a concrete remains in a homogenous and plastic state throughout the concreting operation and segregation under water is prevented. It turns out that both the processes yield exactly the same results as far as the material obtained in the core hole is concerned.

Wet Process 3: (WP 3)

In this process, the steel pipe was inserted into the water such that the tube was approximately 2 to 3 inches above the bottom of the core hole. This process could be adopted only for the core hole with a 12" diameter, since the diameter of the tremie pipe was 6".

Table 2.2.5 shows the summary of test results for the nine pours carried under the wet condition. Detailed analysis of observations and results is documented in Section 2.4.

Pumping of concrete into the rocket

After setting up the apparatus, concrete was pumped into the rocket using the concrete pump. The height of the drop was mainly determined by the length of the boom used. For the simulation of the actual depth of the drilled shaft, it was required that the boom stayed exactly vertical and that the length of the boom be equal to the depth of the drilled shaft we are trying to simulate.

In each experiment approximately two cubic yards of concrete was placed into the rocket. The rate of pour was not constant as we would expect it in the field. The flow thorough the bottom clear PVC pipe was videotaped.

Evacuation of concrete from the rocket

After the pour, the filled core hole (clear PVC pipe) was to be detached from the rocket. However, before that, 2 cu yd of concrete was evacuated from the steel cylinder. The steel cylinder had a bolted, valve arrangement that could be used to evacuate the concrete. A 6" opening was deemed enough for the concrete to flow out of the rocket. The flowing concrete was guided by a PVC chute into the bucket of a backhoe (see Figure 2.2.14). In the process WP 1, the water was not pumped out of the rocket before evacuating the concrete. This caused the water to splash all around through the opening as shown in Figure 2.2.19. To overcome this splashing of water and ensure clean evacuation of concrete, in the processes WP 2 and WP 3, the excess water was first

pumped out of the rocket before evacuating the concrete. The concrete was then disposed of.

Post pour operations

The clear PVC pipes were detached from the rocket using a clamp and a forklift (Figures 2.2.21 and 2.2.22). The 6" filled core weighed about a 150 lb and the 12" core weighed 550 lb. As shown in Figure 2.2.22, the cores were grabbed by a forklift using clamps and were placed vertically into 3 ft deep holes that were drilled into the ground on site. The intent of the placement was twofold, I) to keep the cores in their working position and II) Placement in ground ensured that they would stay vertical in a safe position without toppling.

Figure 2.2.14 – Evacuation of concrete from the rocket

After disposal of concrete, the rocket was thoroughly cleaned from the inside using a power washer.

Figure 2.2.15 Complete Setup. Date: 07/30/2007, Ht of Drop: 30'

Figure 2.2.16 Complete Setup Date: 08/01/2007, Ht of Drop: 70'

Figure 2.2.17 Complete Setup. Date: 08/07/2007, Ht of Drop: 70'

Figure 2.2.18 Complete Setup Date: 02/15/2008, Ht of Drop: 100'

Figure 2.2.19 – Water Gushing out of rocket during evacuation of concrete poured under wet condition

Figure 2.2.20 - Removing the concrete filled clear PVC pipe with an impact wrench

Figure 2.2.21 – Clamps holding PVC pipes to enable their movement with forklift

2.2.4 Testing Program

Initially it was decided to carry a total of 24 pours out of which 12 were in the dry condition and 12 in the wet condition (under water). Two types of slumps were to be tested in the 24 pours. Table 2.2.2 shows the key parameters of each test.

Figure 2.2.22 – Placement of PVC pipes

Table 2.2.2 – Initial Testing Program

Condition	Size of verification core	Height of pour	TxDOT Class of Concrete	Slump (in)	No of Tests
Dry	6", 12"	30', 70' & 100'	Class C	5-1/2, 7-1/2	12
Wet (Under water concreting)	6", 12"	30', 70' & 100'	Class SS	7, 9	12

On the first pour (experiment), it was observed that a concrete of slump 5-1/2" filled the 6" verification core. It was clearly evident that the concrete of higher slump would fill the verification core as a higher value of slump would mean lesser resistance to flow. Consequently, the number of tests were reduced from 24 to 12 as only 1 slump of concrete was used in the tests. As a result, the final testing scheme was as specified in Table 2.2.3.

Table 2.2.3 – Summary of Modified test program

Item	Class of Concrete	Slump[1] in	Height of Pour Ft	Core Size	Remarks	Date.
Day 1 – Dry Pour	C	6	30	6"	Core filled instantly	30th July 2007
Day 2 – Dry Pour	C	6	70	6", 12"	Core filled instantly	1st August 2007
Day 3 – Dry Pour	C	6	100	6", 12"	Core filled instantly	2nd August 2007
Day 4 – Wet Pour	SS	7	70	6", 12"	Core filled instantly	7th August 2007
Day 5 – Wet Pour	SS	7	100	6", 12"	Core filled instantly	13th August 2007
Day 6 – Wet Pour	SS	9	30	6", 12"	Refer Table 2.2.5	14th February 2008
Day 7 – Wet Pour	SS	9	100	6", 12", 12"	Refer Table 2.2.5	15th February 2008

2.2.5 Materials

The concrete used in this experiment was in accordance with the TxDOT specifications item 416 [5]. Table 2.2.4 gives the specifications limits for the concrete used in drilled shafts.

---

[1] This is the measured value of slump after adding the admixture and rotating the mixer drum.

Table 2.2.4[2] - Concrete for Drilled Shafts [5]

Drilled Shaft Type	Concrete
Non-reinforced	Class A
Reinforced	Class C
Slurry and under water Placement	Class SS

Table 2.2.5 – Summary of pours under wet condition

Wet Pour Number	Size of Verification core, in	Process adopted	Remarks – Material obtained in the core
1	6	WP 1	Weakly cemented Sand-gravel mixture
2	12	WP 1	Weakly cemented Sand-gravel mixture
3	6	WP 1	Weakly cemented Sand-gravel mixture
4	12	WP 1	Weakly cemented Sand-gravel mixture
5	6	WP 2	Weakly cemented Sand-gravel mixture
6	12	WP 3	Good Quality concrete
7	6	WP 2	Weakly cemented Sand-gravel mixture
8	12	WP 2	Weakly cemented Sand-gravel mixture
9	12	WP 3	Good Quality concrete

TxDOT specifications for Class C and Class SS concrete are given in Table 2.2.6. The recommended slump values for the concrete used in drilled shafts are given in Table 2.2.7. The prescribed slump values are higher because low slump values make placement of concrete difficult resulting in defects in drilled shafts [1]. Also, on large jobs in which the placement of concrete may take hours, slump loss may result in defects in the drilled shafts [1].

Tests were carried out using the concrete mix meeting the specifications given in Table 2.2.8. For the details of the mix design, see Appendix A.

---

2 Refer to Table 2.6 and Table 2.7 for more details.

218

Table 2.2.6 – TxDOT Specifications for concrete. [6]

Class of Concrete	Design Strength, Min. 28 day f_c' (psi)	Maximum W/C ratio	ASTM C33 gradation	General Usage
C	3600	0.45	467	Drilled shafts, bridge substructure, bridge railing, culverts, head walls
SS	3600	0.45	57,67,7	Slurry displacement shafts, underwater drilled shafts

Table 2.2.7 - Slump Requirements for concrete used in drilled shafts. [5]

Placement Type	Minimum Acceptable Placement Slump in	Recommended placement and design slump in	Maximum acceptable placement slump
Dry	5-1/2	6-1/2	7-1/2
Under water and under Slurry	7	8	9

Table 2.2.8- Concrete Mix

Type of Placement	Concrete	Slump
Dry	Class C	6 in
Wet (Under water concreting)	Class SS	7 in

2.2.6 Summary

In this chapter, details of the testing procedure adopted for the simulation of concrete flow are explained. In the next chapter, design and detailing of the testing apparatus (rocket) is documented in detail.

2.3 DESIGN OF THE TESTING APPARATUS

2.3.1 Introduction

In this chapter, the procedure adopted for the design of the testing apparatus (Rocket) is discussed. This includes the estimation of loads for the apparatus, structural design of various components, drawings and details.

2.3.2 Estimation of Loads

The "Rocket" was built to simulate the flow of concrete into the verification core of a drilled shaft. The primary goal was to investigate the flow of concrete into the verification core as it is placed into the shaft under different conditions. Typically, drilled shafts vary greatly in depths ranging from 30 to 100 ft. Thus, the apparatus was to be designed for the impact of the pumped concrete from 100 ft height. As detailed below, it turned out that the member sizing and structural detailing was mainly governed by the impact load of pumped concrete.

Estimation of Dynamic Load acting on the system due to poured concrete

The impact load of the pumped concrete on the rocket was calculated on the basis of "Conservation of Energy Principle". The rocket was designed such that it could absorb the kinetic energy of the pumped concrete. The estimation of load was done as follows –

To absorb the impact load of the pumped concrete,

Potential energy of the concrete at height H = Energy absorbed by the columns   (3.1)

Potential Energy of the pumped concrete = WH   (3.2)

When columns are subjected to axial load, they deform elastically until first yielding event occurs. During the elastic deformation, the columns absorb energy equal to the area under the stress-strain curve. In Figure 2.3.1, the area under the triangle OAB is the energy absorbed by the column per unit volume, as it deforms from point O to point A elastically.

Energy absorbed by columns per unit volume = $\dfrac{P^2}{2E}$ (3.3)

Therefore total energy absorbed = $\dfrac{P^2 L}{2AE}$ (3.4)
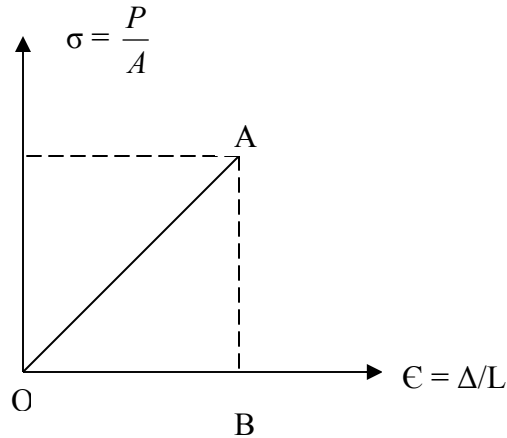
Figure 2.3.1 – Strain energy calculated from stress-strain curve

By equating equation 3.2 and 3.4 we get the expression

Dynamic Load $= P = P_{dynamic} = \sqrt{(2 \cdot K \cdot W \cdot H)}$ (3.5)

Where,

> H = Drop height from which concrete is being pumped into the cylinder (in)
> W = Weight of Concrete being dropped (kip)
> P = Axial Load on columns
> A = Area of the cross section of the column
> E = Young's Modulus of column material
> $K = \dfrac{AE}{L}$ = Axial stiffness of column

In general, K here represents the stiffness of the system, which refers to the force required to produce unit axial deformation in the vertical direction. Thus the energy absorbed is a function of the stiffness of the system. It follows from expression 3.4 that a stiffer system attracts more forces. To this end, expression 3.5 was used to estimate the impact load.

A concrete pump typically pumps concrete with a certain frequency. Since the pump we used for the experiment worked at 30strokes/minute, the flow of concrete was set at 20 cu yd/hour. Thus, the amount of concrete delivered per stroke is calculated as follows

> 20 cu yd/hr = 9 ft^3/minute
> There are 30 strokes/minute
> 9 ft^3 per 30 strokes
> W = 0.3 cu ft / stroke
> W = 0.3 X 0.15 kip/stroke

W = 0.045 kip of concrete per stroke……………………………………….. (3.6)

Thus with every stroke of the concrete pump, 0.045 kip of concrete is pumped into the rocket. This concrete is pumped from heights varying from 30ft to 100ft. For

design purpose, a maximum design height is set as 100 ft. All the calculations are based on this height of drop.

Figure 2.3.2 shows a steel cylinder with 13 ft height and 36 inches internal diameter. The cylinder is resting on a rectangular frame. The rectangular frame is made up of W sections. The frame is supported by 4 inclined columns. The inclined length of column is 110 inches. Columns are assumed to be fixed at the base and pinned at the top.

In this system, 0.045 kips of concrete is pumped from a height of 100 ft. The system is to be sized for the dynamic load due to impact of the falling concrete.
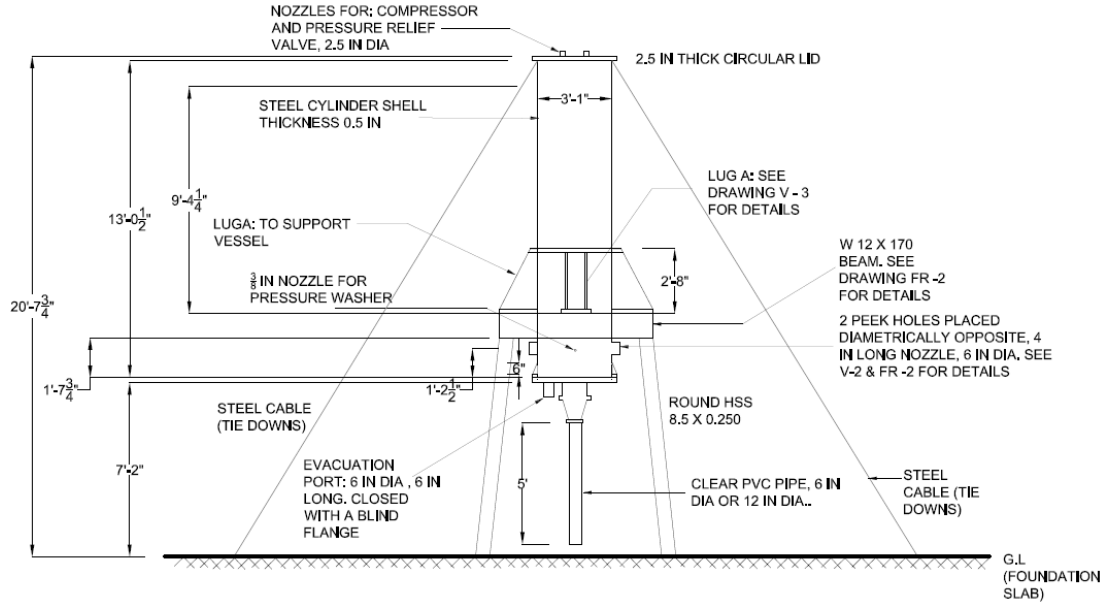
Figure 2.3.2 – Schematic Elevation of Rocket

The steel frame rests on a reinforced concrete slab of size 10ft X 10 ft X 1ft. The slab rests on stiff clay for which modulus of sub-grade reaction is assumed to be 5000 KN/m³ [12]

Data: Discharge from concrete Pump = 20 cu yd /hr
Column: Round HSS 8.500 X 0.25, Area = 6.14 in², E = 29000 ksi
Modulus of Sub-grade Reaction = E_f = 5000 KN/m³ (18.42 lb/in³)
Area of Foundation slab = 100 ft² = 9.29 m²

Therefore, the total stiffness of foundation, K_f = Area of Slab X E_f
$$K_f = 9.29 \text{ X } 5000$$
$$K_f = 46450 \text{ KN/m}$$
$$K_f = 268 \text{ kip/in} \dots\dots\dots\dots\dots\dots\dots\dots\dots \text{ (3.7)}$$

Stiffness of 4 Columns, $Kc = \dfrac{4AE}{L}$

$$Kc = \dfrac{4x6.14x29000}{110}$$

222

$$K_c = 6475 \text{ kip/in} \dots\dots\dots\dots\dots\dots\dots\dots\dots\dots\dots\dots\dots\dots \text{ (3.8)}$$

Where,

A = Cross sectional area of column = 6.14 in^2 (HSS 8.500 x 0.25)
E = Young's modulus of steel = 29000 ksi
L = Length of column = 110 in (Refer Figure 2.3.2)

The foundation and the columns can be considered as springs in series,

$$\text{Stiffness of system} = K = \frac{1}{Kc} + \frac{1}{Kf}$$

$$K = \frac{1}{6475} + \frac{1}{268} \text{ (Equations 3.7, 3.8)}$$

$$K = 257 \text{ kip/in} \dots\dots\dots\dots\dots\dots\dots\dots\dots\dots\dots\dots\dots \text{ (3.9)}$$

Notice that the overall stiffness is controlled by the ground stiffness.

$$\text{Dynamic Load} = P_{dynamic} = \sqrt{2 \text{ x } K \text{ x } W \text{ x } H}$$

$$P_{dynamic} = \sqrt{2 \text{ x } 257 \text{ x } 0.045 \text{ x } 1200}$$

$$\mathbf{P_{dynamic} = 166 \text{ kip}} \dots\dots\dots\dots\dots\dots\dots\dots\dots\dots\dots\dots\dots\dots\dots\dots\dots \text{ (3.10)}$$

Where,

K = stiffness of the system, as computed from Equation 3.9.
H = Height through which concrete is being pumped into the cylinder = 1200 in (100ft)
W = Weight of Concrete being dropped = 0.045 kip (from Equation 3.6)

Thus 166 kip is the value of the dynamic load that acts on the system. This load is applied as an equivalent static load on the system.

Estimation of Dead Load

Table 2.3.1 shows the calculation of dead load for various components of the rocket. Density of steel was assumed to be 489 lb/ft^3 (7850 kg/m^3). Drawings in Appendix B show dimensions of all the components of the rocket in detail.

Estimation of Live Load

ASCE 07-2005 [8] provides minimum load requirements for building structures. The steel frame supporting the steel cylinder was designed for a nominal live load value of 20 psf. The live load carried by the steel frame was mainly during the construction stage during erection of scaffold, support movement of people etc. The total value of live load was obtained by multiplying 20 psf by the plan area of the steel frame.

Plan area of the apparatus is 43 ft^2. Hence total live load is

Live Load, L = 43 x 20 = 1 kip

Table 2.3.1 – Calculation of dead load of the structure

No	Item	Description	Volume ft³	Weight Kip
1	Steel Cylinder	Height = 13', Internal Diameter = 3', thickness = 0.5"	5.2	2.5
2	Lugs	8 trapezoidal Plates (see attached sketch)		1
3	Base Plates	(20" X 15" X 1.5")		1.3
4	Top Ring	ID = 37in, OD = 45in, thickness = 1.5in)		0.3
5	Beams	Length = 22ft, linear density 0.17 k/ft	-	3.75
6	Columns	Length = 37 ft	-	0.7
7	Flanges	OD = 45in, ID = 37in, thickness = 2in	1.2	0.7
8	Clear PVC weight	Linear Density = 11 lb/ft), Length = 5ft	-	0.1
9	Concrete in the steel cylinder	Height = 10', diameter = 3'	71	11
10	Concrete in the Clear PVC pipe	Height = 5', diameter = 1'	11	0.6
11	Steel Lids	Thickness = 2.5' Diameter = 42'	4	2.4
	Total Weight			$\sum$ = 25 k $\sum$ = 13.4 k (Without concrete)

Load Combinations

   Dead load, live load and the dynamic loads acting on the rocket have been calculated in the previous sections. To this end, we calculate the total load using load combinations from ASCE 07 – 2005 [8].

Thus,

Total load[3] = 1.2 D + 1.6 (L + $P_{dynamic}$)……… (ASCE 07-2005, CH 2, section 2.3.2)

Where,

D = Dead Load (from section 3.2.2)

L = Live Load (from section 3.2.3)

$P_{dynamic}$ = Dynamic loading due to pouring of concrete (section 3.2.1, equation 3.5)

Hence,

Load = 1.2 x (25) + 1.6 x (1 + 166)

Load = 297.2 kip

   The load will be transferred to the beams through the lugs that support the steel cylinder. This load will be applied on all the beams as point loads at their mid-span. Hence the point load on each beam will be 74.3 kip. See Figure 2.3.9 showing the magnitude and location of point load on the beam.

Wind Load Analysis for global stability

   Intensity of wind load is taken as 40 psf [8]. The projected area subjected to wind is due to the vertical pressure vessel, beams and the columns. Figure 2.3.3 shows the direction of wind load. Following are the projected areas of various components of the rocket in the direction of wind. For the dimensions of the rocket used in these calculations, refer Figure 2.3.3 (for detailed shop drawings, see Appendix B).

---

[3] Pdynamic was considered as a live load in the load combination. It was computed based on several assumptions and was subject to variations.
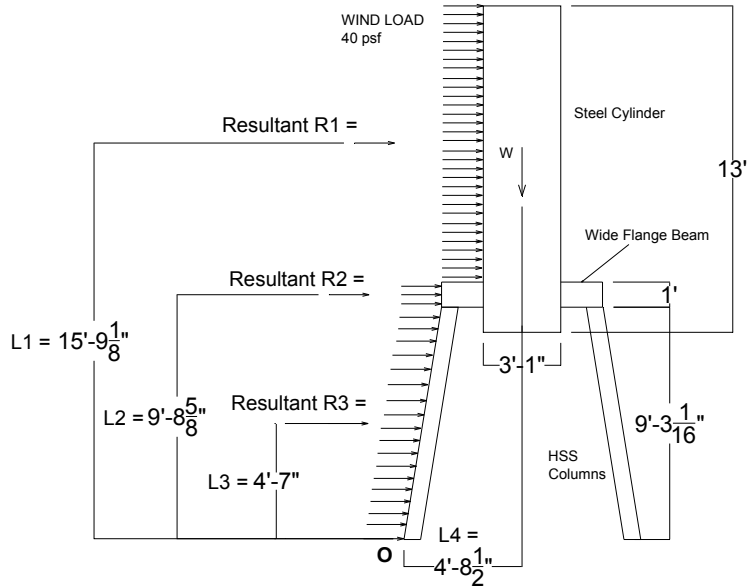
Figure 2.3.3 – Wind Load acting on Rocket

Projected area of columns = 9' X 0.75' X 2X 0.6 (shape factor, [18]) = 8.1 ft^2
Projected Area of Steel Cylinder = 13 X 3 = 39 ft^2
Projected area of Beams = 6.5' X 1.2' = 7.8 ft^2

Global stability analysis:
$\sum M_O = (R_1 \times L_1) + (R_2 \times L_2) + (R_3 \times L_3) - (W \times L_4)$
(R in kip = Projected areas of respective components x Wind Load intensity)
R_1 = 39 x 40 = 1.56 k, (Refer Figure 2.3.3)
R_2 = 7.8 x 40 = 0.312 k, (Refer Figure 2.3.3)
R_3 = 8.1 x 40 = 0.324 k
L_1 = 15.75 ft, L_2 = 9.71 ft, L_3 = 4.58 ft, L_4 = 4.70 ft, (Refer Figure 2.3.3)

Stabilizing moment provided by the dead load of the structure,
$M_s = (W \times L_4)$
W = 13.4 kip (Table 2.3.1, section 3.2.2)
L_4 = 4.7 ft (Figure 2.3.3)
Hence, M_s = (13.4 x 4.7)
M_s = 62.98 k-ft

Overturning moment due to wind load,
$M_{ov} = (R_1 \times L_1) + (R_2 \times L_2) + (R_3 \times L_3)$
M_{ov} = (1.56 x 15.75) + (0.312 x 9.71) + (0.324 x 4.58)
M_{ov} = 29.08 k-ft

Factor of Safety against overturning, $Fs = \dfrac{Ms}{Mov} = 2.165$

Thus, the structure satisfies global stability requirements. The factor of safety against the lateral load is 2.165 which can be considered safe.

226

Estimation of wind loads

Figure 2.3.4 shows plan view of the rocket with the design wind load. As calculated in section 3.2.5, the structure satisfies the global stability requirements. However, the entire structure needs to be designed for the internal stresses that are produced due to the lateral wind load.

Total wind load acting on the various components of the structure are calculated as follows –

Total wind force acting on the steel cylinder = R_1 = 1.56 k (section 3.2.5)

Total wind force acting on the beams = R_2 = 0.312 k (section 3.2.5)

Total wind force acting on the columns = R_3 = 0.324 k (section 3.2.5)
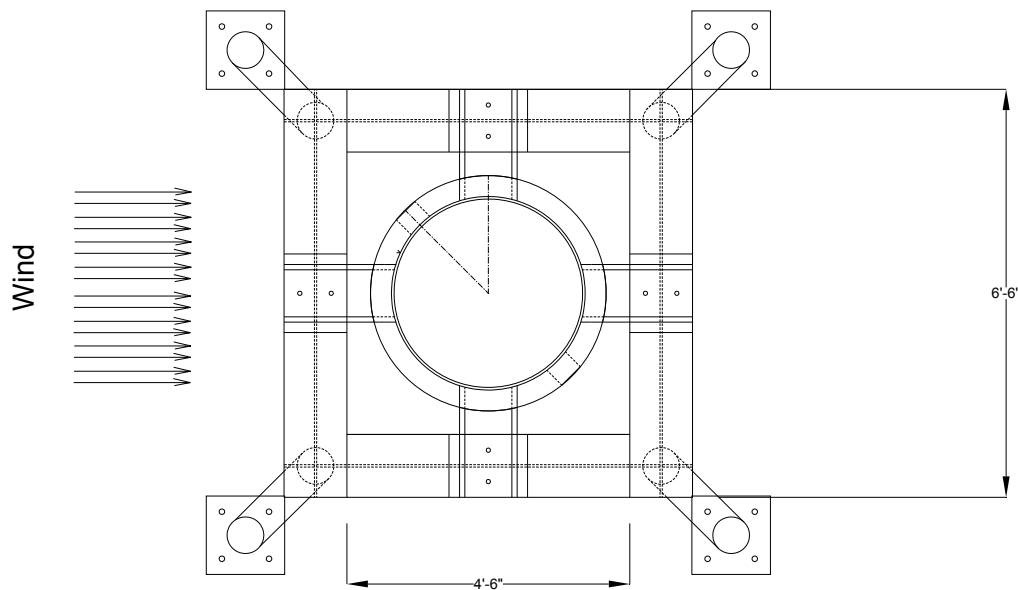
Figure 2.3.4 – Plan view of rocket showing wind

Thus total lateral load = R = R_1 + R_2 + R_3

$$R = 1.56 + 0.312 + 0.324$$
$$R = 2.2 \text{ kip}$$

The wind load acting on the beam is calculated as, R_2 = 0.313 k. This load acts as a uniformly distributed load on the beam. Thus the uniformly distributed load acting on the beam due to wind load on beam can be calculated as follows –

UDL_1 = Total load/span of the beam

$$= 0.312/75$$
$$= 4.16 \text{ lb/in} = 4.16 \times 10^{-3} \text{ k/in}$$

Note: UDL_1 acts as a uniformly distributed load on the beam.

Note that UDL_1 is very small and can be neglected.

2.3.3 Design of Tie-downs

As shown in the Figure 2.3.3, the vertical steel cylinder is supported by the beam at the bottom end and is free at the top end. This causes the lateral wind load (see Figure 2.3.3) acting on the cylinder to produce a cantilever action with respect to the fixed end which is the connection between the beam and the cylinder (through lugs). There are two main factors that make this cantilevered cylinder undesirable. First, the large surface area of the cylinder which produces a significant lateral load (R_1), and the height of the cylinder that produces a large moment arm. To reduce the stresses on the lugs, tie downs or steel cables were provided connecting the top of the cylinder to a support on the ground. This forces the steel cylinder to behave like a simply supported beam at both ends instead of a cantilever with just one fixed connection at the bottom (lugs)

The tie downs also increase the overall stability of the structure and the resistance of the structure to any accidental loading that could occur while placing concrete. The accidental loading could occur because: The hose of the concrete pump can hit the rocket on the top while concrete is being placed. This could result in an additional de-stabilizing moment on the steel cylinder and can overturn the structure. However, estimation of such a load is highly uncertain and depends on a number of factors. Hence, to resist this accidental lateral load, tie downs (steel cables) were relied upon.
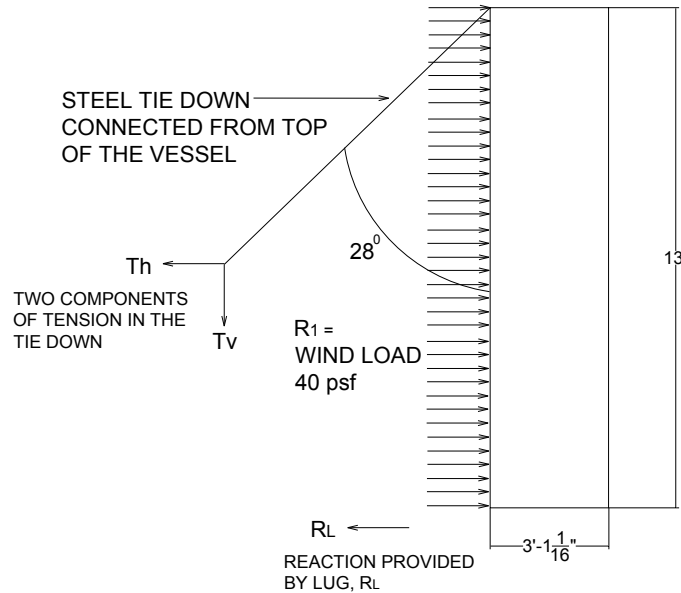
Figure 2.3.5 – Wind force acting on the steel cylinder, resistance provided by tie down and the lug.

The total lateral force acting on the steel cylinder is R_1 = 1.56 k. It is resisted by two components I) Reaction provided by the lug where the steel cylinder is connected to the steel frame and II) Horizontal component in the steel cable tied at the top. From the Figure 2.3.5 we can write,

R_1 (Wind load acting on steel cylinder) = $T_h + R_L$

Also, considering the steel cylinder a simply supported beam at two ends with a uniformly distributed load, we can deduce

$T_h = R_L$

$1.56 = 2 \times R_L$

$R_L = 0.78$ k, $T_h = 0.78$ k

Where T_h is the horizontal component of tension in tie down in the direction of wind.

Thus the horizontal component of tension that the tie down should provide in the direction of the wind is 0.78k. Note that in 3-D space; the tie-down will have 2 components in the horizontal direction and one component normal to the ground.

This wind load acts on the beam where lug is connected. Thus the uniformly distributed load acting on the beam due to wind load on beam can be calculated as follows –

$$\text{UDL}_2 = \frac{R_L}{L_{LUG}}$$

$$= \frac{0.78}{15}$$

$$= 52 \text{ lb/ in} = 52 \times 10^{-3} \text{ k/in} = 0.052 \text{ k/in}$$

Where,

L_{LUG} = Length of the lug = 15" (See drawing V-3 in the appendix B)

Note: UDL_2 acts as a partially distributed load on the beam where it is connected with the

lug (see Figure 2.3.9)

Figure 2.3.9 shows the SAP model with the dead load, live load and the calculated wind load applied at the joint where the steel cylinder is connected to the beams with lugs. To resist the lateral wind force, steel tie downs are provided as shown in Figure 2.3.5-2.3.7.

The tie-downs are designed to resist the wind load. Figures 2.3.6 and 2.3.7 show the details of the tie down. There are four tie-downs provided in a symmetric fashion. Each tie down was tied to a concrete block of dimension 30" x 48" x 60" (Figure 2.3.8). The concrete block weighed about 7500 lb. The blocks were resting on wooden platforms.

The horizontal force T_h shown in Figure 2.3.5 is calculated in section 3.3. Thus the goal is to design tie-downs to resist the total force T_h
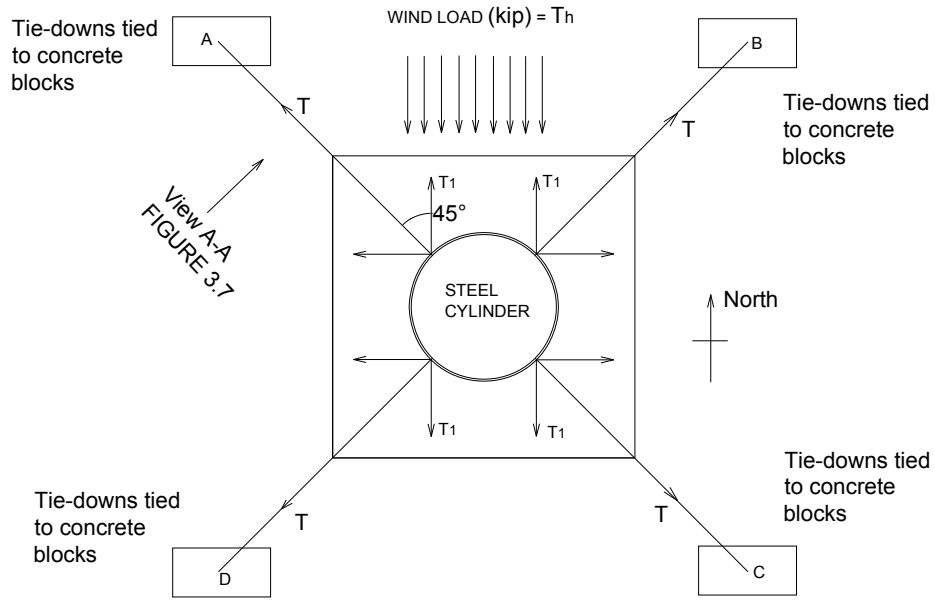
Figure 2.3.6 – Plan view showing the tie downs resisting the wind load
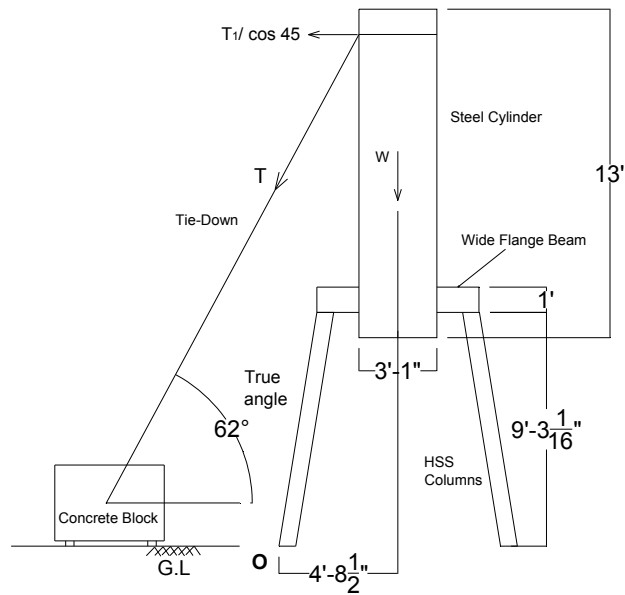
Figure 2.3.7 – Elevation showing the tie down, view A-A

230

From Figure 2.3.6,

$$2 \times T_1 = T_h = 0.78$$
$$T_1 = 0.39 \text{ kip}$$

From Figure 2.3.6,

$$T_1 \cos(45) = T$$

Hence,

$$T = \frac{T_1}{\cos(45)}$$

From Figure 2.3.7

$$T_C = \frac{T}{\cos(90 - 62)}$$

Thus, tension T_C required in the tie down to produce the force T_1 is

$$T_C = \frac{T_1}{\cos 45 \cdot \cos(90 - 62)} = \frac{0.39}{\cos 45 \cdot \cos(90 - 62)}$$

$T_C = 0.624$ kip > 7.5 kip (Weight of the concrete block)

Thus the tie down has to be designed to resist a maximum tensile force of 0.624 kip. Steel cables were used for this purpose. To this end, steel cable with the following specifications was used for the tie-downs.

Tie Down Specifications:
Diameter of Steel Cable: ½"
Ultimate tensile strength of the cable: 4560 lb > T_C = 624 lb.
Material: Stainless steel

Calculation of Shear:

$$\text{Shear, Ts} = \frac{T}{\sin(90 - 62)}$$

$$T_S = \frac{T_1}{\cos 45 \cdot \sin(90 - 62)} = \frac{0.39}{\cos 45 \cdot \sin(90 - 62)} = 1.17 \text{ kip}$$

Coefficient of friction between wood and concrete = μ = 0.62 [19]
Frictional force, $F = \mu N$

       N = Weight of the block = 7.5 kip
       Hence, $F = 0.62 \times 7.5 = 4.65$ kip > 1.17 kip

Thus the frictional force developed between the block and the wooden support was sufficient to resist the shear component of the force in the tie-down. Turn buckles were used to tighten the cables and maintain tension.

Figure 2.3.8 – Tie down tied to concrete block

2.3.4 SAP Model for the Steel Frame

For the analysis and design of the steel frame for various structural actions (Shear, Bending, Torsion) SAP 2000 was used. The base connections were assumed to be fixed and the others were pinned or shear connections. Sections assigned for the analysis of the model were based on the availability. Columns were assigned round HSS 8.500 X 0.25 section and the beams were assigned W 12 X 170 section. Figure 2.3.9 shows the SAP model for the frame with the assigned loads. Notice that the gravity and the live load act vertical while the reaction at the lugs induced due to the wind load acts in a horizontal plane.

Total vertical load applied at the mid-span of each beam is 74.3 kip (section 3.2.4). Lateral load from the wind load is calculated in section 3.2.6. Figure 2.3.9 shows the geometry, loads and the boundary conditions for the steel frame. Also shown are the assigned steel sections.

2.3.5 Results of SAP Analysis

Summary of SAP results

Table 2.3.2 shows the critical design values of actions induced in the beam, columns and connections. Figures 2.3.9-2.3.10 show the Shear Force and Bending moment diagram for the members of the steel frame.

232

Table 2.3.2 – Critical design values

Member	Maximum shear (kip)	Maximum Moment (k-ft)	Maximum Axial force (kip)
Column	0.88	3.4	78.3
Beam	37.1	116.82	14.35
Beam-beam pinned connection	74.3	0	0
Moment connection at column base	0.88	2.44	0
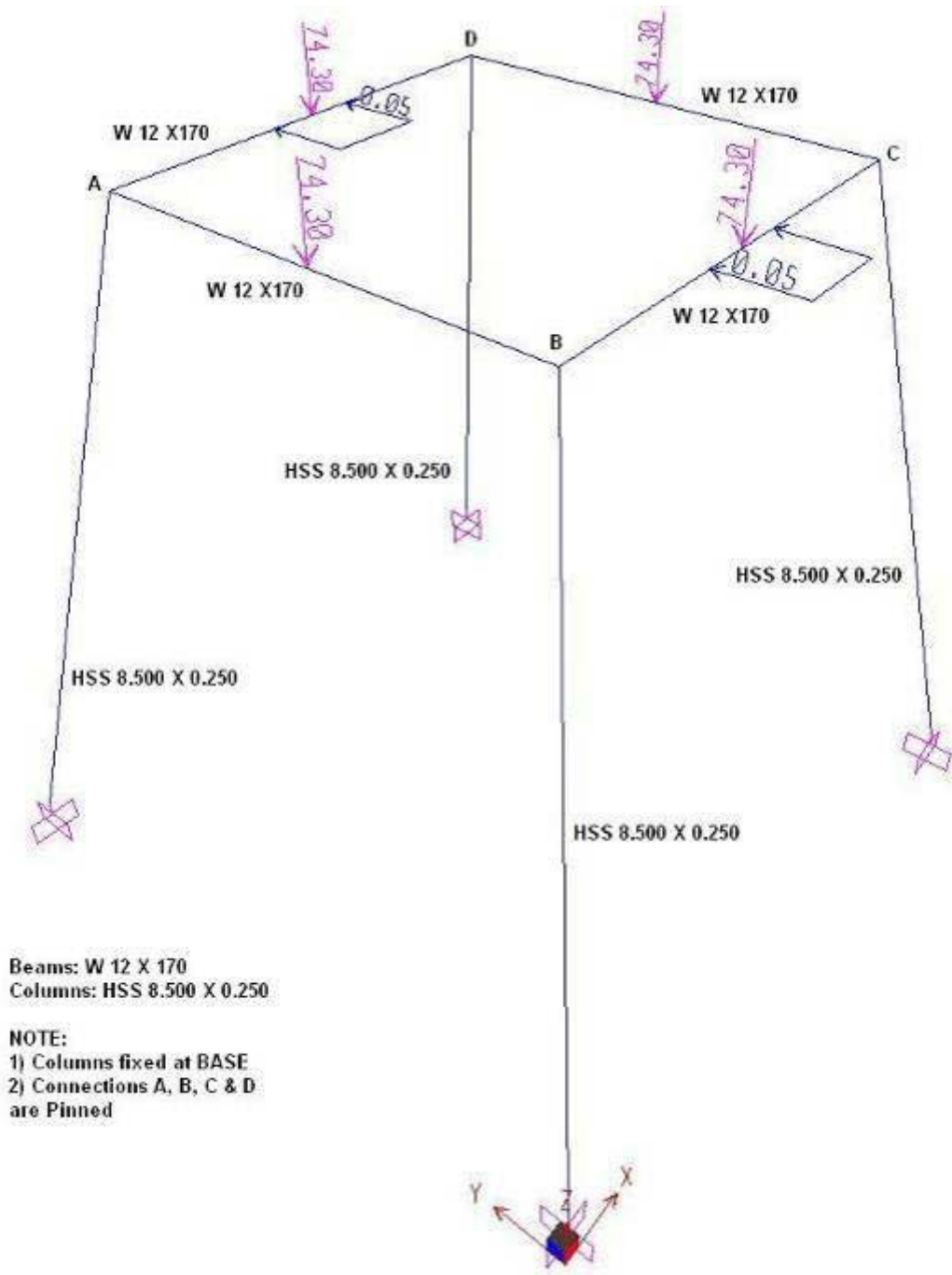
*Figure 2.3.9 SAP Model showing dead load, live load (kip) and the lateral load (kip/in)
applied to the frame through lugs*
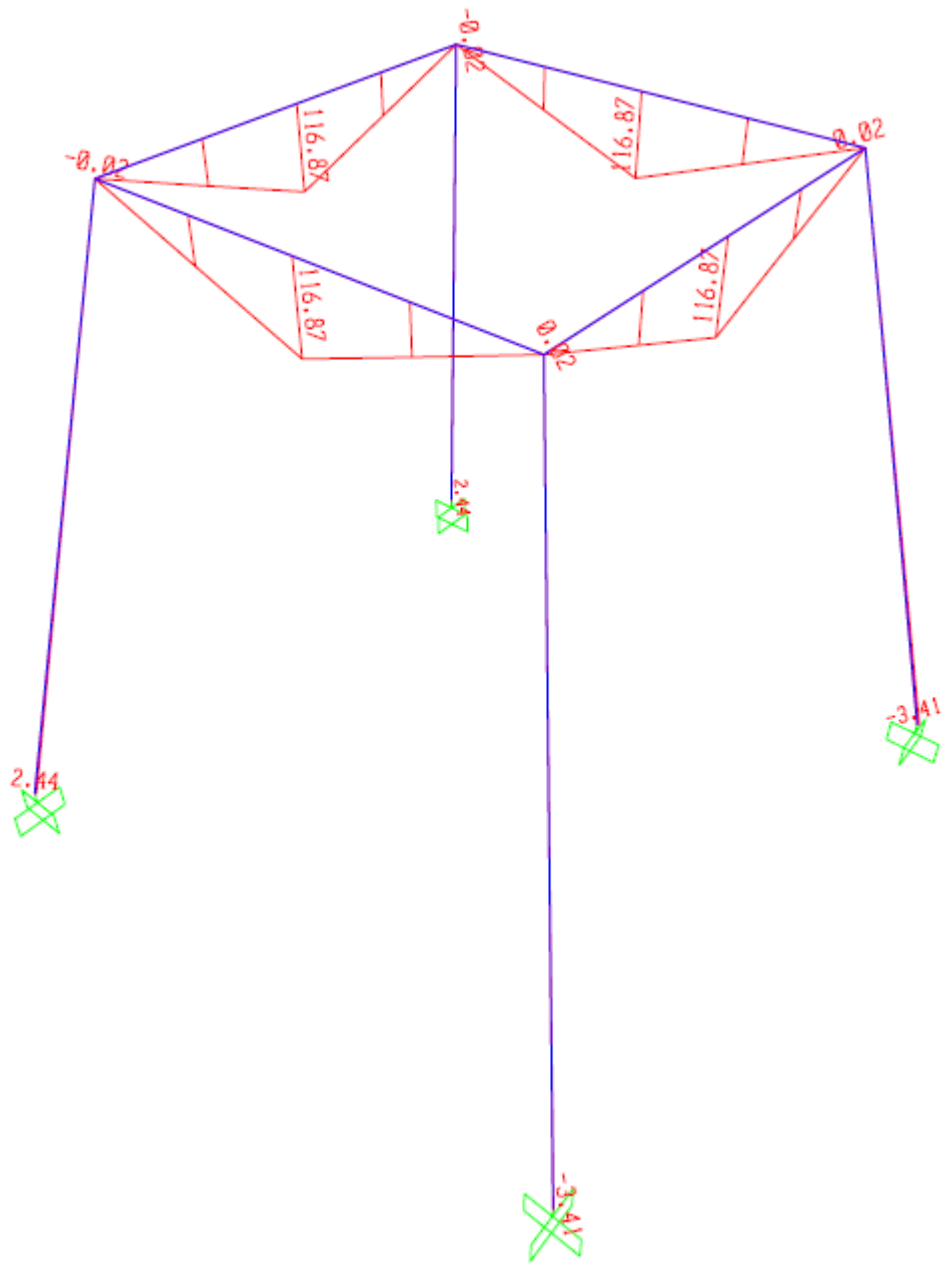
Figure 2.3.10 Bending Moment Distribution in beams and at the fixed base (Units: kip-ft)
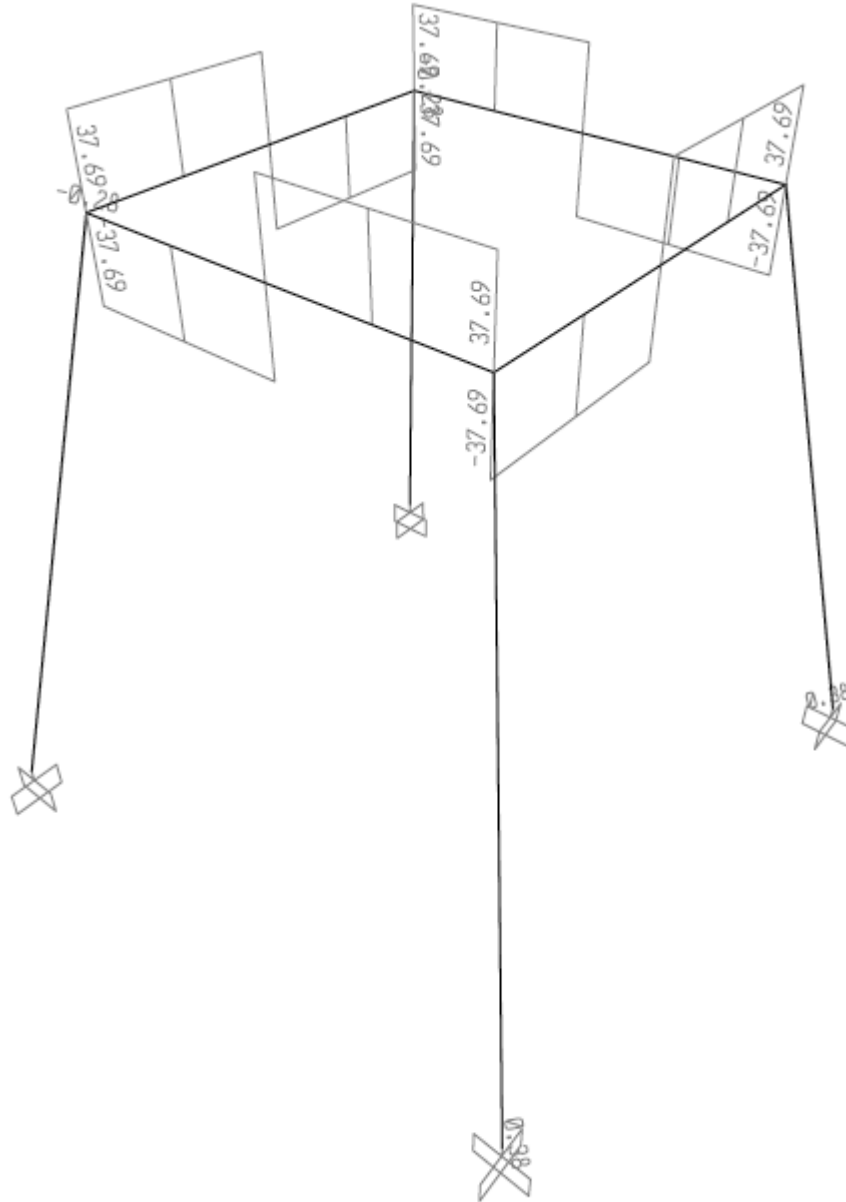
Figure 2.3.11 Shear force Distribution in beams and columns (Unit: kip)

2.3.6 Design of members

The members were designed for the critical design values using SAP 2000. Figures 2.3.12-2.3.13 are the design checks computed using SAP. The SAP design is as per AISC LRFD 93. The loading given for the design purpose in the SAP is the service load and not the factored load. The reason being that in the design process, SAP automatically puts in the factors for the load corresponding to the design standard it is using.

236

Design check for the beam

The beam was designed using SAP 2000. The design standard chosen in SAP was AISC LRFD 93. The beam design carried out in SAP is shown Figure 2.3.12. SAP performs the design checks for the limit state for the assigned section.
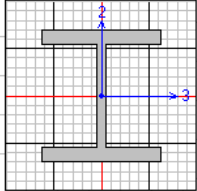
```
AISC-LRFD93 STEEL SECTION CHECK
Combo  : DSTL1
Units  : Kip, in, F



Frame  : 5              Design Sect: W12X170
X Mid  : 60.000         Design Type: Beam
Y Mid  : 97.500         Frame Type : Moment Resisting Frame
Z Mid  : 132.000        Sect Class : Compact
Length : 75.000         Major Axis : 0.000 degrees counterclockwise from local 3
Loc    : 37.500         RLLF       : 1.000


Area   : 49.632         SMajor : 232.439    rMajor : 5.726       AVMajor: 13.440
IMajor : 1627.070       SMinor : 82.160     rMinor : 3.224       AVMinor: 32.656
IMinor : 515.962        ZMajor : 272.154    E      : 29000.000
Ixy    : 0.000          ZMinor : 125.555    Fy     : 42.000


STRESS CHECK FORCES & MOMENTS
    Location        Pu          Mu33         Mu22         Vu2         Vu3          Tu
    37.500      -15.181     1406.943       26.994     37.149      -0.788     -43.914

PMM DEMAND/CAPACITY RATIO
    Governing      Total          P          MMajor       MMinor      Ratio       Status
    Equation       Ratio          Ratio        Ratio       Ratio      Limit       Check
    (H1-1b)        0.147    =     0.004    +   0.137   +   0.006      0.950          OK

AXIAL FORCE DESIGN
                   Pu         phi*Pnc      phi*Pnt
                   Force      Capacity     Capacity
    Axial       -15.181     1713.946      1876.090

MOMENT DESIGN
                   Mu         phi*Mn        Cm       B1       B2       K        L        Cb
                   Moment     Capacity    Factor   Factor   Factor   Factor   Factor   Factor
    Major Moment  1407.201  10287.430     1.000    1.000    1.000    1.000    1.000    1.314
    Minor Moment    26.994   4658.450     0.850    1.000    1.000    1.000    1.000

SHEAR DESIGN
                   Vu         phi*Vn       Stress      Status        Tu
                   Force      Capacity     Ratio       Check      Torsion
    Major Shear    37.149    304.819      0.122         OK        0.000
    Minor Shear     0.788    740.638      0.001         OK        0.000
```

Figure 2.3.12 Design check for beam W 12X170 using SAP 2000

Design check for the column

The column was designed using SAP 2000. The design standard chosen in SAP was AISC LRFD 93. The beam design carried out in SAP is shown Figure 2.3.13. The column is Round HSS 8.500 X 0.250 (Hollow steel section). SAP performs the design checks for the limit state for the assigned section.

237
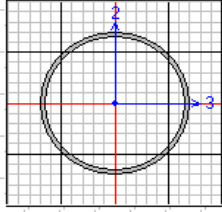
```
AISC-LRFD93 STEEL SECTION CHECK
Combo   : DSTL1
Units   : Kip, in, F



Frame   : 2              Design Sect: HSS8.500X0.250
X Mid   : 11.250         Design Type: Brace
Y Mid   : 11.250         Frame Type : Moment Resisting Frame
Z Mid   : 73.000         Sect Class : Compact
Length  : 122.215        Major Axis : 0.000 degrees counterclockwise from local 3
Loc     : 0.000          RLLF       : 1.000

Area    : 6.480          SMajor : 12.983      rMajor : 2.918          AVMajor: 3.242
IMajor  : 55.177         SMinor : 12.983      rMinor : 2.918          AVMinor: 3.242
IMinor  : 55.177         ZMajor : 17.021      E      : 29000.000
Ixy     : 0.000          ZMinor : 17.021      Fy     : 42.000


STRESS CHECK FORCES & MOMENTS
      Location        Pu         Mu33        Mu22        Vu2        Vu3         Tu
      0.000         -78.676      0.088       64.313     -0.040      0.525       0.005

PMM DEMAND/CAPACITY RATIO
      Governing     Total          P        MMajor      MMinor     Ratio      Status
      Equation      Ratio        Ratio       Ratio       Ratio     Limit      Check
      (H1-1a)       0.468    =   0.379   +   0.000   +   0.089      0.950        OK

AXIAL FORCE DESIGN
                    Pu        phi*Pnc     phi*Pnt
                    Force     Capacity    Capacity
      Axial        -78.676    207.695     244.926

MOMENT DESIGN
                    Mu       phi*Mn      Cm       B1        B2        K        L       Cb
                    Moment   Capacity    Factor   Factor    Factor   Factor   Factor  Factor
      Major Moment  0.088    643.388     0.850    1.000     1.000    1.000    1.000   1.313
      Minor Moment  64.313   643.388     0.601    1.000     1.000    1.000    1.000

SHEAR DESIGN
                    Uu       phi*Un      Stress    Status             Tu
                    Force    Capacity    Ratio     Check            Torsion
      Major Shear   0.040    73.523      0.001      OK               0.000
      Minor Shear   0.525    73.523      0.007      OK               0.000
```

Figure 2.3.13 Design check for column section HSS 8.500 X 0.250 using SAP 2000

2.3.7 Beam-Column Connection Design

Beams were connected with a double angle bolted shear connection. The connections were assumed to be pinned and hence were designed to transfer shear only. Since all the beams were of the same depth, beams were coped both at top and bottom. A standard shear connection was designed as per AISC [7] Table 2.10-1. The connection was designed to resist a force of 74.3 kip (Table 2.3.2). To this end, a pre-designed standard shear connection with the following specifications was chosen from AISC [7] Table 2.10-1. Figures 2.3.14-2.3.18 show the details of the shear connection.

Connection Specifications:

Type: Double Angle Standard Bolted shear connection with beams coped at both ends
Number of Rows of bolts: 3
Type of bolt: 7/8" A325 Bolts
Hole type: Standard

238

Capacity of the shear connection:

The thickness of the beam web $t_w = 0.96$"

Shear capacity of the beam (force/unit web thickness) = 165 k/in [7]

Shear Capacity of the connection = $0.95 \cdot 165 = 158$ kip > 74.3 kips
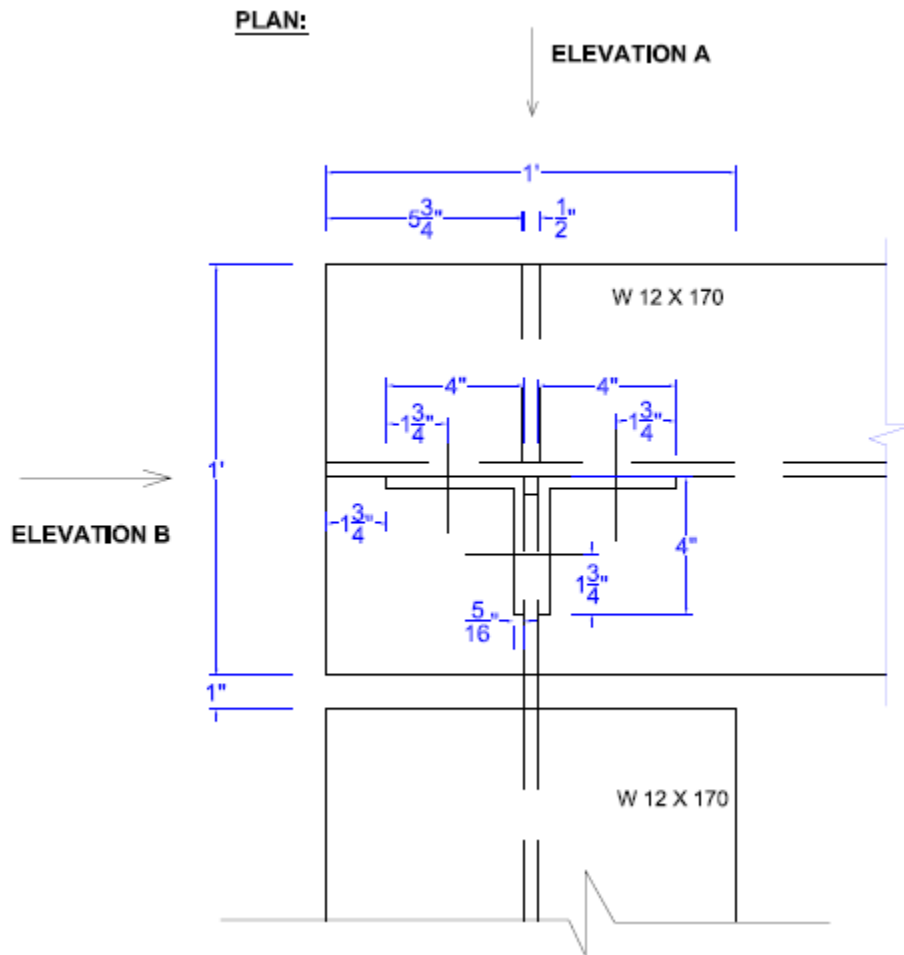
Figure 2.3.14 – Top view of shear connection between beams

7/8 IN A325 BOLTS (3 NOS), BOLT HOLE DIA = $\frac{15}{16}$ IN, BOLT LENGTH = 4IN

W 12 X 170

$\frac{1}{2}$ IN THICK PLATE, $\frac{3}{16}$ IN FILLET WELD

$\frac{7}{8}$ in BOLTS (3 NOS). A325

DOUBLE ANGLE CONNECTION
L : 4 x 4 X 5/16 in

W 12 X 170
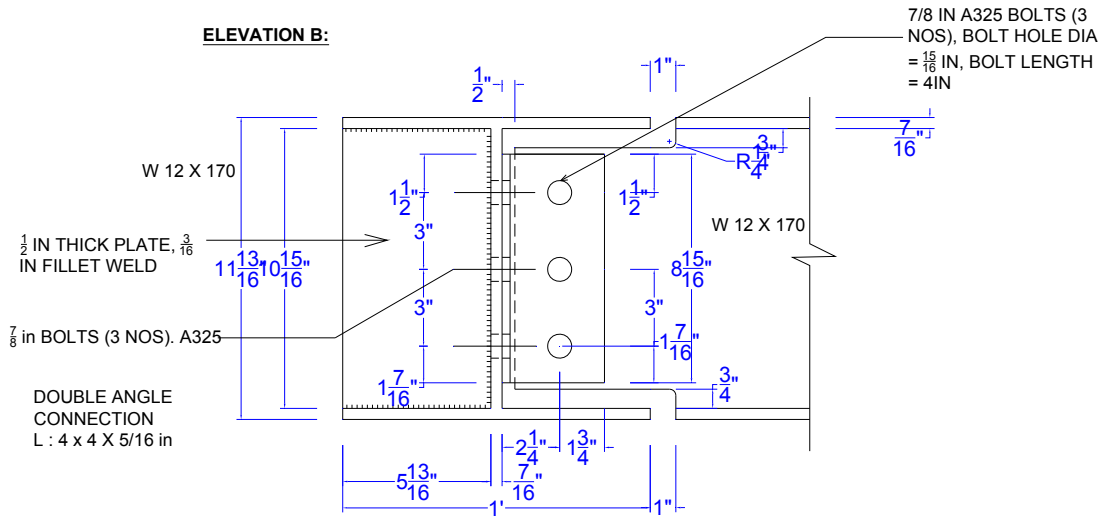
Figure 2.3.15 - Shear connection between beams: Elevation B

ELEVATION A:

W 12 X 170

$\emptyset\frac{15}{16}$"

$\frac{7}{8}$ IN A325 BOLTS L = 5 IN

$\frac{1}{2}$ IN THICK PLATE FOR REINFORCEMENT WELDED TO THE BEAM, $\frac{3}{16}$ IN WELD

ROUND HSS 8.5 X 0.250 COLUMN WELDED TO BEAM FLANGE BY $\frac{5}{16}$" FILLET WELD(DOES NOT SHOW TRUE ANGLE IN THIS DRAWING)
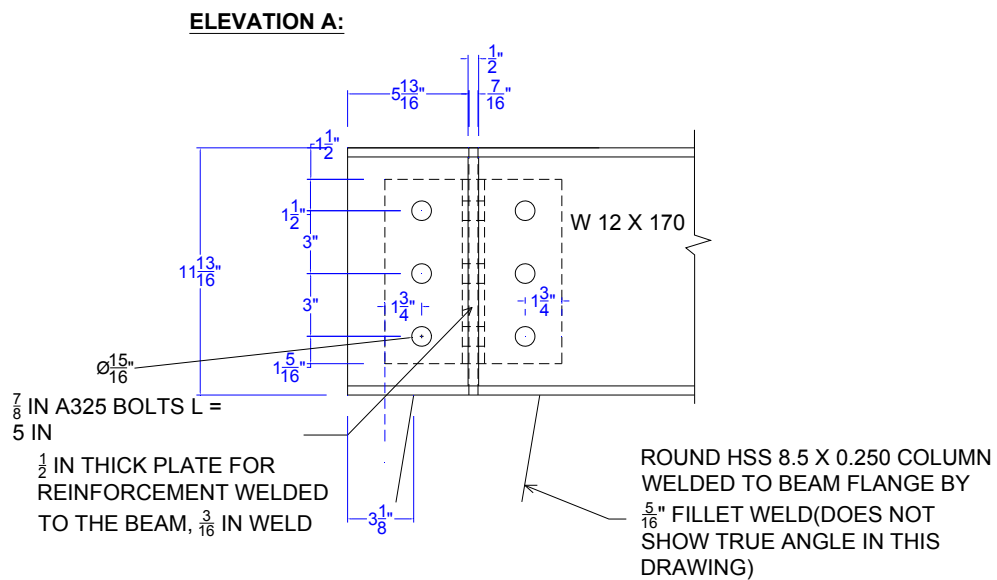
Figure 2.3.16 - Shear connection between beams: Elevation A

240

Figure 2.3.17 – Double angle shear connection between beams

Figure 2.3.18 - Double angle shear connection between beams

2.3.8 Design of Lugs

<u>Definition</u>: Lug is the component that is connected to the pressure vessel and transfers the dead load and live load acting on the steel cylinder to the steel frame. It is provided to support the pressure vessel. The weight of the vessel is transferred to the supporting frame through the lugs. The lugs are designed for the static and dynamic load. The lug is not a standard component used in building design and its design was not based on the limit state concept. The lug was designed as per the allowable stress design concept. Support lugs are limited to vertical pressure vessels with small to medium diameters (1 to 10ft) and moderate height to diameter ratios (H/d = 5-2) [9]. To this end, reference [9] was used to design the lug. Reference [9], Section 2.4, illustrates a detailed procedure for the design of lugs supporting vertical pressure vessels. Typical Sketch of a Lug is shown in Figure 2.3.19.

From the load calculations,

Total load, F = 74.3 kip (section 3.2.4)
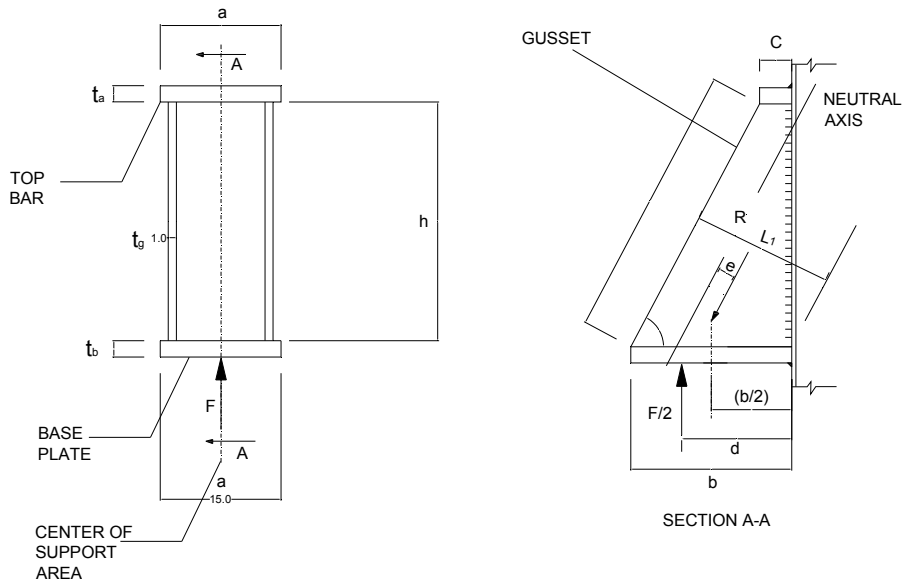
Figure 2.3.19 – Typical lug assembly with the design force 'F'

In our case, (Refer Figure 2.3.19, 2.3.21)
h = 30 in
a = 15 in
t_g = 1 in
 b= 20 in
d = 15 in
α= arc tan $\left(\dfrac{h}{b}\right)$= arc tan $\left(\dfrac{30}{21}\right)$ = 55^0
c = 4 in

Figure 2.3.20 – Lug connected to steel cylinder

Gusset thickness, T_G:

The gusset plates can be assumed to be eccentrically loaded plates. Combined stress in one gusset due to load $\dfrac{F}{2}$ consists of bending stress and compressive stress.

Let us assume thickness of gusset plate, $t_g = 1"$ and check if the stresses in the plate are less than the allowable stresses.

Let S_c be the allowable stress in compression for the plate. Allowable compressive stress in the plate is a function of its radius of gyration and length. S_c can be computed from the relation given in reference [18] as,

$$S_c = \frac{18{,}000}{1 + \dfrac{1}{18{,}000} \cdot \left(\dfrac{L}{r}\right)^2} = \frac{18{,}000}{1 + \dfrac{1}{18{,}000} \cdot \left(\dfrac{36.62}{0.289}\right)^2} = 9513 \text{ psi } [18],$$

Where,

$$L = \frac{h}{\sin \alpha} = \frac{30}{\sin 55} = 36.62 \text{ in (See Figure 2.3.19)}$$

r = radius of gyration of plate = 0.289 x t_g = 0.289 x 1 = 0.289

From Figure 2.3.19 we can write,

$$R = \frac{F}{2 \cdot \sin \alpha} \qquad\qquad (1)$$
$$L_1 = b \cdot \sin \alpha$$

$$e = \left(d - \frac{b}{2}\right) \cdot \sin \alpha$$

Maximum compressive stress, S_a due to compression and bending is,
From Figure 2.3.19,

$$S_a = \left(\frac{R}{L_1 t_g} \right) + \left(\frac{6e \cdot R}{L_1^2 \, t_g} \right)$$

$$t_g = \frac{R}{L_1 \cdot S_a} \left(1 + \frac{6e}{L_1} \right) \qquad\qquad (2)$$

Substituting expressions for R, L_1 and e from (1) into (2), we get expression for gusset thickness as

$$t_g = \frac{F \cdot (3d - b)}{\left(Sa.b^2 . Sin^2\alpha \right)} \qquad\qquad (3)$$

$$tg = \frac{74.3 \cdot (3 \cdot 14 - 20)}{(22 \cdot 20^2 \cdot . Sin^2 55°)} = 0.6" < 1"$$

Top Bar Plate can be assumed to be a simply supported beam of span 'a' and cross section of width 't_a' and depth 'c'. The plate/beam has a uniformly distributed load of w $= \frac{Fd}{h}$.

Bending moment $M = \frac{w \cdot a^2}{8} = \frac{F \cdot d}{a \cdot h} \cdot \frac{a^2}{8} = \left(\frac{Fda}{8h} \right)$

The maximum bending stress in the beam can be written as

$$S_b = \frac{6M}{t_a c^2} = \left(\frac{6}{t_a c^2} \right) \left(\frac{Fda}{8h} \right)$$

$$t_a = \frac{0.75 \cdot (F \cdot d \cdot a)}{S_b \cdot c^2 \cdot h} = \frac{0.75 \cdot (74.3 \cdot 15 \cdot 15)}{20 \cdot 4^2 \cdot 30} = 1.3 \text{ in}$$

Where, S_b is the allowable stress in bending for the bar material.
For A36 Grade steel, allowable stress in Bending = S_b = 20 ksi [7]
Use 1 ½" thick top plate. In order to reduce construction cost and time, a continuous circular ring was used instead of a top bar.

Weld Size calculation:
The weld attaching the lug to the vessel carries the vertical shear force, F and moment $F \cdot d$
Length of weld per lug = L_w = ($4 \cdot h + 2 \cdot a$) = 150"
Shear = f_1 = F/L_w = (74.3/150) = 0.50 k/in

$$\text{Bending} = f_2 = \frac{F \cdot d}{a \cdot h + \left(\dfrac{h^2}{3}\right)} = \frac{74300 \cdot 15}{15 \cdot 30 + \left(\dfrac{30^2}{3}\right)} = 1.78 \, \text{k/in}$$

Section modulus of welds forming rectangular pattern is given by $a \cdot h + \left(\dfrac{h^2}{3}\right)$ [23]

$\text{Resultant} = f = \sqrt{f^2{}_1 + f^2{}_2} = \sqrt{0.50^2 + 1.78^2} = 1.84 \, \text{k/in} = 1840 \, \text{lb/in}$

Strength of fillet weld, $\varphi \cdot (F_w) = \varphi \cdot (0.6 \cdot F_{EXX}) = 0.75 \cdot (0.6 \cdot F_{EXX})$

For a E60 electrode, $F_{EXX} = 60$ ksi

$\varphi \cdot (F_w) = 0.75 \cdot (0.6 \cdot 60{,}000) = 27{,}000$ psi

$\text{Weld size} = \left(\dfrac{f}{\varphi \cdot F_w}\right) = \left(\dfrac{1840}{27{,}000}\right) = 0.07$ in

½" fillet weld was provided since the thicker plate to be welded (gusset) was 1" thick. See the lug drawing in Figure 2.3.21.
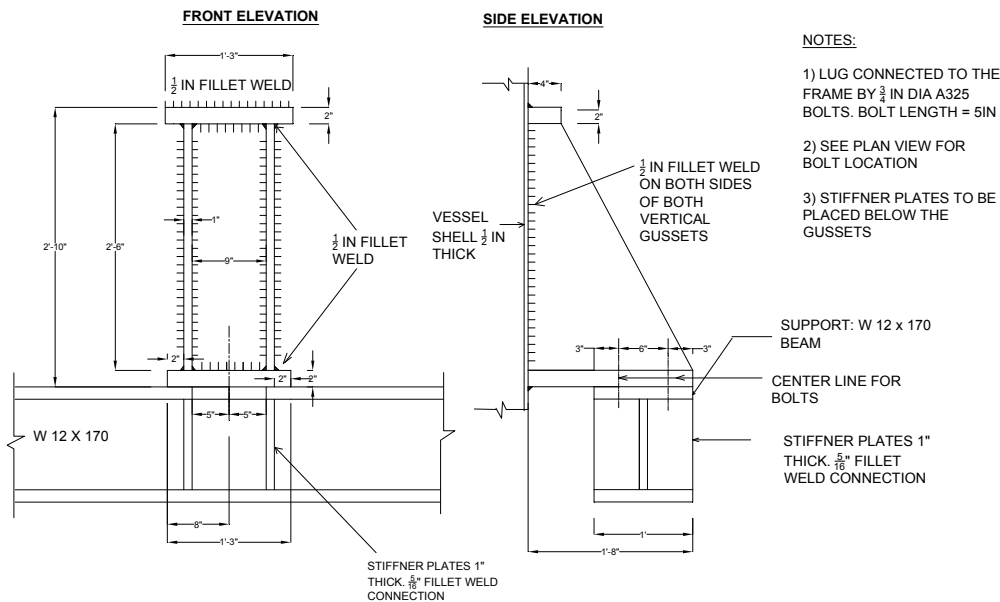
Figure 2.3.21 – Details of Lug

2.3.9 SAP Model for Foundation Slab

Owing to the high dynamic force, it was decided to rest the rocket on a foundation slab instead of footings. The site contained stiff clay and hence footings were inadequate to carry the high load and avoid problems due to differential settlement.

The foundation slab was designed as a plate resting on an elastic foundation. The RCC slab was 1' thick and 10' X 10' in plan. Each column of the rocket was bolted to the slab through a base plate of 15" X 15". Thus the area transferring the load from each column to the foundation slab was 225 in². Since the vertical load under each column is

245

74.3 kip (section 3.2.4), the pressure acting under each column can be computed as follows:

Uniform load under base plate $= \dfrac{Load}{A_e} = \dfrac{74.3 \cdot 1000}{225} = 330$ psi

Figure 2.3.22 shows the loading for slab. A uniform load of intensity 330 psi is applied at the corners over an area of 225 in².
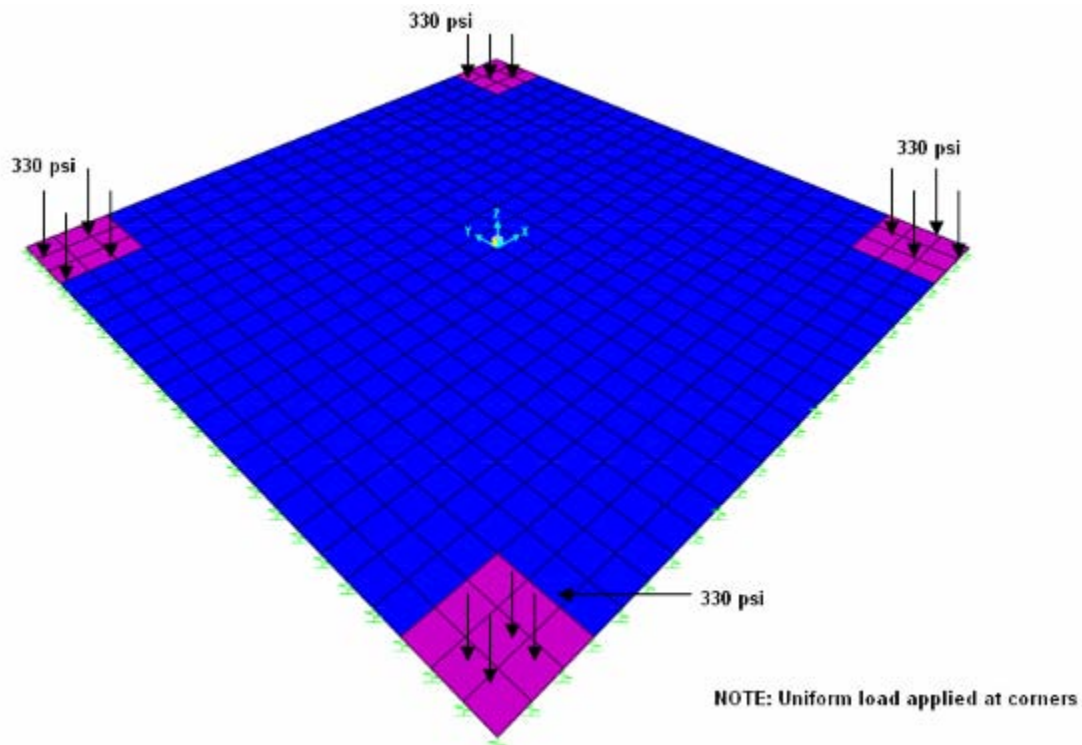
Figure 2.3.22 – Uniformly distributed pressure applied at corners of slab.

The slab was modeled as a plate resting on elastic foundations. To this end, a finite element model was developed in SAP 2000 in which the 10' x 10' foundation slab was meshed into 24 x 24 shell elements connected at nodes. Each node was then assigned a spring support whose stiffness was computed from the modulus of the sub-grade reaction. Figure 2.3.23 shows the model of slab with the clay modeled as springs with stiffness K. The stiffness of spring attached to the node is computed from the tributary area associated with that node. Figure 2.3.24 shows a typical internal node **A** where slab elements are connected. The tributary area for this node is

$A_t = 5$ x $5 = 25$ in²
Modulus of Sub-grade Reaction $= E_f = 5000$ KN/m³ (18.42 lb/in³) [12]
Stiffness of spring $= A_t$ x $E_f = 25$ X $18.42 = 460.5$ lb/in

Thus a spring of stiffness 0.46 k/in is assigned at each node in a direction perpendicular to the plane of the slab. At the nodes along the edges of the plate (slab), the

spring stiffness is half since the tributary area is half and at the corners, the stiffness is 25% as the tributary area is $1/4^{th}$. Figure 2.3.23 shows the finite element model of the slab with springs assigned at each node
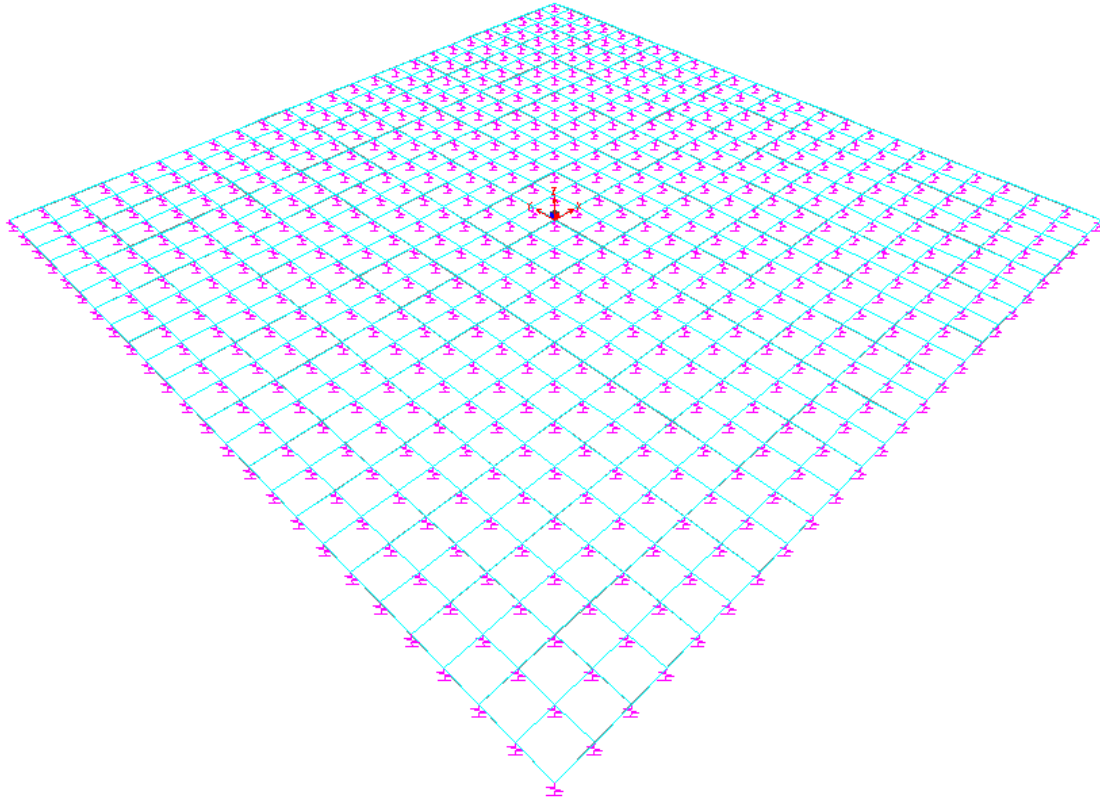
Figure 2.3.23 –FE model of the slab. Springs attached at nodes represent the ground.
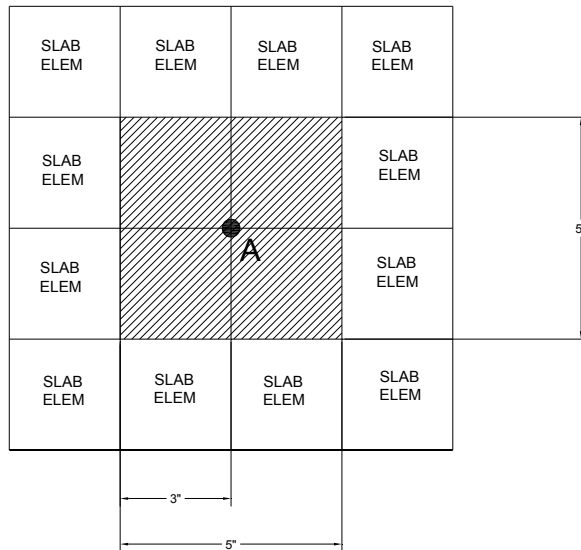
Figure 2.3.24 – Calculation of spring stiffness assigned at each node
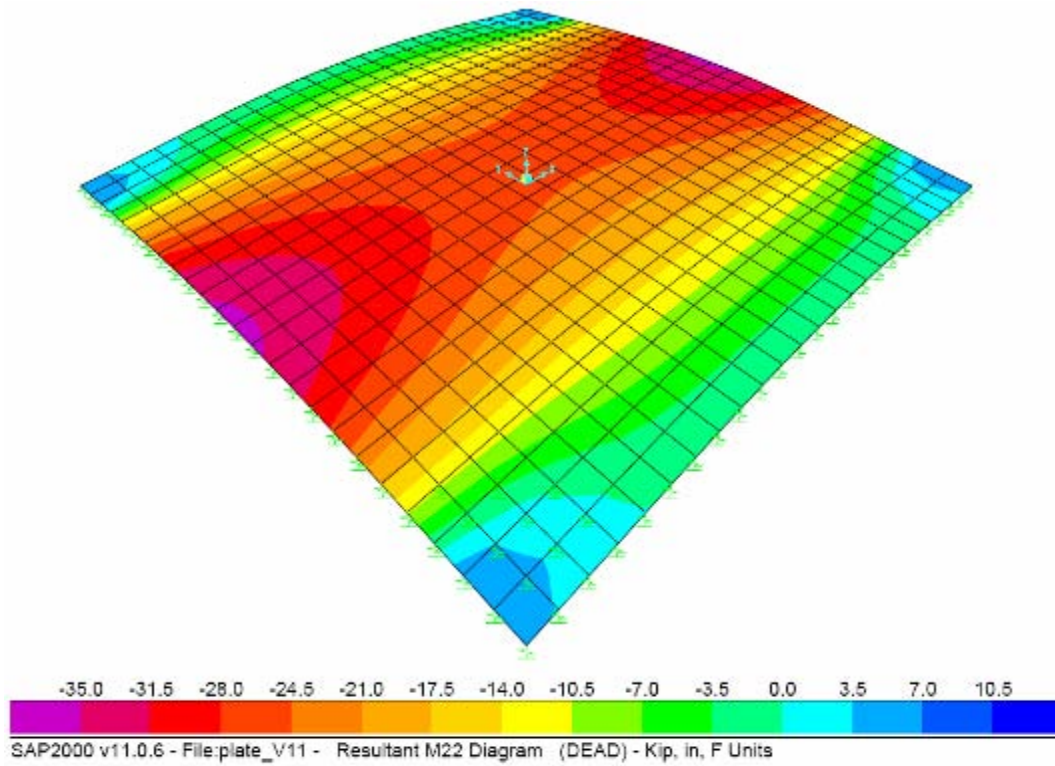
Figure 2.3.25 – Results of the FE model of the slab. Bending moments induced in the slab in each orthogonal direction.

Shell element with the following attributes was used in the analysis of the slab
Type: Thick Plate;
Element Type: Shell;

Thickness:
Membrane: 12"
Bending: 12"
Material: Concrete
Properties:
$f'_c = 4000$ psi
$E = 57 \sqrt{f'_c} = 57 \sqrt{4000} = 3605$ ksi, [13]
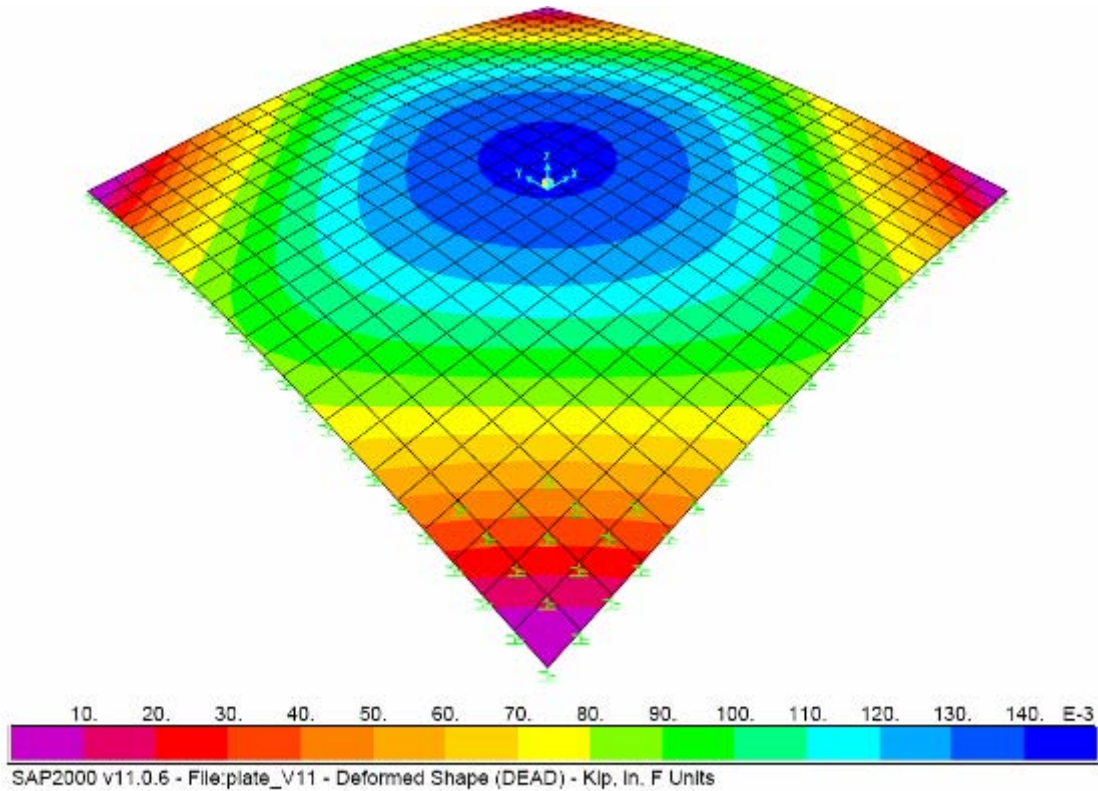
Figure 2.3.26 – Deformed shape. Displacement contour for the slab

The slab geometry and the loading are symmetric in both the direction and hence the bending moments in both the orthogonal directions are the same as shown in Figure 2.3.25

2.3.10 Design of Foundation Slab

Figure 2.3.25 shows variation of bending moment in the concrete slab. The slab was designed using the maximum bending moment (See Figure 2.3.25).

Data: $f_c^{'} = 4000$ psi
$F_y = 40$ ksi

Design moment = 35 kip-in (from Figure 2.3.25)

$$R = \frac{M}{\phi b d^2} = \frac{35,000}{0.9 \cdot 12 \cdot 12^2} = 22.5 \, \text{psi}$$

From [22], Ratio of steel required in the cross section to provide R = 22.5 psi is
$\rho = 0.0015$
Area of steel required = $\rho A = 0.0015 \times 12 \times 12 = 0.19 \, \text{in}^2$

249

Use #4 bars with 12" spacing, which give a steel area of 0.20 in^2. Figure 2.3.27 shows the reinforcement details for the slab.
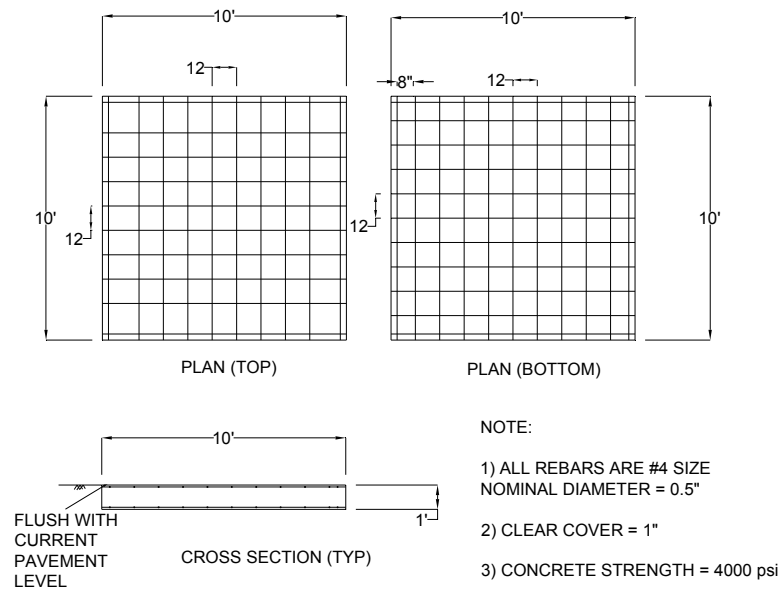
Figure[4] 2.3.27 – Plan showing reinforcement details

2.3.11 Design of Steel Cylinder

Steel cylinder was designed as a pressure vessel with flat closures at both ends. In case the concrete failed to flow into the verification core, the vessel would be filled with concrete up to three quarters of its height and would then be pressurized with compressed air at 100 psi. This would mimic the static pressure head of the concrete at the bottom of a drilled shaft and assist the concrete flow. Considering the maximum depth of drilled shaft to be 100ft, the static pressure head that would be required was estimated to be 100 psi. Thus the requirement was that the vessel be designed to resist hoop stresses resulting from a uniform pressure of 100 psi. A safety release valve was attached to the top lid of the pressure vessel that would release the air pressure above 100 psi. The concrete would produce linearly varying stresses in the vessel and thus induce some bending moments apart from the hoop stresses. However, these actions were considered negligible because, I) the height of concrete was approximately 6 ft, which would result in maximum pressure of 5.5 psi. Compared to the air pressure of 100 psi, this stress was considered negligible. To this end, the sizing of the steel cylinder was based on the following design parameters.

Data:
Inner Diameter of cylinder = d =36"
Material = A500 steel, Grade B [29]
Minimum tensile strength = F_t =58 ksi

---

[4] All are #4 bars

Maximum working pressure = P = 100 psi
Joint Efficiency = E = 0.5

The value of 0.5 for joint efficiency is a very conservative value. This value is chosen on the basis of the quality of fabrication of the vessel, weld inspection etc. This value assumes that there is no special inspection such as X-ray testing for the welds, performed on the joint of the pressure vessel. Thus, efficiency of the joint to transfer the load (In this case the hoop stresses) is reduced by 50% in the design. For the allowable stresses in pressure vessels, the typical factor of safety is taken as 3.5 and applied to minimum specified tensile strength. [26]

Design:

Thickness requirement of the pressure vessel $= t = \dfrac{p \cdot d}{2 \cdot f \cdot E}$,

f = acceptable stress level for the vessel in tension caused by the hoop stress.

$f = \dfrac{F_t}{3}$

$f = \dfrac{58}{3} = 19.33 \text{ ksi} = 19333 \text{ psi}$

Therefore,

$t = \dfrac{100 \cdot 36}{2 \cdot 19333 \cdot 0.5}$

t = 0.2"

Use a ½" thick steel cylinder.

2.3.12 Design of Flanges

The pressure vessel is provided with a slip on flange on both ends to cap it with steel lids. The flanges will be designed to resist the internal pressure. The design procedure adopted here has been illustrated in reference [9]. Figure 2.3.28 shows a free body Diagram of a Flange with various forces acting on it. The flange was designed considering the following design parameters.

Data:
Design Pressure = p = 100 psi,
Bolting Steel – A325
Gasket Material = Neoprene
Yield factor for neoprene gasket = m = 0.5 [15]
Minimum design seating stress for the gasket[5], y = 0 psi [15]
Shell Thickness = 0.5"

---

[5] It is the yield stress at which the gasket material yields. The gasket has to yield in order to seal a joint. Neoprene being a very soft material, this value is 0 psi and minimal tightening of bolts ensures yielding of gasket.

Shell inside diameter = 36"
Shell outside diameter (ID of Flange) = B = 37"
Allowable stress for the flange material = f =17,500 psi [28]
Material: SA - 105
Type: ASME B16.5 Slip on Flange, Forged [27]
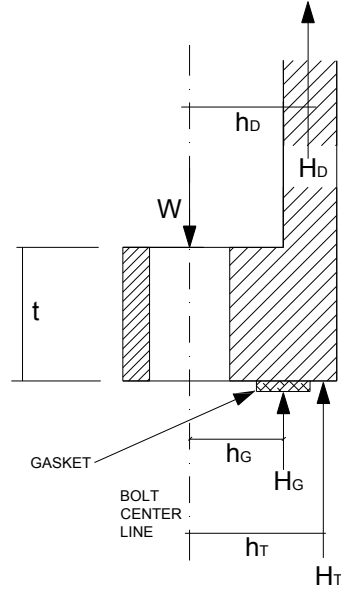
Figure 2.3.28– Forces acting on the blind and flange
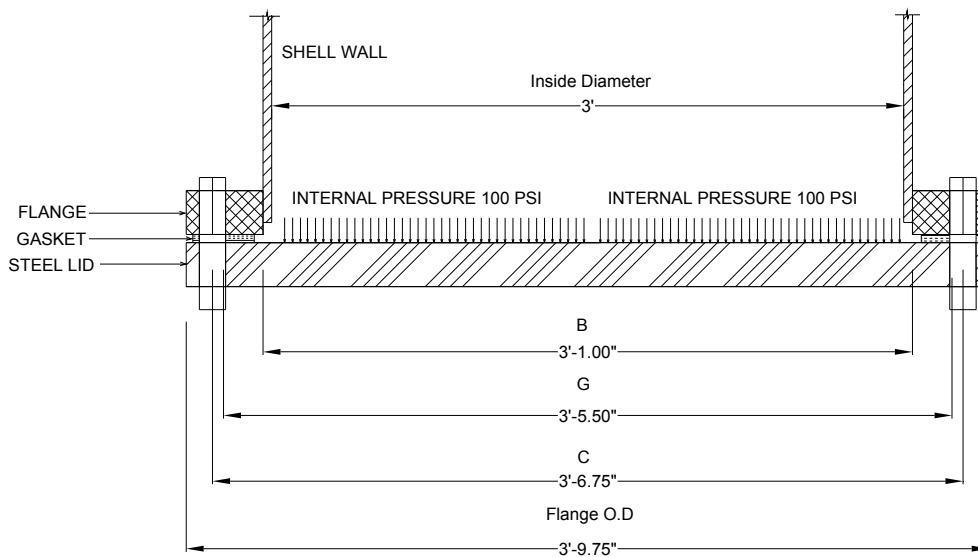
Figure 2.3.29– Internal pressure acting on the blind and flange

252

Calculation of Gasket Width

In reference [10], the ratio between the outer diameter, d_o, and the internal diameter, d_i, for the gasket is given by

$$\frac{do}{d_i} = \sqrt{\frac{y - p \cdot m}{y - p \cdot (m+1)}}$$

d_o = Outside diameter of gasket

d_i = Inside diameter of gasket

$$\frac{do}{d_i} = \sqrt{\frac{0 - 0.5 \cdot 100}{0 - 100 \cdot (0.5 + 1)}} = 0.57$$

Assume d_i = 38 in (0.5" from the shell, see Figure 2.3.29)

do = 0.57 x 38 = 21.66 in

Gasket width = $\dfrac{d_o - d_i}{2} = \dfrac{21.66 - 38}{2} = -8.17$ in

Negative value implies that there is no minimum required width of gasket based on yield criterion. Hence gasket width should be chosen from a practical stand point
Use gasket of width 3.5" (Commercially available neoprene gasket for 36", #150 flanges).

$$G = N_g + d_i = 3.5 + 38 = 41.5 \, \text{in}$$

G = Mean gasket diameter

N_g = Width of gasket = 3.5"

Bolt Loads

Two bolt loads exist: the load developed by tightening up the bolts, Wm_1, and that which exists under the operating conditions, Wm_2. The bolt load for the tightening up condition must exert sufficient force, H_y, on the gasket to cause yielding of the gasket in order to produce a tight joint. This load is equal to the effective area of the gasket times the gasket yield stress, or

$$Wm_1 = H_y = (b \cdot \pi \cdot G \cdot y)$$

b is the effective gasket or joint contact surface seating width. According to reference [17], b is defined as

$$b = b_0 \text{ If } b_0 \le 0.25$$

$$b = \frac{\sqrt{b_0}}{2} \text{ If } b_0 > 0.25$$

In our case,

$$b_0 = \left(\frac{N_g}{2}\right) = \left(\frac{3.5}{2}\right) = 1.75"$$

Since $b_0 > 0.25$, $b = \frac{\sqrt{b_0}}{2} = \frac{\sqrt{1.75}}{2} = 0.66"$

$$Wm_1 = H_y = (0.66 \cdot \pi \cdot 41.5 \cdot 0) = 0 \text{ lb}$$

The bolt load under the operating condition consists of the force necessary to resist the internal pressure and to keep the gasket tight during the operation. The internal pressure produces an end force, H, given by

$$H = \left(\frac{\pi \cdot G^2}{4} \cdot p\right) = \left(\frac{\pi \cdot 41.75^2}{4} \cdot 100\right) = 135,265 \text{ lb} = 135.26 \text{ kip}$$

Load required to keep joint tight under operation, H_p, is given by

$$H_p = (2 \cdot b \cdot \pi \cdot G \cdot m \cdot p) = (2 \cdot 0.66 \cdot \pi \cdot 41.75 \cdot 0.5 \cdot 100) = 8623 \text{ lb}$$

Total operating load
$Wm_2 = H + H_p$
$Wm_2 = 135,265 + 8623 = 143,888 \text{ lb} = 143.88 \text{ kip}$
$Wm_2 > Wm_1$

Calculation of minimum bolt area

$$Am_1 = \left(\frac{Wm_2}{f_a}\right) = \left(\frac{143.88}{18}\right) = 7.99 \text{ in2},$$

Where,
f_a = allowable tensile stress in A325 bolts =18 ksi[6] [14]
Choose 1 1/2" diameter bolt,
Bolt area = 1.76 in^2

We choose a bolt circle diameter of 42.75 in

---

[6] Allowable stress in bolt for pressure vessel is taken as 20% of the minimum specified tensile strength of the bolt. Minimum specified tensile strength of A325 bolt = 90 ksi. Hence allowable stress is 18 ksi.

C = 42.75 in

Outer Diameter, A = Bolt Circle Diameter + 2E

A = 42.75 + 2 x 1.5 = 45.75 in (see Figure 2.3.29),

E is the cover = 1.5" [10]

Flange Thickness

The various axial forces on the flange produce bending moments. The summation of the moments is taken about the bolting axis.

For bolting-up condition, the design load is given by

$$W = \frac{1}{2}(A_b + A_m)f_a$$

$$W = \frac{1}{2}(7.92 + 56.54) \cdot 18000 = 587{,}464 \text{ lb} = 587.4 \text{ kip}$$

Here;
A_b is the actual total cross sectional area of bolts
A_m is the total required cross sectional area

The corresponding lever arm is given by

$$h_G = \frac{1}{2}(C - G)$$

$$h_G = \frac{1}{2}(42.75 - 41.5) = 0.625 \text{ in}$$

The flange moment is as follows
$$M_a = (W \cdot h_G)$$
$$M_a = 587.4 \cdot 0.625 = 367.16 \text{ kip-in}$$

For operating condition (W = W$_{m1}$),

In operating condition, a force equal to the internal pressure times the area of the pipe is exerted on the flange. This force H_D can be calculated as,

H_D = Area of blind x Internal Pressure.

$$H_D = \left(\frac{\pi}{4} \cdot B^2 \cdot p\right) = \left(\frac{\pi}{4} \cdot 37^2 \cdot 100\right) = 107{,}467 \text{ lb} = 107.46 \text{ kip}$$

The lever arm h_D is

255

$$h_D = \left(\frac{C-B}{2}\right) = \left(\frac{42.75-37}{2}\right) = 2.875 \text{ in}$$

The moment M_D is

$$M_D = (H_D \cdot h_D) = (107.46 \cdot 2.875) = 308.94 \text{ kip-in}$$

H_G is given by

$$H_G = W_{m2} - H = 143.88 - 135.26 = 8624 \text{ lb} = 8.62 \text{ kip}$$

The corresponding lever arm is

$$h_G = \frac{C-G}{2} = \frac{42.75-41.5}{2} = 0.625 \text{ in}$$

The moment is given by M_G,
$$M_G = (H_G \cdot h_G) = (8.62 \cdot 0.625) = 5.39 \text{ k-in}$$
$$H_T = H - H_D = 135.26 - 107.46 = 27.8 \text{ k}$$
$$h_T = \frac{h_D + h_G}{2} = \frac{2.875 + 0.625}{2} = 1.75$$

The moment is given by M_G,
$$M_T = (H_T \cdot h_T) = (27.8 \cdot 1.75) = 48.65 \text{ k-in}$$

The summation of moment for the operating condition,
$$M_0 = M_D + M_G + M_T$$
$$M_0 = 308.94 + 5.39 + 48.65 = 362.98 \text{ k-in}$$

Since $M_a > M_0$,

$$M_{max} = M_a = 367.16 \text{ k-in}$$

Calculation of flange thickness:

Define, $K = \dfrac{A}{B} = \dfrac{45.75}{37} = 1.23$

A is Outer diameter of flange = 45.75 in (See Figure 2.3.29)
Thickness of flange can be calculated from the expression,

$$t = \frac{\sqrt{YM_{max}}}{\sqrt{fB}} \quad [16]$$

f = allowable stress in flange material = 17,500 psi
In reference [16], factor Y is defined using K from the following expression as

$$Y = \frac{1}{K-1} \cdot \left(0.66845 + 5.71 \cdot \frac{K^2 \cdot \log(K)}{K^2 - 1} \right)$$

$$Y = 9.26 \qquad [16]$$

$$t = \frac{\sqrt{9.26 \cdot 367160}}{\sqrt{17500 \cdot 37}} = 2.29 \text{ in}$$

To this end, a flange with thickness of 2.5 in, with OD 46" was used. This is a standard #150 rated, Slip-On flange.

2.3.13 Design of Blinds

The 36" blind flanges were not custom fabricated. A standard 36" blind with the following specification was used,
Pressure Rating: 150#
Diameter: 36"
Material: SA - 105
Allowable Stress, f_y = 17.5 ksi [26], [28]
However, the design for 36" blinds was verified using the classical theory of plates and shells. The blinds were analyzed as circular lids with uniform pressure and simply supported at their rims.

Design:
Thickness = h = 2.5"
Pressure = q = 0.100 ksi (100 psi)
Radius of lid = a = 20.5"
Maximum stress is given by the expression,

$$\sigma_{max} = \frac{3 \cdot (3+\nu)}{8} \cdot \frac{q \cdot a^2}{h^2} \quad [11],$$

Where ν is the Poisons ratio for the material, ν = 0.3 for steel. This gives:

$$\sigma_{max} = \frac{3 \cdot (3 + 0.3)}{8} \cdot \frac{0.1 \cdot 20.5^2}{2.5^2} = 11.75 \text{ ksi}$$

Thus the maximum stress σ_{max} is within the allowable stress limit which is 17.5 ksi.

2.3.14 Summary

In this chapter, details of the design of the rocket are illustrated in detail. The detailed results of the experiment and interpretation are presented in Section 2.4.

2.4 EXPERIMENTAL RESULTS AND INTERPRETATION

2.4.1 Introduction

Details of the experimental procedure, setup and testing apparatus have been discussed in Section 2.2. Observations of the experimental results have also been briefly mentioned in Section 2.2. In this chapter, the results of the experiment and their interpretation are discussed in detail.

2.4.2 Core Recovery

The primary goal of the research was to study the state of material in verification cores after the concrete is placed. After all the pours were over, the cores (PVC pipes) that were obtained and preserved were recovered for testing and observations. Testing primarily included the investigation of the material properties in the verification core. The conditions, dry and wet, in which the concrete was placed into the verification core yielded different types of material in the core. As mentioned in Section 2.2, solid cured concrete was obtained in the verification core when the concrete was placed in dry conditions. In the wet process 3 (WP 3), when the steel tube was at the bottom of the verification core, solid cured concrete was found in the core. In all other wet processes, the material obtained in the core hole was weakly cemented material, which was a matrix of sand-gravel mixture. The core recovery consisted of the following two operations.

1) Cutting the PVC pipes into sections

In this operation, PVC pipes were cut with a portable gas powered rotary saw. The saw utilized a 14" diameter, diamond bit, rotary blade. The PVC pipe was cut into approximately 4 to 5 pieces. Length of each piece was approximately 12". The top part of the PVC pipe near the flange area and the bottom part near the cap area were discarded because the material at the ends was likely to be affected by disturbance caused during handling of the PVC pipes. Figure 2.4.1 shows cutting operation of the PVC pipe. The cutting time for the 6" pipe filled with concrete was approximately 40 minutes and for the 12" pipe filled with concrete it was about 70 minutes. For the PVC pipes filled with sand-gravel (PVC pipes filed under wet conditions yielded a sand-gravel mixture, see details later), the cutting times were 15 minutes for the 6" pipe and about 30 minutes for the 12" pipe.

Figure 2.4.1 – Cutting the PVC pipe

Material Testing

After the 5 foot long PVC pipes were cut into pieces, material contained in each piece was observed and appropriate testing methods were adopted to characterize its strength and stiffness. Properties of the material obtained in the verification core under both dry and wet condition are discussed in the subsequent sections.

2.4.3 Cores obtained by concrete Pouring in the Dry

A total of 5 PVC pipes were filled under the dry condition: they consisted of 3-6" diameter and 2-12" diameter pipes. As PVC pipes were impermeable, moisture in the concrete was trapped inside and helped curing of concrete. Figures 2.4.2 and 2.4.3 respectively show a 6" and a 12" PVC pipe filled with cured concrete.

Cylindrical concrete cores were recovered from each piece of PVC pipe to perform uniaxial compression (UCS) tests as per ASTM C 39 [20]. The test cylinders obtained from the 6" PVC pipes were 6" X 10" cylinders. The concrete cylinders from the 6" pipe were obtained by stripping off the surrounding PVC material with a table saw. This procedure of extracting cores from the 6" pipe was preferred over coring as it was much faster and efficient than coring. Also, ASTM C 39 [20] recommends the use of a 6" diameter cylinder for getting the compressive strength of concrete. Figure 2.4.4 shows the removal of PVC material. The cylinder's ends were then cut and ground to obtain 10" long samples. Figure 2.4.5 shows a typical sample obtained for UCS from the 6" core.

Concrete samples were obtained from the 12" PVC pipes by coring. The samples were 4" in diameter and 8" long with an aspect ratio of 2. Figure 2.4.6 shows the coring of concrete samples from the 12" PVC pipes.

Uniaxial compressive strength tests were performed on the concrete cylinders obtained from both pipes (6" and 12"). The tests were conducted as per ASTM C 39. Figure 2.4.7 and Table 2.4.1 show the compressive strength test data along the length of the PVC pipes. Notice that:

1) The compressive strengths from the 12" cores are consistently higher than the ones obtained from the 6" cores. This was an anticipated result because of better consolidation of concrete in the 12" diameter pipe compared to the 6" diameter pipe.

2) The 6" verification core, concrete strength and Young's Modulus decreased as the height of drop increased.

Figure 2.4.2 – 6" PVC pipe containing cured concrete

Figure 2.4.3 – 12'' PVC pipe containing cured concrete

Figure 2.4.4 – Concrete cylinder extracted by cutting the clear PVC pipe

Figure 2.4.5 – UCS Sample obtained from 6'' PVC pipe

Figure 2.4.6 – Samples cored from 12'' PVC pipe

DRY PLACEMENT - 6" CLEAR PVC

	Top L =7"		Top L =8"		Top L =9.75"
1	L =10.5" NO DATA	1	L =10" 5000 psi	1	L =9.8" Fractured before test
2	L =11.6" 6890 psi	2	L =13.5" 4190 psi	2	L =9.9" 3600 psi
3	L =15.75" 7190 psi	3	L =12" NO DATA	3	L =13.5" NO DATA
4	L =9.75" 7250 psi	4	L =10.5" 5570 psi	4	L =10.5" 3320 psi

Day 1
30' POUR

f_{avg} = 7110 psi
E = 4800 ksi

Day 2
70' POUR

f_{avg} = 4920 psi
E = 3990 ksi

Day 3
100' POUR

f_{avg} = 3460 psi
E = 3350 ksi

DRY PLACEMENT - 12" CLEAR PVC

	Top L =7"		Top L =8"
1	L =10.5" NO DATA	1	L =10" 7870 psi
2	L =11.6" 6850 psi	2	L =13.5" 9200 psi
3	L =15.75" 8040 psi	3	L =12" 8500 psi
4	L =9.75" 7420 psi	4	L =10.5" NO DATA

Day 2
70' POUR

f_{avg} = 7440 psi
E = 4910 ksi

Day 3
100' POUR

f_{avg} = 8520 psi
E = 5260 ksi

Figure[7] 2.4.7 – State of concrete in the clear PVC pipes under dry condition

---

[7] Numbers 1,2,3,4 denote the sequence of the samples from top to bottom of the PVC pipe. L denotes length of each sample

Table 2.4.1 - Unconfined compressive strength values of the concrete samples.

Process	Height of Pour ft	Specimen No[8]	Core Size	UCS (psi)	Young's Modulus (ksi)[9]	Young's Modulus (ksi)[10]
Dry Placement	30	1	6"	No Data	-	
	30	2	6"	6890	4730	3280
	30	3	6"	7190	4830	3410
	30	4	6"	7250	4850	-
	70	1	6"	5000	4030	-
	70	2	6"	4190	3690	-
	70	3	6"	No Data	-	-
	70	4	6"	5570	4250	-
	100	1	6"	No Data	-	-
	100	2	6"	3600	3420	-
	100	3	6"	No Data	-	-
	100	4	6"	3320	3280	-
	70	1	12"	No Data	-	3340
	70	2	12"	6850	4720	-
	70	3	12"	8040	5110	-
	70	4	12"	7420	4910	-
	100	1	12"	7870	5060	3380
	100	2	12"	9200	5470	-
	100	3	12"	8500	5260	-
	100	4	12"	No Data	-	-
Wet Process 3	30	1	12"	11000	5980	-
	30	2	12"	11000	5980	-
	100	1	12"	7250	4850	-
	100	2	12"	6950	4750	-
	100	3	12"	8440	5240	-
Average Value	-	-	6"	5380	4135	3345
			12"	8410	5210	3360

The values of Young's Modulus for the concrete shown in Table 2.4.1 were computed based on equation 4.1 given in the ACI 318-05 [13], section 8.4.1 (Building code requirements for structural concrete)

$$E = 57 \times \sqrt{f_c'} \qquad\qquad 4.1$$

f_c' = Compressive strength of concrete (psi)
E = Young's Modulus in ksi

---

[8] Figure 4.7 shows the location of the specimen in the PVC pipe.
[9] Young's Modulus computed based on ACI 318-05
[10] Young's Modulus obtained from tri-axial test of concrete samples

2.4.4 Cores obtained by concrete Pouring in the Wet

The placement of concrete under the wet conditions was carried out with three different processes. These processes are described in detail in Section 2.2 and are referred as WP1, WP2 and WP3. The cores obtained under processes WP1 and WP2 yielded a sand-gravel matrix. The nature and properties of the sand-gravel matrix in WP1 and WP2 varied with the core size and the process adopted. The phenomenon was attributed to the washing of cement from the concrete as the water escaped out through the PVC pipe during the placement of concrete. The material was too weakly cemented to extract cores out of it and hence characterization of its strength was not based on uniaxial compressive strength tests as a result.

The sand-gravel mixture was found to be well compacted in the 12" pipes and comparatively loose in the 6" pipes. The structure of the mixture also showed honey-combing in some areas. Figures 2.4.8- 2.4.9 show the state of sand-gravel mixture in the clear PVC pipes. The pieces of PVC pipes either contained a weakly cemented sand gravel mixture (WC) (Figure 2.4.9) or mixture that was not-cemented (NC) (Figure 2.4.8). Since it was difficult to carry out any type of tests to determine the strength and stiffness of weakly cemented material, its stiffness estimation was based on its dynamic characterization. Dynamic tests were carried out to determine the P-wave velocity in them. The stiffness of the material was estimated based on the P-wave velocity in this material. For the WC material, Figures 2.4.10 and 2.4.11 show the values of P-wave velocity.

Figure 2.4.8 – 12" Sample obtained in the wet condition with No Cementation

Figure 2.4.9 – Sample obtained in the wet condition with partial/weak cementation

WET PLACEMENT - 6" CLEAR PVC

1) Vp REPRESENTS THE
P-WAVE VELOCITY IN THE
MATERIAL IN FT/SEC

	Top L =8"
1	L =10.5" WC Vp = 3100
2	L =14" WC Vp =1700
3	L =11" NC
4	L =10.5" NC

Day 4
30' POUR

	Top L =9"
1	L =11.25" WC Vp =2500
2	L =11.5" WC
3	L =10.25" NC
4	L =10.25" NC

Day 5
100' POUR

WET PLACEMENT - 12" CLEAR PVC

	Top L =9"
1	L =12" WC Vp = 4100
2	L =12" WC Vp = 3700
3	L =10.5" WC
4	L =11" WC

Day 4
30' POUR

	Top L =9.5"
1	L =12" WC Vp = 2109
2	L =12" WC Vp = 2070
3	L =12" NC
4	L =10" WC Vp = 2059

Day 5
100' POUR

Figure 2.4.10[11] State of Sand Gravel mixtures in clear PVC pipes under wet condition

---

[11] Numbers 1,2,3,4 denote the sequence of the samples from top to bottom of the PVC pipe. L denotes length of each sample. For the Non-cemented material (NC), figure in the parenthesis shows the peak friction angle for the material. For the Weakly Cemented material (WC), the figure with units FT/S shows the P-wave velocity in the material

WET PLACEMENT - 6" CLEAR PVC

Day 6
30' POUR

	Top L =3"
1	L =13" WC $V_p = 1348$
2	L =13.5" WC $V_p = 2734$
3	L =13" WC $V_p = 8060$
4	L =18" NC

Day 7
100' POUR

	Top L =6"
1	L =13.5" WC $V_p = 2244$
2	L =14.5" WC $V_p = 1527$
3	L =12" NC
4	L =14" NC

NOTE:

ALL THE VALUES OF V_p HAVE
UNITS OF FT/SEC

WET PLACEMENT - 12" CLEAR PVC

Day 6 - WP 3
30' POUR

	Top L =9"
1	L =12" 11000 psi
2	L =12" 11000 psi
3	NO DATA

Day 7 - WP 3
100' POUR

	Top L =9"
1	7250 psi
2	L =12" 6950 psi
3	L =12" 8440 psi

Day 7 - WP 2
100' POUR

	Top L =9.5"
1	L =12" WC $V_p = 4200$
2	L =12" WC $V_p = 3180$
3	L =12" WC $V_p = 2780$
4	L =10" WC $V_p = 2230$

Figure 2.4.11[12] State of Sand Gravel mixtures in clear PVC pipes under wet condition

---

[12] Numbers 1,2,3,4 denote the sequence of the samples from top to bottom of the PVC pipe. L denotes length of each sample. WP 2 – Wet Process 2, WP 3 – Wet Process 3.

2.4.5 Characterization of the non cemented material

The non cemented material was generally characterized as a sand-gravel mixture. The shear strength of such material is typically characterized by its peak friction angle. Class SS concrete that was used for the underwater pour contains coarse aggregate with maximum size of 1" (see Appendix A for mix design). Sieve analysis was carried out on the material obtained in the PVC pipes, the sieve analysis indicated that the material obtained at the bottom of the verification core is mostly coarse aggregates. This resulted since the sand and the cement paste are washed from the concrete as it flows through the water into the verification hole.[13]. The results of the sieve analyses are shown in Figures 2.4.12 and Figure 2.4.13. The density of the material is about 95 lb/ft^3 (60% - 65% of the concrete density). As can be seen from the mix design of Class SS concrete in Appendix A, the concrete contains 60% coarse aggregates by weight, which is close to the density of the material obtained in the core.

Details of sample chosen for sieve analysis: Sample A.
Sample: 6" PVC pipe
Placement Condition: Wet
Height of Pour: 30'
Sample Obtained from bottom 18" of PVC pipe. (See Figure 2.4.11)
Quantity of Material obtained: 27.83 lb
Density: 94.5 lb/ft^3 (63% of dry concrete density).
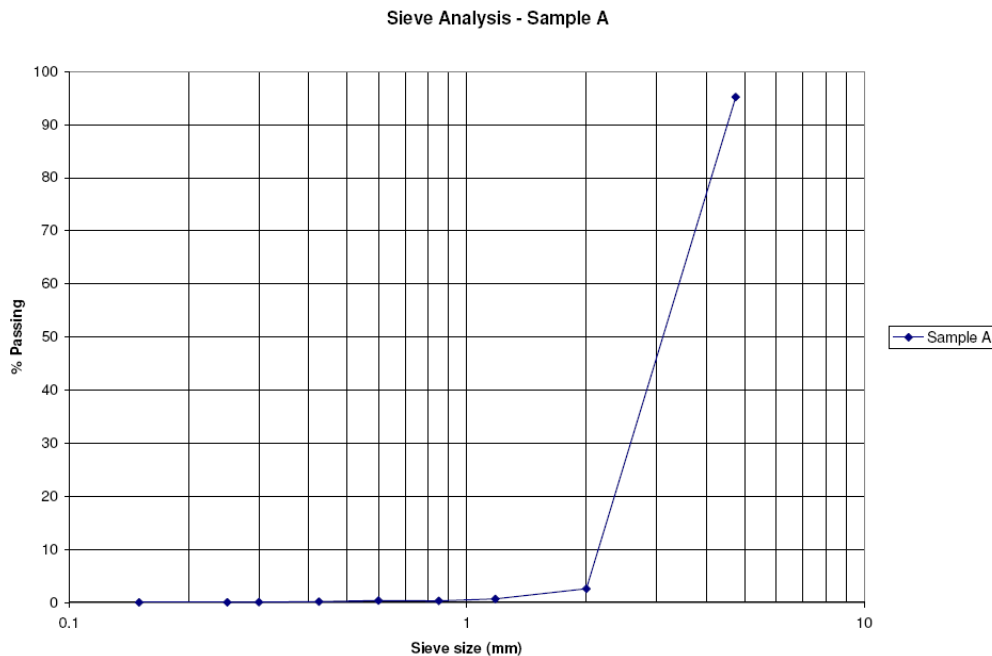
Figure 2.4.12 – Sieve Analysis of gravel: Sample A

---

[13] For proper cementation, fine aggregates are as necessary as cement paste as they fill the voids in the coarse aggregates. The absence of cementation in this case is a result of loss of both cement paste and fine aggregates.

<u>Details of sample chosen for sieve analysis: Sample B</u>.

Sample: 6" PVC pipe
Placement Condition: Wet
Height of Pour: 100'
Sample Obtained from bottom 26" of PVC pipe. (See Figure 2.4.11)
Quantity of Material obtained: 41.67 lb
Density: 98.2 lb/ft^3 (65% of dry concrete density).
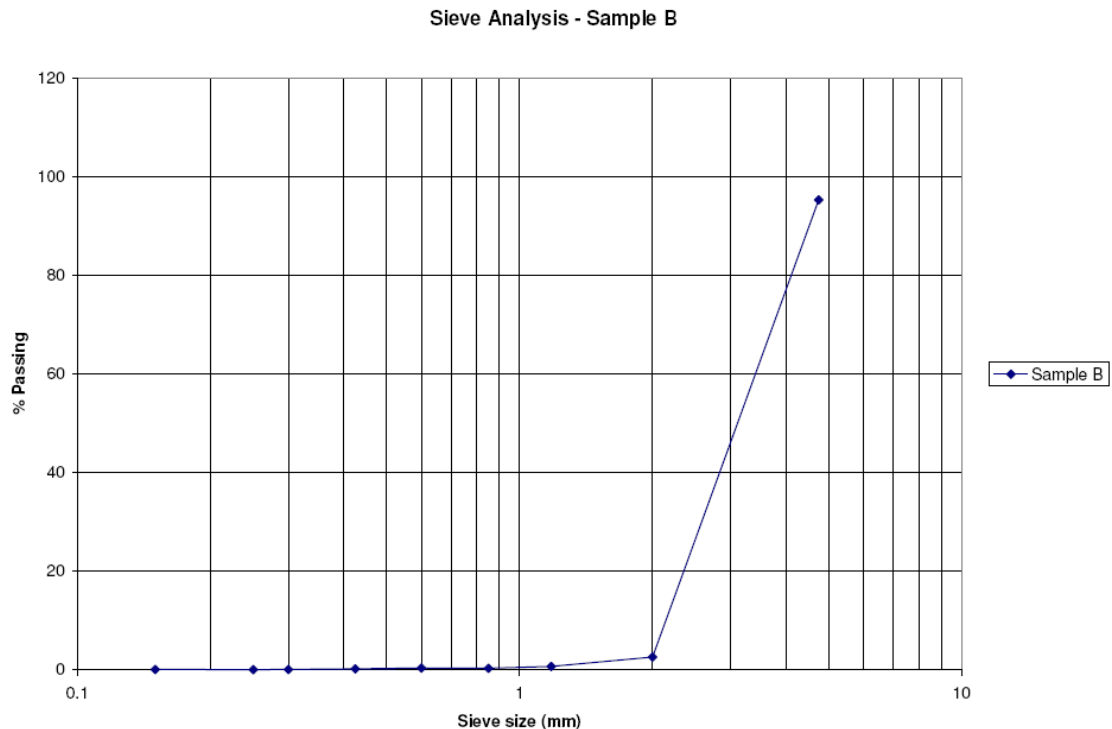
Figure 2.4.13 – Sieve Analysis of gravel: Sample B

Determination of strength and deformability of non cemented material

The strength of the gravel is characterized by friction angle. To determine the shear strength of the gravel, direct shear tests were carried out on the gravel with different normal loads. Details of the direct shear test are illustrated in section 4.5.2. Young's Modulus of gravel was determined by carrying out Oedometric tests on the same sample.

Direct Shear test

Sample Preparation

The direct shear apparatus consisted of a circular shear box made of two cylindrical halves of 6" diameter and 3" height. Figure 2.4.14 shows a schematic of a direct shear box and the application of load. As it can be seen from Figure 2.4.14, Shear

270

Force T is applied to the top part of the shear box. The top part moves relative to the bottom part. The normal force is applied on the top of the top half of the box. The gravel to be tested was placed in the shear box. To replicate the density of the sand-gravel mixture in the verification core, the material was weighed and placed in the shear box until the density of gravel matched that found in the PVC pipe. As discussed in section 4.5, two samples were used in the sieve analysis. The density of material considered in the direct shear test was taken as mean value of both samples.
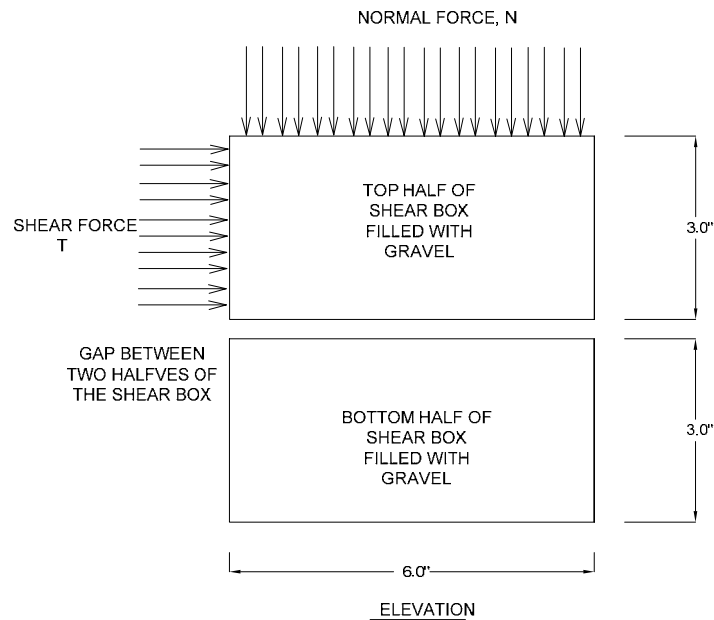
Figure 2.4.14 – Schematic diagram showing two halves of the shear box

Density of Sample A: 94.5 lb/ft^3
Density of Sample B: 98.22 lb/ft^3

Density of sample used in direct shear test: $\left(\dfrac{94.5 + 98.22}{2} \right) = 96.36 \text{ lb/ft}^3$

271

Figure 2.4.15 – Sample setup for the direct shear test

From Figure 2.4.14 it can be seen that the two halves of the shear box are separated by a small gap. This gap was filled with modeling clay. Gap ensures that the shearing plane passes through the sample tested only and that there is no contact between the halves of the shear box during the test.

B) Perform the test

Typical depth of the drilled shaft varies from 30' to 100' [1]. The normal loads for which the direct shear test was carried out were calculated based on these typical depths of drilled shafts.

Normal load, σ= $\gamma \cdot z$

Where γ is the density of the soil

z is the depth.

Normal loads were calculated assuming a soil density of 130[14] lb/ft³. Table 2.4.2 shows the values of three normal loads which were used for the direct shear tests.

Table 2.4.2 - Normal loads for the direct shear test

Depth (z) ft	Normal Stress Psi	Normal Stress MPa
30	27	0.2
50	45.14	0.3
80	72	0.5

---

[14] Typical density of shales.

Thus three direct shear tests were carried out corresponding to each normal load. Following steps were carried out to run the direct shear test

1) Prepare the sample and setup the apparatus
2) Start the test by increasing the normal stress from 0 to the desired value.
3) Once the desired normal stress is reached, apply shear displacement on the top part of the shear box at a constant rate of 1mm/minute [30].
4) The apparatus records the shear displacement, shear stress, normal stress and normal displacement as a function of time.
5) The test was terminated at shear displacement of 25 mm [30]
6) Return the sample to its original configuration by applying displacement in reverse direction.
7) Repeat the test for another value of normal stress.
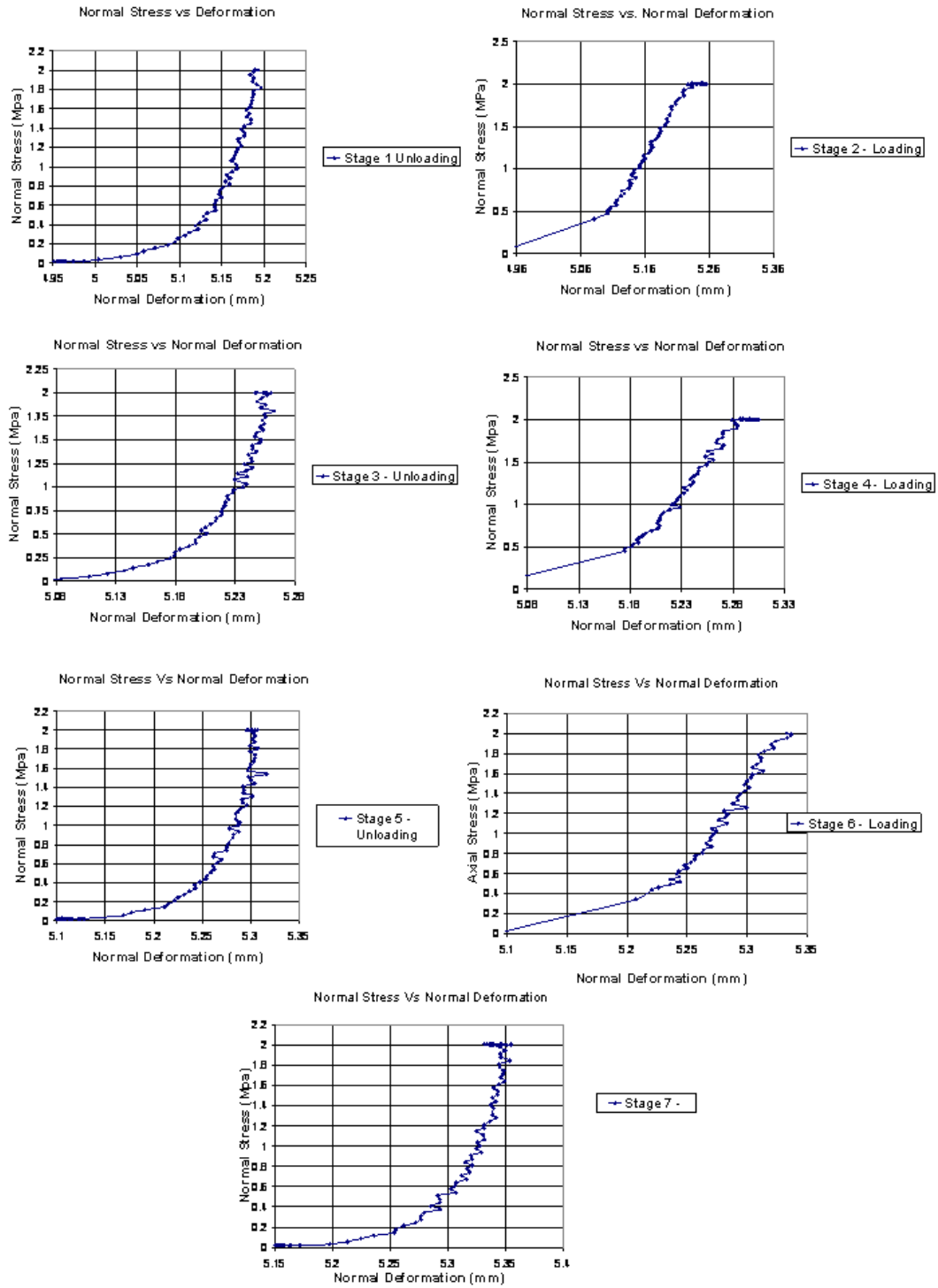
Figure 2.4.16 – Axial Stress vs. Axial Deformation plots for the gravel

274

Oedometric test

Oedometric test was run on the same sample of gravel to determine its Young's Modulus. The test was run in 7 stages of alternate loading and unloading. The normal stress on the sample was first increased from 0 to 2 Mpa. Stage 1 of the test was started with unloading from 2 to 0 Mpa. Figure 2.4.16 shows the axial stress vs. axial deformation curves for all the stages of the test. It can be seen from the data that the data can be fit to a bilinear model as shown in Figure 2.4.17.
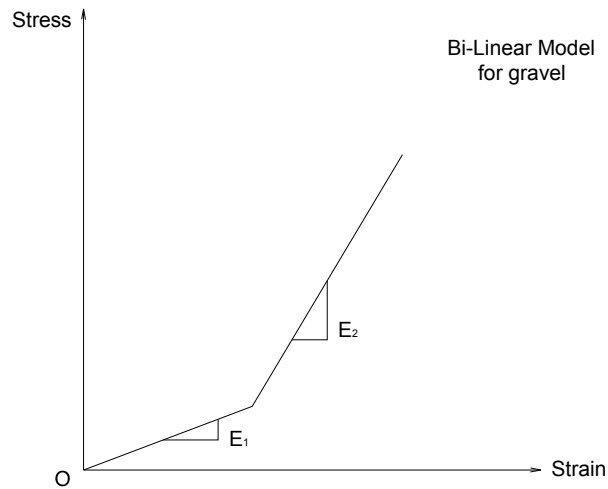
Figure 2.4.17 – Bi-linear model for gravel

Table 2.4.3 gives two values of Young's Moduli (bi-linear model with two slopes) for the gravel for each stage. A poisons ratio of 0.30 was used to obtain these values [25]

Table 2.4.3 - Young's Modulus for gravel

Stage	Young's Modulus E_1 (ksi)	Young's Modulus E_2 (ksi)
1 - Unloading	45	464
2 - Loading	51	193
3 - Unloading	37	489
4 - Loading	54	244
5 - Unloading	32	527
6 - Loading	53	295
7 - Unloading	47	549
Average Value	Loading – 53	Loading – 244
	Unloading – 41	Unloading – 507

Test results and interpretation

Table 2.4.4 shows the summary of direct shear test data. Figure 2.4.18 shows a plot of shear stress vs. Normal stress for the test data. A linear trend line is used to fit the data. This yields a friction angle of 52^0 for the gravel with cohesion intercept of 0.07 Mpa (10 psi).

Table 2.4.4 Summary of results from the direct shear test on gravel

Depth (z) ft	Normal Stress (MPa)	Peak shear stress (MPa)
30	0.2	0.3
50	0.3	0.4
70	0.5	0.6
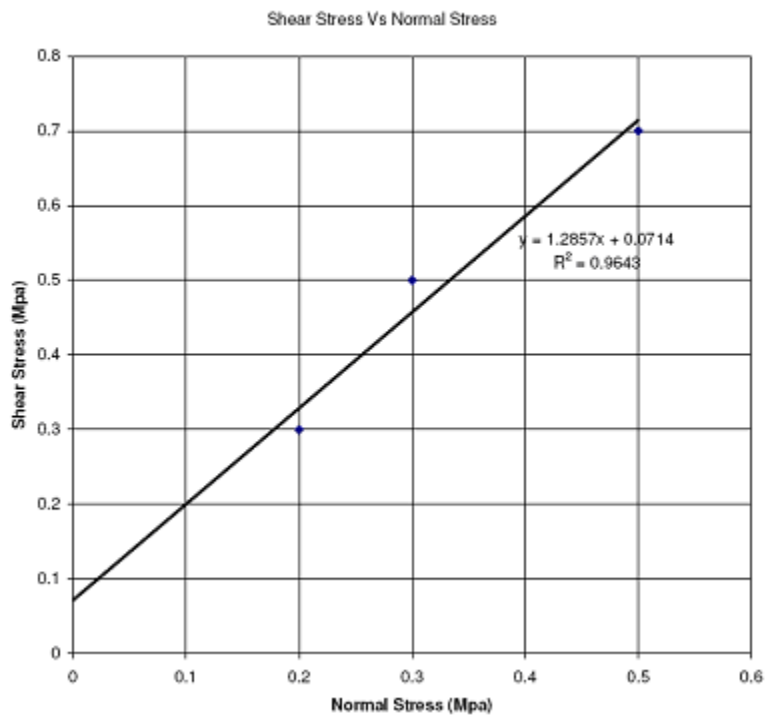
Figure 2.4.18 – Shear stress vs. normal stress curve from the direct shear test

2.4.6 Characterization of weakly cemented material

Figure 2.4.9 shows a specimen of weakly cemented material. The material could not be cored due to its low strength. Hence the characterization of its stiffness was based on its dynamic characteristics. A test called a 'free-free' test was carried out on the samples that contained weakly cemented sand gravel mixture. Details of this test are explained below.

'Free-Free test' is a Non Destructive Test (NDT) which is based on the principle of wave propagation. A P-wave is allowed to propagate through a soil sample and the velocity of the wave in the soil medium is computed based on the time taken for the wave to traverse a given path of known length. In general, wave velocity increases with increase in the stiffness of the material.

To obtain, consistent test data, it is desirable to have both the ends of the sample as flat as possible. The sample preparation involves the following steps.

I) Trim the ends of the sample as flat as possible

II) Attach a steel washer of ½" diameter, using epoxy glue, at both ends concentric to the face of the sample. The steel washer provides with a smooth surface that can be used to attach the receiver (typically a magnet) at one end and to tap a hammer at the other end.

The test was performed in the laboratory and required the following four instruments:

a) An oscilloscope – This is an electronic device capable of receiving electric signals, analog or digital and displays on a screen the variation of amplitude of an electrical signal with respect to time.

b) A small hammer- This device can produce a P-wave when tapped against any material which is capable of transmitting such a wave. This hammer is connected to the oscilloscope.

c) An oscilloscope with 2 channels: one to read the amplitude of the wave produced by the hammer and the second to read the wave received at the other end of the sample using a receiver/transducer

d) A computer to record and store the data captured by the oscilloscope

Procedure:

1) The sample is laid flat on the table as shown in Figure 2.4.19.

2) Measure length of the sample. If the ends of the sample are not flat which is the case in weakly cemented samples, measure the length at different points and note the mean value. Denote the length of the sample as L.

3) There are 2 wires/cords that are connected to two independent channels of an oscilloscope.

4) One end of the channel is connected to a transducer that can sense the P-wave and convert the amplitude of the P-wave into an electrical signal. The transducer is a small round shaped button that can be glued to either end of the cylindrical sample.

5) The other end of the sample is simply tapped with a hammer

6) On the screen of the oscilloscope, record the time delay between the transmitted P-wave and the received wave at the other end. Denote this time as t.

The velocity of the P-wave, V_p can be computed as, $V_p = \dfrac{L}{t}$. The Young's Modulus of the material in the direction parallel to the length of the sample can be computed from the following expressions [24].

$$V_p = \frac{\text{Travel Distance}}{\text{Travel Time}} \qquad\qquad \text{Body wave velocity}$$

$$M = V_p^{\ 2} \cdot \rho \qquad\qquad \text{Constrained Modulus}$$

$$E = \frac{M \cdot (1+\upsilon)(1-2\upsilon)}{(1-\upsilon)} \qquad\qquad \text{Young's Modulus}$$

From the above expressions [24], the Young's Modulus of the material is proportional to the square of the P-wave velocity in the material. Thus the stiffness of the material increases as the square of the increase in the P-wave velocity.
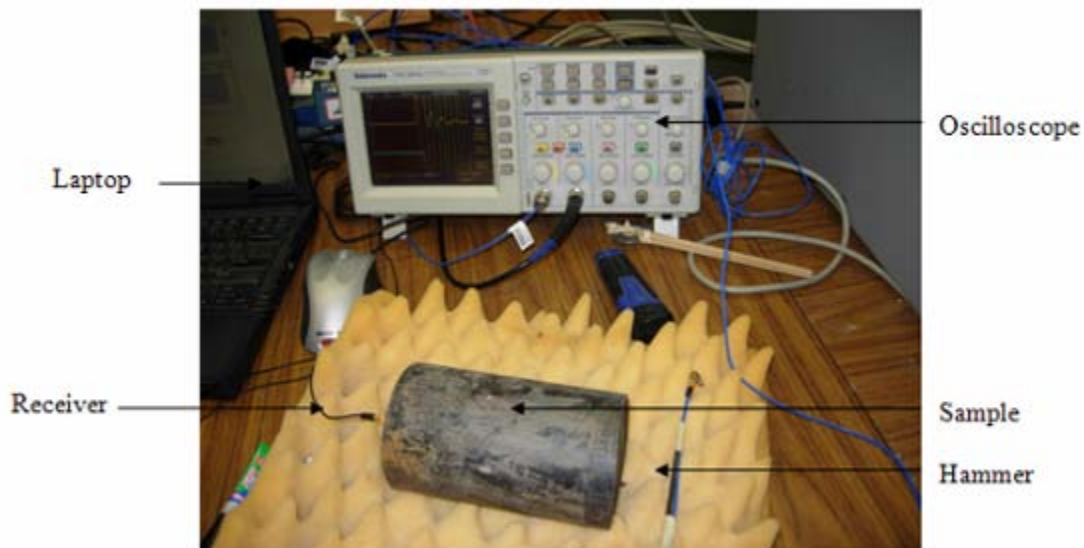
Figure 2.4.19 – Typical test setup for dynamic test carried on weakly cemented samples

Note that the value of Young's Modulus E is an approximate estimate of the stiffness of the material as the value of Poisson's ratio is assumed here and not evaluated from any experiment. The Poison's ratio was assumed to be 0.30 [25]. Table 2.4.5 shows the values of Young's Modulus for the weakly cemented samples.

Typical value of P-wave velocity for concrete is of the order of 14,000 ft/s. The P-wave velocity values for the weakly cemented samples are in the range 15% – 20% of the value in concrete. This shows that the stiffness of the weakly cemented material in the direction along the depth of the verification core is about 2.5% - 4% of the stiffness of concrete. (Since stiffness is proportional to the square of velocity)

Table 2.4.5- Strength characteristics of samples obtained in the wet condition

Wet Process	Height of Pour ft	Specimen	Core size in	Specimen Condition	P-Wave Velocity (fps)	Density PCF	Young's Modulus[15] ksi
WP 1	30	1	6"	WC	3100	78.58	121
	30	2	6"	WC	1700	81.20	38
	30	3	6"	NC	NA	0.00	-
	30	4	6"	NC	NA	0.00	-
	100	1	6"	WC	2500	98.87	99
	100	2	6"	WC	-	0.00	-
	100	3	6"	NC	NA	0.00	-
	100	4	6"	NC	NA	0.00	-
	30	1	12"	WC	4100	104.79	282
	30	2	12"	WC	3700	102.05	224
	30	3	12"	NC	-	0.00	-
	30	4	12"	NC	-	0.00	-
	100	1	12"	WC	2109	108.48	77
	100	2	12"	WC	2070	105.04	72
	100	3	12"	NC	NA	0.00	-
	100	4	12"	WC	2059	110.16	75
WP 2	30	1	6"	WC	1348	96.84	28
	30	2	6"	WC	2734	105.03	126
	30	3	6"	WC	8060	119.13	-
	30	4	6"	NC	NA	0.00	-
	100	1	6"	WC	2244	94.62	76
	100	2	6"	WC	1527	90.62	34
	100	3	6"	NC	NA	0.00	-
	100	1	12"	WC	3250	96.43	163
	100	2	12"	WC	3180	95.47	155
	100	3	12"	WC	2780	101.48	126
	100	4	12"	WC	2230	96.69	77
Average Value			6"	WC	2166	95.6	75
			12"		2830	102.3	139

---

[15] WC here means weakly cemented sand-gravel mixture. NC means not cemented.

Young's Modulus is calculated for weakly cemented samples based on dynamic tests. The constrained modulus of the specimen is related to the young's modulus and the P-wave velocity. For the non cemented material, Young's Modulus was computed from the axial test.

2.4.7 Observations and conclusions

Flow of concrete at the bottom of the drilled shaft was studied under wet and dry conditions using the 'Rocket'. The key observations are as follows –

i) In dry conditions, verification core is completely filled with concrete. In wet conditions, verification core is completely filled with weakly cemented sand-gravel mixture.

ii) In dry conditions, the compressive strength of concrete is equal to the concrete strength in the drilled shaft. The properties of material recovered in the 6" and 12" core were different. The strength of the concrete obtained in the dry conditions in the 12" core was higher than the concrete strength in the 6" core by 60 to 150% (see Figure 2.4.7), because better consolidation was be achieved in the 12" core. This is also evident from the values of P-wave velocity in the material obtained from the 12" core (see Figure 2.4.10).

iii) Under wet conditions WP1 and WP2 (refer Section 2.2 for details of these processes); the verification core fills with sand-gravel mixture. However, in the wet process 3 (WP 3), the verification core fills with concrete. Thus, the verification core hole fills with concrete only if the steel tube used to place the concrete is at the bottom of the core hole, which is impractical under normal field condition. The verification core does not get filled with concrete if the steel tube used for placing the concrete is not at the bottom of the core hole.

iv) When pouring in the wet (WP1 and WP2), the bottom half of the verification core filled with non-cemented gravel-sand mixture ($\varphi = 52^{o}$), while the upper half of the verification core filled with weakly cemented material ($V_p = 2000$ fps).

2.4.8 Recommended Material Properties

Strength and deformability properties of materials obtained in the core are presented in this chapter. The data may be used to compute the load-deformation response of the drilled shaft.

Dry Condition:

When the concrete is placed in the dry condition, material obtained in the verification core is concrete. Table 2.4.6 gives the strength and deformability parameters of the concrete that will be used in the numerical analysis. The material properties assigned will be uniform along the entire depth of the verification core.

Table 2.4.6 – Properties of material in the core - Dry Condition

6" Core	Height of Pour (ft)	Strength of Concrete[16] f'_c (psi)	Young's Modulus[17] (ksi)
	30	7110	4800
	70	4920	3990
	100	3460	3350
12" Core	70	7440	4910
	100	8520	5260

Wet Condition:

When the concrete is placed in the wet condition, material obtained in the verification core is weakly cemented sand-gravel mixture in the upper half of the verification core and non cemented gravel in the bottom half. It is seen from the dynamic testing of the weakly cemented material that the strength of this material is extremely low and this material cannot be classified as rock. The material property assigned along the entire depth of the verification core for the wet condition will be the peak friction angle of the gravel obtained from the direct shear tests. Table 2.4.7 gives the property of material that will be used in the numerical analysis for wet condition.

Table 2.4.7[18] – Properties of material in the core - Wet Condition

Material	Peak friction angle (degrees)[19]	Young's Modulus ksi
Weakly Cemented	52	6" Core – 75
		12" Core – 139
Non - Cemented	52	Refer Table 2.4.3

2.4.9 Summary

In this chapter experimental results for strength and deformability of materials obtained in the verification core have been explained in detail. Tables 2.4.6 and 2.4.7

---

[16] Specified is the average compressive strength. See Table 4.1
[17] Specified is the average value of Young's Modulus. See Table 4.1
[18] See Table 4.5
[19] From Figure 4.18

give the properties of the material that will be used in the numerical analysis of the drilled shaft.

2.5 SUMMARY AND CONCLUSIONS

2.5.1 Summary of Observations

1) The verification core of the drilled shaft is completely filled with concrete when concrete is placed in drilled shafts in the dry. For underwater pours, a combination of weakly cemented and non-cemented sand gravel mixture filled the verification core. Figure 2.5.1 shows the variation of the material obtained in the verification core under dry and wet conditions.
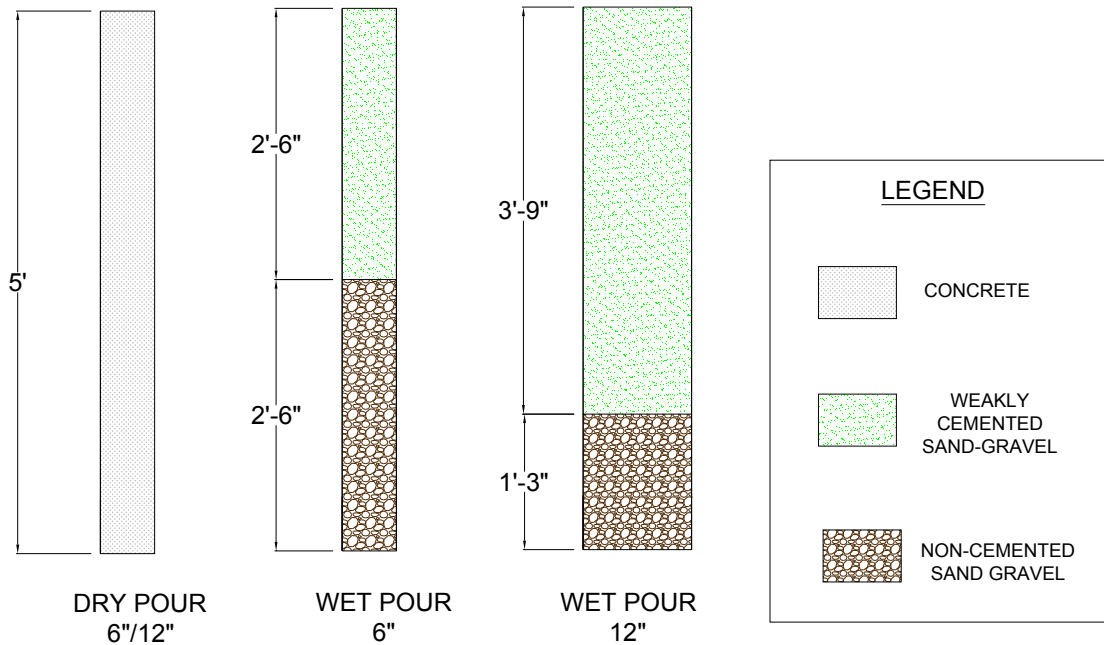
Figure 2.5.1 – Material Profile in the verification core of the drilled shaft

2) In dry conditions, the compressive strength of concrete exceeded the TxDOT Specifications. The properties of material recovered in the 6" and 12" core were different. The strength of the concrete obtained in the dry conditions in the 12" core was higher than the concrete strength in the 6" core by 60 to 150% because better compaction can be achieved in the 12" core. This is confirmed by the values of P-wave velocity.

3) Under wet conditions, the verification core fills with concrete only if the tremie or pump pipe used to place the concrete is inserted to the bottom of the core hole.

283

4) When pouring in the wet, the verification core does not get filled with concrete if the steel tube used for placing the concrete is not at the bottom of the core hole. In this case, the bottom half of the verification core is filled with non-cemented gravel-sand mixture ($\varphi = 52^o$), while the upper half of the verification core filled with weakly cemented material (Vp = 2000 fps) as can be seen in Figure 2.5.1. Placing the tremie at the bottom of the core hole is impossible in the field and only possible in the experiment (controlled condition) with 12'' or larger core hole.

2.5.2 Conclusions

It is proven that the verification core fills with concrete or sand gravel mixture when concrete is placed in the drilled shafts. The properties of the material obtained in the verification core are also presented here. These properties can be used in the numerical analysis of drilled shafts.

REFERENCES

1) Deep foundations for Transportation Facilities, Mark McClelland, P.E., Geotechnical Branch Manager, CIGMAT – 2005 Conference and Exhibition

2) Personal communication with Marcus Galvan of Texas Department of Transportation (MGALVAN@dot.state.tx.us)

3) Construction Practices and Defects in Drilled Shafts. O'Neill, M W

4) Effects of Minor Anomalies on Axial Capacity of Drilled Shafts

5) Item 416 – Drilled shaft foundations - Standard Specifications for Construction and Maintenance of Highways, Streets, and Bridges. Adopted by the Texas Department of Transportation, June 1, 2004.

6) Item 421 – Hydraulic cement concrete - Standard Specifications for Construction and Maintenance of Highways, Streets, and Bridges. Adopted by the Texas Department of Transportation, June 1, 2004.

7) AISC Steel Construction Manual- 13th Edition

8) ASCE 7 -2005 (American society of Civil Engineers) -Minimum design loads for buildings and other structures -

9) Pressure vessel design handbook – Second Edition, Henry H Bednar, P.E.

10) Process Equipment Design – Lloyd E Brownell, Edwin H Young

11) Mechanics of Materials- Boresi, Schmidt, R. J. and Sidebottom, 3rd Edition, 1993 Page 456

12) Foundation Analysis and Design, 5th Edition, 1996 Page 505 Joseph E Bowles

13) ACI 318 - 05 (American Concrete Institute) – Building code requirements for structural concrete

14) Process Equipment Design – Lloyd E Brownell, Edwin H Young, Page 24, section 2.3b

15) Process Equipment Design – Lloyd E Brownell, Edwin H Young, and Page 228 – Gasket factors for commonly used gasket materials.

16) Process Equipment Design – Lloyd E Brownell, Edwin H Young, Page 238, Figure 12.22

17) Process Equipment Design – Lloyd E Brownell, Edwin H Young, Section 2.12 – Design of Flanges. Pages 239-244.

18) Pressure vessel design handbook – Second Edition, Henry H Bednar, P.E. Page 154

19) http://www.roymech.co.uk/Useful_Tables/Tribology/co_of_frict.htm

20) ASTM C 39 (American standard for testing of Materials) – Standard test method for compressive strength of cylindrical concrete specimens.

21) ACI 318 - 05 (American Concrete Institute) – Building code requirements for structural concrete

22) Design of Concrete Structures – Arthur H Nilson, George Winter Eleventh Edition, Page 862 Table A. 6a

23) Steel Structures – Salmon & Johnson, Fourth Edition Page 254

24) Principles of Soil Dynamics - Braja M. Das

25) Experimental determination of the coefficient of lateral pressure ξ and Poisson's ratio μ for non-cohesive soils - Soil Mechanics and Foundation Engineering, Volume 4, Number 4 / July, 1967, G. E. Lazebnik, A. A. Smirnov and V. I. Simakov

26) The ASME Boiler and Pressure Vessel Code Section VIII, Division 1, 1998 Edition – Allowable Stresses

27) ASME/ANSI B16 - Standards of Pipes and Fittings

28) A 105 / SA 105 - Standard Specification for Carbon Steel Forgings for Piping Applications

29) ASTM A 500/A 500M Standard Specification for Cold-Formed Welded and Seamless Carbon Steel Structural Tubing in Rounds and Shapes

30) ASTM D 3080 Standard Test Method for Direct Shear Test of Soils Under Consolidated Drained Conditions

Chapter 3. EFFECT OF VERIFICATION CORE HOLE ON TIP CAPACITY

3.1 INTERPRETATION OF LABORATORY TEST

3.1.1 Introduction

Section 3.1 presents the material parameters determined from laboratory test results discussed in Section 1.5. These values are utilized in numerical analyses and discussed in Section 3.2. The regression technique is used to obtain the degraded properties of clay shales after any length of drying time. Section 3.2 presents the discussion of results of the numerical simulation which was used to quantify the effect of the verification core hole on the drilled shaft tip capacity. Section 3.3 includes summary of overall project, design recommendations for the drilled shafts with verification core, and conclusions.

Section 1.5 presented experimental test results on six Texas formations, and the results were discussed in terms of elastic modulus, internal friction angle, cohesion, mass density, water content, and slake durability index (SDI). This section presents the interpretation of the experimental results, the material parameters determined from laboratory, those of content that filled in verification core. The material properties of concrete which fills in the verification core during concrete cast were obtained from the thesis of A. Raibagkar, which describes Task 4 under the same TxDOT project 5825. The obtained material parameters are used for numerical analyses in Section 3.2.

3.1.2 Methodology

The Mohr-Coulomb paramateres required for analysis in the finite element method software (PLAXIS 8.4) include the following: elastic modulus, internal friction angle, cohesion, mass density, Poisson's ratio, dilation angle, and interface strength. The most critical of theses parameters include: elastic modulus, internal friction angle, and cohesion. The deformability and strength parameters were obtained from the triaxial compression tests of Section 1.5. Clay shales such as Taylor Marl, and Navarro Shale exhibit decrease in shear strength as drying-duration increases, while the decrease is not observable for Del Rio Clay, and Eagle Ford Shale. All formations display significant reduction in the elastic modulus. In this section, an approach to acquire suitable strength and elastic modulus parameters according to drying-duration is introduced.

Strength Parameters (φ, c)

Clay shales exhibiting degradation

The clay shales discussed in this section are the Taylor Marl, and Navarro Shale. It should be noted that the strength parameters are obtained at the peak stress of the stress-strain relationship, and that the triaxial tests are carried out in undrained condition.

Figure 3.1.1 provides the principal stress difference as related to air drying-duration of Taylor Marl. The plot reveals clear reduction of principal stress difference. From the figure, three series of data points are available for three confining pressures of 1, 2, and 3 MPa. The series of data points per each confining pressure are fitted to exponentially decaying regression curves as given below:

$$\sigma_1 - \sigma_3 = a \cdot e^{-bt} + c \qquad \text{Equation 3.1-1}$$

where the principal stress difference is in MPa, a, b, and c are parameters of the regression equation which best fits the test data sets. Three parameters (a, b, c) of Equation 3.1-1 were obtained per each confining pressure (1, 2, and 3 MPa) and were tabulated   in

Table 3.1.1. Using the equation 3.1-1, the principal stress difference can be directly obtained by inserting drying-duration (t). For example, the principal stress difference of Taylor Marl that is dried for 4 hours can be calculated by plugging drying-duration (t) of 4 hours into Equation 3.1-1 with parameters a, b, and c obtained from

Table 3.1.1. Consequently, the major principal stresses (σ_1) can be calculated per each confining pressure and drying-duration, and the results obtained are provided in Table 3.1.2. It should be noted that the tabulated values are obtained from the regression curve, not from individual data points from triaxial tests.
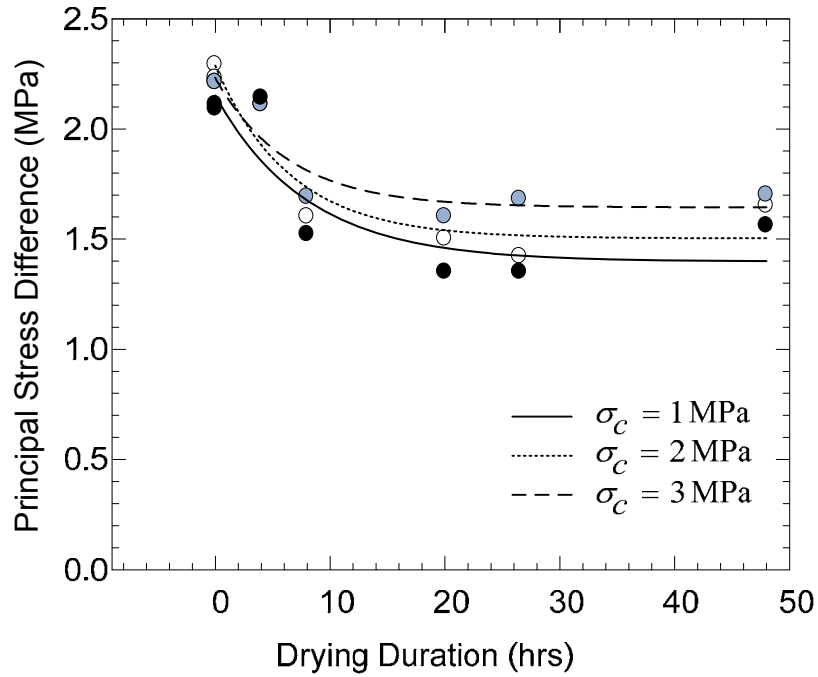
Figure 3.1.1 Principal stress difference variation with drying-duration of Taylor Marl

Table 3.1.1 Obtained parameters of fitting curves for three confining pressures of Taylor Marl

Parameters	$\sigma_c = 1$ MPa	$\sigma_c = 2$ MPa	$\sigma_c = 3$ MPa
a (MPa)	0.754	1.504	1.644
b (hr^{-1})	0.125	0.784	0.588
c (MPa)	1.398	0.153	0.157
r^2	0.808	0.893	0.896

Table 3.1.2 Calculated major and minor principal stresses per drying-duration of Taylor Marl

σ_3	Major Principal Stress (σ_1, MPa)					
	t = 0 hr	t = 4 hr	t = 8 hr	t = 16 hr	t = 24 hr	t = 48 hr
1 MPa	3.15	2.86	2.68	2.50	2.44	2.40
2 MPa	4.29	3.93	3.73	3.57	3.52	3.50
3 MPa	5.23	4.96	4.81	4.69	4.66	4.64

Three major and minor principal stresses determine engineering properties such as internal friction angle and cohesion of the Mohr-Coulomb model; thus, friction angle and cohesion per each drying-duration are available. In order to obtain such values, the major and minor principal stresses from Table 3.1.2 are plotted for separate drying-durations as displayed in Figure 3.1.2. The Mohr-Coulomb failure envelopes passing through the data points are provided in y-intercepts and slopes, which are converted to internal friction angle and cohesion for individual drying-durations. It should be mentioned that data points are plotted on the Modified Mohr-Coulomb diagram in Figure 3.1.2 in which the x-axis is confining pressure (σ_3) and the y-axis is the major principal stress (σ_1). The Modified Mohr-Coulomb diagram is given by:

$$\sigma_1 = 2c\frac{\cos\phi}{1-\sin\phi} + \sigma_3\frac{1+\sin\phi}{1-\sin\phi} \qquad \text{Equation 3.1-2}$$

Therefore, the y-intercept, d, in the Modified Mohr-Coulomb diagram is converted to cohesion using the equation below:

$$c = \frac{d \cdot (1-\sin\phi)}{2 \cdot \cos\phi} \qquad \text{Equation 3.1-3}$$

and the internal friction angle, φ, can be calculated from the slope using the following equation:

$$\phi = \sin^{-1}\left(\frac{\tan\psi - 1}{\tan\psi + 1}\right) \qquad \text{Equation 3.1-4}$$

where ψ is a slope of the regression line. The friction angle and cohesion for Taylor Marl are given in Table 3.1.3.

Table 3.1.3 Friction angle and cohesion of Taylor Marl per drying-duration

Drying-duration	0 hr	4 hr	8 hr	16 hr	24 hr	48 hr
Slope	1.04	1.05	1.07	1.10	1.11	1.12
Friction angle (˚)	1.1	1.5	2.0	2.7	3.2	3.5
y-intercept (MPa)	2.14	1.81	1.60	1.40	1.32	1.27
Cohesion (kPa)	1050	883	775	665	623	598
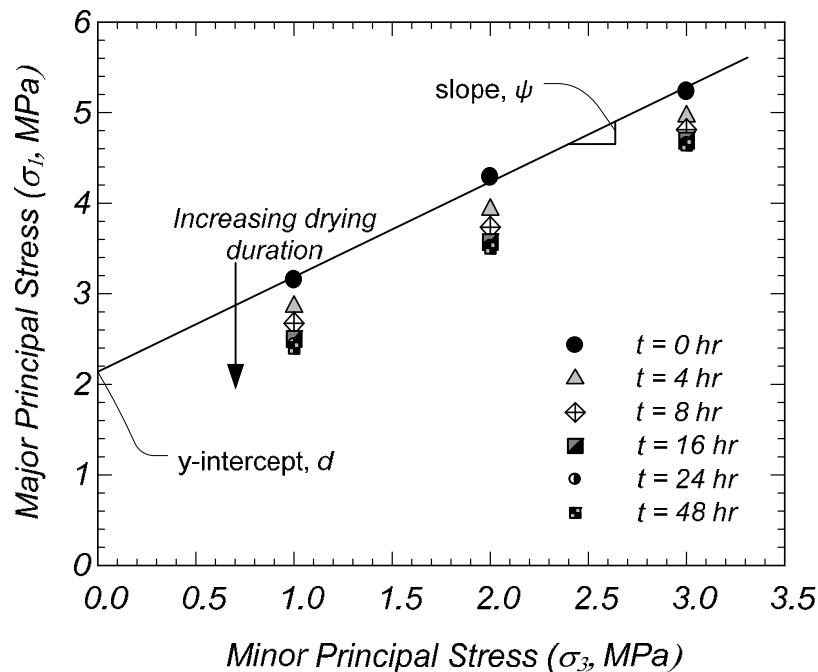
Figure 3.1.2 Calculated major and minor principal stresses for different drying-durations of Taylor Marl

292

Triaxial tests on Navarro Shale, however, were subject to a single confining pressure (1 MPa) because the multi-stage triaxial test was not possible. In performing the multi-stage triaxial test, the Navarro Shale specimen that underwent the first confining pressure (1 MPa) is highly different from fresh shale; thus, only principal stress differences under 1 MPa confining pressure are available. From the triaxial test results obtained, Navarro Shale is significantly affected by drying-duration (Figure 5-59). The regression equation parameters and correlation coefficient (r^2) of Navarro Shales are given in Table 3.1.4. Indeed, the principal stress differences under confining pressures of 2 and 3 MPa are obtained only at t=0 hr (Figure 5-59). Thus, the principal stress differences at t=0 hr are used to extrapolate those at different drying-duration by keeping the internal friction angle of Navarro Shales the same for all drying-durations. The extrapolated major principal stress for Navarro Shale is tabulated in Table 3.1.5. Major and minor principal stresses of Del Rio Clay are plotted on Modified Mohr-Coulomb diagrams in Figure 3.1.3. Friction angle and cohesion are calculated in the same manner used for Taylor Marl and are listed in Table 3.1.6. Cohesions for Navarro Shales were lower than that of Taylor Marls, and the friction angles remained constant.

Table 3.1.4 Obtained parameters of fitting curves of Navarro Shale (1 MPa)

Parameters	$\sigma_c = 1$ MPa
a	0.155
b	1.507
c	0.019
r^2	0.808

Table 3.1.5 Calculated major and minor principal stresses per drying-duration of Navarro Shale

σ_3	Major Principal Stress (σ_1, MPa)				
	t = 0 hr	t = 4 hr	t = 8 hr	t = 16 hr	t = 24 hr
1 MPa	2.66	2.55	2.45	2.28	2.12
2 MPa	3.63	3.52	3.42	3.24	3.09
3 MPa	4.84	4.73	4.63	4.45	4.30
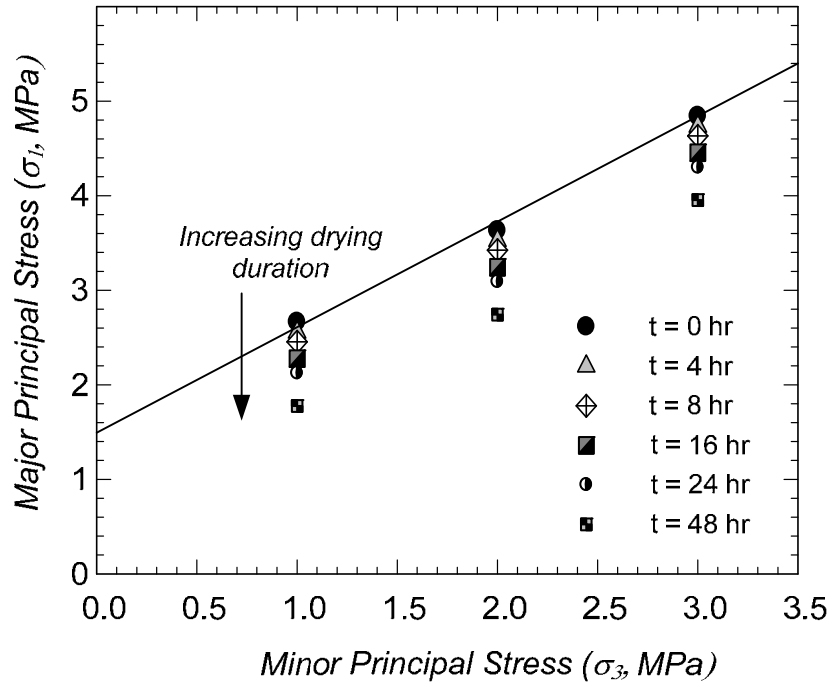
Figure 3.1.3 Calculated major and minor principal stresses for different drying-durations of Navarro Shale

Table 3.1.6 Friction angle and cohesion of Navarro Shale per drying-duration

Drying-duration	0 hr	4 hr	8 hr	16 hr	24 hr
Slope	1.09	1.09	1.09	1.09	1.09
Friction angle (°)	2.6	2.6	2.6	2.6	2.6
y-intercept (MPa)	1.53	1.43	1.33	1.15	0.99
Cohesion (kPa)	733	682	634	549	475

Clay shales exhibiting no degradation

As opposed to Taylor Marl and Navarro Shale, Del Rio Clay and Eagle Ford Shale do not exhibit reduction in principal stress difference according to drying-duration (Figure 5-22 for Del Rio Clay and Figure 5-35 for Eagle Ford Shale). Therefore, their internal friction angle and cohesion are obtained from the regression line fitting all test results. Figure 3.1.4 and Figure 3.1.5 present the entire multi-stage triaxial test results on Del Rio Clay and Eagle Ford Shale, respectively. Approximately five data points are plotted per each confining pressure, and the regression line is drawn fitting all the data points. For Del Rio Clay, the y-intercept and slope of the regression line are 0.5 MPa and 1.135, from which the internal friction angle and cohesion were calculated to be 235 kPa

and 3.6°, respectively. The same methodology is applied to Eagle Ford Shale, and the values were calculated to be 12.7° and 462 kPa.

Elastic Modulus

The elastic moduli of all four clay shales display considerable reduction as drying-duration increases. The regression equation of the elastic modulus best fitting available data points is in the identical form that is used for strength parameters in the previous section. The equation is the exponentially decaying one with three parameters as shown below.

$$E = a \cdot e^{-b \cdot t} + c \qquad\qquad \text{Equation 3.1-5}$$
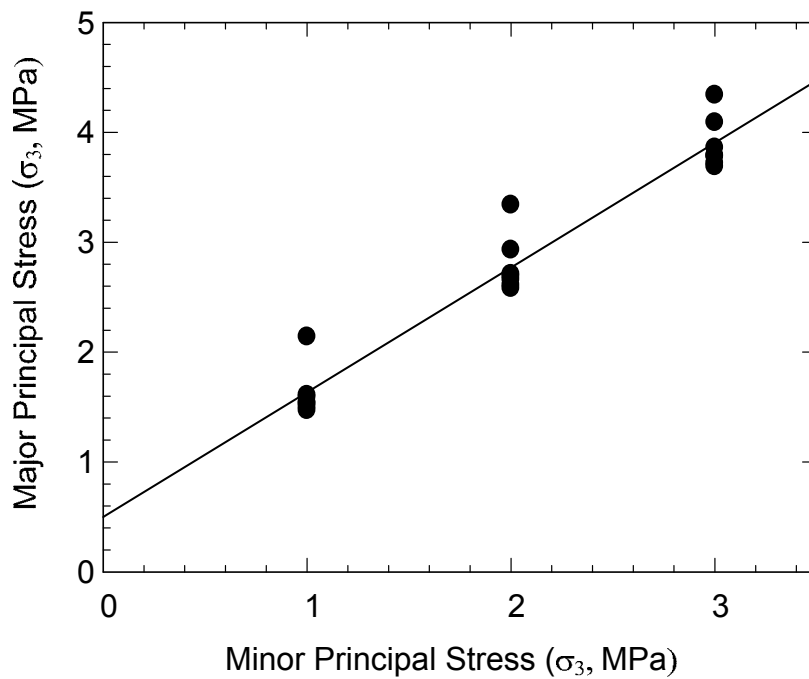
Figure 3.1.4 Failure envelope of Del Rio Clay on Modified Mohr-Coulomb diagrams
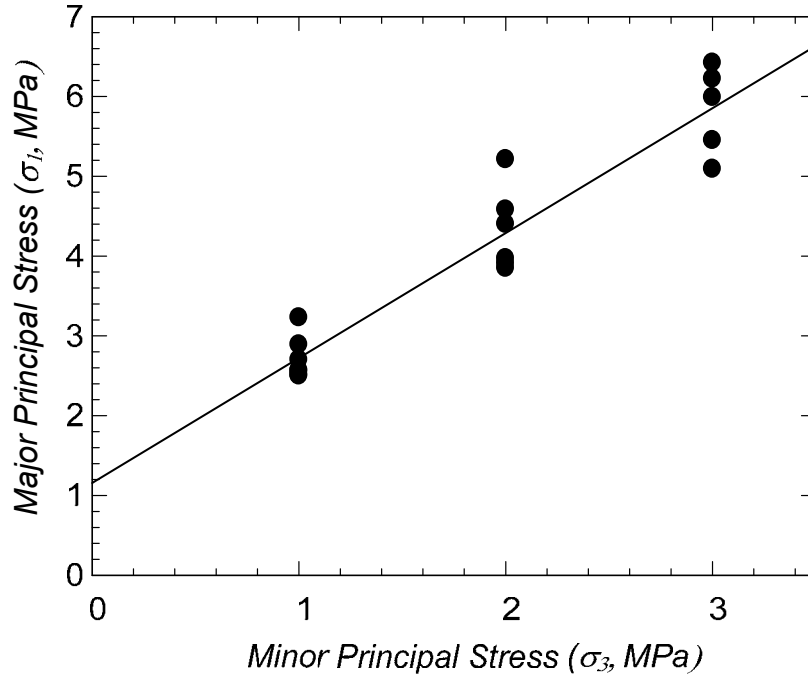
Figure 3.1.5 Failure envelope of Eagle Ford Shale on Modified Mohr-Coulomb diagrams

The variation of the elastic modulus of Del Rio Clay, Eagle Ford Shale, Taylor Marl, and Navarro Shale is given in Figure 3.1.6. Each figure provides the parameters obtained of the regression equation with correlation coefficient. The elastic modulus is calculated to be the biggest for Eagle Ford Shale and the lowest for Del Rio Clay. The elastic modulus of each formation is measured only from the stress-strain curve under 1 MPa confining pressure because the elastic modulus obtained at 2 or/and 3 MPa confining pressure is likely to differ slightly from that obtained at 1 MPa confining pressure. In addition, the elastic modulus of 2 and 3 MPa confining pressure was measured from the test specimen that underwent imminent failure during multi-stage triaxial tests. Therefore, the elastic modulus at 1 MPa confining pressure properly represents the behavior of fresh clay shales and, subsequently, is used for numerical analysis. Also, 1 MPa confinement appears to be closer to the *in situ* stress condition than greater confinements because the overburden pressure at depth of the typical drilled shafts tipped on is less than 1 MPa.
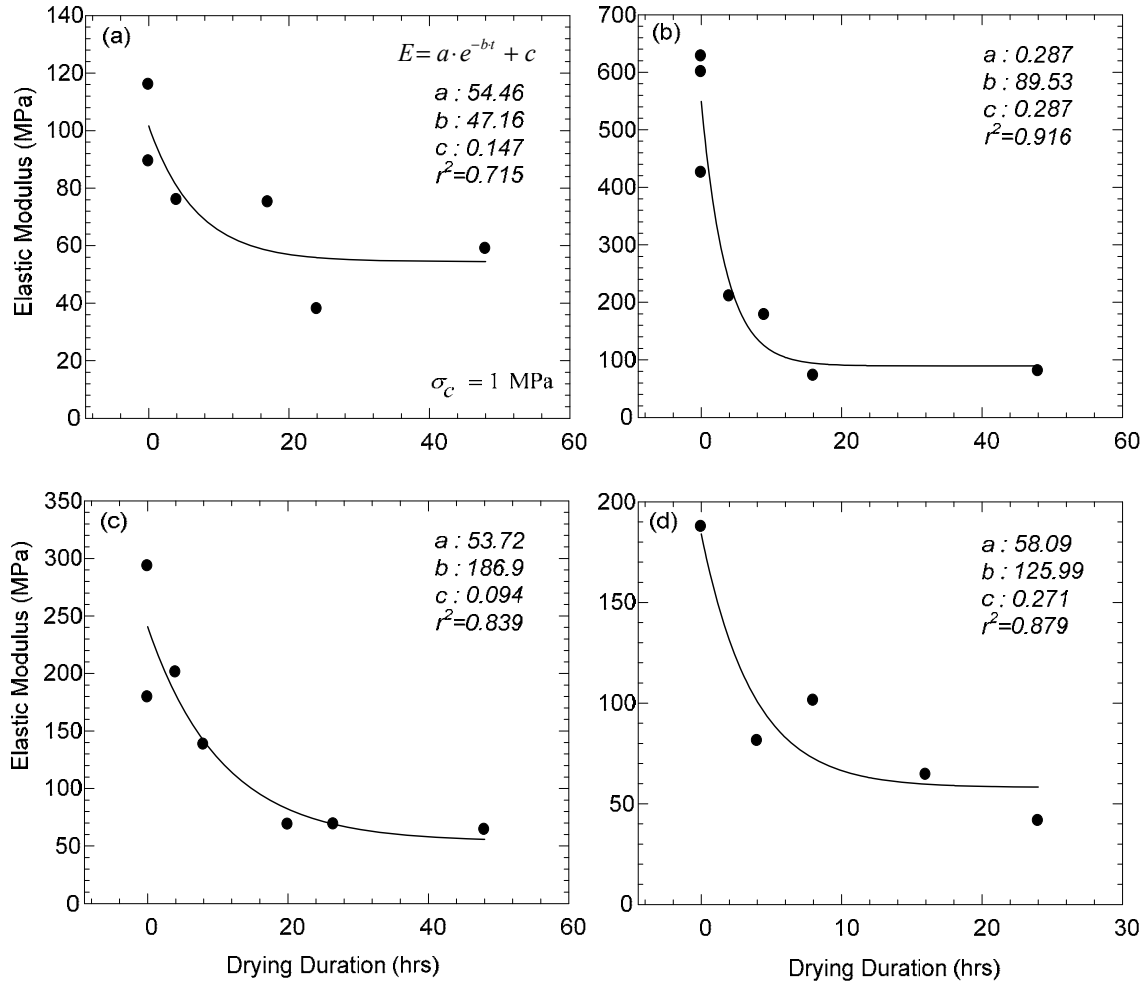
Figure 3.1.6 Variation of elastic modulus with drying-duration of: (a) Del Rio Clay, (b) Eagle Ford Shale, (c) Taylor Marl, and (d) Navarro Shale.

3.1.3 Summary of Material Parameters

Clay Shales

The material property parameters of the four clay shales are tabulated in Table 3.1.7 through Table 3.1.10. The tables include drying-duration, material model, elastic modulus, Poisson's ratio, friction angle and cohesion, mass density, interface coefficient, and thickness of degraded zone. Poisson's ratio and dilation angle are necessary parameters for the Mohr-Coulomb model. Poisson's ratio was assumed to be 0.15 for the concrete section of drilled shafts (Hassan, 1994) and 0.3 for all clay shales. The dilation angles of all materials were assumed to be 0° for numerical simulations because the clay shales are not expected to be dilative.

The interface coefficient, *R*, of PLAXIS was assumed to be 0.5 for the interface between clay shale and concrete. It should be noted that the interface coefficient, *R*, is not a measured value but a conservatively assumed value. The low coefficient will result in small increase of side resistance along the verification core, which leads to conservative

297

evaluation of the effect of the verification core. Interface elements are used to model soil-structure interaction, which is represented by Coulomb criterion:

$$\tau < \sigma_n \cdot \tan\delta + c_i \qquad\qquad \text{Equation 3.1-6}$$

where $\tan\delta = R\tan\phi$, $c_i = R\,c$, and φ and c are soil friction angle and cohesion, respectively. Since the interface element remains elastic as long as Equation 3.1-6 is satisfied, only small displacements can occur elastically; otherwise, the interface element becomes plastic and deforms permanently without additional force (slip).

Finally, thickness in the tables refers to thickness of the degraded region induced by one cycle of drying and wetting of the clay shales at the perimeter of the verification core; the values were imported from Table 1.6.4 and Figure 1.6.14.

Table 3.1.7 Input material parameters of Del Rio Clay

Drying-duration (hr)	Material	E (MPa)	ν	φ (deg)	c (kPa)	Ψ (deg)	ρ_{unsat} (Mg/m³)	ρ_{sat} (Mg/m³)	R	Thickness (cm)
0	MC	101.6	0.3	3.6	235	0	2.16	2.16	0.5	0
4	MC	80.7	0.3	3.6	235	0	2.16	2.16	0.5	13
8	MC	69.0	0.3	3.6	235	0	2.16	2.16	0.5	13
16	MC	59.0	0.3	3.6	235	0	2.16	2.16	0.5	13
24	MC	55.8	0.3	3.6	235	0	2.16	2.16	0.5	13
48	MC	54.5	0.3	3.6	235	0	2.16	2.16	0.5	13

* MC: Mohr-Coulomb model

Table 3.1.8 Input material parameters of Eagle Ford Shale

Drying-duration (hr)	Material	E (MPa)	ν	φ (deg)	c (kPa)	Ψ (deg)	ρ_{unsat} (Mg/m^3)	ρ_{sat} (Mg/m^3)	R	Thickness (cm)
0	MC	549.2	0.3	12.7	462	0	2.02	2.09	0.5	0
4	MC	235.6	0.3	12.7	462	0	2.02	2.09	0.5	0
8	MC	136.0	0.3	12.7	462	0	2.02	2.09	0.5	13
16	MC	94.2	0.3	12.7	462	0	2.02	2.09	0.5	13
24	MC	90.0	0.3	12.7	462	0	2.02	2.09	0.5	13
48	MC	89.5	0.3	12.7	462	0	2.02	2.09	0.5	13

Table 3.1.9 Input material parameters of Taylor Marl

Drying-duration (hr)	Material	E (MPa)	ν	φ (deg)	c (kPa)	Ψ (deg)	ρ_{unsat} (Mg/m^3)	ρ_{sat} (Mg/m^3)	R	Thickness (cm)
0	MC	240.7	0.3	1.1	1050	0	2.08	2.10	0.5	0
4	MC	181.9	0.3	1.5	883	0	2.08	2.10	0.5	13
8	MC	141.6	0.3	2.0	775	0	2.08	2.10	0.5	13
16	MC	95.1	0.3	2.7	665	0	2.08	2.10	0.5	13
24	MC	73.2	0.3	3.2	623	0	2.08	2.10	0.5	13
48	MC	55.7	0.3	3.5	598	0	2.08	2.10	0.5	13

Table 3.1.10 Input material parameters of Navarro Shale

Drying-duration (hr)	Material	E (MPa)	ν	φ (deg)	c (kPa)	Ψ (deg)	ρ_{unsat} (Mg/m^3)	ρ_{sat} (Mg/m^3)	R	Thickness (cm)
0	MC	165.3	0.3	2.6	733	0	2.03	2.03	0.5	0
4	MC	122.7	0.3	2.6	682	0	2.03	2.03	0.5	13
8	MC	89.3	0.3	2.6	634	0	2.03	2.03	0.5	13
16	MC	50.1	0.3	2.6	549	0	2.03	2.03	0.5	13
24	MC	47.9	0.3	2.6	475	0	2.03	2.03	0.5	13

Filled-in Concrete (from Chapter 2)

This section reviewed the work done by Raibagkar in Chapter 2 estimating the material properties of concrete that filled in the verification core. Within the same TxDOT project, Raibagkar conducted Task 4 that dealt with the prediction of material properties of concrete in verification cores. The concrete properties turned out to be different for different pouring conditions: in the presence of water in the core hole, the material properties of poured concrete varied depending on the verification core diameter, while for dry pours, the concrete strength in the core hole was of similar strength as the concrete in the drilled shaft.

When pouring in the dry, the UCS of solid concrete obtained in the verification core averaged 37.2 MPa (5,400 psi) and 55.2 MPa (8,000 psi) for the diameters 15.2 cm (6 in) and 30.5 cm (12 in), respectively. Therefore, the specified minimum design strength of 24.8 MPa (3,600 psi) was used because it represents a lower bound for class "C" concrete (Texas Department of Transportation Standard Specification for Construction and Maintenance of Highways, Streets, and Bridges, 2004, page 524). The elastic modulus was estimated from the compressive strength using the equation given in ACI 318-08 (American Concrete Institute, 2008).

$$E_c = 57 \times \sqrt{f'_c}$$
<div align="right">Equation 3.1-7</div>

where f'_c is compressive strength of concrete in psi and E_c is Young's modulus in ksi; thus, the elastic modulus of concrete was calculated to be 23,580 MPa (3,420 ksi). The concrete was assumed to be an isotropic, homogeneous and elastic solid with a Poisson's ratio of 0.15, which is typically used for concrete of drilled shafts (Hassan, 1994).

When pouring in the wet, the upper half of the verification core hole filled with weakly cemented sand gravel mixture, whereas non-cemented sand gravel mixture filled at the bottom half. For details of the test procedure and results, see Chapter 4. The elastic modulus, and mass density of weakly cemented mixtures are experimentally estimated and averaged to be 514.3 MPa (75 ksi) and 1.53 Mg/m^3 (95.6 pcf) for a diameter of 15.2 cm (6 in), and 958.4 MPa (139 ksi) and 1.64 Mg/m^3 (102.3 pcf) for a diameter of 30.5 cm (12 in). However, the strength parameters for the weakly cemented mixture are not available because the mixture was not testable using conventional testing methods. The strength parameters for non cemented mixture were used, which will result in a slightly conservative estimation. The input parameters implemented into the numerical analysis were interpolated for verification core diameters of 25.4 cm (10 in) and 35.6 cm (14 in), based on the results for verification cores of 15.2 cm (6 in) and 30.5 cm (12 in), and the final parameters are shown in Table 3.1.11.

A linear elastic model was adopted for a concrete filled verification core hole, because the solid concrete is much stronger than for clay shales studied in this project. Since the concrete will not fail earlier than the clay shales, the concrete was modeled with linear elastic material properties. For core holes filled with weakly-cemented mixtures or sand and gravel, a Mohr-Coulomb model was adopted. The dilation angle of the material was set to be 22.1˚ using the following equation (PLAXIS Version 8, 2002, page 3-8):

$$\psi = \varphi - 30°$$
<div align="right">Equation 3.1-8</div>

Table 3.1.11 Input material parameters for verification core hole filling concretes

Pouring Conditions (verification core diameter in cm)	Material	E (MPa)	ν	φ (deg)	c (kPa)	Ψ (deg)	ρ_{unsat} (Mg/m^3)	ρ_{sat} (Mg/m^3)	R
Dry	LE	23,580	0.15	n/a	n/a	n/a	2.37	2.37	0.5
Wet (15.2 cm)	MC	514.3	0.15	52.1	71.7	22.1	1.51	1.51	0.5
Wet (25.4 cm)	MC	810.1	0.15	52.1	71.7	22.1	1.60	1.60	0.5
Wet (35.6 cm)	MC	1,107	0.15	52.1	71.7	22.1	1.68	1.68	0.5

* VC: verification core

* WC: the concrete is poured in wet condition, Solid: the concrete is poured in dry condition

* LE: linear elastic

Limestone and Chalk

Table 3.1.12 displays material parameters of the Edwards Limestone and Austin Chalk. As discussed in Section 1.5, those formations are not affected by one cycle of drying and wetting and are characterized as durable formations. The average elastic moduli of the formations are estimated to be 13,167 MPa for Edwards Limestone and 2,320 MPa for Austin Chalk, which is lower than that of TxDOT Class "C" structural concrete. The Poisson's ratio for both formations was set at 0.3.

The calculation of friction angle and cohesion follows the process used for Eagle Ford Shale and Del Rio Clay in Section 1.7.2. All test results were plotted on Modified Mohr-Coulomb Diagrams in Figure 3.1.7 and Figure 3.1.8, and engineering properties were obtained from: 1) averaging strength regardless of confining pressure for Edwards Limestone and 2) a regression line fitting all data points for Austin Chalk. The friction angle was set to zero for Edwards Limestone because the formation exhibits severe scatter and the effect of confining pressure appears to be negligible. The undrained shear strength (S_u) was calculated to be 36,010 kPa. For Austin Chalk, the friction angle and cohesion were calculated to be 27° and 5,590 kPa, respectively. The elastic modulus for both rocks was estimated by averaging moduli at 1 MPa confining pressure.
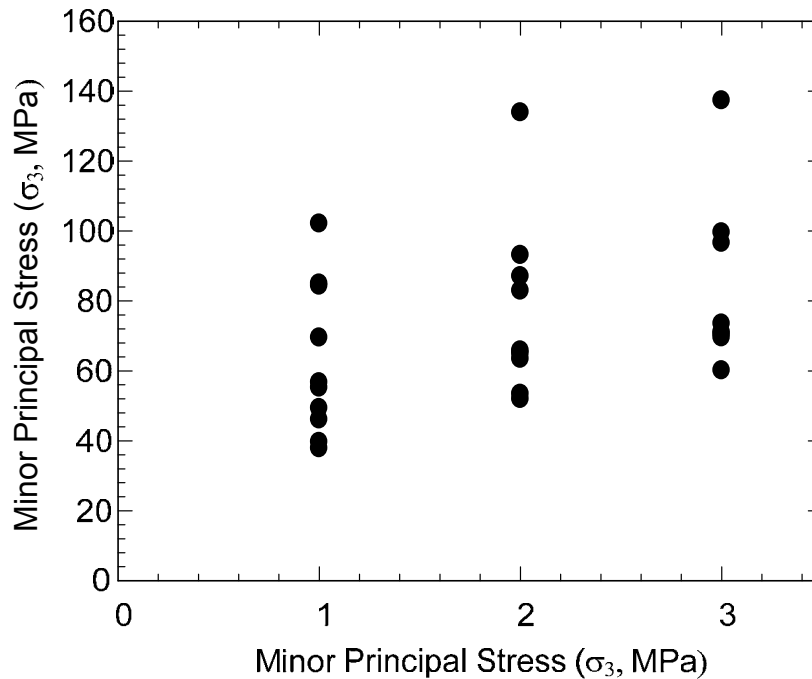
Figure 3.1.7 Major and minor principal stresses of Edwards Limestone

305
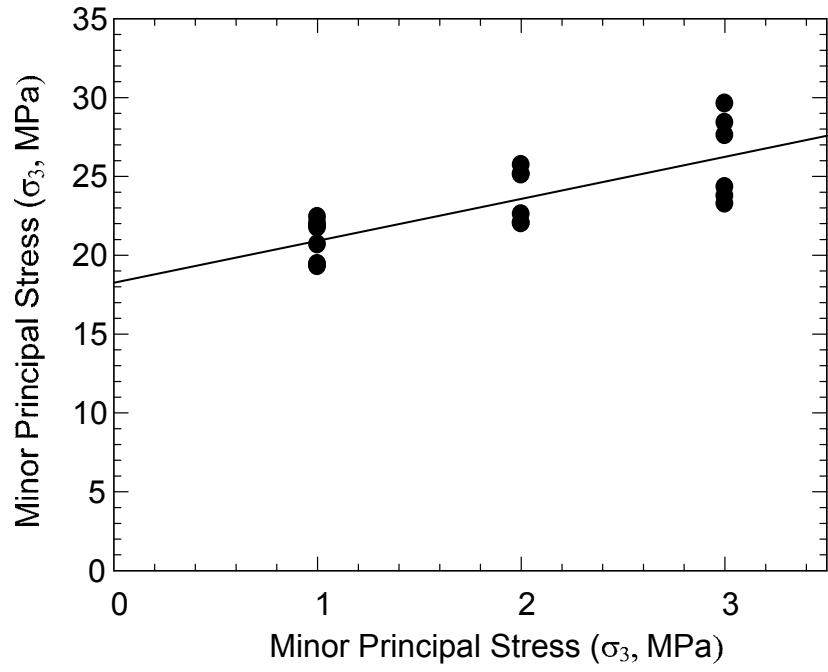
Figure 3.1.8 Failure envelope of Austin Chalk on Modified Mohr-Coulomb diagrams

Table 3.1.12 Input material parameters of Edwards Limestone and Austin Chalk

Formation	Material	E (MPa)	ν	φ (deg)	c (kPa)	Ψ (deg)	ρ_{unsat} (Mg/m^3)	ρ_{sat} (Mg/m^3)	R
Edwards Limestone	MC	13,167	0.3	0	36,010	0	2.50	2.54	0.5
Austin Chalk	MC	2,320	0.3	27	5,590	0	2.27	2.28	0.5

3.2 NUMERICAL ANALYSIS

3.2.1 Introduction

Material parameters of degradable clay shales were derived from series of laboratory tests using the regression technique in Section 3.1. The material parameters obtained were assigned to models of drilled shafts implemented into finite element method software, PLAXIS, to estimate the point bearing capacity of drilled shafts that embedded into degradable clay shales. This section presents: 1) the numerical model created in the PLAXIS, 2) the load-displacement curve at the shaft base obtained from parametric studies, 3) proposed capacity reduction factors, and 4) t-z analysis results. In PLAXIS, the Mohr-Coulomb model was selected to define yield surface of clay shales. The ultimate point bearing capacity at the shaft base was determined at displacements equal to 5%, and 10% of shaft diameter (D) from the load-displacement curves. It should be mentioned that the numerical analyses carried out in this section were not calibrated using full scale load tests because the objective of this research is to provide the relative magnitude of point bearing capacity of drilled shafts with a verification core hole to that of drilled shafts without a verification core hole. Therefore, the point bearing capacity of drilled shafts without a verification core hole (reference model) was compared to that of drilled shafts with a verification core hole that is subject to different drying conditions. The ratio of point bearing capacity under influence of the verification core hole to the reference value is called the "reduction factor," which can be used to estimate the point bearing capacity of drilled shafts affected by the verification core hole.

Vipulanandan et al. (2007) conducted parametric studies on the effect of a verification core hole on the drilled shafts socketed in soft rock using PLAXIS. From their study, it was found that the bearing capacity factor, N_c, decreases by 4% when the core hole diameter is 10% of shaft diameter (D). On the other hand, the reduction reaches 40% when the core hole diameter is 40% D. Although the previous study has identified this potential problem with verification core holes, it focuses solely on the case in which the verification core hole is empty, without any in filling. We have shown in this study that this does not occur (Chapter 2). This section investigates the effect of a verification core hole that is filled with concrete or sand-gravel mixtures.

3.2.2 Numerical Modeling

Axisymmetric 15-node triangular elements are used to represent soil continuum, and the soil-structure interaction was modeled using interface elements. The 15-node triangular elements provide the 4th order of interpolation to estimate displacements at nodes, and stress and strains are calculated at 12 Gaussian integration points (PLAXIS Version 8, 2002a). The interface element is necessary when the contact between structure and soil is believed to be sheared severely. Approximately 2,500 triangular elements were utilized in the analyses. This section discusses the geometry of drilled shafts, the constitutive model, simulation procedures, and varied parameters.

Model Geometry

Figure 3.2.1 depicts the geometry of drilled shafts embedded into clay shales. The left and right boundaries were modeled with fixed horizontal displacement, and the bottom of the model was fixed in both the horizontal and vertical direction. The right and bottom boundaries were set far from the drilled shafts to prevent the stress developed near the shaft base from reaching these boundaries. The right boundary is at 15.2 m (50 ft) away from the center of the drilled shafts, and the bottom boundary is at 10 m (33 ft) below the tip of the verification core. The drilled shaft is 9.1 m (30 ft) long and 0.9 m (3 ft) wide. In order to reduce computing time without sacrificing the accuracy of the results, the mesh was refined at the region near the drilled shafts and became coarser further from the shafts.

The area at the bottom of drilled shafts was magnified in Figure 3.2.2 to clarify the degraded zone and the verification core hole. The diameter of the verification core hole is 35.6 cm (14 in), and the length is 2.1 m (7 ft). A degraded zone 12.7 cm (5 inch) thick surrounds the verification core hole. It should be noted that Figure 3.2.1 and Figure 3.2.2 present the case in which the diameter of the verification core is 35.6 cm (14 in), but 15.2 cm (6in) and 25.4 cm (10 in) verification core diameter are also included in this study.
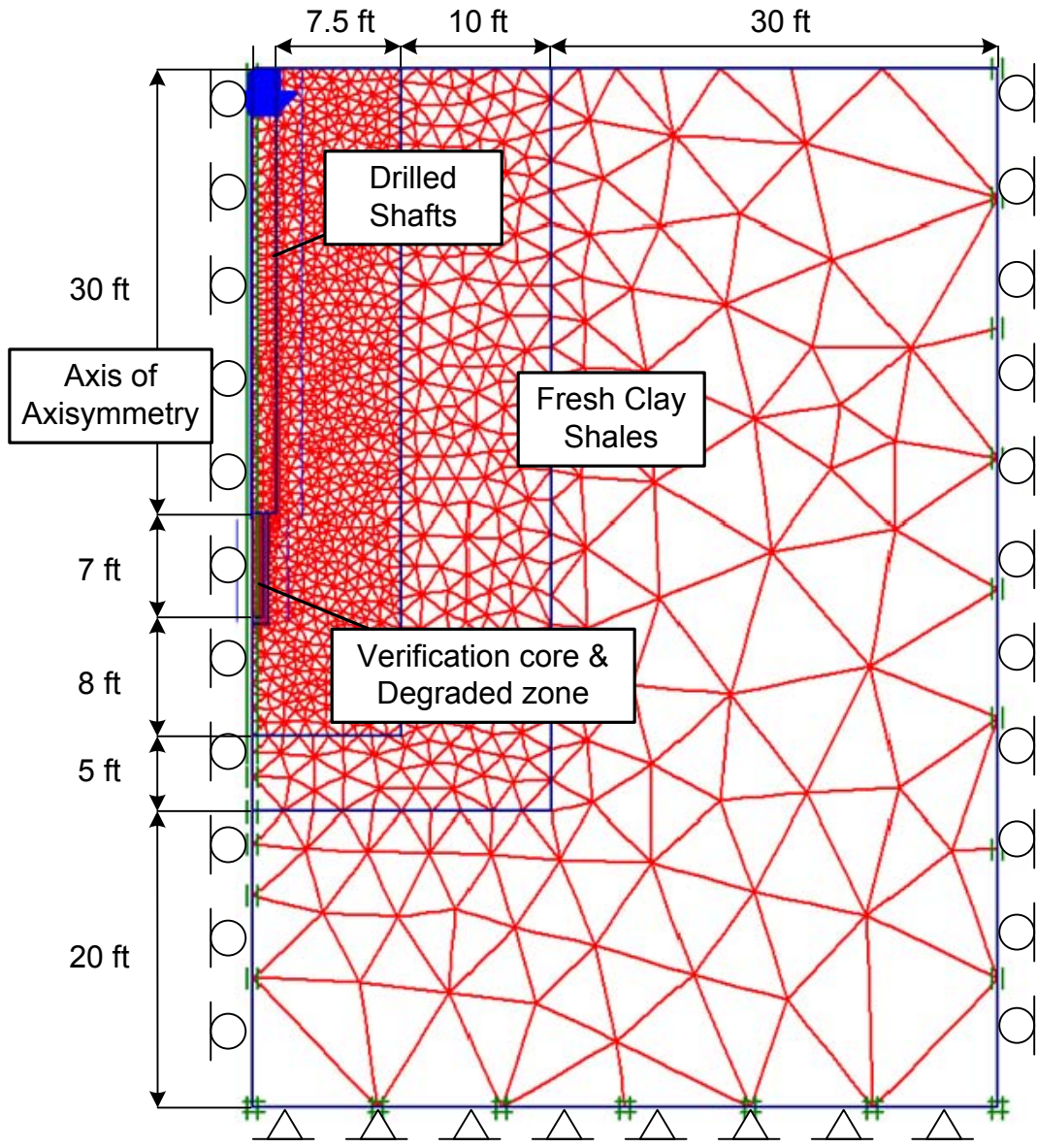
Figure 3.2.1 Geometry and mesh of numerical model in PLAXIS
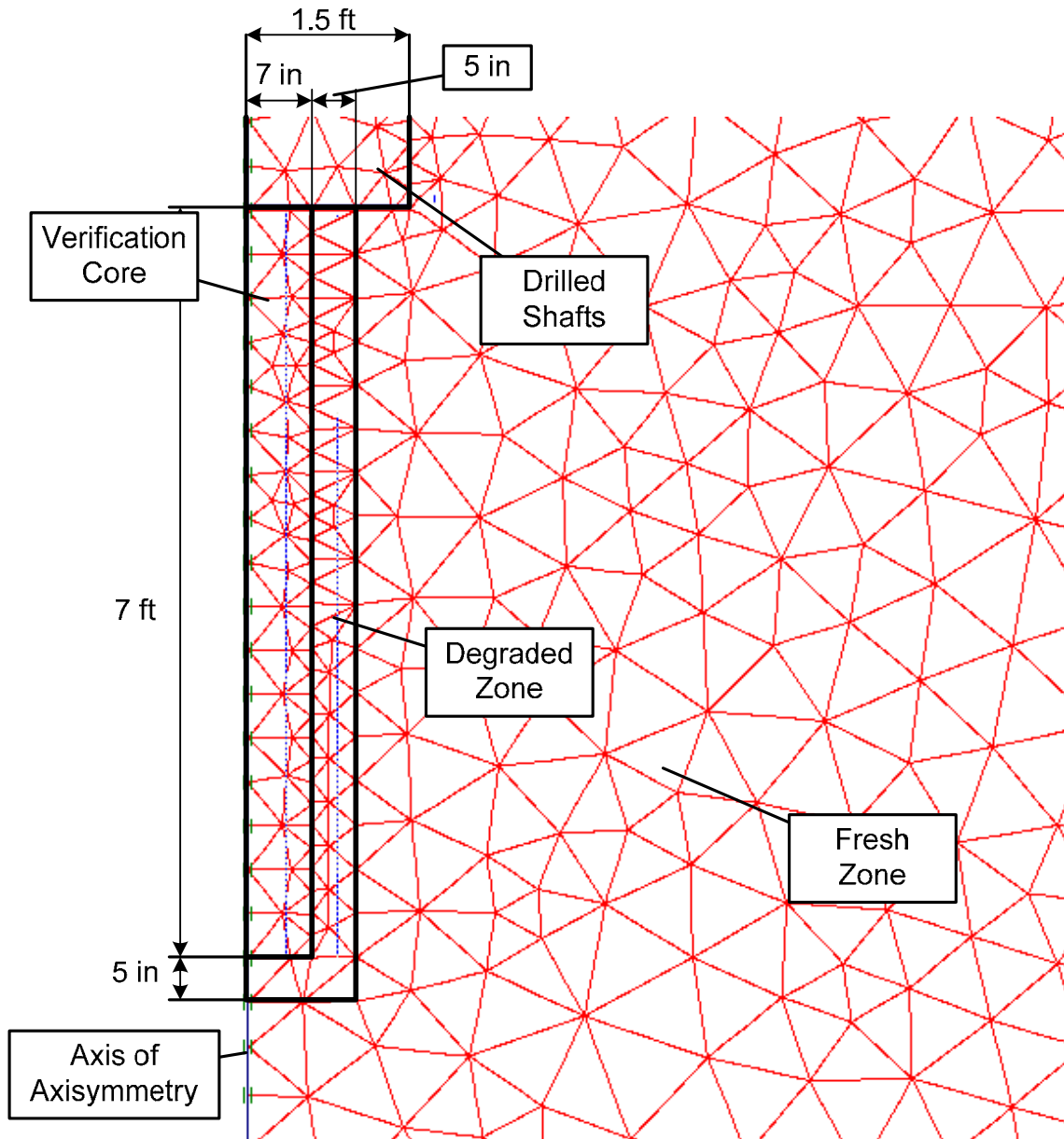
Figure 3.2.2 Close up view of the verification core and the adjacent region

Constitutive Model

    The Mohr-Coulomb model used in PLAXIS analysis is linear elastic perfectly plastic. Although the Mohr-Coulomb model does not include all non-linear features of geomaterials, the model is widely used in engineering practice because it is powerful but simple and adopts strength parameters that can be easily obtained (e.g. friction angle, cohesion, elastic modulus, Poisson's ratio, and dilation angle, etc.). However, it should be noted that the stiffness of soil element does not increase with the confining pressure.

    In principal stress space, the Mohr-Coulomb failure criterion is represented by sets of 6 inequalities as follows (PLAXIS Version 8, 2002b):

$$f_{1a} = \frac{1}{2}(\sigma_2' - \sigma_3') + \frac{1}{2}(\sigma_2' + \sigma_3')\sin\phi - c\cos\phi \le 0$$

$$f_{1b} = \frac{1}{2}(\sigma_3' - \sigma_2') + \frac{1}{2}(\sigma_3' + \sigma_2')\sin\phi - c\cos\phi \le 0$$

$$f_{2a} = \frac{1}{2}(\sigma_3' - \sigma_1') + \frac{1}{2}(\sigma_3' + \sigma_1')\sin\phi - c\cos\phi \le 0$$

Equation 3.2-1

$$f_{2b} = \frac{1}{2}(\sigma_1' - \sigma_3') + \frac{1}{2}(\sigma_1' + \sigma_3')\sin\phi - c\cos\phi \le 0$$

$$f_{3a} = \frac{1}{2}(\sigma_1' - \sigma_2') + \frac{1}{2}(\sigma_1' + \sigma_2')\sin\phi - c\cos\phi \le 0$$

$$f_{3b} = \frac{1}{2}(\sigma_2' - \sigma_1') + \frac{1}{2}(\sigma_2' + \sigma_1')\sin\phi - c\cos\phi \le 0$$

where σ_1, σ_2, and σ_3, are principal stresses, φ is the friction angle, and c is cohesion of material. The yield surface bounded by Equation 3.2-1 is shown in Figure 3.2.3 in principal stress space exhibiting a hexagonal cone extending from the origin, in which case the cohesion is equal to zero. A tension cut-off is introduced when cohesion is greater than zero because soil cannot sustain tensile stress. The dilation angle, elastic modulus, and Poisson's ratio are required in the model; the dilation angle, ψ, defines the plastic flow at yield surface, and elastic modulus and Poisson's ratio define the elastic behavior within yield surface. The elastic modulus used in PLAXIS is a secant modulus at 50% of maximum strength (Figure 3.2.4).

Simulation Procedure

In PLAXIS, a staged construction scheme is available, which allows users to simulate construction procedures; at each stage, the geometry of the model, the applied load, and water level can be modified to simulate the realistic stress state induced by construction. A total of three phases were used in this study. Figure 3.2.5 presents the construction procedure of drilled shafts and verification cores starting from Stage 0. At Stage 1, the shaft hole and verification core hole were augered from ground surface by deactivating the clay shale elements that will be replaced with concrete element at Stage 2. One of the simulations does not include augering the verification core hole, which is used as a reference model to compare with drilled shafts affected by a verification core. At Stage 2, the concrete placement was simulated by activation of solid concrete in drilled shaft holes; however, the material that fills in the the verification core hole is different depending on the pouring conditions. The verification core hole is filled with a sand-gravel mixture in an underwater pour and with solid concrete in a dry pour. At the same stage, the element of degraded clay shales is activated around the verification core hole. It should be noted that the properties of degraded clay shales assigned at the degraded region vary depending on the geologic formation and drying-duration. The material properties can be seen in Section 3.1.3. At Stage 3, the shaft head was displaced vertically displaced by 12 cm to result in shaft head displacement exceeding 10% D.
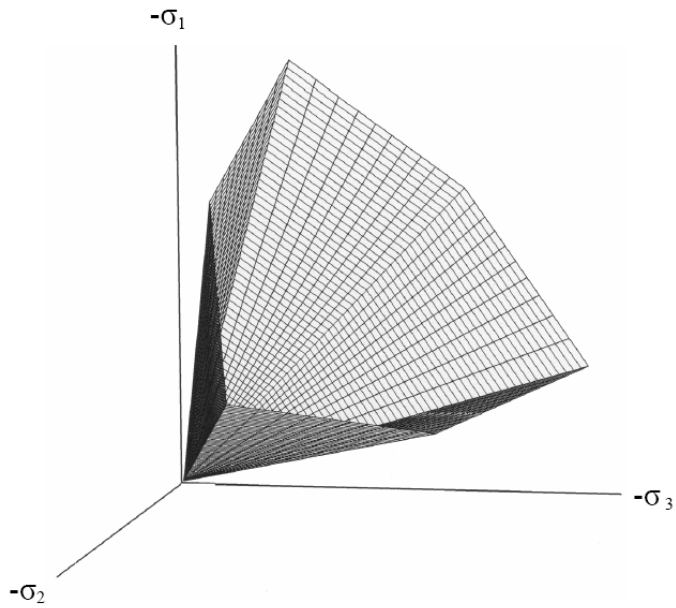
Figure 3.2.3 The Mohr-Coulomb yield surface in principal stress space (PLAXIS Version 8, 2002b)
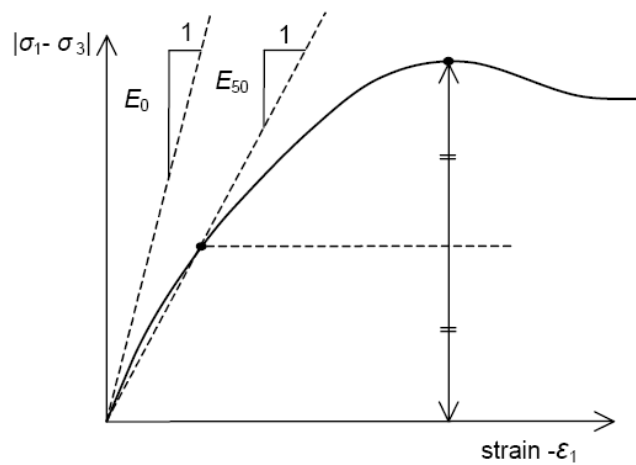
Figure 3.2.4 Definition of E_0 and E_{50} for standard drained triaxial test results (PLAXIS Version 8, 2002b)
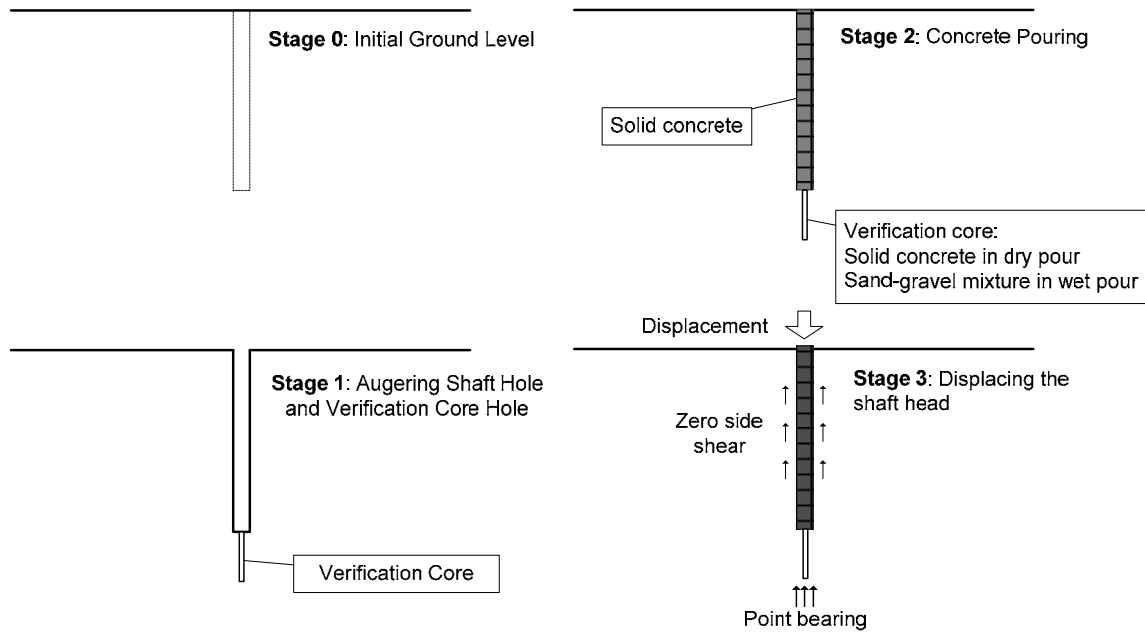
Figure 3.2.5 Construction simulation procedure in PLAXIS

Parametric Studies

Using the representative drilled shaft geometry in the numerical model, the constitutive model, and simulation procedures, parametric studies were performed by varying drying-duration and drying-condition. The varied parameters include 6 drying-durations (0, 4, 8, 16, 24, and 48 hours) and 3 different core hole diameters (6, 10, and 14 in). For additional information, 4 additional analyses were carried out for each core hole diameter and for each clay shale: 1) drilled shafts without a verification core, 2) drilled shafts with an empty verification core hole, 3) drilled shafts with a verification core hole that is filled with solid concrete (dry pour), and 4) drilled shafts with a verification core hole that dries for 48 hours and later the water in the hole is pumped out. The fourth case represents that the shale surrounding core hole degrades but the core hole is filled with concrete. This analysis is to measure the tip capacity improvement when the core hole is filled with concrete simply by pumping water before concrete cast.

In load-displacement curves, the first case is denoted as "no hole (reference)"; the second and the third cases are denoted as "with empty hole" and "dry pour," respectively. The fourth case is named "48 hour drying and pumping" to indicate that the verification core hole is dried for 48 hours and the water in the verification core hole is pumped out prior to concrete pour. The only difference between the "48 hour drying and pumping" and "wet pour after 48 hour drying" is the condition of the material that fills in the verification core hole. The material of the former is solid concrete, whereas that of the latter is a sand-gravel mixture.

Table 3.2.1 summarizes the assigned property for the degraded zone and the status of the material that fills in the verification core hole for each name, which refers to conditions and geometry of the verification core hole. Assigned property refers to the

314

material property that is assigned to the degraded zone 12.7 cm (5 in) thick. For example, 0 means that the assigned material property is fresh clay shale, and 48 means the property assigned is after a 48-hour dry time. Regarding the material in the verification core hole, solid refers to solid concrete whose properties are the same for concrete used in Table 3.1.9. Mixture indicates the filled-in material is sand-gravel mixture whose properties are given in Table 3.1.9.

Table 3.2.1 Assigned material for the degraded region and the verification core

Name	Drying-duration for assigned properties (hour)	Verification core
No hole (reference)	0	n/a
With empty hole	0	Empty
Dry pour	0	Solid
48 hour drying and pumping	48	Solid
Wet pour without drying	0	Mixture
Wet pour after 4 hour drying	4	Mixture
Wet pour after 8 hour drying	8	Mixture
Wet pour after 16 hour drying	16	Mixture
Wet pour after 24 hour drying	24	Mixture
Wet pour after 48 hour drying	48	Mixture

3.2.3 Results of Numerical Analyses

Load-displacement curves of drilled shafts reveal the relationship between applied load and resultant displacement of the shafts. The side shear resistance along the shaft was neglected in the model to focus solely on the point bearing capacity. The point bearing capacity of this report represents the summation of point bearing capacity of drilled shafts and the side resistance of the material in the core hole. The side resistance of the core hole is included in the calculation of point bearing capacity because the core hole is the only difference between "core models" and "reference model," and the total side resistance of the drilled shafts is considered identical. Therefore, the load-displacement curves from numerical analyses of this study produce the displacement of the shaft tip and resulting from the load at the shaft head. The displacement at the shaft tip does not differ significantly from that at the shaft head since the stiffness of concrete is high. The ultimate point bearing capacity of drilled shafts does not merely depend on

the ultimate resistance of the foundation soils. For example, in cohesionless soils, the resistance continues to increase as the foundation is displaced downward, and the load-displacement curve does not reach a plateau. In such a case, serviceability of the structure dictates the capacity rather than resistance itself.

Point bearing capacity is developed at larger displacements compared to those required to develop side shear resistance. Previous research has shown that displacements of 5% of the shaft diameter (D) is typically required to fully develop the point bearing capacity of drilled shafts (O'Neill and Reese, 1999). Figure 3.2.6 exhibits an example of the relationship between normalized displacement and normalized ultimate point bearing capacity of drilled shafts in cohesive soil (page 290, O'Neill and Reese, 1999). The point bearing of drilled shafts increases considerably until the displacement reaches 3%D at which point the capacity increases at a reduced rate until 5%D where the ultimate point bearing capacity is believed to be developed. Another resource defines that 10 – 15% of the shaft diameter is required for full point bearing capacity (Bruce, 1986). Hence, 5%D and 10%D were selected as displacements for full development of the point bearing capacity.

Figure 3.2.7 presents the schematic load-displacement curves of drilled shafts at the shaft base under various conditions. The point bearing capacity is obtained directly from load-displacement curves at 5%D and 10%D: P_A indicates the point bearing capacity of the reference model, P_B indicates "wet pour after 4 hour drying," and P_C refers to "wet pour after 48 hour drying." The reduction factor is calculated by dividing P_B or P_C by P_A; thus, the reduction factor for "wet pour after 4 hour drying" is P_B/P_A. The reduction factors are good indicators to estimate the effect of the verification core.

In this section, three sets of load-displacement curves are presented for each clay shale studied. Each set includes 10 load-displacement curves that represent various drying conditions and in-fill material of the verification core hole. The point bearing capacity was obtained at two displacements (5%D and 10%D) for each load-displacement curve. This makes a list of approximately 60 point bearing capacities per clay shale: 2 readings times 10 conditions times 3 core diameters. The reduction factors were calculated accordingly.
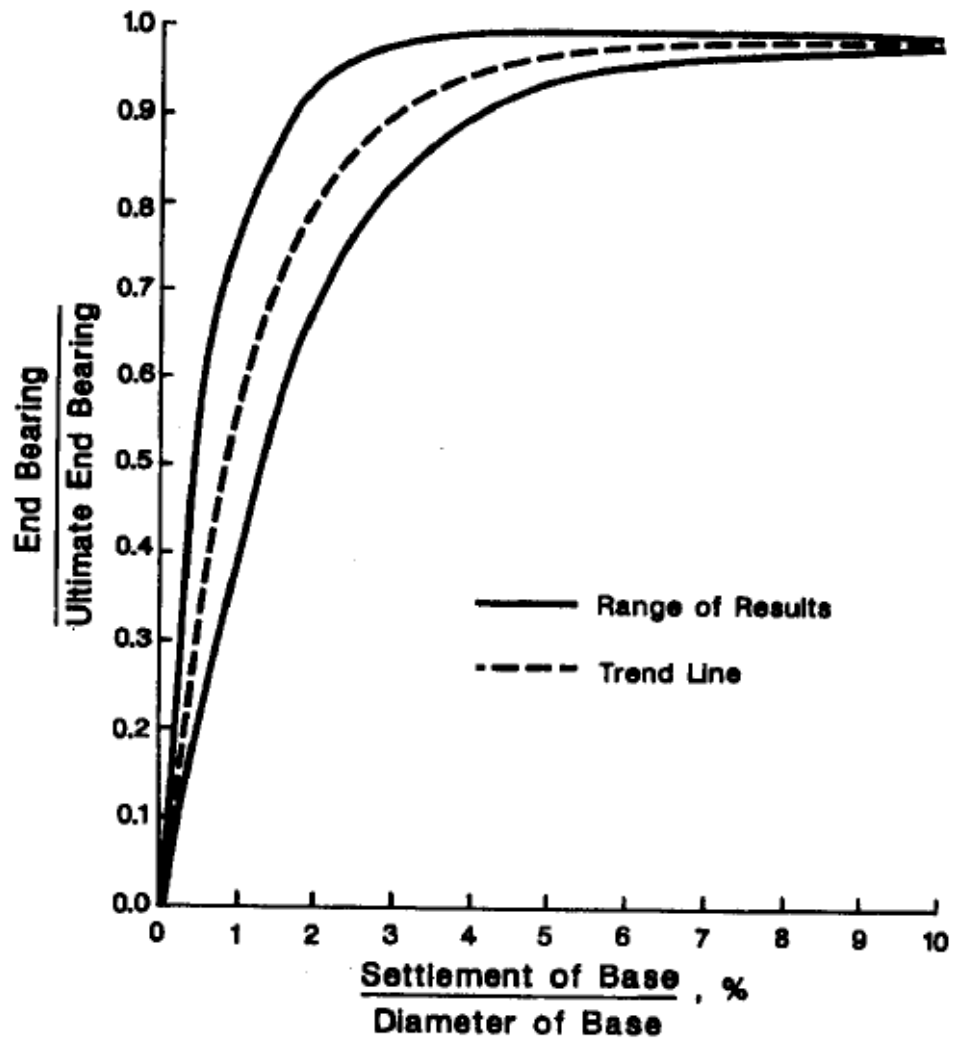
Figure 3.2.6 Normalized base load transfer for a drilled shaft in cohesive soil (O'Neill and Reese, 1999)
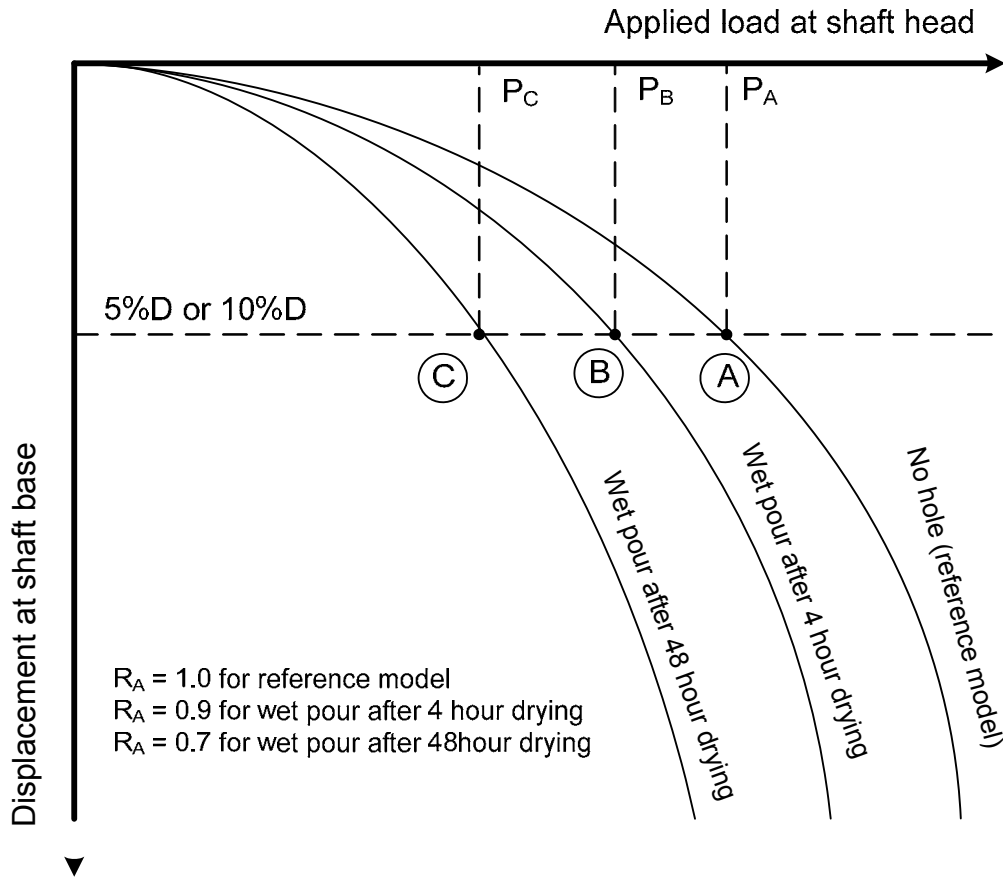
Figure 3.2.7 Definition of point bearing capacity and reduction factor

Del Rio Clay

The load-displacement curves of drilled shafts in Del Rio Clay are shown from Figure 3.2.8 through Figure 3.2.10. The horizontal dotted lines at 5%D and 10%D of tip displacement represent the limit for point bearing capacity that is tabulated in Table 3.2.2. The point resistance for the reference model was estimated to be 1,285 and 1,544 kN respectively at 5%D and 10%D displacement. The point bearing capacity of drilled shafts with verification cores were calculated to be higher than that of the reference model in all cases except for "with empty hole," indicating that the verification core filled with concrete improves the performance of drilled shafts. The drilled shaft with the empty verification core, which does not occur in reality, is the only case weaker than the reference model. For the following discussion, "core models" denotes the drilled shafts with the verification core hol, whereas the reference model denotes the drilled shafts without the verification core hole.

The reduction factor is used for easy evaluation of the point bearing capacity of "core models" compared to the reference model; the values are given in Table 3.2.3. The reduction factor for the reference model is unity. The point bearing capacity may decline to 40% the capacity of the reference model when the core hole is not in filled. However,

318

all other "core models" exhibit higher values since the strength of sand-gravel mixture that fills in the verification core hole is stronger than the Del Rio Clay. The effect of the verification core hole increases as the core hole diameter increases. The point bearing capacity increases the most for "dry pour" with a concrete-filled verification core hole of 35.6 cm (14in) diameter. The increase in drying-duration causes only a nominal decrease in point bearing capacity. Increasing the verification core diameter increases the point bearing capacity considerably. Hence, the contribution of material that fills in the verification core hole (either concrete or sand-gravel mixture) to the point bearing capacity appears to be dominant when the shafts are constructed on Del Rio Clay. Except for the case in which the verification core hole is empty, the reduction factors are always greater than 1 in Del Rio Clay. The increase in the resistance induced by materials filled in the core should exceed the decrease as a result of degradation of Del Rio Clay.

Figure 3.2.8 Load-displacement curves at shaft base with 6 in verification core in Del Rio Clay

319

Figure 3.2.9 Load-displacement curves at shaft base with 10 in verification core in Del Rio Clay

Figure 3.2.10 Load-displacement curves at shaft base with 14 in verification core in Del Rio Clay

Table 3.2.2 Summary of point bearing capacity of drilled shafts in Del Rio Clay

VC diameter	Tip Displacement	Point Bearing Capacity (kN)									
		No hole (reference)	Empty	Dry	Pumping	0	4	8	16	24	48
15.2 cm (6 in)	0.05D (4.6cm)		1,017	1,418	1,369	1,339	1,329	1,322	1,313	1,312	1,309
	0.1D (9.1cm)		1,076	1,685	1,639	1,632	1,625	1,619	1,612	1,610	1,608
25.4 cm (10 in)	0.05D (4.6cm)	1285 at 0.05D	789	1,499	1,432	1,429	1,413	1,402	1,386	1,381	1,379
	0.1D (9.1cm)	1544 at 0.1D	814	1,770	1,709	1,724	1,713	1,705	1,695	1,692	1,690
35.6 cm (14 in)	0.05D (4.6cm)		614	1,585	1,508	1,520	1,501	1,486	1,469	1,463	1,459
	0.1D (9.1cm)		634	1,861	1,792	1,815	1,803	1,793	1,781	1,777	1,775

Table 3.2.3 Summary of reduction factors of drilled shafts in Del Rio Clay

VC diameter	Tip Displacement	Reduction Factor									
		No hole (reference)	Empty	Dry	Pumping	0	4	8	16	24	48
15.2 cm (6 in)	0.05D (4.6cm)	1.00	0.79	1.10	1.07	1.04	1.03	1.03	1.02	1.02	1.02
	0.1D (9.1cm)		0.70	1.09	1.06	1.06	1.05	1.05	1.04	1.04	1.04
25.4 cm (10 in)	0.05D (4.6cm)		0.61	1.17	1.11	1.11	1.10	1.09	1.08	1.08	1.07
	0.1D (9.1cm)		0.53	1.15	1.11	1.12	1.11	1.10	1.10	1.10	1.09
35.6 cm (14 in)	0.05D (4.6cm)		0.48	1.23	1.17	1.18	1.17	1.16	1.14	1.14	1.14
	0.1D (9.1cm)		0.41	1.21	1.16	1.18	1.17	1.16	1.15	1.15	1.15

Eagle Ford Shale

It was pointed out in Section 1.5.4 that the elastic modulus of Eagle Ford Shale decreases as the drying-duration increases but that the strength is independent of drying-duration. The reduction of the elastic modulus lessens the stiffness of drilled shafts, accordingly resulting in lower point bearing capacity as drying-duration increases. Figure 3.2.11 through Figure 3.2.13 present the load-displacement curves of drilled shafts embedded into Eagle Ford Shale. It is clearly shown that the effect of the verification core hole as well as that of drying-duration increases as the verification core hole diameter increases. The behaviors of load-displacement curves differ significantly between verification core hole diameters of 35.6 cm (14 in) and 15.2 cm (6 in) because the volume of sand-gravel mixture significantly increases for the larger diameter verification cores holes. In addition, the cross-sectional area of the degraded zone is larger for the larger diameter verification core hole. The load-displacement curve of the reference model (no core) plots in the middle of other curves at 5%D displacement, but the capacity trend falls more than the other curves as the shaft displaces further. As a consequence, the point bearing capacity of the reference model tends to be low at large displacement relative to that of "core models." The higher capacity of "core models" at large displacement is likely due to the high friction angle of sand-gravel mixture in wet pour. As confining pressure increases, the increase of the strength of sand-gravel mixture is significant, whereas that of Eagle Ford Shale, whose friction angle is 12.7° (Section 3.1.2), is small; hence, the resistance of "core models" exceeds that of the reference model at large displacement.

The capacities obtained at 5% and 10%D of displacement are summarized in Table 3.2.4, and the corresponding reduction factors are summarized in Table 3.2.5. The point bearing capacity of the reference model for Eagle Ford Shale is estimated to be 5,185 and 6,504 kN at 5%D and 10% D displacement, respectively. Interestingly, the point bearing capacity of "core models" for Eagle Ford Shale may be smaller than the reference model when Eagle Ford Shale is dried longer than 8 hours. The point bearing capacity increases for "dry pour" because the verification core hole is filled with solid concrete, which contributes to additional resistance. At most, 16% of additional resistance is expected when drilled shafts are constructed in dry conditions and the size of the verification core hole is 35.6 cm (14 in). The additional resistance decreases as the verification core size decreases.

The point bearing capacity decreases as drying-duration increases. However, the point bearing capacity increases in fresh shale but decreases for degraded shale as the verification core diameter increases. This finding is repeated for Taylor Marl and Navarro Shale. This is intriguing because the finding indicates that the large diameter core is advantageous in the fresh condition, but a small diameter core is advantageous in the degraded condition.

Dewatering the verification core hole enhances the point bearing capacity as a result of solid concrete in the verification core hole. It should be noted that the "48 hour drying and pumping" indicates that the Eagle Ford Shale of the degraded zone is dried for 48 hours and the verification core hole is filled with solid concrete because the concrete is poured in the dry. Even though the point bearing capacity decreases by as much as 10% when Eagle Ford Shale has been dried for 48 hours, solid concrete in the verification

323

core hole compensates for the reduction, resulting in similar capacity to that of the reference model. Interestingly, a similar finding is repeatedly observed for other clay shales.
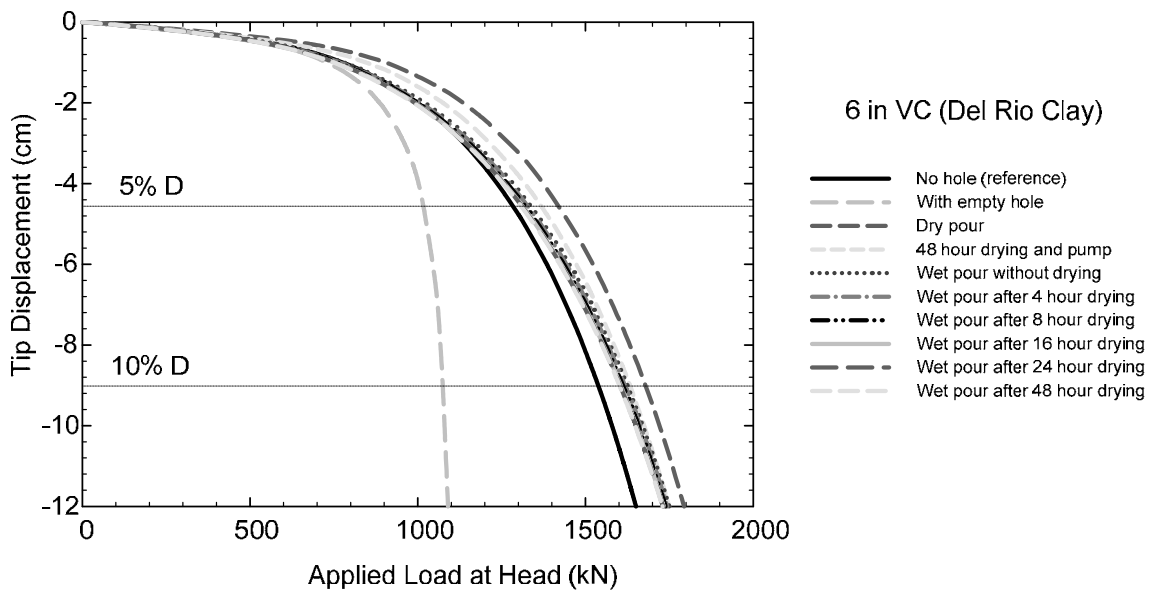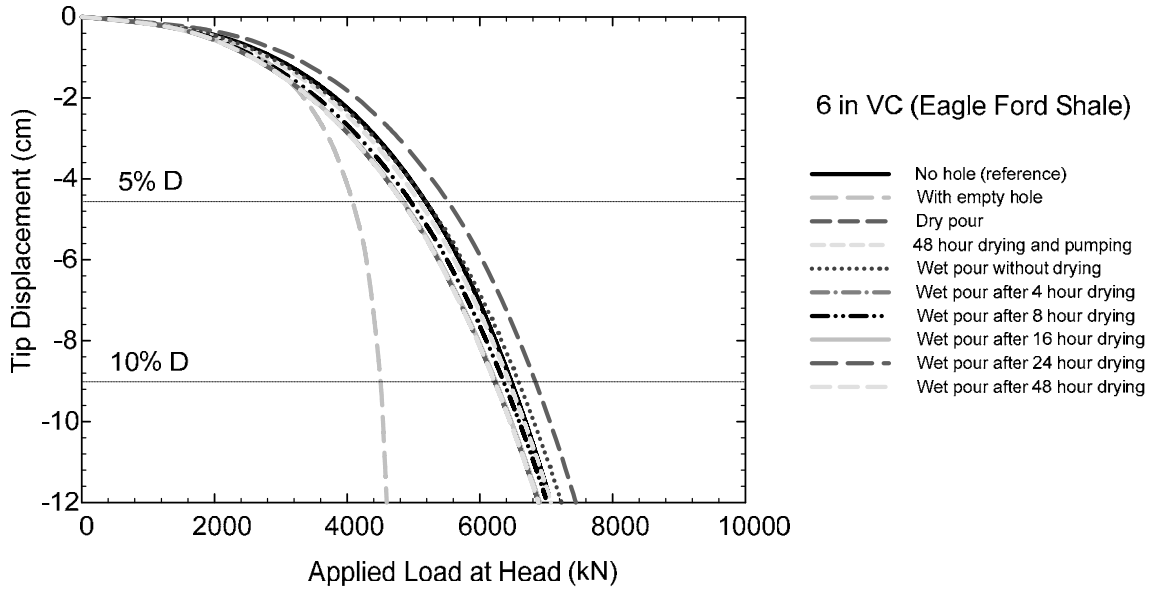

Figure 3.2.11 Load-displacement curves at shaft base with 6 in verification core in Eagle Ford Shale
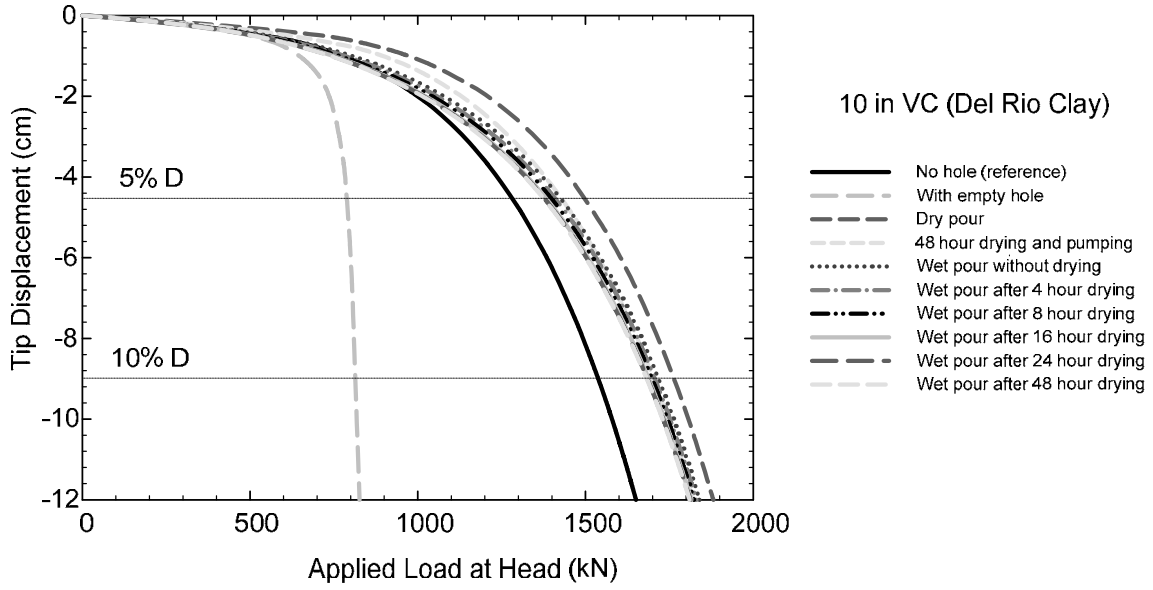

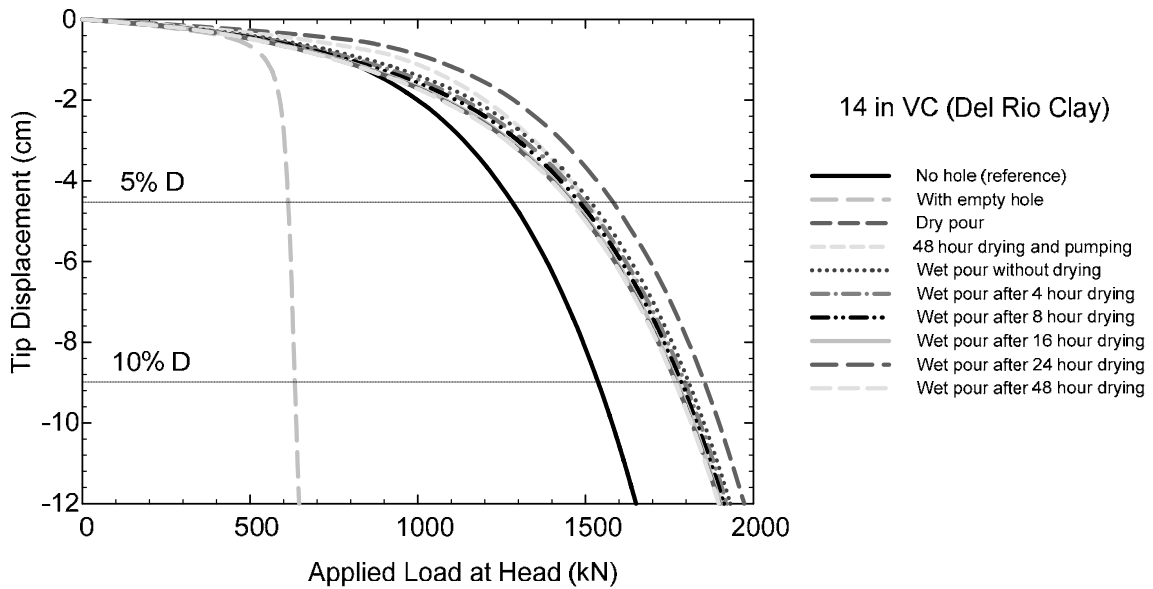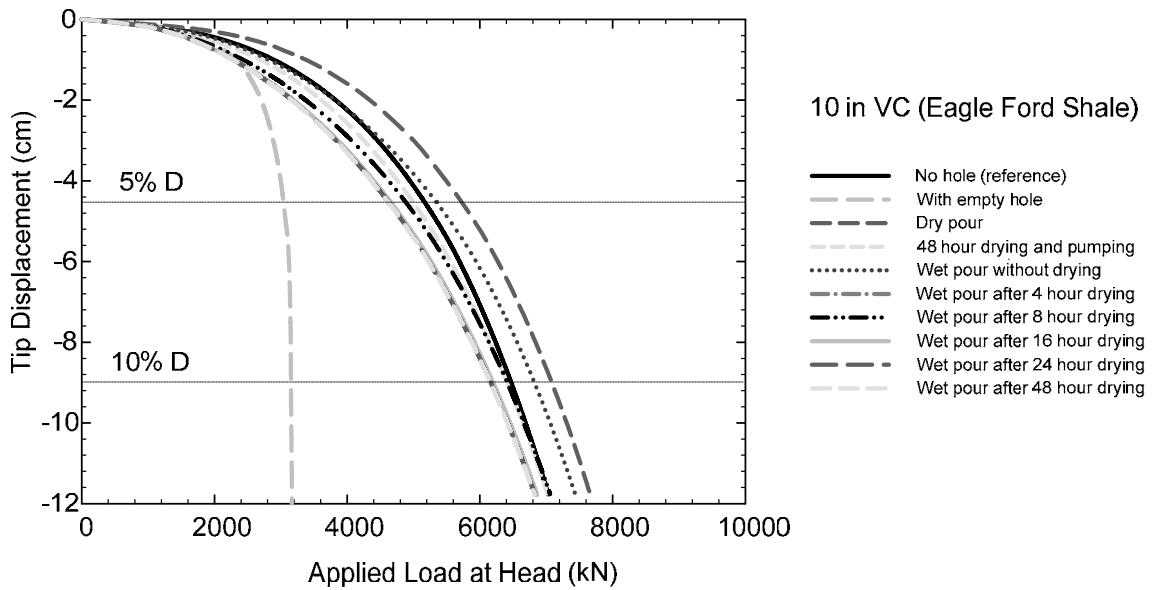*Figure 3.2.12 Load-displacement curves at shaft base with 10 in verification core in Eagle Ford Shale*

Figure 3.2.13 Load-displacement curves at shaft base with 14 in verification core in Eagle Ford Shale

Table 3.2.4 Summary of point bearing capacity of drilled shafts in Eagle Ford Shale

VC diameter	Tip Displacement	No hole (reference)	Point Bearing Capacity (kN)							
			Empty	Dry	Pumping	0	8	16	24	48
15.2 cm (6 in)	0.05D (4.6cm)	5,185 for 0.05D 6,504 for 0.1D	4,084	5,516	5,091	5,193	4,960	4,849	4,834	4,832
	0.1D (9.1cm)		4,509	6,866	6,472	6,614	6,392	6,271	6,255	6,253
25.4 cm (10 in)	0.05D (4.6cm)		3,043	5,739	5,014	5,363	4,902	4,676	4,643	4,638
	0.1D (9.1cm)		3,154	7,117	6,441	6,859	6,450	6,235	6,202	6,198
35.6 cm (14 in)	0.05D (4.6cm)		2,248	5,998	5,089	5,606	4,989	4,684	4,641	4,636
	0.1D (9.1cm)		2,279	7,401	6,556	7,135	6,619	6,335	6,294	6,289

Table 3.2.5 Summary of reduction factors of drilled shafts in Eagle Ford Shale

VC diameter	Tip Displacement	No hole (reference)	Reduction Factor							
			Empty	Dry	Pumping	0	8	16	24	48
15.2 cm (6 in)	0.05D (4.6cm)	1.00	0.79	1.06	0.98	1.00	0.96	0.94	0.93	0.93
	0.1D (9.1cm)		0.69	1.06	1.00	1.02	0.98	0.96	0.96	0.96
25.4 cm (10 in)	0.05D (4.6cm)		0.59	1.11	0.97	1.03	0.95	0.90	0.90	0.89
	0.1D (9.1cm)		0.48	1.09	0.99	1.05	0.99	0.96	0.95	0.95
35.6 cm (14 in)	0.05D (4.6cm)		0.43	1.16	0.98	1.08	0.96	0.90	0.90	0.89
	0.1D (9.1cm)		0.35	1.14	1.01	1.10	1.02	0.97	0.97	0.97

Taylor Marl

The effect of the verification core holes was found to be significant for the drilled shafts built in Taylor Marl. Figure 3.2.14 through Figure 3.2.16 present the load-displacement curves of drilled shafts for three verification core hole sizes. Compared to previous clay shales, the trend of the curves is similar but the effect of drying-duration is more distinct compared to previous clay shales. The point bearing capacity of "dry pour" is considerably higher than the other "core models" and the reference model. The point bearing capacity of the reference model is relatively high at small displacement, indicating that the verification core negatively influences the point bearing capacity at small displacements. The point bearing capacity of the reference model, on the other hand, is small at large displacement, indicating that the effect of the verification core positively affects the point bearing capacity. The effect of drying-duration is more significant for a 35.6 cm (14 in) diameter verification core than for a 15.2 cm (6 in) diameter core.

The point bearing capacity of drilled shafts for Taylor Marl obtained at 5% and 10%D are tabulated in Table 3.2.6, and the reduction factors are shown in Table 3.2.7. The point bearing capacity of the reference model is 4,433 and 5,346 kN at 5%D and 10%D displacement, respectively. The point bearing capacity is likely to increase in dry pour by as much as 26%, but the capacity declines by as much as 14% for "wet pour after 48 hour drying" of a 35.6 cm (14 in) diameter core. Dewatering the verification core prior to concrete pour makes the point bearing capacity of "48 hour drying and pumping" similar to that of the reference model. Although the drying-duration significantly reduces the point bearing capacity at large displacement, the point bearing capacity of "core models" may be higher than that of the reference model at large displacement levels.
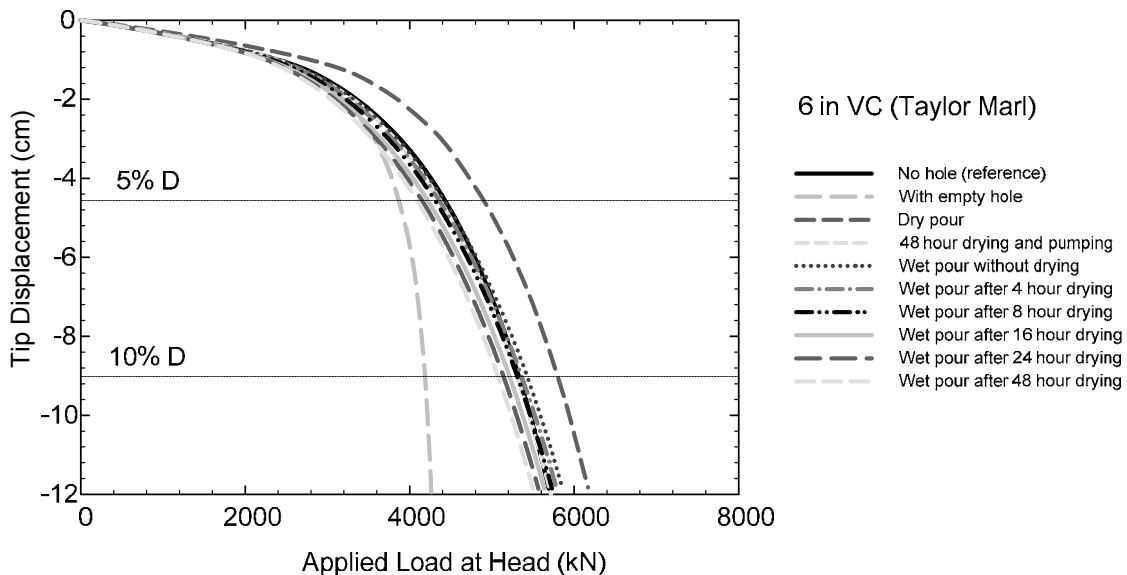
Figure 3.2.14 Load-displacement curves at shaft base with 6 in verification core in Taylor Marl
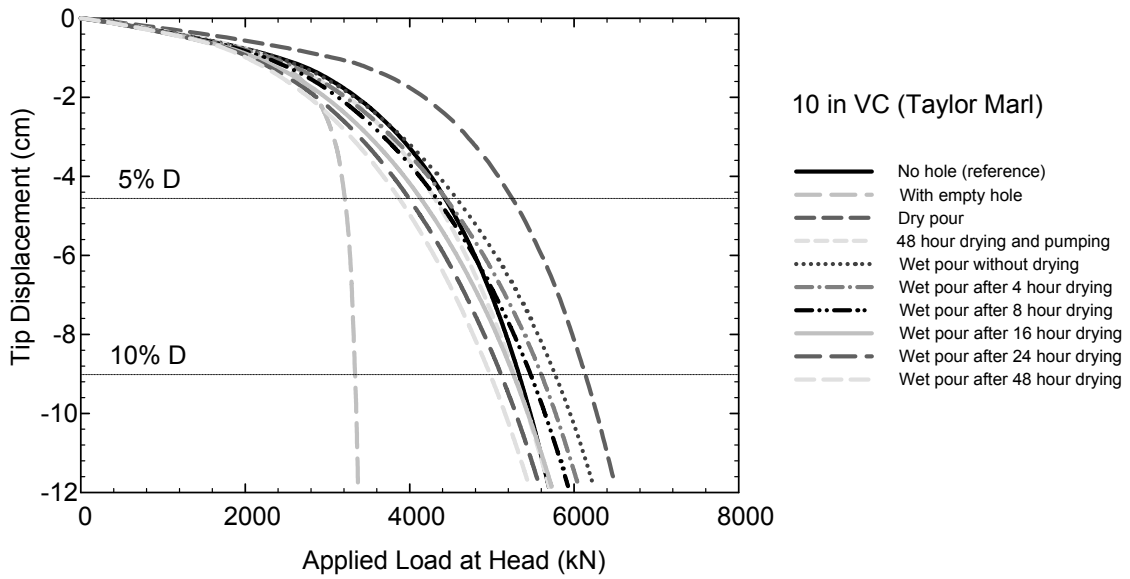
Figure 3.2.15 Load-displacement curves at shaft base with 10 in verification core in Taylor Marl
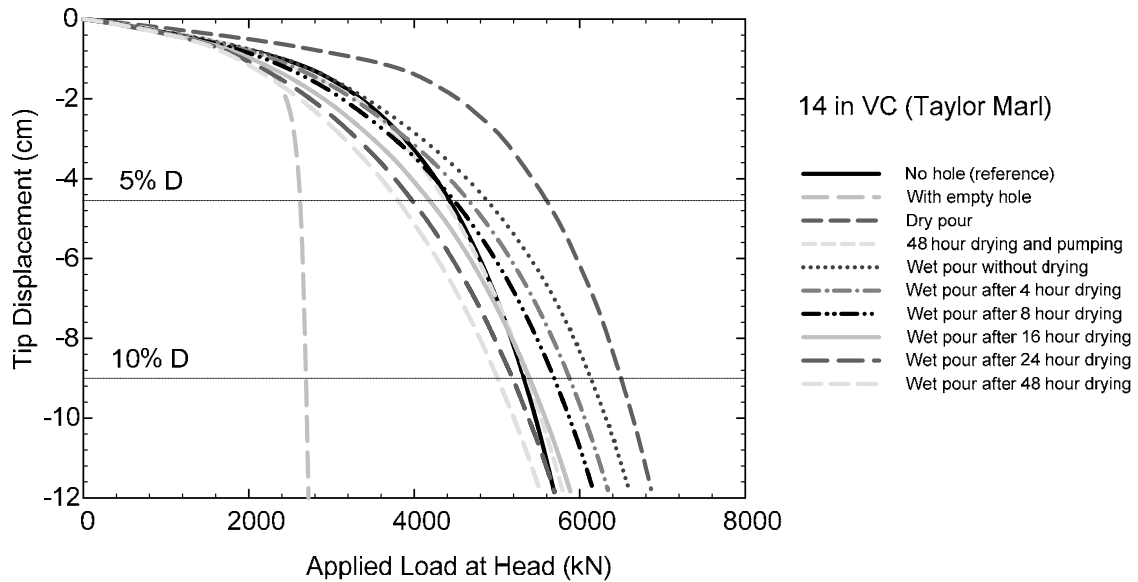
Figure 3.2.16 Load-displacement curves at shaft base with 14 in verification core in Taylor Marl

Table 3.2.6 Summary of point bearing capacity of drilled shafts in Taylor Marl

VC diameter	Tip Displacement	Point Bearing Capacity (kN)									
		No hole (reference)	Empty	Dry	Pumping	0	4	8	16	24	48
15.2 cm (6 in)	0.05D (4.6cm)		3,868	4,903	4,365	4,424	4,362	4,312	4,222	4,153	4,092
	0.1D (9.1cm)		4,191	5,817	5,771	5,451	5,383	5,330	5,236	5,162	5,097
25.4 cm (10 in)	0.05D (4.6cm)	4433 at 0.05D	3,211	5,245	4,307	4,573	4,442	4,331	4,138	3,995	3,875
	0.1D (9.1cm)	5346 at 0.1D	3,338	6,151	5,298	5,794	5,624	5,494	5,285	5,135	5,004
35.6 cm (14 in)	0.05D (4.6cm)		2,622	5,603	4,380	4,890	4,666	4,490	4,195	3,983	3,812
	0.1D (9.1cm)		2,693	6,516	5,395	6,160	5,904	5,718	5,422	5,218	5,034

Table 3.2.7 Summary of reduction factors of drilled shafts in Taylor Marl

VC diameter	Tip Displacement	Reduction Factor									
		No hole (reference)	Empty	Dry	Pumping	0	4	8	16	24	48
15.2 cm (6 in)	0.05D (4.6cm)	1.00	0.87	1.11	0.98	1.00	0.98	0.97	0.95	0.94	0.92
	0.1D (9.1cm)		0.78	1.09	1.08	1.02	1.01	1.00	0.98	0.97	0.95
25.4 cm (10 in)	0.05D (4.6cm)		0.72	1.18	0.97	1.03	1.00	0.98	0.93	0.90	0.87
	0.1D (9.1cm)		0.62	1.15	0.99	1.08	1.05	1.03	0.99	0.96	0.94
35.6 cm (14 in)	0.05D (4.6cm)		0.59	1.26	0.99	1.10	1.05	1.01	0.95	0.90	0.86
	0.1D (9.1cm)		0.50	1.22	1.01	1.15	1.10	1.07	1.01	0.98	0.94

Navarro Shale

Significant degradation has been observed from laboratory tests on Navarro Shale (Section 1.5.4) in terms of strength as well as elastic modulus. Consequently, significant reduction of point bearing capacity of drilled shafts embedded into Navarro Shale is observed in Figure 3.2.17 through Figure 3.2.19. Similar to other clay shales, the point bearing capacity of "dry pour" is the highest, and that of "with empty hole" is the lowest. The effect of the verification core hole is greater for the larger diameter verification core hole. The effect of a verification core hole of 15.2 cm (6 in) appears to be negligible, whereas considerable differences are exhibited for larger diameters (25.4 and 35.6 cm). Once again, the load-displacement curves obtained from the reference model and from "48 hour drying and pumping" were very similar.

The point bearing capacity obtained at 5% and 10%D of displacement is summarized in Table 3.2.8, and corresponding reduction factors are summarized in Table 3.2.9. The point bearing capacity of the reference model was estimated to be 3,236 and 3,956 kN at 5%D and 10%D displacement, respectively. The point bearing capacity decreases by as much as 10% at 24 hours of air drying as drying-duration increases. The degradation of Navarro Shale was too severe to perform a triaxial test on the specimen; thus, the load-displacement curve for "wet pour after 48 hour drying" was not obtained. Dry pour enhances the point bearing capacity by a maximum of 26% of the capacity of the reference model.
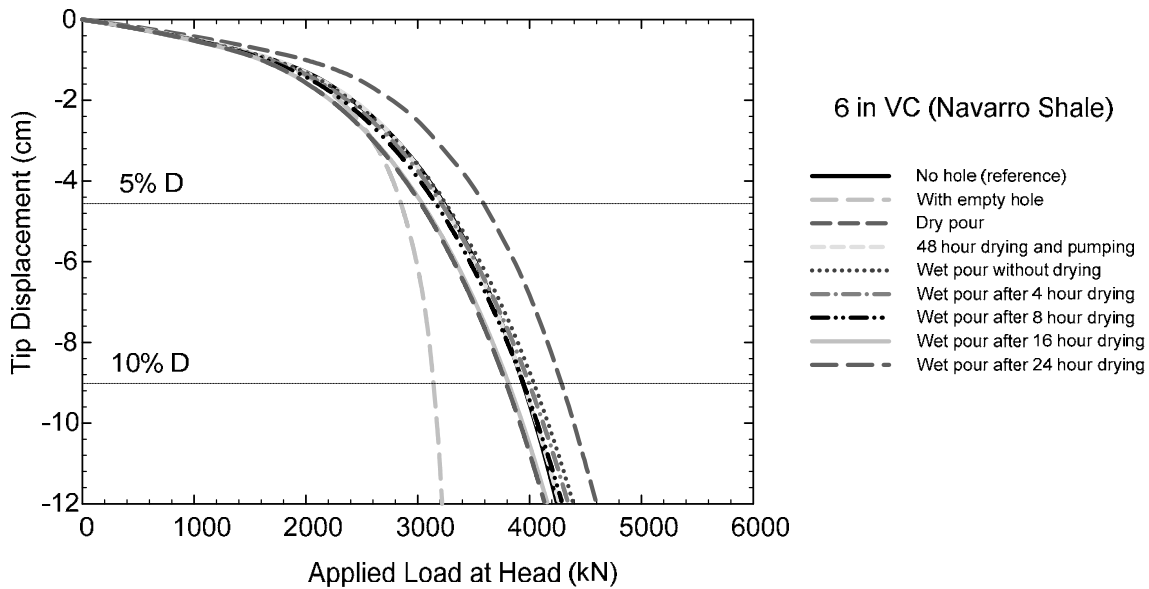
Figure 3.2.17 Load-displacement curves at shaft base with 6 in verification core in Navarro Shale

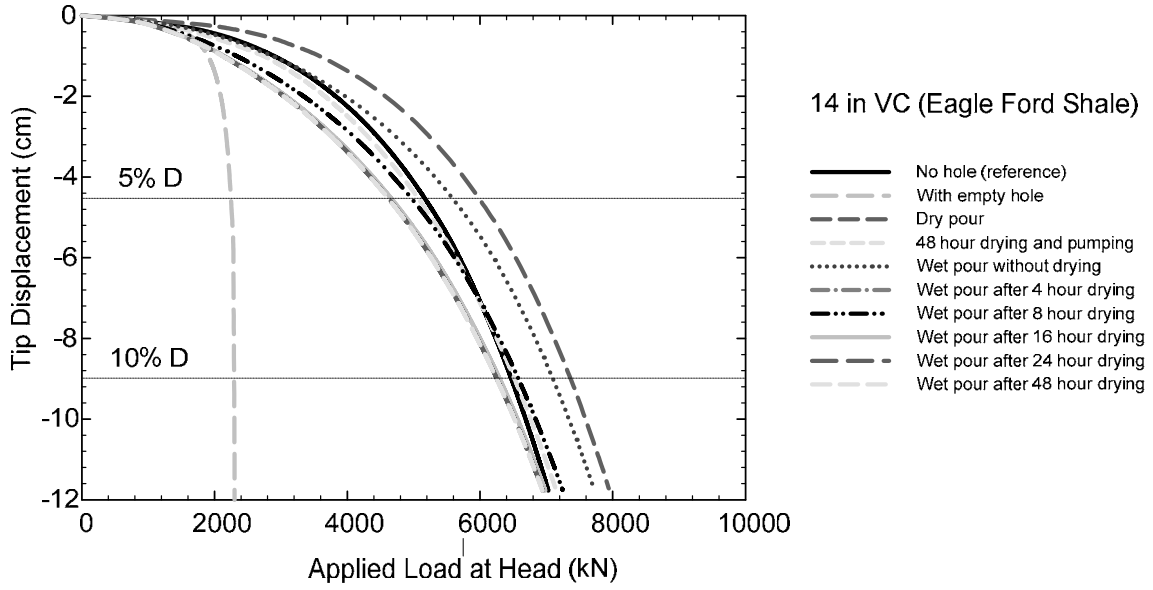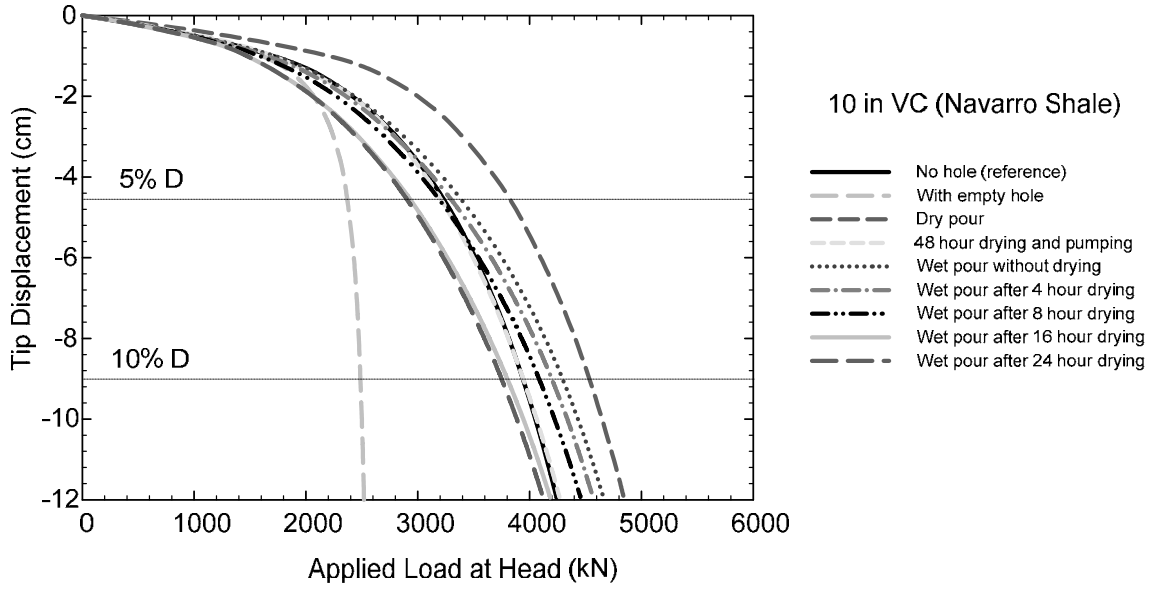*Figure 3.2.18 Load-displacement curves at shaft base 10 in verification core in Navarro Shale*
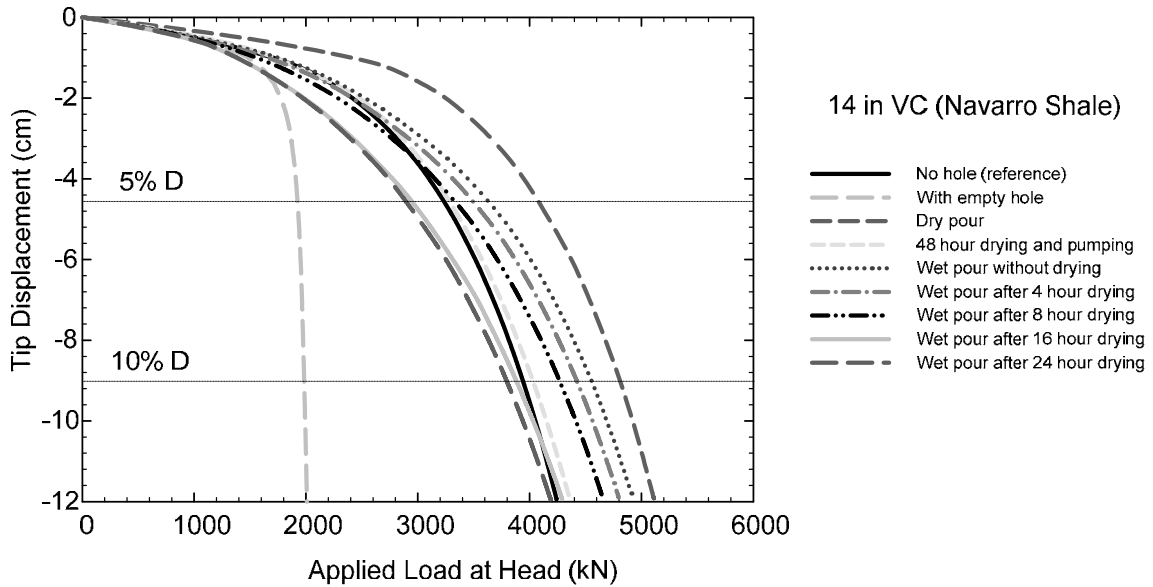
Figure 3.2.19 Load-displacement curves at shaft base with 14 in verification core in Navarro Shale

Table 3.2.8 Summary of point bearing capacity of drilled shafts in Navarro Shale

VC diameter	Tip Displacement	Point Bearing Capacity (kN)								
		No hole (reference)	Empty	Dry	Pumping	0	4	8	16	24
15.2 cm (6 in)	0.05D (4.6cm)		2,852	3,592	3,226	3,253	3,214	3,166	3,043	3,031
	0.1D (9.1cm)		3,145	4,298	3,963	4,057	4,013	3,962	3,829	3,807
25.4 cm (10 in)	0.05D (4.6cm)	3,236 at 0.05D	2,371	3,825	3,211	3,393	3,303	3,196	2,937	2,908
	0.1D (9.1cm)	3,956 at 0.1D	2,489	4,549	3,961	4,316	4,219	4,106	3,822	3,770
35.6 cm (14 in)	0.05D (4.6cm)		1,925	4,078	3,286	3,634	3,497	3,335	2,950	2,897
	0.1D (9.1cm)		1,986	4,823	4,047	4,574	4,398	4,288	3,902	3,815

Table 3.2.9 Summary of reduction factors of drilled shafts in Navarro Shale

VC diameter	Tip Displacement	No hole (reference)	Reduction Factor							
			Empty	Dry	Pumping	0	4	8	16	24
15.2 cm (6 in)	0.05D (4.6cm)	1.00	0.88	1.11	1.00	1.01	0.99	0.98	0.94	0.94
	0.1D (9.1cm)		0.79	1.09	1.00	1.03	1.01	1.00	0.97	0.96
25.4 cm (10 in)	0.05D (4.6cm)		0.73	1.18	0.99	1.05	1.02	0.99	0.91	0.90
	0.1D (9.1cm)		0.63	1.15	1.00	1.09	1.07	1.04	0.97	0.95
35.6 cm (14 in)	0.05D (4.6cm)		0.59	1.26	1.02	1.12	1.08	1.03	0.91	0.90
	0.1D (9.1cm)		0.50	1.22	1.02	1.16	1.11	1.08	0.99	0.96

3.2.4 Load Transfer Analysis (t-z analysis)

The purpose of this section is to predict the total bearing capacity by coupling side shear resistance with point bearing capacity because the two resistances occur simultaneously. Although the current study focuses solely on the point bearing capacity, it should be interesting to investigate the extent of the reduction of total bearing capacity as a result of the verification core hole. Therefore, load transfer analysis was employed to predict the total load-displacement curve, by which the total bearing capacity can be obtained.

The load transfer analysis is a numerical approach to estimate the settlement of pile, dividing it into several elements, which are represented by series of pile springs and soil springs. Figure 3.2.20 exhibits the divided elements of pile that is subject to load Q at the pile head. The element is supported by soil springs that represent side shear and point bearing of the pile, and the springs are fixed to rigid boundary. The elastic deformation of the ith pile element can be calculated by the equation for the spring constant as given below:

$$K_i = \frac{A_i \cdot E_i}{L_i}$$

Equation 3.2-2

where A_i is the shaft cross-sectional area, E_i is the elastic modulus, and L_i is a length of the ith pile element. The diameter and length of drilled shafts of this study is 0.91 cm (3 ft) and 9.1 m (30 ft) respectively, and the elastic modulus of drilled shafts is 23.6 GPa (3420 ksi). The shafts were divided into 25 elements, each 0.37 m (1.2 ft) long. The soil resistance can be modeled by two non-linear curves: t-z curve for side shear and q-z curve for point bearing capacity. One example of a dimensionless q-z curve is shown in Figure 3.2.6.

The load-displacement curve at the shaft base (q-z curve) is directly adopted from PLAXIS analysis in Section 3.2.3. The load-displacement curve selected is that of "wet pour after 48 hour drying" of a verification core 35.6 cm (14 in) in Taylor Marl (Figure 3.2.16). The point bearing capacity at 10%D (5,034 kN) was assumed to be the ultimate value; thus, the point bearing capacity increases up to 10%D and then remains constant. The shape of the q-z curve is shown in Figure 3.2.21.
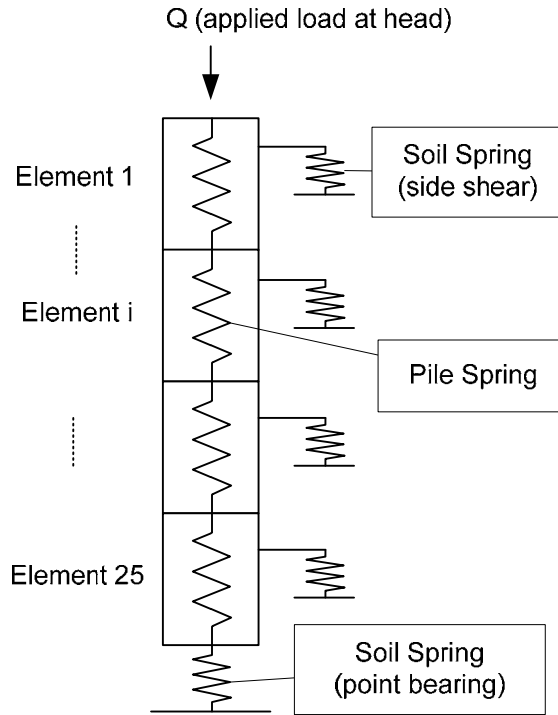
Figure 3.2.20 Schematic drawing of segmented pile and springs used for load transfer analysis
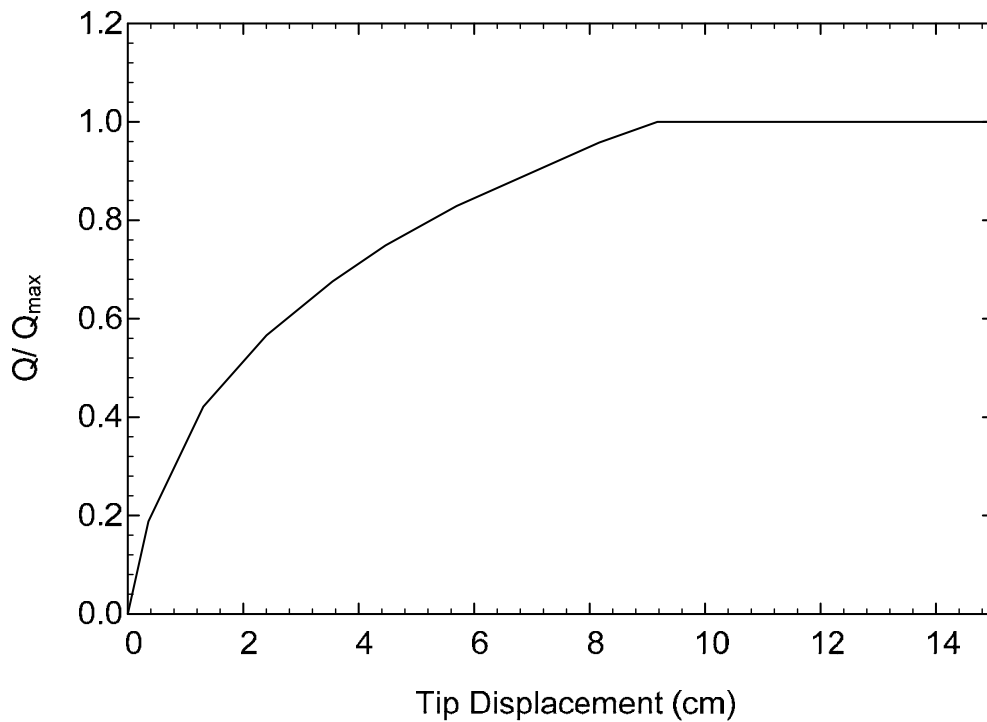
Figure 3.2.21 q-z curve used in load transfer analysis

The load-displacement curve for side shear (t-z curve) is not within the scope of this research. Hence, for simple calculation, the shape of the t-z curve was assumed such that the side shear is fully developed at 0.8%D displacement (0.73 cm) and decreases to residual value, which

337

is assumed to be 0.9 of the maximum at large displacement. In addition, the t-z curves of all elements were assumed to be identical, as is shown in Figure 3.2.22. Another important assumption made is the side shear resistance. The undrained shear strength (S_u) of overburden clay was assumed to be 95.8 kPa (2 ksf) that represents the S_u of firm-stiff clay. Using α method, the unit side shear is estimated by:

$$f_s = \alpha \, S_u \qquad\qquad\qquad \text{Equation 3.2-3}$$

where α is the adhesion factor that correlates undrained shear strength, S_u, and unit side shear, f_s. The 0.55 of the adhesion factor was used as recommended by O'Neill and Reese (1999); the unit side shear was calculated to be 52.7 kPa along the shafts and does not change with depth. The degradation of the clay was not taken into account. The side resistance of each element was 55 kN; thus, the total side resistance was calculated to be 1,383 kN, which is approximately 27% of point bearing capacity. The purpose for clarifying the magnitude of the point bearing capacity and side resistance is to recognize the contribution of each component to the total load-displacement curve. The contribution of point bearing capacity to the total load-displacement curve will decrease as the relative magnitude of side shear increases. Additional load transfer curve for higher strength clay was conducted to investigate the contribution of side shear when the magnitude of side shear is similar to the point bearing capacity.

    The load transfer analyses were carried out by first displacing the shaft base and iterating from the first element until compatibility among side shear, end bearing, and displacement is achieved. When the compatibility is satisfied in the first element, the load transferred from the first element is applied to the bottom of the second element, and iterated again until compatibility of the second element is achieved. At the end of iteration, head displacement and the applied load is obtained at the top element per base displacement, by which the full range of the load-displacement curve is obtained. A simple calculation to obtain the displacement and resultant force in one element is described below as an example.
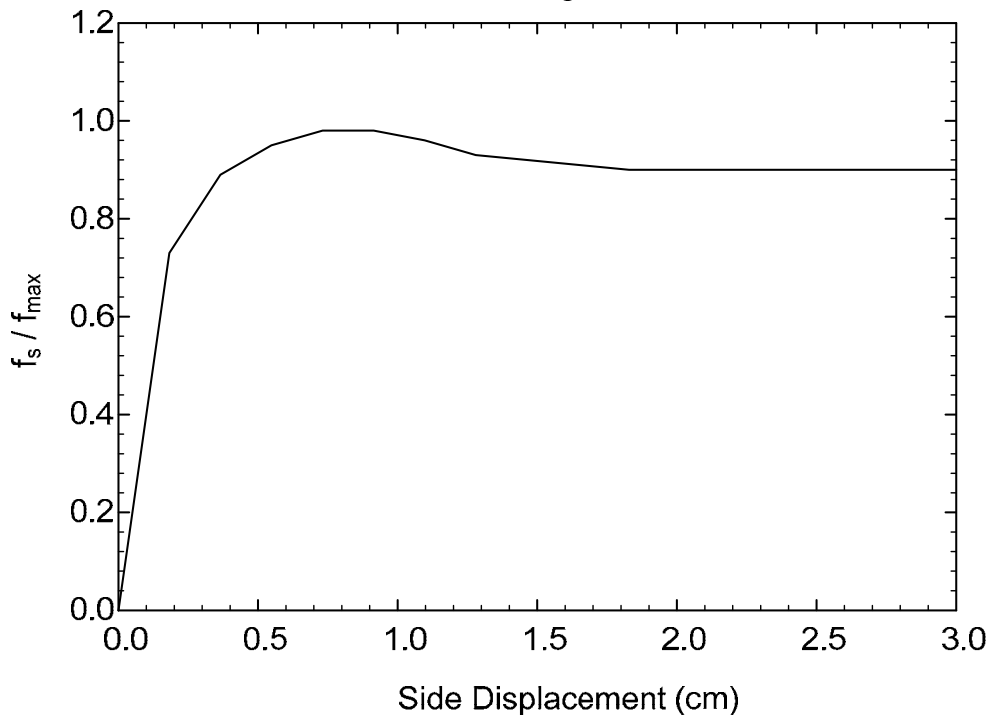
Figure 3.2.22 t-z curve used for load transfer analysis

338

Figure 3.2.23 depicts a 0.37 m (1.2 ft) long element in force equilibrium with base force, Q_b, and top force, Q_t, and side resistance, F_s. Let's assume that the imposed base displacement is 4 cm; then the corresponding base load is 3,589 kN that is directly available from the q-z curve (Figure 3.2.21). The top force is initially assumed to be zero. Thus, the average force in the element is half the base force (1,793 kN), from which top displacement of the element as a result of element compression can be estimated using the spring constant given in Equation 3.2-2. The spring constant was calculated to be 423 MN/cm, and the element compression by the base force is calculated to be 0.0042 cm. Therefore, the displacement at the top of the element is 4.0042 cm, and the relative displacement at the middle of the element is 4.0021 cm. Then, the side shear at the middle can be obtained from the t-z curve (Figure 3.2.22) and is 49.8 kN. From force equilibrium, the top force, Q_t, is calculated to be 3,639 kN by adding F_s and Q_b. Since the top force, Q_t, is updated, the average force in the element is updated to 3,614 kN, from which elastic compression of the element is updated. Repeat the same procedure until compatibility is achieved in the element, and the final top force, Q_t, will be transferred to the upper element as a base force.

Q_t

E = 23.6 Gpa
D = 0.91 m

F_s

0.37 m

Q_b
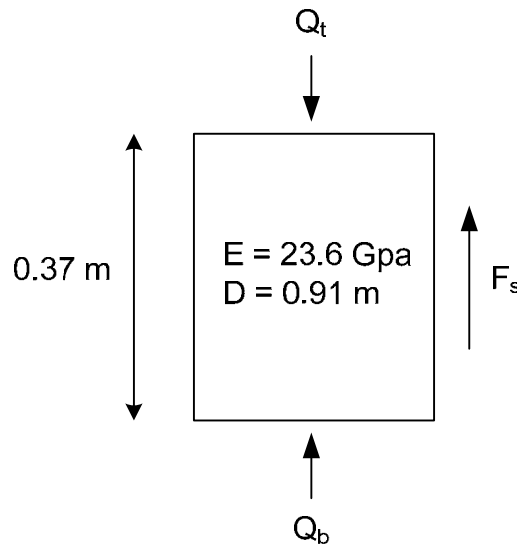
Figure 3.2.23 An element of drilled shafts used for load transfer analysis

From load transfer analyses, total load-displacement curves are drawn for "wet pour after 48 hour drying" and for the reference model in Figure 3.2.24 when the drilled shafts are installed and modeled in a cohesive soil with 95.8 kPa of undrained shear strength. For reference, Davisson's Criterion (Davisson, 1972) for drilled shafts is drawn in the figure, and the equation is given by:

$$\delta = 0.15\,inch + \frac{PL}{AE} + 0.05\,D \qquad\qquad \text{Equation 3.2-4}$$

where the first term is the displacement required to fully mobilize side shear resistance, the second term is elastic compression of the shaft, and the third term is the displacement to mobilize full point bearing capacity. The total capacity defined by Davisson's Criterion is 5,773 kN for the reference model and 5,192 kN for "wet pour after 48 hour drying." The reduction of total resistance is approximately 10%. Comparatively, the reduction of the capacity obtained from

339

load-displacement curves under the same condition was 14% at 5%D and 6% at 10%D displacements, respectively. The reduction of point bearing capacity appreciably affects the total shaft capacity.

High side shear may reduce impact on total shaft capacity resulting from the reduced point bearing capacity. Undrained shear strength of 349.5 kPa was adopted for a new analysis; the undrained shear strength results in side shear as large as point bearing capacity. Both side shear and point bearing capacity was approximately 5,000 kN, and the resulting total load-displacement curve is presented in Figure 3.2.25. The total resistance of the reference model is 9,227 kN and decreases to 8,649 kN as a result of degradation at the shaft tip, indicating that total resistance drops by 6%. The reduction of total resistance may be negligible in this case, but it should be considered in clay with low to high strength.
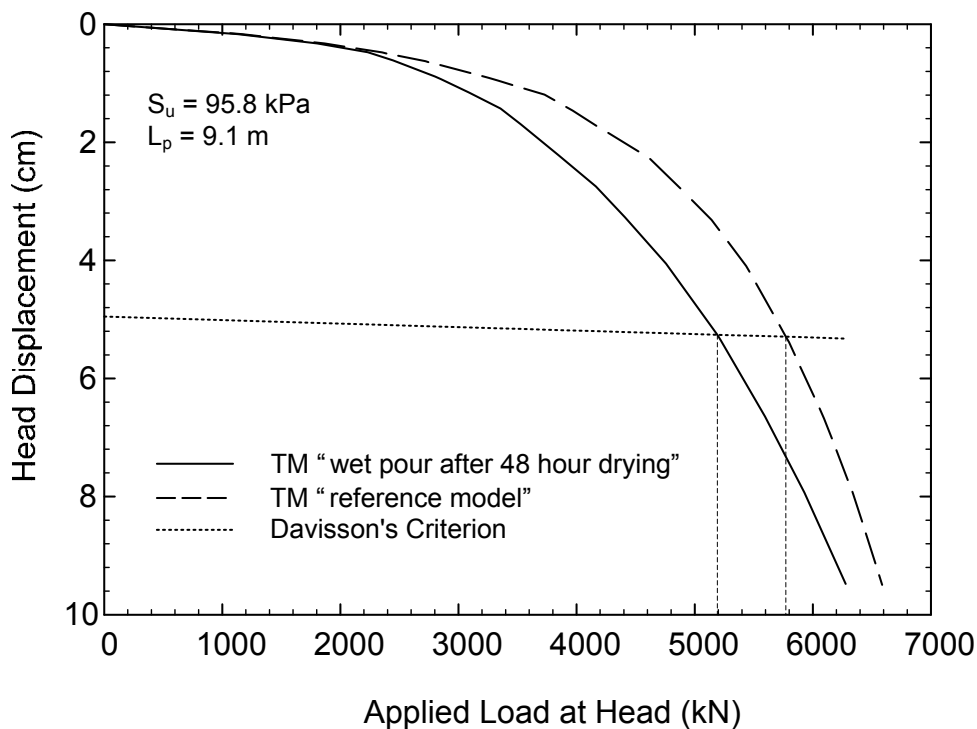
Figure 3.2.24 Load-displacement curves obtained from load transfer analysis using side resistance of 27% the point bearing capacity

340
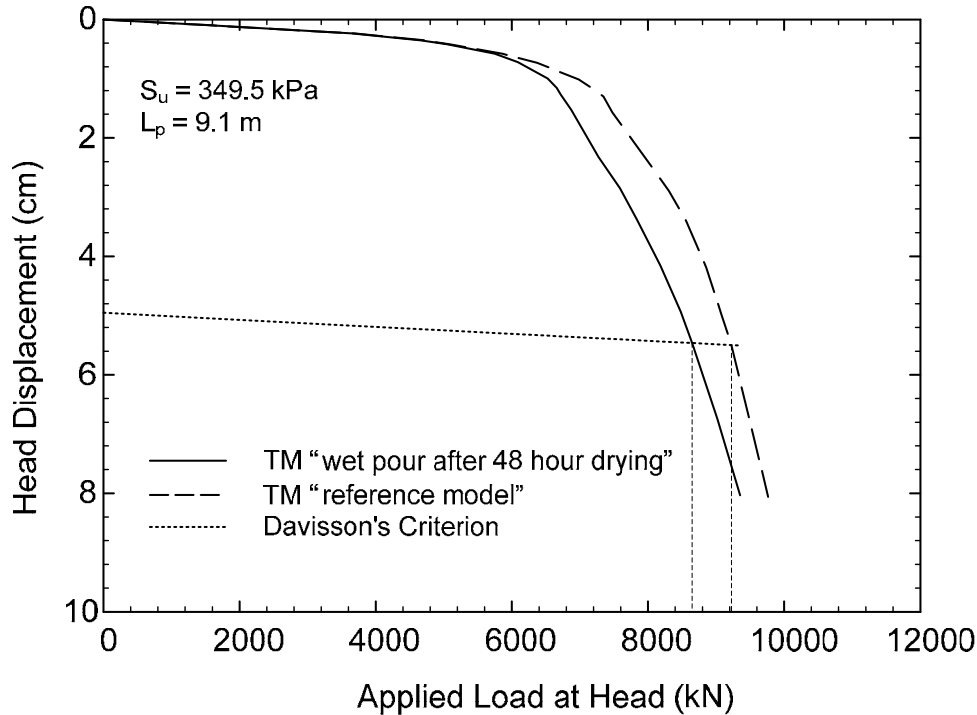
Figure 3.2.25 Load-displacement curves obtained from load transfer analysis using side resistance of 100% the point bearing capacity

3.2.5 Discussion

Series of load-displacement curves were derived for various conditions using the finite element method (FEM). An axisymmetric numerical model was created in FEM software, PLAXIS, and the material parameters from Section 3.1 were used with the Mohr-Coulomb failure criterion. Point bearing capacity of drilled shafts is determined at 5%D and 10%D displacements from load-displacement curves, and the obtained values were used to calculate reduction factors that relate the point bearing capacity of the reference model to that of "core models." From the results of numerical analyses, the following is commonly observed for four clay shales: 1) the point bearing capacity of "dry pour" is always the largest. 2) The effect of the verification core hole increases as the core hole size increases. 3) The effect of drying-duration increases as the core hole size increases. 4) Dewatering the verification core hole prior to concrete placement enhances the point bearing capacity ("48 hour drying and pumping") to close to that of the reference model. 5) The load-displacement curve of the reference model behaves stiffly in the beginning of loading, but the overall stiffness drops at large displacement.

The reduction factors obtained for four clay shales indicate that the verification core hole may increase the point bearing capacity when the founding material in its fresh state is already relatively weak, such as with Del Rio Clay (see Table 3.2.3). Moreover, the verification core hole that is filled with solid concrete as a result of "dry pour" always provides greater point bearing capacity than the reference model. Dewatering the verification core hole prior to concrete pour compensates for the degradation of clay shales at the perimeter of the verification core hole by allowing additional resistance from solid concrete in the verification core hole. In most cases, the reduction or increase in point bearing capacity induced by the verification core hole is within 10% of the point bearing capacity of the reference model.

341

From the foregoing discussion, it is clear that the materials that fill in the verification core, whether solid concrete or sand-gravel mixture, make up for the loss of point bearing capacity caused by the degraded clay shales. One reason may be the high elastic modulus of the filled-in materials compared to that of four clay shales, which results in stiff behavior of drilled shafts with a verification core. However, the point bearing capacity of drilled shafts with a verification core hole, which is filled with sand-gravel mixture, tends to be lower than that of the reference model at small displacement, meaning that the stiffness of the shafts is less at the start of loading. This observation is likely due to the low cohesion value for sand-gravel mixture, which leads the sand-gravel mixture to plastic limit earlier than the clay shales. Consequently, the plastic deformation of sand-gravel mixture occurs at small displacement (small loading), resulting in low capacity.

Load transfer analyses were conducted for drilled shafts bearing on Taylor Marl and surrounded by cohesive soils. The point bearing capacity of "wet pour after 48 hour drying" and the reference model of Taylor Marl was used to create a q-z curve. The t-z curve was created based on assumed displacement for full side shear and on side shear obtained by applying the assumed S_u to α method. Total load-displacement curves including point bearing and side shear were generated to evaluate the effect of the verification core hole on the total capacity of drilled shafts. It was found that the portion of point bearing capacity of drilled shafts in clay shales is large compared to the side shear resistance; therefore, the reduction in total resistance is also recognizable. However, the increase in undrained shear strength of cohesive soil reduces the effect of the verification core hole as a result of reducing the relative contribution of point bearing capacity. The point bearing capacity of drilled shafts tipped on clay shales is very high; thus, the side shear from high strength cohesive soil does not affect the total capacity significantly. It should be pointed out that the total load-displacement curve will vary significantly depending on shaft geometry, strength of surrounding soils, and foundation soils at the shaft base etc. For example, significantly long drilled shafts bearing on very soft material will result in a different conclusion; the effect of the verification core may not be appreciable in total resistance.

3.3 CONCLUSIONS AND RECOMMENDATIONS

3.3.1 Conclusions

The verification core refers to a core hole at least 1.5 m (5ft) long that must be excavated at the bottom of drilled shafts for visual inspection to determine whether the founding material is as strong as is called for in design. The clay shales at the perimeter of the excavated verification core hole may deteriorate as a result of air-drying and subsequent wetting that occurs during construction. The degraded engineering properties of clay shales were estimated from laboratory tests including: multi-stage triaxial tests, slake durability tests, and jar slake tests. The following are findings from laboratory tests (Table 1.5.4):

- The principal stress difference of Del Rio Clay and Eagle Ford Shale is not affected by drying-duration, but is related to water content

- The principal stress difference of Taylor Marl and Navarro Shale decreases considerably as drying-duration increases

- The elastic modulus of all four clay shales drops significantly when clay shales are dried and wetted

- The slake durability index (SDI) tends to increase at low water content

- The engineering properties of Edwards Limestone and Austin Chalk are not affected by one cycle of drying and wetting

- Severe slaking of Eagle Ford Shale occurs after 8 hours of air drying and subsequent wetting

- Severe slaking of Del Rio Clay, Taylor Marl, and Navarro Shale occurs after 4 hours of air drying and wetting

In order to estimate the thickness of the degraded zone around the verification core hole, full-scale condition degradation tests were carried out near the City of Dallas, and NX-size investigation cores were obtained for laboratory testing. From extensive laboratory tests and the full-scale degradation condition test, the following determinations were made about the thickness of the degraded zone:

- The thickness of the degraded zone at the perimeter of the verification core does not exceed 12.7 cm (5 in) from the core wall of Eagle Ford Shale

- Based on jar slake test results, the maximum thickness (12.7 cm) of the degraded zone can be assumed for Eagle Ford Shale that is dried for 8 hours or longer and wetted and for other clay shales that are dried for 4 hours or longer and wetted

- The degraded zone at the bottom of drilled shafts is assumed to be reamed out before concrete pouring (Figure 1.6.14)

- The dried clay shales that have not been re-wetted are assumed to be fresh; consequently, the thickness is set to zero

- The maximum thickness (12.7 cm) can be assumed to be identical for all clay shales

- Engineering properties of Eagle Ford Shale is strongly affected by spatial variability

The effect of the verification core on the point bearing capacity of drilled shafts was investigated using finite element method (FEM) software, PLAXIS in Section 3.2. The results from laboratory tests were converted to input material parameters for Mohr-Coulomb failure criterion (Section 3.1). The load-displacement curves at the shaft tip were created from PLAXIS analyses, and the point bearing capacity was obtained at 5%D and 10%D displacement. The capacities btained were used to calculate reduction factors that relate the point bearing capacity of the reference model (without a verification core) with that of "core models" (with a verification core). The reduction factors can be used to check whether the verification core hole will have an impact on shaft capacity. Based on the results of numerical analyses (Section 3.2.3), the following conclusions are drawn:

- The effect of the verification core hole is dependent on the soil formation, core size, drying-duration, and the state of material filling the core hole upon concrete placement

- The reduction of point bearing capacity of "core models" is typically within 10% to a maximum of 14% (for Taylor Marl (Table 3.2.7)) of the capacity of the reference model

- The point bearing capacity of "dry pour" is the largest for all four clay shales tested

- The effect of the verification core hole increases as core size increases

- The effect of dry-duration is more significant in a larger diameter core hole

- Dewatering the verification core hole prior to concrete placement considerably improves the point bearing capacity of drilled shafts

- The point bearing capacity of the reference model tends to be larger at small displacement, while that of the "core model' tends to be larger at large displacement

- The verification core hole augered in weak clay shales such as Del Rio Clay improves the point bearing capacity (c.f. the principal stress difference of Del Rio Clay, which is typically less than 1 MPa)

3.3.2 Recommendations on Drilled Shafts with Verification Core

Design Stage

Running the jar slake test on the founding material is recommended to estimate the extent of degradation upon drying and wetting (Section 1.4.6). The Navarro Shale was the most degradable formation in this study, followed by Taylor Marl, Del Rio Clay, and Eagle Ford Shale in that order. When the drying-duration for severe degradation is defined by the jar slake tests, it is recommended that the founding material not be dried for longer than the defined drying-duration.

The reduction factors listed in Section 3.2.3 can be applied to the point bearing capacity of the reference model to account for the effect of the verification core. However, the reduction factors greater than 1 should be set to 1.

344

Construction Stage

Based on numerical analyses, the author concluded that the verification core hole does not significantly influence the point bearing capacity of drilled shafts. The critical basis for the conclusion is that the verification core hole was always found to be filled with either concrete or sand-gravel mixture (Chapter 2), which have higher shear strength than the tested clay shales. The point bearing capacity for empty verification core holes may be reduced by as much as 65% (Table 3.2.5).

It was found in Chapter 2 that the verification core hole is filled with solid concrete in dry pour. From numerical analyses, it was found that the solid concrete in the core leads to high point bearing capacity from additional side shear resistance developed along the solid concrete. Hence, the effect of the verification core is never detrimental in dry pour. However, even in wet pour, dewatering the verification core hole prior to concrete pour ensures solid concrete filling in the core, which considerably compensates for the loss of point bearing capacity induced by drying and wetting.

3.3.3 Recommendations for Future Study

The following topics may improve the quality of the current study:

- Full-scale load tests can be used to calibrate the assumed input parameters in the numerical model. In particular, the interface coefficient, R, needs calibration to represent a realistic side shear resistance of the verification core

- Full-scale degradation tests on other formations may result in more accurate estimation of the thickness of the degraded zone for individual formations

- More laboratory tests on slurry-soaked specimens are necessary because slurry is frequently used to support the shaft hole wall.

As separate topics related to the current study, the following may be interesting to investigate:

- Use the reduced engineering properties to estimate reduced side shear resistance of drilled shafts. The degradation engineering properties of clay shales are applicable to side shear resistance because drying occurs not only at the verification core hole but also at the shaft hole wall.

- Develop a standard to determine durable rocks and non-durable rocks based on Cation Exchange Capacity and the adsorption isotherm curve

REFERENCES

American Concrete Institute (2008). "Building code requirements for structural concrete," *ACI 318-08 and Commentary*. Farmington-Hills, Michigan, p 107.

Bruce, D. A. (1986). "Enhancing the performance of large diameter piles by grouting," *Ground Engineering*, Vol. 19, No. 4, pp 9-15.

Davisson, M. T. (1972). "High capacity piles," *Proceedings, Soil Mechanics Lecture Series on Innovations in Foundation Construction*. Illinois Section, Chicago: American Society of Civil Engineers, pp 81-112.

Hassan, K. (1994). "Analysis and design of drilled shafts socketed into soft rock." *Ph.D. Dissertation*, Department of Civil Engineering, University of Houston.

O'Neill, M. W., and L. C. Reese (1999). "Drilled shafts: construction procedures and design methods," *FHWA Publication No. FHWA-IF-99-025*. McLean, VA: Department of Transportation, Federal Highway Administration.

PLAXIS Version 8 (2002a). "Finite element code for soil and rock analysis," *Balkema, Rotterdam*.

PLAXIS Version 8 (2002b). "Material models manual," *Balkema, Rotterdam*.

Texas Department of Transportation (2004). "Standard specifications for construction and maintenance of highways, streets, and bridges." Texas.

Chapter 4. FINAL CONCLUSIONS AND RECOMMENDATIONS

Project 0-5825 found that:

1) When shales are first dried and then rewetted and concrete is poured in the wet, the verification core reduces the tip capacity by a maximum of 10% (14% for Taylor Marl)
2) In all other cases, the verification core does not decrease the tip capacity

Therefore, it is recommended that TxDOT should consider modifying the construction practice in shales when verification cores are used by limiting the stand up time between completion of the drilled shaft and placement of concrete. If this modification is not adopted, TxDOT should consider a reduction in point bearing capacity. Minimum core diameter should be 10 in.

Appendix A: Specifications – Materials, tools and various accessories of rocket.

A) Specifications for Steel components used in Rocket

I) 36" diameter steel cylinder

Photograph:

Length: 20'
Inner Diameter: 36"
Wall Thickness: 1/2"
Steel Grade: Extra-Heavy A-500 API-5L Grade B

II) 36" diameter blind flange (top and bottom)

Photograph:

Specifications:

Diameter: 36"
Pressure Rating: #150 (psi)
Thickness: 2 ½"
Steel Grade: SA-105 059-B16.1
No of bolts: 32
Bolt diameter: 1 ½"

III)   36" raised face, slip-on lap joint (top and bottom)

Photograph:

Specifications:

Diameter: 36"
Pressure Rating: #150 (psi)
Thickness: 2.5"
No of bolts: 32
Bolt diameter: 1 ½"
Steel Grade: SA-105 059-B16.1, Forged

B) General Specifications

I) 6" gaskets
Photograph:

Specifications:

Material: Neoprene
Rating: #150 psi
Bolt diameter: ¾"
No of bolts: 8

II) 12" gaskets

Photograph:

Specifications:

Material: Neoprene
Rating: #150 psi
Bolt diameter: 7/8"
No of bolts: 12

III) 36" gaskets

Specifications:

Material: Neoprene
Rating: #150 psi
Bolt diameter: 1 ½"
No of bolts: 32

IV) Clear PVC pipes

Specifications:

    Material: Clear PVC
    Manufacturer: Harvel Plastics, Inc
    Flange Type: 6" – Slip on flange
                12" – Van Stone Flange

Specifications for the PVC Pipes

Type	Inner Diameter in	Wall Thickness	Maximum permissible pressure Psi[20]	Number of bolts in the flange	Bolt size in
6" Schedule 40	6.031	0.280	90	8	¾
6" Schedule 80	6.031	0.432	140	8	¾
12" Schedule 40	11.889	0.406	70	12	7/8

---

[20] Gives the maximum allowable working pressure at a temperature of 73 F. For higher temperatures, de-rating factors specified by the manufacturer need to be used. Detailed specifications can be downloaded from Manufacturer's website.

V) Master flow grout.

MASTERFLOW® 928

Ready-To Use, Non-Shrink, High Strength Grout

Description of Product

MASTERFLOW® 928 is a specially prepared, ready-to-use, non-shrink, high-strength grout. It is formulated for use at any consistency from fluid to damp pack for precision grouting of equipment, concrete systems, structural building members, curtain walls, precast wall panels, beams and columns. It contains natural aggregates and provides a grout that is similar in appearance to concrete and mortar. MASTERFLOW® 928 is the ideal product to use for a natural coloured grout.

Fields of Application

MASTERFLOW® 928 is recommended for:

- Grouting and precision equipment, baseplates, soleplates and columns.
- Grouting applications where shrinkage must be eliminated and where high-strength grout similar in appearance to concrete and mortar is required or desired.
- Non-shrink grouting of precast wall panels, beams and columns.
- Anchoring bolts, reinforcing bars and rods.

Features and Benefits

- A ready-to-use grout that hardens free of bleeding, settlement or drying shrinkage when mixed and placed at any consistency-fluid, flowable, plastic or damp pack.
- A grout that retains good workability upto 1 hour at 20°C.
- A non-shrink grout that can be pumped into intricate areas or areas inaccessible to conventional grouting methods.
- A non-shrink grout for use where a grout similar in appearance to concrete and mortar is required and desired.
- A grout that develops high strengths at flowable consistency without vertical confinement.

Technical Data/Typical Properties

Plastic density	2160 Kgm⁻³
Plastic expansion (ASTM C827)	+0.2%
Hardened expansion(CRD621)	+0.2%
Bleed	Nil
Air content	3.5%
Flexural Strength (BS 6319:Pt7)	7 days 7.5 NMM⁻² / 28 days 8.5 NMM⁻²

Compressive strengths of MASTERFLOW® 928 (at 20%)

Consistency

	Plastic (1) MPa (N/mm²)	Fluid (2) MPa (N/mm²)
1 day	40	29
3 days	58	35
7 days	68	46
28 days	80	60
Average air contents:	4.2%	

(1) 95% flow on flow table , ASTM C230, 5 drops in 3 seconds
Plastic consistency of 3 L water per 25 kg bag MASTERFLOW® 928

(2) 25 -30 seconds flow, by Corps of Engineers Flow Cone Method CRD-C 611 or Cerilh Cone Method
Fluid consistency at 4.6 L water per 25 kg bag MASTERFLOW® 928

Note

The data shown is based on controlled laboratory tests. Reasonable variations from the results shown can be expected. Field and laboratory tests should be controlled on the basis of the desired placing consistency rather than strictly on the water content.

If the work requires that strength tests be made at the jobsite or in the laboratory, do not use cylinder moulds. Consult your MBT Feb Representative or Technical Services Department for special procedures required when mixing and casting cubes of fluid, non-shrink grout for compressive strength tests.

January 2004

REF NO. 0090
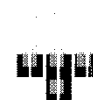
VI) Mix Design for Class C concrete

Mix Design Submittal

Date: **May 16, 2007**
Contractor: **TxDOT**

Mix Design: **#1494**

Mix Description: **Class C TxDOT/ Super/ No Air**

MIX SPECIFICATIONS

Strength: 3600 Psi
Slump: 7" – 9"
Air: 1 to 2% Entrapped
W/C Ratio: 0.40

MATERIALS	SOURCE	ASTM STANDARDS		WEIGHTS
Cement	TXI	ASTM C – 150	I/II	423 LBS
Fly Ash	HEADWATERS	ASTM C – 618	F	141 LBS
Coarse Aggregate	TXI	ASTM C - 33	1"	1887 LBS
Fine Aggregate	TXI	ASTM C - 33		1372 LBS
Admixture	POZZ 80	ASTM C - 494	A	22 OZS
Admixture	PS 1466	ASTM C - 494	F	47 OZS
Admixture		ASTM C - 260		
Max Water				225 LBS

VII) Mix Design for Class SS concrete

Mix Design Submittal

Date: **May 31, 2007**
Contractor: **TxDOT**

Mix Design: **#2440**

Mix Description: **Class SS TxDOT/ Super/ No Air**

MIX SPECIFICATIONS

Strength: 3600 Psi
Slump: 7" – 9"
Air: 1 to 2% Entrapped
W/C Ratio: 0.40

MATERIALS	SOURCE	ASTM STANDARDS		WEIGHTS
Cement	TXI	ASTM C – 150	I/II	428 LBS
Fly Ash	HEADWATERS	ASTM C – 618	F	230 LBS
Coarse Aggregate	TXI	ASTM C - 33	1"	1833 LBS
Fine Aggregate	TXI	ASTM C - 33		1226 LBS
Admixture	POZZ 80	ASTM C - 494	A	26 OZS
Admixture	PS 1466	ASTM C - 494	F	46 OZS
Admixture		ASTM C - 260		
Max Water				262 LBS

VIII) Specifications for Stabilizer used in concrete

BASF

The Chemical Company

Description

Delvo Stabilizer ready-to-use, liquid admixture is used for making more uniform and predictable high-performance concrete. Delvo Stabilizer admixture retards setting time by controlling the hydration of portland cement and other cementitious materials while facilitating placing and finishing operations. It can be used to stabilize returned plastic concrete and concrete washwater to reduce waste and increase profits. Delvo Stabilizer admixture meets ASTM C 494/C 494M requirements for Type B, retarding, and Type D, water-reducing and retarding, admixtures.

Applications

Recommended for use in:

- Stabilization of concrete washwater
- Stabilization of returned plastic concrete
- Stabilization of freshly batched concrete for long hauls
- 4x4™ Concrete
- Pumped concrete, shotcrete (wet mix) and conventionally-placed concrete
- Plain, reinforced, precast, prestressed, lightweight and normal weight concrete
- Pervious concrete

DELVO® STABILIZER

Hydration Controlling Admixture

Features

- Reduced water content required for a given workability
- Retarded setting time characteristics
- Improved workability
- Reduced segregation

Benefits

- Provides flexibility in the scheduling of placing and finishing operations
- Offsets the effects of slump loss during extended delays between mixing and placing
- Reduces waste associated with concrete washwater and returned concrete
- Increased strength – compressive and flexural

Performance Characteristics

Rate of Hardening: The temperature of a concrete mixture and the ambient temperature (forms, earth, air, etc.) affect the hardening rate of concrete. At higher temperatures, concrete hardens more rapidly which may cause problems with placing and finishing.

One of the functions of Delvo Stabilizer admixture is to retard the set of concrete. Within the normal dosage range, it will generally extend the working and setting times of concrete containing normal portland cement, fly ash, slag cement and silica fume approximately 1 hour to 5 hours compared to a plain concrete mixture. This depends on job materials and temperatures. Trial mixes should be made under approximate job conditions to determine the dosage required.

Compressive Strength: Concrete produced with Delvo Stabilizer admixture will develop higher early (within 24 hours) and higher ultimate strengths than plain concrete when used within the recommended dosage range and under normal, comparable curing conditions. When Delvo Stabilizer admixture is used in heat-cured concrete, the length of the preheating period should be increased until the initial set of the concrete is achieved. The actual heat-curing period is then reduced accordingly to maintain existing production cycles without sacrificing early or ultimate strengths.

Guidelines for Use

Dosage: Delvo Stabilizer admixture is recommended for use at a dosage of 4 ± 1 fl oz/cwt (260 $\pm$ 65 mL/100 kg) of cementitious materials for most concrete mixtures using average concrete ingredients. Because of variations in job conditions and concrete materials, dosages other than the recommended amounts may be required. In such cases, contact your BASF Construction Chemicals representative. For concrete washwater and returned concrete stabilization, utilize Delvo charts or the Delvomatic™ software to determine the appropriate dosage rates.

Master
Builders

359

Appendix B: Fabrication drawings for the ROCKET

NOZZLES FOR: COMPRESSOR AND PRESSURE RELIEF VALVE, 2.5 IN DIA

2.5 IN THICK CIRCULAR LID

LUG A; SEE DRAWING V - 3 FOR DETAILS

W 12 X 170 BEAM. SEE DRAWING FR -2 FOR DETAILS

2 PEEK HOLES PLACED DIAMETRICALLY OPPOSITE, 4 IN LONG NOZZLE, 6 IN DIA. SEE V-2 & FR -2 FOR DETAILS

STEEL CYLINDER SHELL THICKNESS 0.5 IN

LUGA: TO SUPPORT VESSEL

$\frac{3}{8}$ IN NOZZLE FOR PRESSURE WASHER

ROUND HSS 8.5 X 0.250

CLEAR PVC PIPE, 6 IN DIA OR 12 IN DIA..

STEEL CABLE (TIE DOWNS)

EVACUATION PORT: 6 IN DIA , 6 IN LONG, CLOSED WITH A BLIND FLANGE

STEEL CABLE (TIE DOWNS)

G.L (FOUNDATION SLAB)

2'-8"

3'-1"

6"

5'

$1'-2\frac{1}{2}"$

9'-4$\frac{1}{4}$"

13'-0$\frac{1}{2}$"

1'-7$\frac{3}{4}$"

7'-2"

20'-7$\frac{3}{4}$"

FOUNDATION PLATE 1.5 IN THICK, 15 X 15 IN. COLUMN WELDED TO THE FOUNDATION PLATE BY $\frac{5}{16}$ IN FILLET WELD.

FOUNDATION SLAB : 10 FT X 10FT (REINFORCED CONCRETE)

6'-6"

7'-8$\frac{3}{4}$"

1'-3"

PEEK HOLE NOZZLE 5 IN DIA, 4 IN LONG

Ø7"

ROUND HSS 8.5 X 0.250

W 12 X 170

45°

4"

R1'-6"

1"

1.5 IN THICK STEEL PLATE 15 X 12 IN

7'-8$\frac{3}{4}$"

-10'-

4'-6"

6'-6"

6'-11$\frac{3}{4}$"

8'-5$\frac{3}{4}$"

STEEL CYLINDER, SHELL THICKNESS 0.5 IN

$\frac{3}{4}$ In A325 BOLT BOLT HOLE $\frac{13}{16}$ IN, 4 BOLTS FOR EACH CENTER PLATE

10'

2'-7$\frac{1}{2}$"

1'-3"

LUG A ELEVATION

SIDE ELEVATION

FRONT ELEVATION

NOTES:

1) LUG CONNECTED TO THE FRAME BY $\frac{3}{4}$ IN DIA A325 BOLTS. BOLT LENGTH = 5IN

2) SEE PLAN VIEW FOR BOLT LOCATION

3) STIFFNER PLATES TO BE PLACED BELOW THE GUSSETS

SUPPORT: W 12 x 170 BEAM

CENTER LINE FOR BOLTS

STIFFNER PLATES 1" THICK. $\frac{5}{16}$" FILLET WELD CONNECTION

$\frac{1}{2}$ IN FILLET WELD ON BOTH SIDES OF BOTH VERTICAL GUSSETS

VESSEL SHELL $\frac{1}{2}$ IN THICK

$\frac{1}{2}$ IN FILLET WELD

CENTER LINE FOR BOLTS IN FLUSH WITH THE BEAM CENTER LINE

STIFFNER PLATES 1" THICK. $\frac{5}{16}$" FILLET WELD CONNECTION

W 12 X 170

2"

3'-6"

1'-3"

1'

1'-8"

4"

1'-2"

1"

$\frac{1}{2}$ IN FILLET WELD

2"

9"

1"

2"

2'-6"

2'-0"

2"

1"

5"

5"

5"

1'-3"

ELEVATION A:

W 12 X 170

ROUND HSS 8.5 X 0.250 COLUMN WELDED TO
BEAM FLANGE BY ⅜" FILLET WELD(DOES NOT
SHOW TRUE ANGLE IN THIS DRAWING)

⅜ IN THICK PLATE FOR REINFORCEMENT
WELDED TO THE BEAM ⅜ IN WELD

⅞ IN A325 BOLTS L = 5 IN

PLAN:

ELEVATION A

W 12 X 170

W 12 X 170

ELEVATION B

ELEVATION B:

HP 12 X 53

HP 12 X 53

⅜ IN THICK PLATE ⅜ IN FILLET
WELD

⅞ IN BOLTS (2) A325

DOUBLE ANGLE CONNECTION
L 1.4 x 4.5"(8) in

FLANGE & BOTTOM LID

	Dwg. No.	Date	
	V - 2	12th APRIL 2007	Revision1: 5th June 07

NOTE: A36 GRADE STEEL

BOTTOM LID

STIFFNER: $\frac{1}{2}$ IN THICK, 7 IN DEEP

Ø3'-5"

BOTTOM STEEL LID: 2.5 IN THICK

12" TO 6" TAPERING NOZZLE FOR CLEAR PVC

Ø1$\frac{1}{16}$"

A325 BOLTS 1.5 IN 32 NOS, L = 7 IN

BOLT HOLE: 1.5 IN DIAMETER

1'-8"

1"

Ø1"

1$\frac{1}{2}$"

5$\frac{3}{8}$"

1'-8$\frac{9}{16}$"

Ø3'-5"

4$\frac{3}{16}$"

1$\frac{1}{2}$"

1'-4"

1'-4$\frac{15}{16}$"

Ø3'-7"

Ø3'-5"

Ø3'-1"

Ø3'

Ø6"

5 IN LONG NOZZLE (EVACUATION PORT)

A325 Bolts 1.5 In, 32 nos , L = 7IN

BOLT HOLE: 1.5 IN

PLAN VIEW

STIFFNER: $\frac{1}{2}$ IN THICK, 7 IN DEEP

2$\frac{1}{2}$"

4"

1'-9$\frac{1}{2}$"

1'-3$\frac{1}{2}$"

6$\frac{5}{8}$"

1"

TAPERING NOZZLE FROM 12" ID TO 6" ID

6"

3'-7"

4$\frac{1}{2}$"

4"

7"

5 IN LONG NOZZLE (EVACUATION PORT)

SECTION B-B

BOTTOM FLANGE

Ø3'-7"

3"

4"

TRIANGULAR STIFNERS: 6 IN HIGH, 3 IN BASE, $\frac{1}{2}$" THICK. FILLET WELDED TO THE SHELL AND FLANGE WELD SIZE $\frac{3}{8}$ IN

1$\frac{3}{4}$"

PLAN VIEW

PEEK HOLE OPENINGS

STEEL SHELL THICKNESS 0.5 IN

FILLET WELD $\frac{3}{8}$ IN

TRIANGULAR STIFNERS: 6 IN HIGH, 3 IN BASE, $\frac{1}{2}$ IN THICK. FILLET WELDED TO THE FLANGE AND SHELL

1"

6"

3'

3'-7"

2"

1"

6"

4"

6"

1'-6$\frac{1}{2}$"

SECTION A-A

NOTE: SEE DRAWING V-1 FOR FLANGE WELD DETAILS.

	FD – 1	21ST MAY 2007
	Dwg. No.	Date

PLAN (BOTTOM)

10'

12'

8"

12'

PLAN (TOP)

10'

10'

12'

12'

10'

CROSS SECTION (TYP)

10'

1'

FLUSH WITH
CURRENT
PAVEMENT
LEVEL

NOTE:

1) ALL REBARS ARE #4 SIZE
NOMINAL DIAMETER = 0.5"

2) CLEAR COVER = 1"

3) CONCRETE STRENGTH = 4000 psi

367

Appendix C: Video DVD

Appendix D: Photographs DVD